



MONASH University

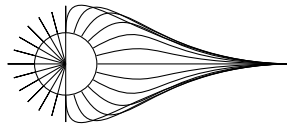
SPECTROSCOPIC INVESTIGATION OF THE
SOLAR ATMOSPHERE

Daniela Adriana Lăcătuș

School of Mathematical Sciences
Monash University
Australia
2018



SPECTROSCOPIC INVESTIGATION OF THE SOLAR ATMOSPHERE



Thesis submitted to Monash University,
in fulfilment of the requirements for the degree of
Doctor of Philosophy

by

Daniela Adriana Lăcătuș
M.Sc. B.Sc.

Main Supervisor: Dr. Alina Donea
Associate Supervisor: Prof. Paul Cally

© Daniela Adriana Lăcătuș 2018

I certify that I have made all reasonable efforts to secure copyright permissions for third-party content included in this thesis and have not knowingly added copyright content to my work without the owner's permission.

“The surface of the Earth is the shore of the cosmic ocean. On this shore we’ve learned most of what we know. Recently, we’ve waded a little way out, maybe ankle-deep, and the water seems inviting. Some part of our being knows this is where we came from. We long to return, and we can because the cosmos is also within us. We’re made of star stuff. We are a way for the cosmos to know itself.”

Carl Sagan

Abstract

Solar flares are the most energetic events that take place in our small corner of the Universe, releasing $\sim 10^{32}$ erg in a matter of a few seconds. Some of the energy is carried away from the Sun by accelerated plasma and high energy radiation. The rest of the energy is transported to the lower atmospheric layers by non-thermal particles ionizing the medium they go through. The energy is thus converted to radiation and the effect is seen as emission enhancements in chromospheric and transition region lines.

Observations of the solar atmosphere in broad-band filters have long been used to understand the global evolution of the different structures. However, these filters contain contributions from multiple elements, thus a straightforward correlation between the plasma parameters and the observed intensity can be misleading. Spectroscopy reveals the emission in the corresponding spectral profile, in which different line contributions can be easily identified. The interpretation is now limited only by complications inherent to the formation of each spectral line.

We focused on the emission of the lower atmosphere as seen in the emission lines recorded by the *IRIS* mission, with special emphasis on the evolution of the Mg II *k* and *h* resonance lines. The source function of these lines varies with wavelength and depends on the optical depth, therefore, they sample a wide range of atmospheric conditions, from the photosphere as seen in the far wings to the high chromosphere at line centre.

The need to establish a baseline of emission characteristics prompted a detailed analysis of quiet sun conditions, in different magnetic environments, in order to extract network and inter-network emission characteristics. Their photospheric acoustic signal was also investigated.

The flare analysis was centred on the evolution of emission in different stages of the flare development. We analyse the triggering mechanism, line enhancements and the subsequent relaxation of the atmosphere. The acoustic signatures were also investigated and their relation to the overlying atmosphere was highlighted.

One of the flares in our analysis was followed by a peculiarly long lived and broad emission in most of the observed lines. We employed analytical methods to identify the processes that can create such a profile and establish some of the characteristics of the emitting plasma.

Abbreviations

AR	Active region
CH	Coronal Hole
QS	Quiet Sun
PF	Post flare
TR	Transition Region
UV	Ultraviolet
NUV	Near Ultraviolet
FUV	Far Ultraviolet
EUV	Extreme ultraviolet
SXR	Soft X-Ray
HXR	Hard X-ray
R_{\odot}	Solar radius
FOV	Field of view
AU	Astronomical unit
LOS	Line of sight
LTE	Local Thermodynamic Equilibrium
MHD	Magneto-hydro-dynamic
IRIS	Interface Region Imaging Spectrograph
SG	Spectrograph onboard IRIS
SJI	Slit-Jaw Imager onboard IRIS
SDO	Solar Dynamics Observatory
AIA	Atmospheric Imaging Assembly onboard SDO
HMI	Helioseismic and Magnetic Imager onboard SDO
RHESSI	Reuven Ramaty High Energy Solar Spectroscopic Imager
GOES	Geostationary Operational Environmental Satellite
Hinode	Japanese Solar-B mission

Monash University

Thesis including published works declaration

Declaration for thesis based or partially based on conjointly published or unpublished work

I hereby declare that this thesis contains no material which has been accepted for the award of any other degree or diploma at any university or equivalent institution and that, to the best of my knowledge and belief, this thesis contains no material previously published or written by another person, except where due reference is made in the text of the thesis.

This thesis includes two (2) original papers published in peer reviewed journals and three (3) original papers in preparation.

The main theme of this thesis is the effect of solar conditions, from quiet Sun to dynamic active regions, on the emitted spectral profile.

The ideas, development and writing up of all the papers in the thesis were the principal responsibility of myself, the candidate, working within the School of Mathematical Sciences under the supervision of Dr. Alina Donea and Prof. Paul Cally.

The inclusion of co-authors reflects the fact that this work came from active collaboration between researchers and acknowledges input into team-based research.

My contribution to the published papers involved the following:

Th. Chap. /Sec	Publication title	Status	Nature and % extent of candidate's contribution	Co-authors nature and % extent of contribution	Co-author Monash student
3	Chromospheric and photospheric characteristics of quiet sun conditions	not submitted	75% Key ideas, data analysis and interpretation, analytical calculations, writing and editing of paper.	A.Donea 20%: acoustic analysis and interpretation, draft review; C. Lindsey 5%: discussion	No No
4.1	On the flare and filament eruption of 11 March 2015: from photosphere to corona	not submitted	85% Key ideas, data analysis and interpretation, analytical calculations, writing and editing of paper.	A. Donea 15%: acoustic analysis, draft review.	No
4.2	On the weak seismicity of the 29 March 2014 solar flare	not submitted	50% Key ideas, upper atmosphere data analysis and writing relevant section of the paper.	A. Donea 45%: key ideas, interpretation and photospheric analysis, writing section draft; P. Cally 5%: discussions	No No
4.4	Are All Flare Ribbons Simply Connected to the Corona?	Published 2017 ApJ 838, 138J	25%: Data analysis, writing and editing for relevant section of paper.	P. Judge 25%: interpretation and analytical work, paper editing; A.R.Paraschiv 45%: magnetic field analysis and section writing; A. Donea & C. Lindsey 5% discussion	No Yes No
5	An Explanation of Remarkable Emission-line Profiles in Post-flare Coronal Rain	Published 2017 ApJ 842, 15L	85% Key ideas, data analysis and interpretation, analytical calculations, writing and editing of the paper.	P. Judge 10%: analytical calculations and draft review; A. Donea 5% discussion	No No

I have renumbered and reordered sections of submitted or published papers in order to generate a consistent presentation within the thesis.

**Candidate's
Signature**

	Date 30.09.2018
---	---------------------------

The undersigned hereby certify that the above declaration correctly reflects the nature and extent of the candidate's contributions to the published work. In instances where I am not the responsible author I have consulted with the responsible author to agree on the respective contributions of the authors.

**Main Supervisor's
Signature**

	Date 30.09.2018
---	---------------------------

Table of Contents

Outline

1	Introduction	1
1.1	The Sun in Time	1
1.2	The Modern Sun	2
1.3	Line emission	5
1.4	Formation of the Mg II lines	7
1.5	The Mg II lines in history	10
2	Observational Data, Calibrations and Analysis Techniques	13
2.1	Interface Region Imaging Spectrograph	13
2.1.1	Residual thermal correction	15
2.1.2	Absolute intensity calibration	15
2.1.3	Profile moments	16
2.1.4	Profile features identification	17
2.2	Solar Dynamics Observatory	19
2.2.1	Helioseismic Magnetic Imager Data for Helioseismic Holography	21
2.3	Additional Data	22
3	Statistics of Quiet Sun Emission	25
3.1	Introduction	26
3.2	The Data	28
3.3	Spectral Analysis	30
3.3.1	Mg II moment maps	31
3.3.2	Mg II emission features	34
3.3.3	Magnetic field correlation	39
3.3.4	Statistical Properties	39
3.4	Photospheric acoustic analysis	42
3.4.1	Results	43
3.5	Summary and Discussion	46
4	Flaring Atmosphere Spectroscopy	49
4.1	Introduction	50
4.2	March 11, 2015 X2.1 flare	51
4.2.1	High energy emission	54
4.2.2	Spectral signatures in <i>IRIS</i> data	56
4.2.3	Filament eruption	63
4.2.4	Emission Measure analysis	65
4.2.5	Magnetic field evolution	66
4.2.6	Seismic activity	68
4.3	March 29, 2014 X1.0 flare	73
4.3.1	Seismic activity	75

4.4	Disconnected chromospheric ribbon	77
4.5	Summary and Discussion	79
5	Peculiar Profiles in Coronal Rain	83
5.1	Introduction	83
5.2	Observations	86
5.3	Analysis	91
5.3.1	Summary of observed properties	91
5.3.2	A reference model	92
5.3.3	Strand optical depths	93
5.3.4	Background opacities near 2800 Å	94
5.3.5	$k:h$ ratio and radiation anisotropy	95
5.3.6	Frequency-integrated intensities	96
5.3.7	Doppler widths and shifts	96
5.3.8	Mg II h and k and the $3d - 3p$ transitions	97
5.3.9	Dielectronic recombination	97
5.3.10	Sudden onset of post-flare coronal rain emission.	98
5.3.11	Origins of the broad lines	99
5.4	Discussion	99
6	Conclusions and Prospects	101
	References	105
	Appendices	I
	List of Figures	I
	List of Tables	VII



Outline

The present work focuses on the influence of impulsive events on the solar atmosphere as deduced from the spectral analysis of chromospheric and transition region lines. We first consider the simplified set of conditions as described by the quiet sun properties in order to strengthen our understanding of flaring introduced changes. The large scale destabilisation of the atmosphere as a consequence of the reconnection is also explored.

A short introduction is included in **Chapter 1**. The evolution of our view of the Sun as a star up to the present day, when we still do not have a complete understanding of most of the processes that take place, is presented. The layers of the solar atmosphere are discussed, with an emphasis on their characteristics as deduced from observations. The second part of the chapter will focus on the formation of line emission and will provide an overview of the Mg II transitions, together with important landmarks in understanding these lines.

An overview of the data used in this study is provided in **Chapter 2**. The focus falls on the *IRIS* data, both spectral and context imagery. The observational details of the instrument are reviewed and the calibrations applied are discussed, namely residual orbital variations and absolute intensity computation. The profile moment and quartile analyses are discussed as data analysis techniques. Data from other instruments is also used, therefore a brief description of the instrument and the data products is included.

Chapter 3, contains a discussion of the quiet sun emission as seen in the emission of the Mg II resonance lines. We employ a statistical analysis approach in order to determine cross correlation between different observational characteristics, in order to establish a baseline for the analysis of the flaring atmosphere in the subsequent chapters. The acoustic emission of the underlying photosphere is also considered.

In **Chapter 4**, the behaviour of the flaring solar atmosphere is investigated in detail for the X2.1 flare of March 11, 2015. We explore the triggers, evolution of the spectral emission, as well as the acoustic signatures of flares. The magnetic field configuration and its role in the eruption is also discussed. Special consideration is given to the propagation of energy from the reconnection site to the lower atmosphere, but the impact of the flare on the heliosphere is not ignored. In addition to the large X-class flare analysed, we also explore the connectives of a small chromospheric flare to the overlying corona.

Chapter 5, analyses the broad, red-shifted and long lasting peculiar emission profiles observed in the wake of a strong X-class flare in chromospheric and transition lines. Given the observational characteristics we deduce that we are faced with some kind of coronal rain phenomena. As the profiles are unlike any previously seen, we take some inspiration from recent high resolution observations, and employ analytical methods to probe the conditions and properties of the atmosphere that may give rise to such profiles. By elimination, we are able to construct a consistent explanation of the peculiar profiles as the result of unresolved Alfvénic motions within the falling plasma, generated in the impulsive phase of the flare that slowly decay to radiation.

The last chapter, **Chapter 6**, discusses the results of the present work in the context of the current state of the field of solar physics, and draws some concluding remarks. It also puts forward some potential future projects and challenges.

Chapter 1: Introduction

“...for in the sciences the authority of thousands of opinions is not worth as much as one tiny spark of reason in an individual. Besides, the modern observations deprive all former writers of any authority, since if they had seen what we see, they would have judged as we judge.”

Galileo Galilei

The key concepts for understanding the solar atmosphere, solar events and their line emission will be summarised in this chapter. A short historic introduction to solar observations is also included in order to put the recent advancements into context. The solar layers are described with their most important properties, as well as some puzzling headaches that still linger in our understanding of the Sun. The formation of line emission in general and of the Mg II lines in particular is briefly reviewed, together with a historical overview of important landmarks in the observation and modelling of the Mg II emission.

1.1. The Sun in Time

For most of human history, the Sun had been taken for granted as an eternal source of light and in most cultures it was worshipped as a life-giving God. Its sudden disappearance, during solar eclipses, was a cause of panic and dread for the onlookers. The Sun’s perfection remained undisputed for a long time, but humans are curious creatures and started to notice ‘holes’ in the face of the mighty Sun. Some ancient cultures had some sparse drawings of such irregularities, but the Chinese were the first to systematically write down about such observations, when near sunset or sunrise, the face of the Sun seemed to carry some dark patches, usually thought to be birds, but always a bad omen.

The nature of these patches remained a mystery and even their existence was ignored or forgotten until quite recently, in the 17th century, when the telescope was first used to look at the sky. Many observers started pointing the new instrument at the Sun and saw dark spots on the projected image. Some thought that they may be some yet unseen satellites of the Earth or small planets, as the idea of an imperfect Sun was too hard to fathom. Galileo (1613) took a giant’s step by challenging the perfection and placing the spots on the face of the Sun. Based on impressively detailed observations, he noted that the spots moved together in a coherent manner, crossing the disk in about a month, changed their shape as they move, and when they were close to the edges of the disk. Using geometric reasoning he concluded that they can not be far from the surface. Figure 1.1 contains one of his drawings, showing a large and complex sunspot group toward the lower left of the image, together with a number of smaller sunspots, distributed across the solar disk.

Two more centuries of slow progress followed, while we got used to the idea of a changing Sun (and that the Earth is no longer the centre of things) and got better and better at building

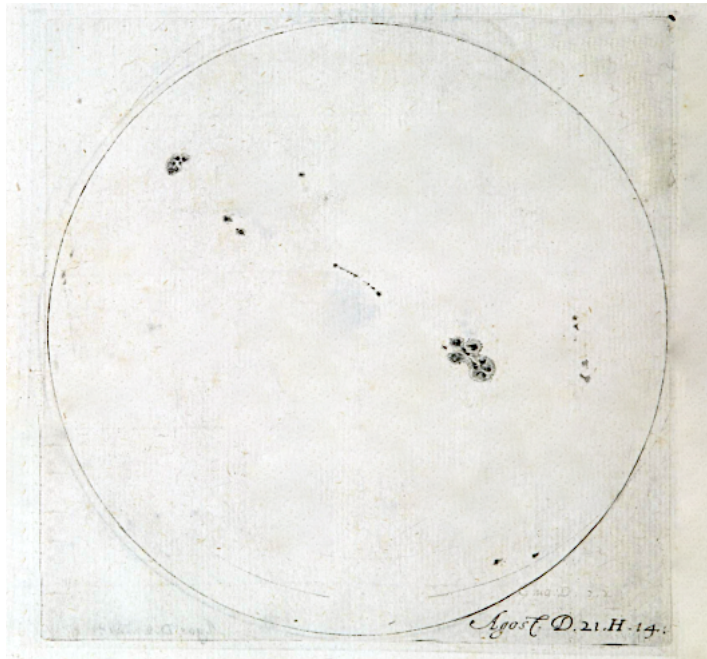


Figure 1.1: Drawing of the solar disk with a number of sunspot groups present, excerpt from [Galileo \(1613\)](#) catalogue of solar observations.

telescopes. As our instrumentation and understanding of the physical processes evolved we continued to find new ways to dissect the light from the Sun and extract intimate details about the composition and conditions in the different layers. We built models that we slowly amended and corrected over time and, with the advancements in computing, we can use our theories to recreate some of the solar conditions and events in complicated, computationally expensive, simulations.

However, comparing the simulation results with the solar conditions remains challenging, since our models and theories are far from realistic. We aim at a complete and exhaustive description of all the processes and their inter-relations, so we keep gathering clues. The Sun has lost its God status, but its role as a life-giver still endures. We now know quite satisfactory how the Sun has influenced our evolution and how it can still affect our modern lives. The road to our current level of understanding, started by meticulous observers and by open-minded and persistent individuals, still continues over the horizon.

1.2. *The Modern Sun*

The Sun is an average star of G2 V spectral type, with a surface temperature of 5770 K, located in one of the spiral arms of an average galaxy, in an ever expanding Universe. In terms of mass, it is made of 71.5% Hydrogen, 27.1% Helium, while all the other elements sum up to a mere 1.4% ([Asplund et al., 2009](#)). Although seemingly small, the percentage of heavy elements is higher than that of most stars. The high metallicity is due to the Sun being a second generation star, formed ~ 5 billion years ago from the collapse of a cloud of dust and gas, containing the remains of first generation stars. The Sun will shine for another ~ 5 billion years, becoming brighter as it gradually runs out of fuel and turns into a red giant. Eventually, the core's grasp on the outer layers will decay and the outer envelopes will expand to form an ephemeral planetary nebula, while the core will endure as a white dwarf slowly fading away.

The interior structure of the Sun has long been a mystery, but by studying the solar oscillations and how these waves propagate, we have been able to identify the different layers. We now have models and theories that provide good explanations for the observed characteristics. Based on such models we can better understand the evolution of the sun as a star, the formation of heavier elements, and its ultimate demise as it runs out of nuclear fuel.

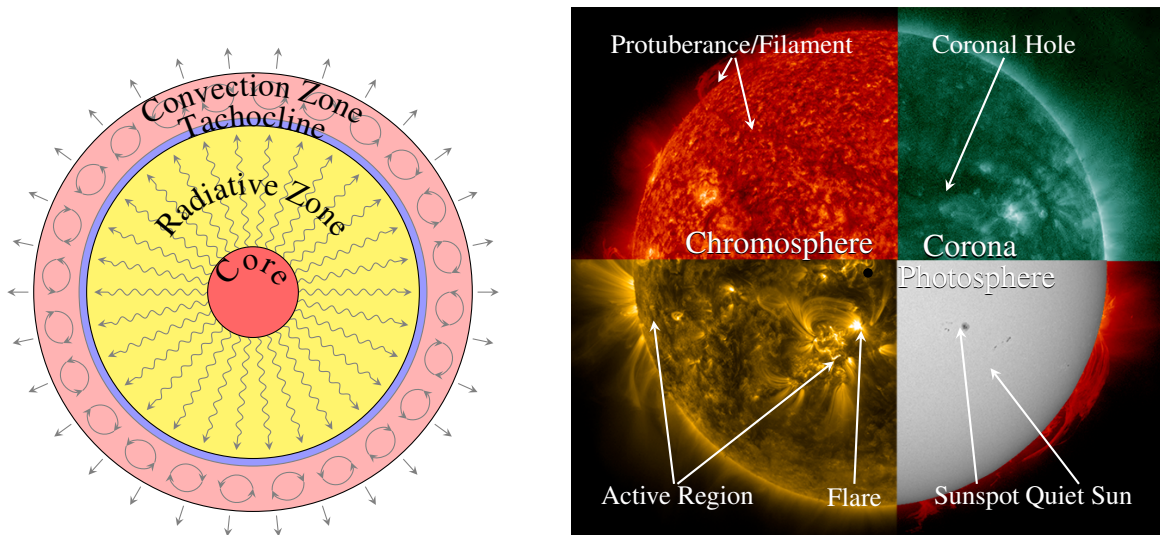


Figure 1.2: *Left Panel:* Schematic of the layers of the solar interior. The energy from the nuclear fusion in the Core is transported outwards by collisions within the Radiative Zone, then by convective motions in the Convection Zone, before finally escaping at the solar surface, the photosphere. The transition from radiative to convective dominated transport takes place the thin Tachocline. *Right Panel:* Solar atmospheric layers. The Photosphere, with its sunspots, the complicated Chromosphere, and the hot Corona with its active regions.

The left panel of Figure 1.2 contains a schematic representation of the solar interior layers and the dominating mode of energy transport within that layer.

The *Core* is the innermost part of the Sun, extending up to $0.2 R_{\odot}$ (solar radius), but containing more than half of the solar mass. Under the effect of huge gravitational forces the material here reaches unimaginable pressures of $10^{17} \text{ dyn cm}^{-2}$ (some 250 billion times the atmospheric pressure we feel on Earth) and temperatures exceeding 10^7 K . These extreme conditions are enough to ignite hydrogen fusion. This reaction produces helium and is accompanied by the release of energy as photons and neutrinos.

The photons thus produced then start their million of years journey colliding their way through the *Radiative zone*, which extends from $0.2 R_{\odot}$ to $0.7 R_{\odot}$. The length of the journey is given by the high density of this medium, which makes the mean free path between collisions small, meaning the photon goes through billions of interactions, being absorbed and re-emitted, not always in the right direction, before the medium conditions change.

The *Tachocline* is the thin interface layer that constitutes the transition from the purely radiative interior to the convective envelope subjected to differential rotation. This layer is thought to play an important role in dynamo theories dealing with the formation of the solar magnetic field.

As the temperature decreases near the top of the radiative zone, metals (anything heavier than Helium) go through recombination, increasing the opacity of the medium. Therefore radiation is no longer an efficient energy transport mechanism, leading the development of instabilities that cause the formation of convection cells. These cells lift hot plasma to the surface where it radiates some of its energy, thus cooling, before falling back to heat again, thus repeating the cycle. This is the *Convection zone*, reaching from $0.7 R_{\odot}$ to the bottom of visible solar surface, and plays a crucial role in the formation of all the observed solar features.

The solar atmospheric layers have been defined based on temperature and density characteristics, but their boundaries are not smooth surfaces, but are influenced by the local conditions. The right panel of Figure 1.2 highlights some of the important features that can be seen in the different atmospheric layers, from the photospheric quiet sun to the flaring corona.

The *Photosphere* starts where the bubbling plasma becomes transparent to radiation, the

so called $\tau = 1$ surface, and extends up to about 500 km, where the temperature reaches a minimum, $T_{\min} = 4400$ K. It is characterised by a smooth decrease in density and temperature, with the transport of energy between particles being ruled by collisions. The most notable features in this layer are caused by deep rooted concentrations of magnetic field poking their twisted structures through the surface, inhibiting convection and giving rise to regions of cooler plasma: the sunspots. In intensity continuum images they are seen as a dark core, called umbra, surrounded by slightly lighter penumbral region. The solar activity cycle has been measured using the variation of the number and complexity of sunspots. What we describe as quiet sun conditions is dominated by granulation, which was the first non-uniformity observed and studied (Gibson, 1973). Another feature is produced by groups of granulae, forming ~ 2 Mm supergranular structures, that host in their boundaries small concentrations of magnetic field.

The *Chromosphere* is the second layer, extending from the T_{\min} up to about 2000 km. Its existence was first noted as reddish structures at the disk edges during solar eclipses, produced mainly by hydrogen emission. The density continues to drop smoothly, while the temperature increases to some 10^4 K in the first 500 km, followed by an extended temperature plateau. The plateau results from the fickle balance between the non-radiative heating and radiative losses, mainly of singly ionised ions (Mg II, Ca II, etc.). The chromosphere appears as highly structured small scale features produced by the presence of magnetic field and is optically thick in most emission and absorption lines. This makes the interpretation of observations challenging, as the emitted light is only loosely related to the plasma conditions. Important features in this layer are the enhanced emission surrounding magnetic field concentrations, from sunspots to the fainter network overlaying the supergranular boundary.

The *Transition Region*, is as its name suggests, is a very thin layer of only ~ 100 km hosting the sudden change, from the mildly hot chromosphere to the scorching temperatures of the corona. The temperatures increase from 10^4 K to some 10^6 K, while the density continues to drop. Part of the reason for the sudden temperature increase is the total ionisation of neutral hydrogen (H I), that is the dominant element in the cooling of plasma. With its total ionisation, no other element is abundant enough to take up radiative cooling duties. Most of the other elements are also further ionised, and no longer provide efficient cooling.

The *Corona* is the outermost layer of the solar atmosphere and extends out into the heliosphere. Before modern observations, it could only be seen as faint emission around the solar disk in total eclipse observations. The temperatures here are of the order of 10^6 K, but the density is low. The high temperature means that everything is highly or fully ionised, with line emission from highly ionised iron being a matter of mystery for a while in the past. The high ionisation of the plasma imposes the frozen in field conditions: the magnetic field traps the plasma and they move together. Radiation from these ionised ions and thermal conduction dominate cooling. This leads to magnetic structures clearly visible in coronal emission. Continuous observations of this layer reveal a very dynamic environment, with extended loop structures connecting regions of intense activity. The evolution and interconnectivity of these structures can destabilize due to a number of reasons, from relative motions to the appearance of new magnetic field concentrations, and produce solar flares. These are reconnection events that allow the release of some of the stored energy and the relaxation of the overall structure.

One would expect the temperature to decrease uniformly when moving away from the solar surface, but observations show that this is true only for a brief interval, before increasing again, first slowly, then abruptly to reach coronal temperatures similar to those in the solar core. This behaviour has sparked a long standing debate in the community centred around the process responsible for transporting energy from the photosphere to the corona, capable of sustaining these high temperatures. The top candidates for solving this debate are the wave and the nanoflare heating mechanisms (see reviews of Nakariakov and Verwichte (2005) and

Parnell and De Moortel (2012)). The first proposes that waves excited in the photosphere carry energy along the magnetic field lines, energy that gets dissipated in the high atmosphere. The second relies on ubiquitous small scale reconnection events to continuously inject energy into the corona. While both models can produce the high temperatures observed, they are both under the detection limit of current observations, furthermore, the heating may be a result of both these processes acting together.

1.3. Line emission

The formation of emission lines from different solar layers is governed by the conditions inherent to that layer (density, pressure, etc.) which affect the distribution of energy of sources or sinks. In order to understand how these are connected we need to delve into how different radiative processes work and how they come together to produce the observed emission profiles.

The intensity measured at a given wavelength (I_λ) is the result of integrating the number of photons, all having the same energy, recorded in a given temporal interval, on a small cross-sectional area, in a given solid angle, thus it is measured in units of $\text{erg s}^{-1} \text{cm}^{-2} \text{sr}^{-1} \text{\AA}^{-1}$. By summing the emission over multiple wavelengths we obtain the integrated intensity in units of $\text{erg s}^{-1} \text{cm}^{-2} \text{sr}^{-1}$. The intensity at a given frequency (I_ν) can be calculated from $I_\lambda = I_\nu c/\lambda^2$, where c is the speed of light.

As the radiation passes through a given layer, photons of a given wavelength can be absorbed or can lead to additional emission within the layer, or can be entirely scattered out of the beam. The change in the emission intensity along a geometric length ds is given by the radiative transfer equation

$$\frac{dI_\lambda}{ds} = j_\lambda - I_\lambda \alpha_\lambda \quad (1.1)$$

where j_λ is the monochromatic emissivity, or how much radiation is added to the beam, and α_λ is the monochromatic linear extinction, or how much of the radiation is absorbed or scattered within the medium (the sum of the κ_λ absorption and σ_λ scattering coefficients). Dividing equation (1.1) by the extinction coefficient we obtain: the ratio between the emissivity and extinction coefficients representing the source function of that medium, S_λ , and the product between the extinction coefficient and the geometric path length defining the monochromatic optical depth variation, $d\tau_\lambda = -\alpha_\lambda ds$. The optical depth is considered to increase in the opposite direction to the geometric direction, as it is considered from the observer's vantage point. The transfer equation then becomes

$$\frac{dI_\lambda}{d\tau_\lambda} = I_\lambda - S_\lambda \quad (1.2)$$

Solving this first order differential equation we obtain the formal solution of the transfer equation, describing the intensity after its passage through the medium, with $\tau_{\lambda,0} > \tau_\lambda$, as

$$I_\lambda(\tau_\lambda) = I_{\lambda,0} e^{-(\tau_{\lambda,0} - \tau_\lambda)} + \int_{\tau_\lambda}^{\tau_{\lambda,0}} S_\lambda(t) e^{\tau_\lambda - t} dt \quad (1.3)$$

where $I_{\lambda,0}$ is the initial intensity in front of the medium and dt is a small optical depth interval within the medium.

If the source function of the medium is zero we are left only with the first term on the RHS which gives an intuitive description of the optical depth as being a measure of the transparency of a medium, representing the fraction of light not scattered or absorbed ($I/I_{\lambda,0} = e^{-\Delta\tau_\lambda}$, where $\Delta\tau_\lambda = \tau_{\lambda,0} - \tau_\lambda$). If $\Delta\tau_\lambda > 1$, the material is considered to be optically thick, as most photons cannot pass through without being scattered or absorbed. The observed intensity will be purely given by the source function of the medium. When $\Delta\tau_\lambda < 1$, the material is considered to be optically thin and most photons can escape without interaction.

In the case of the Sun a semi-infinite plane-parallel approximation of the low atmosphere is adequate, therefore the intensity observed will be influenced by the angle ϑ , between the line-of-sight (LOS) and the direction of propagation, namely by $\mu = \cos \vartheta$. Thus the emergent intensity at $\tau_\lambda = 0$ and $\mu > 0$ will be

$$I_{\lambda,0}(\mu) = \int_0^\infty S_\lambda(t) e^{-t/\mu} dt/\mu \quad (1.4)$$

The Eddington-Barbier approximation states that the emergent intensity is given by the source function from the location where the optical depth is equal to μ : $I_\lambda(0, \mu) \approx S(t = \mu)$.

In Local Thermodynamic Equilibrium (LTE) conditions of high densities and optical depths, the source function can be assumed to be equal to Planck function

$$B_\lambda(T) = \frac{2 h c^2}{\lambda^5} \frac{1}{e^{hc/\lambda k_B T} - 1} \quad (1.5)$$

where h is the Planck constant, k_B is Boltzmann constant and T is the temperature of the plasma.

However, in the case of the solar chromosphere, non-LTE conditions dominate. The source function depends on both temperature and the radiation field, namely on both the Planck function and on the mean intensity $J_\lambda = 0.5 \int_{-1}^1 I_\lambda d\mu$, as

$$S_\lambda = \epsilon_\lambda B_\lambda + (1 - \epsilon_\lambda) J_\lambda \quad (1.6)$$

where $\epsilon_\lambda = \kappa_\lambda/\alpha_\lambda$ is the destruction probability of a photon and the mean intensity $J_\lambda = \Lambda[S_\lambda]$, computed using the monochromatic Lambda operator Λ , first proposed by [Scharmer \(1981\)](#).

Based on [Carlsson and Stein \(1997\)](#) the emergent intensity along the line of sight is

$$I_\lambda = \frac{1}{\mu} \int \frac{\alpha_\lambda}{\tau_\lambda} S_\lambda \tau_\lambda e^{-\tau_\lambda/\mu} ds \quad (1.7)$$

The equation can be divided in three terms: the source function S_λ , the $\alpha_\lambda/\tau_\lambda$ term which is sensitive to mass motion and the attenuation term $\tau_\lambda e^{-\tau_\lambda/\mu}$, that peaks near $\tau_\lambda = 1$.

In non-LTE condition the detailed balance of level populations and the interactions of the radiative field with the different elements in the composition of the plasma becomes important. Line emission is obtained when an electron moves from an upper to a lower bound energy level of an atom or ion, and releases a photon equal to the energy difference between the two layers. But in order to determine the electronic configuration, we need to understand how the element can be excited to a higher energy level and, because the elements can not be treated individually, but as statistical entities, we need to understand how the equilibrium between emission and absorption is achieved. The Einstein coefficients are the mathematical constructs used to describe the transition probability between different energy levels of an element.

Spontaneous radiative de-excitation is the process through which an electron in an upper excited level (u) emits a photon and decays to a lower energy level (l). A_{ul} is the Einstein coefficient for spontaneous de-excitation and measures the transition probability from state u to l , per second, per particle in level u . It is summed over the whole profile, providing transition probability for the whole line. The spontaneous de-excitation rate per cm^{-3} is given by $n_u A_{ul}$.

Radiative excitation refers to the process through which an electron in a lower level absorbs a photon and jumps on a higher energy level corresponding to the energy of the incoming photon. The Einstein coefficient for this transition, B_{lu} , measures probability of such a transition occurring.

Induced radiative de-excitation consists of the decay of an electron to a lower energy level by photon emission in the presence of an external radiative field. B_{ul} describes the probability of this process.

Collisional excitation refers to the induced jump to an upper energy level of an electron initially on a lower level as a consequence of energy exchange during a collision with a

free electron. A portion of the kinetic energy of the incoming electron is transferred to the bound electron and used to jump to a higher energy level. C_{lu} gives the number of collisional excitations from l to u per second per number of particle in state l .

Collisional de-excitation describes the energy exchange between a bound electron and a free one, when the bound particle loses energy to the free particle and decays to a lower energy level. C_{ul} represents the number of collisional de-excitations from the higher energy level to the lower one, per second, per particle in excited state u .

When the de-excitation process is independent on the process that brought the atom in the excited state we are dealing with complete redistribution (CRD), the electron has no memory of previous interaction, thus it can be re-emitted anywhere in the line. If previous interaction can influence the resulting emission we are dealing with a partial redistribution (PRD) formalism for the emitted wavelength.

For collisional processes the transition rate between level a and b (where a and b can be either the upper or lower energy level) is given by

$$n_a C_{ab} = n_a N_e \int_{v_0}^{\infty} \sigma_{ab}(v) v f(v) dv \quad (1.8)$$

where n_a is the number of particles in energy level a , N_e the electron density in the medium, $\sigma_{ab}(v)$ is the electron collision cross-section and $f(v)$ is the normalised velocity distribution (usually Maxwellian). (Rutten, 2003)

The relations between the Einstein coefficients are given by the Einstein relations

$$\frac{B_{lu}}{B_{ul}} = \frac{g_u}{g_l} \quad (1.9)$$

$$\frac{A_{ul}}{B_{ul}} = \frac{2h\nu_{lu}^3}{c^2} \quad (1.10)$$

$$\frac{C_{ul}}{C_{lu}} = \frac{g_l}{g_u} \exp(-h\nu_{lu}/k_B T) \quad (1.11)$$

where g_l and g_u are the statistical weights of the energy levels, and are equal to $2J + 1$ (J is the angular momentum quantum number) and ν_{lu} is the frequency of the photon resulting from the transition.

In practice, the collisional excitation rate is given by

$$C_{lu} = \frac{8.63 \times 10^{-6} \Upsilon(T_e)}{g_u \sqrt{T_e}} \quad (1.12)$$

where the constant is from Maxwellian integration of cross sections over all thermal speeds making Υ (the effective collision strength) a function of T_e only (Gabriel and Jordan, 1971).

All the possible transitions between a two-level atom and their corresponding Einstein coefficient are schematically presented in Figure 1.3.

1.4. Formation of the Mg II lines

Magnesium (Mg) is one of the most abundant chemical elements and is 18 times more abundant than Calcium (Ca) in the solar chromosphere, and thus it provides information about regions higher in the solar atmosphere and is more sensitive to the variations of the chromospheric conditions. The chromosphere has long been observed in H α and Ca II H and K emission, both of which lie at the edge of the visible part of the electromagnetic spectrum. Observations of the Mg II lines have only recently become routinely performed. Some of the most important lines of the singly ionised ion, Mg II, are the h and k resonance lines and the subordinate triplet lines, all located around 2800 Å in the near ultraviolet (NUV). The “resonance line” term refers simply to any transition from an excited state to the ground level

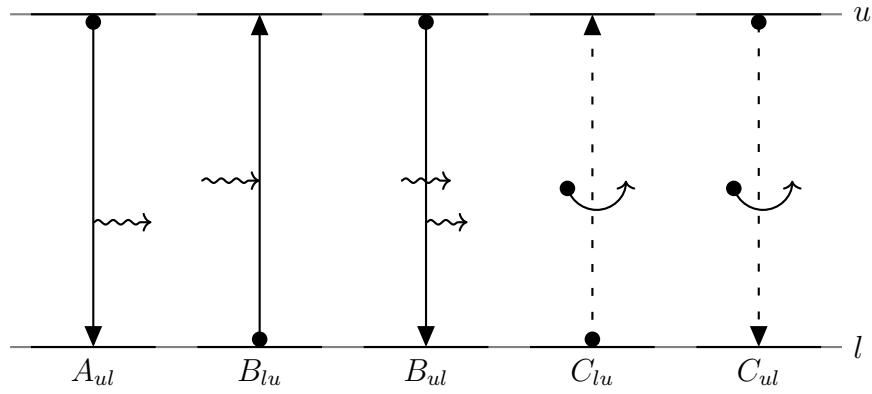


Figure 1.3: Bound-bound transition schematic for a two-level-atom along with the corresponding Einstein coefficients for that type of transition. The continuous line transition refers to radiative processes, while the dashed lines refers to collisional processes.

of that ion. The ion is easily excited by photo-excitation or by electron impacts (Sigut and Pradhan, 1995). The k and h lines are a doublet pair as they share the same lower energy level. Doublet lines are characteristic to atoms or ions that have only one external electron.

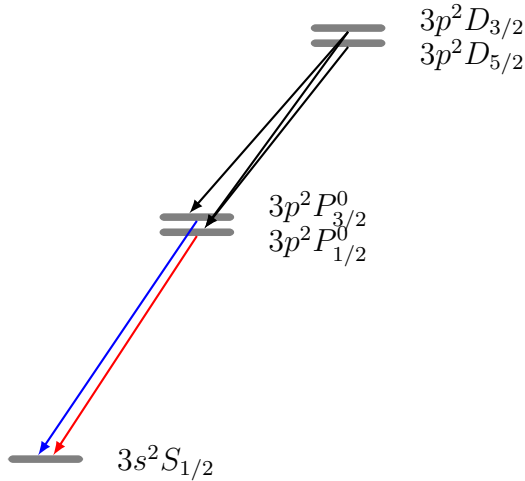


Figure 1.4: Schematic of the Mg II ion transitions discussed and used in our analysis. For simplification, only the first five levels of the Mg II ion are depicted. The k line is shown in blue, while the h line is in red. The subordinate triplet lines are in black. The energy difference between the $3p - 3s$ and the $3d - 3p$ is similar, meaning all of the discussed lines emit within a narrow 15 Å interval.

The k and h lines correspond to the $3p - 3s$ transitions from the $3p^2 P_{3/2}^0$ and $3p^2 P_{1/2}^0$ excited levels to the $3s^2 S_{1/2}$ ground level, respectively. The close values of their air wavelengths (2795.5 Å and 2802.7 Å, respectively) is the result of the very small energy difference between their upper levels. In the solar spectrum, these lines are optically thick and are seen as deep absorption lines due to the presence of the Mg II ion in the solar chromosphere, absorbing the continuum radiation of the photosphere. This means that the line opacity varies with wavelength. Also, the line source function is sensitive to the rise of temperature at the lower boundary of the chromosphere, where it starts to depart from a pure Planck function. This implies that the intensity of the emitting radiation no longer reflects the local thermal conditions. The line goes back into emission close to line centre, but collisional scattering and the total decoupling from the Planck function leads to a decrease in the observed intensity in the core.

Following the naming convention for the Ca II K line (Hale and Ellerman, 1904), the central self-reversed core is named k_3 and is generally formed in the high chromosphere, some 200 km under the transition region. It is flanked by two emission peaks, dubbed k_{2r} and k_{2v} corresponding to the red and blue (violet) sides of the core, respectively, and emerging from the mid-chromosphere. The outer minima, surrounding the emission peaks, are termed k_{1r} and k_{1v} and originate from close to the T_{\min} region. The same naming convention applies to the Mg II h line, but due to its lower opacity, only half of that of the k line, the spectral features correspond to a few tens of kilometres lower in the solar atmosphere and are more decoupled from the

Table 1.1: Important Mg II lines

Mg II Lines	λ_{air} Å	$\lambda_{vac.}$ Å	upper	lower	$g_u - g_l$	f_{lu}	A_{ul} [$10^8 s^{-1}$]	$\log gf$
k	2795.5	2796.34	$3p^2 P_{3/2}^0$	$3s^2 S_{1/2}$	4-2	6.08-01	2.60+00	0.64
h	2802.7	2803.54	$3p^2 P_{1/2}^0$	$3s^2 S_{1/2}$	2-2	3.03-01	2.57+00	1.3
t1	2790.8	2791.64	$3p^2 D_{3/2}$	$3p^2 P_{1/2}^0$	4-2	9.37-01	4.02+00	1.9
t2	2797.9	2798.74	$3p^2 D_{3/2}$	$3p^2 P_{3/2}^0$	4-4	9.38-02	7.98-01	0.39
t3	2798.0	2798.84	$3p^2 D_{5/2}$	$3p^2 P_{3/2}^0$	6-4	8.44-01	4.79+00	3.5

Spectral information extracted from [Kelleher and Podobedova \(2008\)](#).

local temperature field. [Linsky and Avrett \(1970\)](#) discussed the origin of the Ca II profile characteristics and compare them to the Mg II emission. The self-reversal in the emission cores vanishes $8''$ above the limb, and the lines become effectively thin at about $20''$ in the proximity of an active region, and even lower for quiet sun conditions ([Doschek and Feldman, 1977](#)).

The energy difference between the $3p - 3s$ and the $3d - 3p$ levels is almost equal, making the subordinate triplet lines to emit at wavelengths close to the resonance lines. One of the subordinate lines is the blue wing of the k line, at 2790.8 \AA , and corresponds to the transition from the $3p^2 D_{3/2}$ excited level to the $3p^2 P_{1/2}^0$ level. The other two transitions from the $3p^2 D_{3/2}$ and $3p^2 D_{5/2}$ excited levels to the same lower level, $3p^2 P_{3/2}^0$, have wavelengths of 2797.9 \AA and 2798.0 \AA , respectively, and are seen as a blend located between the k and h lines. The triplet lines originate from deeper in the atmosphere than the resonance lines and are all usually seen as shallow absorption features, but in active solar conditions they can go into emission. Due to the high excitation energy and their magnetic dipole number, the upper level is rarely populated by excitation from the ground level. It is more likely to be populated by recombination, thus the presence of these lines may imply cooling of the plasma ([Schmit et al., 2014](#)).

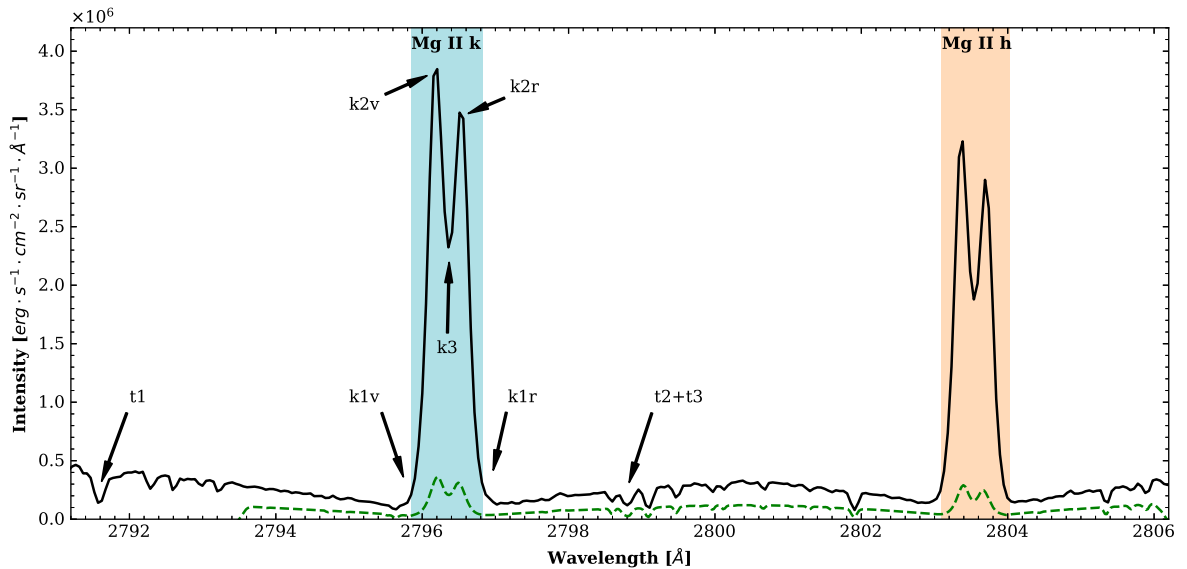


Figure 1.5: Emission profile of Mg II ion in active chromospheric conditions. The positions of the h and k lines are highlighted by the light blue and orange bands, respectively. For the Mg II k line the profile features are indicated by the arrows. The subordinate triplet line positions are also included. The green dashed line represents the quiet sun profile for comparison.

More information on the Mg II transitions characteristics are included in Table 1.1. Figure 1.4 shows a schematic view of the first five levels of the Mg II ion, including the

transitions discussed above. For convenience, the resonance lines have been coloured in red and blue to ease their identification in Figure 1.5, while the subordinate lines have been kept in black.

1.5. *The Mg II lines in history*

The high solar abundance of Magnesium implies strong Mg II emission lines, but their position in the Hartley absorption band of ozone (1950–3500 Å, with maximum absorption at around 2550 Å) make them impossible to observe using ground based resources. Therefore, instruments needed to be developed and carried a few hundred kilometres from the Earth's surface, above most of our atmosphere. As such, the first identification of these lines in the solar spectrum was made around the middle of the 20th century by [Durand et al. \(1949\)](#) using a spectrograph on-board a V-2 rocket. Since then a number of balloon, rocket and satellite borne instruments were used to probe these interesting lines. We discuss the major observing missions and some important landmarks in our interpretation of the observed characteristics.

The earliest full-disk average spectrum containing the Mg II resonance lines was collected by [Johnson et al. \(1953\)](#) and [Garrett et al. \(1962\)](#) using a rocket to fly the spectrograph to about 180 km above ground level. A few years later, [Fredga \(1966, 1969\)](#) reported the first full-disk spectroheliograms in both Mg II *h* 2803 Å and Mg II *k* 2796 Å emission.

Lower altitude, balloon borne instrument observations started with [Lemaire and Blamont \(1967\)](#), who measured the Mg II lines with a spectral resolution of 40 mÅ and obtained 1' resolution limb darkening profiles. Subsequent observations by [Lemaire \(1969\)](#) improved the spatial resolution to 10'' and extended wavelength range, offering detailed profiles and centre-to-limb variation (CLV) of the *k*₂ peak separation.

The first interferogram was obtained by [Bates et al. \(1969\)](#) with a spectral resolution of 30 mÅ and a spatial resolution of ~6''. They noted the profile dissimilarities of the spectra corresponding to different levels of solar activity and pointed out the asymmetries of the *k*₂ peaks, as well as a centre-to-limb variation.

[Lemaire and Skumanich \(1973\)](#) derived average profiles for different solar activity levels, from quiet sun to plage, using balloon observations with 25 mÅ spectral resolution and 7'' spatial resolution. They compared their results with existing chromospheric models available at the time and found a poor correlation between the two, suggesting important physics was missing from the models or the height structure considered for the physical parameters was lacking. In an attempt to solve these discrepancies, [Gouttebroze and Lemaire \(1974\)](#) explored the formation mechanisms of the Mg II resonance lines and concluded that the source functions are not equal at the same depth and that CRD assumption is not suited to correctly reproduce the inner wing emission.

[Milkey and Mihalas \(1974\)](#) performed a series of theoretical calculation considering a frequency-dependent source function, in an attempt to qualitatively reproduce the observed profile features of the Mg II lines. Based on their computed emission profiles, they concluded that the impact of PRD on the inner wing intensities is significant, questioning the use of CRD in the formation calculations for other similar lines.

Up to this point, the uncertainty involved in the observational data acquisition deterred quantitative comparison between observations and models. The first measurements of absolute spectral intensity were performed by [Kohl and Parkinson \(1976\)](#) for two positions on the solar surface: near disk centre and near the limb. Their results enabled [Ayes and Linsky \(1976\)](#) to meaningfully compare synthesised spectra obtained using PRD assumptions and a few of different atmospheric temperature structures, concluding that a slightly higher T_{min} would best fit the observations.

The first space-based observations were obtained from Skylab and were discussed by

[Dosc hek and Feldman \(1977\)](#). They explored the profile variations across different solar structures, from active regions to quiet sun, both on and off disk. [Feldman and Dosc hek \(1977\)](#) further studied the relation between the resonance lines and the subordinate triplet emission at positions above the limb, where effectively thin conditions are satisfied, and used their ratio to obtain estimates of temperature and density. [Moe and Milone \(1978\)](#) analysed the CLV of the averaged spectra containing the Mg II lines.

The emission in the Mg II *k* and *h* lines was estimated to be $\sim 30\%$ of the total chromospheric emission of the Sun by [Linsky and Ayres \(1978\)](#) who used the difference between the integrated emission of these lines and the integrated emission of a purely radiative model to evaluate the non-radiative heating of different stellar chromospheres, from solar-like stars to supergiants.

The LPSP (Laboratoire de Physique Stellaire et Planetaire) instrument on-board the 8th Orbiting Solar Observatory (OSO-8: [Bonnet et al., 1978](#)) was the first satellite-based instrument to observe the Mg II lines. [Kneer et al. \(1981\)](#) used this instrument to obtain $64'' \times 64''$ spectroheliograms of the area around a sunspot in six emission lines, together with line spectra at ~ 70 positions within the FOV. The Mg II doublet emission was compared with the better studied Ca II *K* and *H* lines and the H I $L\alpha$ and $L\beta$ lines. They found similar features in the Mg II and Ca II emission (no central reversal with significant asymmetries), but deduced a non-linear relation between the two elements, which they attributed to the slightly different response of the different elements to the solar atmospheric structure.

[Lemaire et al. \(1981\)](#) further used LPSP data to develop models for plage and quiet sun emission. They attributed the inconsistency found when comparing the models to the real data to inhomogeneities of the emitting plasma or dynamics under the resolution of the instrument. Additionally, they discussed the possibility that a more complex Mg II model (including more energy levels) could improve the fits.

Also using data from the LPSP instrument, [Lemaire et al. \(1984\)](#) reported the first profiles of the Mg II lines during a solar flare, as part of the multi-wavelength observation, including Ca II and H I lines. They found a delay in the emission maxima of the observed lines suggesting a downward propagation of the energy, followed by relaxation times of different lengths. The ratio between the Mg II *k* and *h* lines was found to vary from 1.5 to 0.9 during the flare, with an increase before the flare. The subordinate triplet lines are seen in emission for the first time.

Data from the Ultraviolet Spectrometer and Polarimeter (UVSP: [Woodgate et al., 1980](#)) on the Solar Maximum Mission spacecraft was used by [Henze and Stenflo \(1987\)](#) to measure the linear polarisation of Mg II *k* and *h*. As coherent scattering in spectral lines is the main component of polarisation, according to the calculation of [Auer et al. \(1980\)](#), the amplitude of linear polarisation of the Mg II doublet was expected to be higher than any other observed line. However, the observationally measured polarisation only fitted the outer wings prediction, failing for the line cores.

All these observational and theoretical results were taken into consideration in the radiative transfer calculations for the one-dimensional models of the solar atmosphere of [Vernazza et al. \(1981\)](#). These models, known as VAL-models, were able to reproduce the quiet sun emission, but failed in more active conditions, by overestimating the depth of the self-reversed core (e.g. [Uitenbroek, 1992](#)).

Later, [Lemaire and Gouttebroze \(1983\)](#) explored the impact of high atomic levels on both solar and stellar models and concluded that the cores of the resonance lines are insensitive to the number of levels considered, but can significantly influence the inner wings and the subordinate triplet emission. They also modelled the Mg II source functions changes under flaring conditions, and were able to obtain the transition to emission of the subordinate lines.

The RASOLBA balloon spectra, still holding the record for the highest resolution spectra

obtained for the Mg II k and h lines, is discussed by [Staath and Lemaire \(1995\)](#). They obtained multiple sets of spectral data with 15 mÅ spectral resolution and 1'' angular resolution, using a slit 0'.3 wide and 30'' long, for disk centre positions and across the limb. These spectra are still used as a reference by modern observations.

In a study of solar irradiance variability, [Morrill et al. \(2001\)](#) used 0.15 Å resolution spectra from the ninth rocket flight of the High Resolution Telescope and Spectrograph (HRTS-9) to compute contrast factors for the emission of different solar structures, noting that the Mg II absorption lines behaviour dominates this variability. [Morrill and Korendyke \(2008\)](#) further explored the centre to limb variability of the Mg II k line features: while the k_2 and k_1 intensity decreases with the viewing angle, the k_3 intensity decreases at first then flattens. This effect was associated to the higher formation height of the core in the solar chromosphere.

[West et al. \(2011\)](#) presented new observations of polarisation of Mg II lines from the Solar Ultraviolet Magnetograph Investigation (SUMI: [West et al., 2000](#)) first exploratory flight. However, due to instrumental failure, only the linear polarisation data was correctly acquired, the circular polarisation being unreliable. They hope the next flight will not be affected by similar issues and new polarisation data will be available.

At the same time, [Belluzzi and Trujillo Bueno \(2011\)](#) and [del Pino Alemán et al. \(2016\)](#) offer a new theoretical look at polarisation, by modelling the linear and circular polarisation components of the Mg II k and h lines. They encourage the development of instrumentation that can observe the polarization of these lines, as they would provide crucial details on the poorly explored magnetic structure of the upper solar chromosphere.

The second flight of the *Sunrise* ([Barthol et al., 2011](#)) balloon observatory saw a new addition to the Sunrise Filter Imager (SuFI: [Gandorfer et al., 2011](#)) instrument, namely a new 4.8 Å wide filter centred on the Mg II k line. Due to the low altitude of the balloon flight, they used a 50 seconds exposure for the Mg II channel, which smoothed the observed features. The first analysis of the 0'.2 resolution images recorded in this new filter is presented by [Riethmüller et al. \(2013\)](#), who note the presence of the reverse granulation pattern or shock waves in the quiet sun regions. An in depth comparison to the simultaneously obtained Ca II H filter is offered by [Danilovic et al. \(2014\)](#). The Mg II k emission shows a better intensity contrast, but significant similarities in the structure of the observed features, when compared to the Ca II H channel.

The most recent instrument dedicated to observations of these lines is IRIS ([De Pontieu et al., 2014](#)) with 0'.4 spatial resolution, 25.5 mÅ spectral sampling (resulting in a spectral resolution of 53 mÅ in NUV), and temporal resolution that can go down to 4 s, but covering a small FOV of maximum 175''. More details about this mission are included in the next chapter and observation specific details are included in their respective chapters. In addition to the diagnostic papers written by the *IRIS* team (discussed in Section 2.1), one dimensional calculations of quiet sun emission were performed by [Avrett et al. \(2013\)](#) as an additional resource for the interpretation of *IRIS* data.

Chapter 2: Observational Data, Calibrations and Analysis Techniques

“Equipped with his five senses, man explores the universe around him and calls the adventure Science.”

Edwin Hubble

We analyse observations from the Interface Region Imaging Spectrograph and Solar Dynamics Observatory to better understand the relation between the solar chromosphere and the photosphere in the neighbourhood of active regions and even in the quiet Sun.

In the last few decades, with the advancements in technology, we have launched a number of satellites beyond the restriction of the Earth’s atmosphere. The instruments on-board have been providing us with a wealth of data, most of which is still waiting to be thoroughly analysed. We now have access to unprecedented details of the solar surface over the whole electromagnetic spectrum, from radio to gamma rays.

The present work is largely based on the analysis and interpretation of observational data, from a number of different instruments. Therefore, a few of the characteristics of several important instruments is presented, along with a description of the various types of data available. Additional calibrations are described where required. As each instrument focuses on different aspects of the solar emission, we discuss the analysis techniques used in order to extract the most information from the available data.

Furthermore, given the wide range of cadences in the data, the date and time of the observation in each instrument has been converted to the Julian date format. This conversion was applied in order to ease identification of correlated features in different instruments with as little temporal delay as possible.

2.1. Interface Region Imaging Spectrograph

The Interface Region Imaging Spectrograph (IRIS: [De Pontieu et al., 2014](#)) is a small NASA mission designed to focus on the Sun’s poorly observed high chromosphere and transition region, and provide high quality images and spectroscopic data of these regions, in an attempt to understand the processes leading to coronal heating. It was launched in June 2013 in a Sun-synchronous, low Earth orbit and has since provided unprecedented views of the solar atmosphere, from quiescent conditions to violent solar flares and eruptions. The *IRIS* mission provides high-resolution imaging and spectroscopic observations from the photosphere up to the corona.

IRIS uses a spectrograph (SG) to observe the Sun in three spectral windows, two in the far ultraviolet (FUV: 1332 – 1358 Å and 1389 – 1407 Å) and one in the near ultraviolet (NUV: 2783 – 2834 Å). The spectrograph slit is 0’33 wide and 175” long. The light is then split into three beams, one for each spectral range. The resulting spectra have a spatial resolution of 0’167

and a spectral sampling of 25.5 mÅ and 12.8 mÅ for the NUV and FUV ranges, respectively. Depending on the observation target and the desired cadence of the data, the spectral ranges readout can be confined to a certain interval of interest, while also applying binning of the spatial and/or spectral pixel. The recording time for the spectra at one slit position can be selected from 0.5 seconds to more than 30 seconds.

The most important spectral features in the NUV window are the Mg II *k* and *h* resonance lines and the Mg II subordinate triplet lines, along with the extended red wing of the resonance lines. The FUV windows contain the emission from transition region lines, such as C II and Si IV. They also include the coronal emission of Fe XXI at 1354 Å that can be seen as a response to energetic coronal events.

The spectral data is accompanied by context Slit-Jaw Images (SJI) captured in four wide range filters, two in the NUV and two in the FUV. The NUV filters have a spectral width of 4 Å and are centred at 2832 Å (Mg II red wing, sampling the high photosphere) and 2796 Å (Mg II *k* line from the chromosphere), respectively. The FUV filters are centred at 1400 Å (integrating both lines of Si IV at 1403 and 1394 Å) and 1330 Å (summing over the 1334 and 1335 Å lines of C II), both capturing the transition region emission in a 55 Å passband. The large width of these pass bands means that they also include the continuum contribution and, during a flaring event, the coronal emission of the Fe XXI line (in the 1330 filter). The maximum field of view (FOV) covered is 175'' × 175'', with a spatial resolution of 0'16 per pixel. The exposure time can also be adjusted, with the exposure time selected for the spectral data as an upper limit. Depending on the specific observation, different combinations of SJI are recorded, and due to telemetry restrictions, temporal and spatial scaling are usually employed.

The instrument can work in a wide variety of observing modes, from sit-and-stare, when a single position along a feature of interest is sampled continuously during the observation, to different density rasters (from 2- to 64-step), when a set of positions along the feature are scanned repeatedly. The wavelength range can also be chosen based on the observation target, as recording the full NUV and FUV spectral regions can be both time consuming and wasteful with the on-board storage space. On-board binning of the spectral data is also available. The roll capability offers the opportunity to sample a given solar feature along a desired direction, though some restrictions may apply.

The raw images (level-0) are aligned and corrected for dark current, cosmic ray spikes, bad pixels, and flat field. The resulting data (level-1) have some geometric and wavelength calibration applied and are then recast as rasters and SJI time series based on the observational identifier (OBS-ID). The Level-2 data thus obtained is the recommended data product for scientific use. More recently, the Level-2 data is also corrected for orbital variations (both thermal and spacecraft velocity) of the spectral line positions. The data can be downloaded from the mission's website¹. More recently, a cross search including the related *Hinode* data is also available².

Since its launch, the *IRIS* Team has been working on providing a series of papers related to the formation properties of the main emission lines observed, based on the analysis of synthetic spectral data.

Leenaarts et al. (2013a) used a 10-level+continuum model of the Mg II ion, in different simulated atmospheres to explore the influence of the different radiative transfer characteristics, and extracted general formation properties for the *k* and *h* lines. Leenaarts et al. (2013b) then used these spectra to explore the atmospheric properties that can be obtained by analysing the relation between different observable characteristics of the profile. Pereira et al. (2013) explored the full NUV range and synthesized the emission as seen by the two NUV SJI filters

¹<http://iris.lmsal.com/search/>

²<http://www.lmsal.com/heksearch/>

integrating the Mg II k 2796 Å and Mg II 2832 Å red wing emission. In a subsequent study, [Pereira et al. \(2015\)](#) investigated the diagnostic potential of the Mg II subordinate triplet lines.

Special attention is also given to the C II emission lines in a series of papers, starting with a description of the atomic model used ([Rathore and Carlsson, 2015](#)) followed by an exploration of their diagnostic potential ([Rathore et al., 2015a,b](#)). These lines originate from the upper chromosphere and low TR and can be used as a link between the chromospheric Mg II lines and the TR Si IV emission.

The formation properties of the neutral oxygen O I 1355.6 Å line is modelled by [Lin and Carlsson \(2015\)](#). Being an optically thin emission, the Doppler shift is an average over the whole chromosphere and the line width is a direct measure of the thermal and non-thermal broadening. [Lin et al. \(2017\)](#) also investigate the C I 1355.8 Å line formation. They find that the ratio between the total intensity of these two lines is inversely proportional to the electron density.

2.1.1. Residual thermal correction

Some residual orbital (thermal) variations are still present in the Level-2 data product. We use the `iris_orbitvar_corr_l2s.pro` routine, part of the IRIS SolarSoftware (SSW; [Freeland & Handy 1998](#)) tree, to find and eliminate these thermal variations. The code identifies the photospheric Ni I 2799.474 Å line in the NUV region, located between the k and h lines, fits it with a Gaussian function, and thus can identify any shifts in the positions of its line centroid over the course of the observations. The variation is then fitted with a smoothed spline function to filter out photospheric oscillations. The residuals obtained are anti-correlated between the NUV and FUV channels. The code returns correction arrays for the whole dataset.

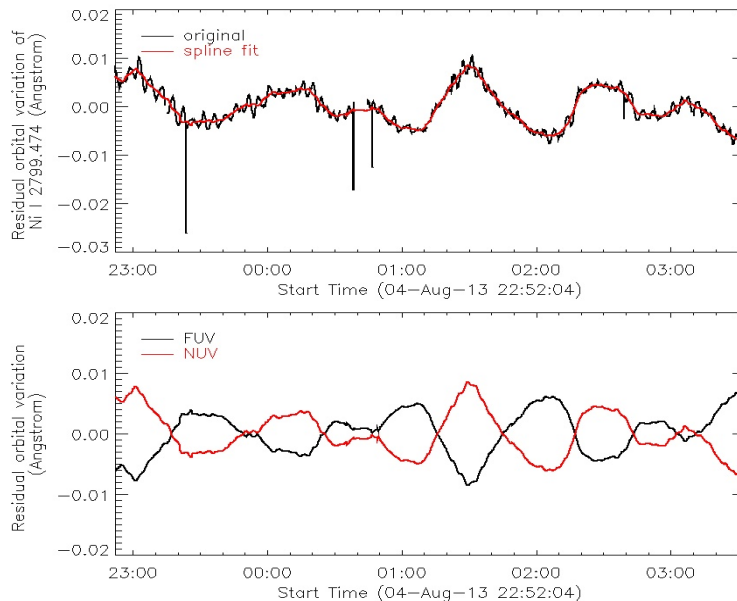


Figure 2.1: Result of the thermal variation wavelength calibration. Top: The variation of the Ni I 2799.474 Å line centroid position and the smooth spline fit. Bottom: The NUV and FUV corrections to be applied to the wavelength array.

Such corrections, although modest in absolute values, need to be accounted for, as they can affect the computed Doppler shifts, especially when discussing small variations within quiet solar conditions. Figure 2.1 shows the result of the residual thermal variation for one *IRIS* dataset. These corrections have been calculated for each individual dataset analysed and the wavelength array has been adjusted accordingly, before any further processing was done.

2.1.2. Absolute intensity calibration

In the interest of consistent analysis and comparison of different *IRIS* observations, we converted the SG level-2 data expressed in Data Number (DN) intensity, $N(\lambda, t)$, as a function

of wavelength and time, to the wavelength and time dependent intensity $I(\lambda, t)$ in physical units of $\text{erg s}^{-1} \text{cm}^{-2} \text{sr}^{-1} \text{\AA}^{-1}$ using the relation adapted from Liu et al. (2015b)

$$I(\lambda, t) = \frac{N(\lambda, t) Q(\lambda) E(\lambda)}{t_{\text{exp}} d\lambda A_{\text{eff}} \Omega} \quad (2.1)$$

In equation (2.1), the exposure time (t_{exp}) of the spectral data and the spectral resolution ($d\lambda$) of the wavelength region analysed are taken from the SG header. It is important to note if spectral binning was used in recording the data, as this will influence the calibration.

To obtain physical units, we need to multiply the intensity by the energy of the photon being recorded $E(\lambda) = h \cdot c \cdot \lambda^{-1}$, where h is Planck's constant in units of $6.63 \cdot 10^{-27} \text{ erg s}$, c is the speed of light $3 \cdot 10^{10} \text{ cm s}^{-1}$ and λ is the emitted wavelength in cm.

$Q(\lambda)$ represents the product between the CCD gain and the number of photons needed to create one electron-hole pair on the detector and is equal to 18 photons/DN for the NUV band and 4 photons/DN for the FUV band, as given in the instrument paper (De Pontieu et al., 2014). If the data were recorded using spectral binning, these values need to be scaled accordingly.

The effective area, A_{eff} , is obtained from the *iris_get_response.pro* routine in the IRIS/SSW tree. Due to instrument degradation, it is important to use the observation date of the analysed dataset when calling this routine.

The solid angle, Ω , is given by the product of the slit size ($0''.33/\text{pixel}$), the spatial resolution (dy) and the area of an arcsecond on the solar disk (s_{arc}), divided by the square of the distance to the Sun for the analysed dataset (D_{\odot} in km from the SG header). $\Omega = 0.33 dy s_{\text{arc}}^2 / D_{\odot}^2$, where $s_{\text{arc}} = 2 D_{\odot} \tan(\pi / (180 \cdot 3600 \cdot 2))$. The IRIS guide suggests using the approximation for the solid angle $\Omega = (\pi / (180 \cdot 3600 \cdot 6)) \cdot (\pi / (180 \cdot 3600 \cdot 3))$. The difference between the two methods is marginal, when keeping everything else constant, as the approximation is simply based on the Taylor expansion around 0 of the tangent function, considering only the first term, as the angle is very small.

2.1.3. Profile moments

We employed spectral moment analysis to measure variations in intensity and departures from a typical emission profile. The procedure was only applied for spectra that have reasonable S/N ratio and can be clearly identifiable above the background. For the strong Mg II resonance lines, this was readily obtained in all solar conditions, but for the FUV region, the S/N ratio for the quiet sun observations is low outside the network regions, so the results must be treated with caution. This analysis was applied to the intensity in physical units of $\text{erg s}^{-1} \text{cm}^{-2} \text{sr}^{-1} \text{\AA}^{-1}$.

For the Mg II profiles, for each analysed spectrum, we have subtracted the intensity of the nearby quasi-continuum. Whenever possible, we used the quasi-continuum region located in the bump between the k and h lines ($2800.34 - 2800.51 \text{\AA}$). In the case of observations that only recorded a very restricted wavelength range around the k line, we were forced to use the quasi-continuum region in the blue wing of the line ($2795.10 - 2795.33 \text{\AA}$).

The average position of the line core was computed for each observation (λ_0 - the rest wavelength of the transition) and then moment analysis was used, i.e. moment i is $\int_{\Delta\lambda} I(\lambda) (\lambda - \lambda_0)^i d\lambda$ to find the integrated intensity of the line, Doppler shift of the line centroid and the wavelength dispersion (line width) of the emission line.

The 0^{th} Moment of a profile, simply represents the integrated intensity or total intensity of the emission peak, is measured in units of $\text{erg s}^{-1} \text{cm}^{-2} \text{sr}^{-1}$ and is defined as

$$I_{\text{core}} = \int I(\lambda) d\lambda \quad (2.2)$$

For a given pixel location (if solar rotation tracking is active for the observation), variations in the total intensity are caused by changes in the activity level of the underlying atmosphere

and are most prominent in the case of flares or highly dynamic active regions, as a consequence of enhanced heating.

The 1st Moment is used to describe the shift of the line centroid, where λ_0 is the average position of the line centroid for a given observation, as small variations of the centroid are caused by the position on the solar disk of the observed region. It is defined as

$$\Delta\lambda = \frac{\int \lambda I(\lambda) d\lambda}{\int I(\lambda) d\lambda} - \lambda_0 \quad (2.3)$$

and is used for the determination of the Doppler shift of the line, in units of km s^{-1}

$$\Delta v = \frac{\Delta\lambda}{\lambda_0} \cdot c \quad (2.4)$$

A positive shift corresponds to plasma downflow (redshift) and negative velocity implies upflow (blueshift). This procedure will only identify shifts within the wavelength range provided, therefore it is important to check the data for abnormal activity that may be excluded by restricting wavelength interval. Furthermore, it will not identify high blueshift associated with highly accelerated erupting material if the profile of the erupting plasma is well separated from the main emission, especially if quasi continuum intensity has been subtracted.

The 2nd Moment characterises the wavelength dispersion of the profile, or how far from line centre photons may still be recorded and considered as part of the line. The dispersion is described by

$$\sigma = \sqrt{\frac{\int (\lambda - \lambda_0)^2 I(\lambda, t) d\lambda}{\int I(\lambda, t) d\lambda}} \quad (2.5)$$

and is used to find the width of the line profile (assuming Gaussian symmetry) in units of $\text{m}\text{\AA}$

$$\text{FWHM} = 2\sqrt{2 \ln 2} \sigma d\lambda \approx 2.35 \sigma d\lambda \quad (2.6)$$

The computed line widths values tend to be higher than the standard Doppler width of the line in regions of increased activity. Sudden temperature enhancements associated to reconnection events can also give rise to profiles with higher line widths.

The 3rd Moment, or the skewness of the profile, describes the symmetry of the line across the line centre and can be used to find the presence of small gradients of motion. A value of 0 describes a symmetric profile.

$$S = \frac{1}{\sigma^3} \frac{\int (\lambda - \lambda_0)^3 I(\lambda) d\lambda}{\int I(\lambda) d\lambda} \quad (2.7)$$

The 4th Moment, also known as kurtosis, measures the departure from a pure Gaussian profile (kurtosis of 3).

$$K = \frac{1}{\sigma^4} \frac{\int (\lambda - \lambda_0)^4 I(\lambda) d\lambda}{\int I(\lambda) d\lambda} \quad (2.8)$$

2.1.4. Profile features identification

The Mg II *k* and *h* lines are normally formed in optically thick conditions. Furthermore, in typical solar conditions, both line cores are in absorption, and important asymmetries can be present. These features hinder interpretation as a single Gaussian fit may overlook or completely miss important line characteristics, whose analysis can provide information on the atmospheric structure. The following discussion in this section focuses on the Mg II *k* line characteristics, but the same analysis has been applied to the Mg II *h* line.

We explore the profile characteristics, by employing quartile analysis (similar to [Kerr et al., 2015](#)) to pinpoint the important spectral features. This technique involves computing the cumulative distribution function (CDF) of the emission within a wavelength range containing

the Mg II k or h lines. We have selected the positions of 15%, 50%, and 85% of the maximum intensity, and considered the line profile is fully included between the 15% and 85% limits. Spikes in the data and bad pixels were removed prior to this summation, by excluding pixels that are saturated or over an order of magnitude brighter than the average of the dataset.

In contrast to [Kerr et al. \(2015\)](#), who used the positions of 25%, 50% and 75% CDF to explore the line symmetry, we use a custom peak identification routine to precisely pinpoint the positions of the emission peaks and the absorption core.

The position of the Mg II central absorption (k_3) was computed by finding the minimum intensity within a few spectral pixels of the 50% CDF. If no such minimum was found the position of the 50% CDF was used instead. This would indicate that most likely the line profile contains no central reversal, as is the case in AR or flaring emission.

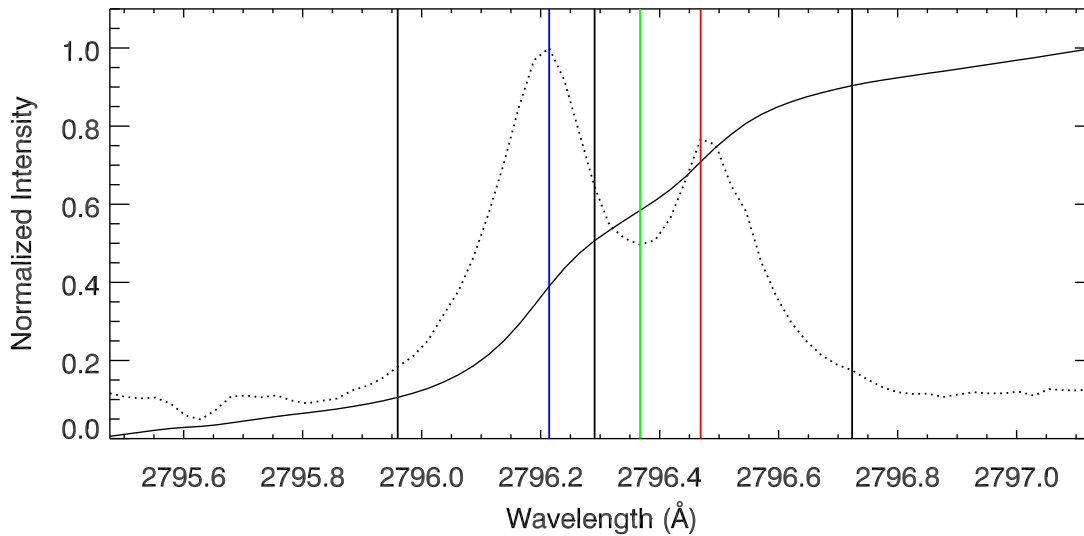


Figure 2.2: Quartile based analysis and peak identification.

The Mg II red peak (k_{2r}) and blue peak (k_{2v}) were then identified by finding the maximum of the emission between the previously identified central reversal and the 85% CDF and 15% CDF, respectively. If no distinctive peaks were identified, then the positions of 75% and 25% CDF were used. This would again indicate a profile with no central reversal.

Figure 2.2 presents the feature identification result for a sample profile. The dotted line represents the Mg II k line emission for a position along the slit, while the continuous line is the cumulative sum of the profile. Both have been normalised and plotted as functions of wavelength. The vertical black lines mark the locations of the 15%, 50%, and 85% of the CDF. The green vertical line indicates the position of the k_3 central reversal. The blue and red vertical lines represent the identified positions of the k_{2v} and k_{2r} peaks, respectively.

A similar, extremum based profile feature extraction, discussed by [Leenaarts et al. \(2013b\)](#), is implemented in the IRIS/SSW tree. Comparison between the results of the two algorithms give marginal differences, especially for unusual profile shapes, while agreeing elsewhere.

[Schmit et al. \(2015\)](#) used a nine-parameter double-Gaussian function to fit the Mg II h line profile and were able to model the majority of the observed profiles accurately. Then they used a similar local extremum finding algorithm to identify the locations of the different profile features.

Once the positions of these profiles features are obtained, we can create emission maps corresponding to these features and thus we can explore their temporal and spatial variation.

The peak separation can also be computed by taking the difference between the k_{2v} and k_{2r} locations

$$W_{k2} = \lambda_{k_{2v}} - \lambda_{k_{2r}} \quad (2.9)$$

This difference is sensitive to velocity gradients in the upper chromosphere, as they introduce a height-dependent wavelength shift, increasing the separation profiles produced in a static atmosphere. However, a local thermal maximum in the low chromosphere can have a similar effect.

The statistical nature of line formation dictates that the wavelength scatter with respect to the line core position should give rise to a symmetric emission profile. However, the observed Mg II resonance lines are rarely symmetric. We are usually faced with profiles where one of the peaks dominates the emission. [Leenaarts et al. \(2013b\)](#) use the relation

$$R^* = \frac{I_{k2v} - I_{k2r}}{I_{k2v} + I_{k2r}} \quad (2.10)$$

to examine the characteristics of the Mg II simulated profiles, and [Schmit et al. \(2015\)](#) apply it to a full-disk mosaic of *IRIS* observations to explore the symmetry of the Mg II *h* line.

Based on the intensities at the previously identified profile positions, we compute the red-blue asymmetry of the emission line, by also considering the corresponding line core intensity, expressed as

$$R_{k2} = \frac{(I_{k2r} - I_{k3}) - (I_{k3} - I_{k2v})}{I_{k2r} - I_{k2v}} = -\frac{1}{R^*} - \frac{2I_{k3}}{I_{k2r} - I_{k2v}} \quad (2.11)$$

If the ratio returns a positive value, then it implies that $I_{k2r} > I_{k2v}$ and the red peak dominates the emission. Negative values imply a profile dominated by the blue peak. Values close to 0 denote nearly symmetric profiles.

The ratio is expected to be sensitive to the average velocity field in the upper chromosphere, as the presence of an upflow above the line formation height will lead to a stronger emission of the red peak, while a downflow will result in blue peak with a higher intensity. This correlation has been long debated for the Ca II resonance lines (e.g. [Carlsson and Stein, 1997](#)).

Another common feature of the Mg II resonance lines profiles is the presence of a central reversal. We compute the depth of this central reversal using

$$D_{k3} = 1 - \frac{2I_{k3}}{I_{k2r} + I_{k2v}} \quad (2.12)$$

Positive values of D_{k3} are representative of profiles for which the central reversal is present, with $D_{k3} \approx 0$ describing a very shallow core and higher values suggesting a deeper absorption feature. Single-peaked profiles will have $D_{k3} < 0$. Based on the analysis of empirical emission profiles, [Leenaarts et al. \(2013b\)](#) have found an inverse correlation between the depth of the k_3 feature and the height of the $\tau=1$ layer. This would imply that a shallow core has the $\tau=1$ layer deeper in the chromosphere. From analysis of observational data, [Schmit et al. \(2015\)](#) concluded that the magnetic field also has an important effect on the depth of the profile.

Additionally, we compute the integrated intensity between the 15% and 85% CDF for both the *k* and *h* lines and extract the intensity ratio between the two emission lines.

$$R_{kh} = \frac{I_k}{I_h} \quad (2.13)$$

We explore the departure from the optically thin ratio of $k : h = 2 : 1$ under different chromospheric conditions.

2.2. Solar Dynamics Observatory

The global effect of flare dynamics in the solar atmosphere was investigated using additional data from NASA's Solar Dynamics Observatory (*SDO*: [Pesnell et al., 2012](#)). The

satellite was launched in February 2010 and has since provided us with continuous high resolution, high cadence, and multi-wavelength views of our Sun, from the photosphere to the highly ionised corona. It contains three science instruments, designed to probe different characteristics of the solar dynamics. The Extreme Ultraviolet Experiment (EVE) is used to measure the variation in the EUV output of the sun, an important step in understanding long time-scale evolution of solar activity.

Information on atmospheric variations was obtained from the Atmospheric Imaging Assembly (*AIA*; [Lemen et al., 2012](#)) instrument. This instrument captures full-disk images of the sun in ten broad-band filters: seven in the extreme ultraviolet (EUV), two in the ultraviolet (UV), and one in visible light. The images are recorded on four 4096 x 4096 pixels CCDs, with a spatial sampling of 0.6 per pixel and a cadence of 12 seconds for the EUV filters and 24 seconds for the UV ones. The main emitting ions for each filter are described below, but observationally, under very active atmospheric condition, they may not be the main contributor to the filter intensity, making interpretation challenging.

The *AIA*94 filter is centred on the 94 Å emission of Fe XVIII, emitting at $\log(T) = 6.8$, which is usually active in flaring coronal conditions, sampling the highest temperature plasmas.

*AIA*131 contains contributions from two different Fe ions formed in different temperature regimes: the Fe VIII at $\log(T) = 5.6$ and the Fe XXI at $\log(T) = 7.0$, thus combining emission from the transition region and the flaring corona.

Emission of the Fe IX 171 Å transition, formed at $\log(T) = 5.8$ and sampling the high transition region and quiet corona, is recorded in the *AIA*171 filter.

*AIA*193 is combining different coronal conditions: quiescent coronal and hot flare plasma conditions, by sampling the Fe XII and Fe XXIV emission, at $\log(T) = 6.2$ and $\log(T) = 7.3$, respectively.

The *AIA*211, centred on the emission of Fe XIV at $\log(T) = 6.3$, and the *AIA*335, centred on the emission of Fe XVI at $\log(T) = 6.4$, contain emission from very similar active region coronal conditions.

The *AIA*304 filter contains emission from He II 304 Å line formed in the high chromosphere and low transition region, at $\log(T) \approx 4.7$, but the source function of the line is decoupled from the Planck function and the plasma is usually optically thick, therefore reliable information regarding the plasma parameters can not be readily extracted.

A C IV line at $\log(T) = 5.0$ together with continuum emission is recorded by the *AIA*1600 filter, thus combining photospheric and transition region emission. The photosphere contributes to most of the emission seen in this filter.

Two continuum filters, *AIA*1700 and *AIA*4500, one in the UV and one in visible light give information on the photosphere and the temperature minimum region at around $\log(T) = 3.7$. The *AIA*4500 images are only recorded once per hour, with an exposure time of a few seconds.

Together these filters cover a temperature range from 6000 K to 10^7 K, but as each filter contains contributions from multiple ions, at different formation temperatures, a straightforward correlation between a given filter and the temperature of the emitting plasma, is impossible. Differential Emission Measure (DEM) inversion techniques need to be used to extract temperature and density information, but such results should be interpreted warily because of the large set of assumptions that are involved.

Due to the complex response of the *AIA* filters to temperature, a straightforward inversion of the recorded counts to physical emissivity units is not a trivial task. In the case of *AIA* observations, only six of the filters can be used in inversions, namely *AIA*94, *AIA*131, *AIA*171, *AIA*193, *AIA*211 and *AIA*335. The remainder of the filters either originate from optically thick plasma or include continuum emission. [Cheung et al. \(2015\)](#) use a sparse matrix inversion method based on the Simplex algorithm to extract DEM information from the emission recorded

by the six *AIA* filters. This method is the fastest to date and is capable of generating reliable full-disk EM (Emission Measure) maps. The obtained EM corresponds directly to the electron number density emitting along the line of sight

$$EM = \int n_e^2 dl \quad (2.14)$$

under a set of assumptions regarding the volume and filling factor of the emitting loops.

The full-disk *AIA* level-1 data for each observation was downloaded using the Stanford University's JSOC export service³, with an additional 30 minutes prior to and after the *IRIS* data exposure interval, to place the evolution of the selected dataset in better temporal context. We then passed the data through the *aia_prep.pro* routine, from the SDO/SSW tree, in order to crop the field of view to a region closer to the FOV of the *IRIS* dataset. The data was also re-spiked, in order to recover flaring pixels.

The Helioseismic Magnetic Imager (*HMI*; Schou et al., 2012) uses the 6173 Å absorption line of Fe I to provide Intensity, Doppler velocity and LOS magnetic field information for the solar photosphere, with a 45 seconds cadence. The full Stokes parameters needed to construct the vector magnetogram are available with a cadence of 12 minutes. The spatial sampling is 0.5 per pixel. The *HMI* data corresponding to each analysed *IRIS* dataset was downloaded using Stanford University's JSOC export service³, allowing an additional one hour temporal buffer, for a better understanding of the magnetic field evolution. The data is rotated by $\sim 180^\circ$ compared to the *AIA* FOV, therefore the images were de-rotated and aligned to the *AIA*1700 filter using the *HMI* intensity continuum data.

After the correct alignment between the data from the different sources was ensured, we selected the data corresponding to the locations under the *IRIS* slit positions, for which spectral information was available. We then compiled the information into a consistent multi-wavelength view of the studied features.

2.2.1. Helioseismic Magnetic Imager Data for Helioseismic Holography

For quantitative studies we will be using acoustic photospheric observations; the focus will be on collecting and processing large datacubes of *SDO* Dopplergram, Magnetic and Continuum Intensity Maps to infer any interesting photospheric conditions, from thermal structure, to flows and magnetic field distribution, and link these with the chromospheric data.

Helioseismic Analysis (Braun et al., 1998) refers to the phase-coherent reconstruction of the observed acoustic waves at the surface, by following p-mode acoustic wave propagation into the subsurface layer, and regressing the propagation back in time to identify the acoustic source location. This approach relies on the fact that as different waves travel into the solar interior, they will be refracted and return towards the surface giving rise to the observed surface waves. We employ the method used by Donea and Lindsey (2005) to explore the link between any detected enhanced photospheric acoustic emissions within the area of interest and their chromospheric counterpart.

The acoustic emission is represented by an egression at any point on the surface \mathbf{r}' and is expressed as

$$\hat{H}_+(\mathbf{r}, \omega) = \int_{\text{pupil}} \hat{G}_+(\mathbf{r}, \mathbf{r}', \omega) \hat{\psi}(\mathbf{r}', \omega) d^2\mathbf{r}' \quad (2.15)$$

where $\hat{\psi}(\mathbf{r}', \omega)$ is the observed complex amplitude signal measured at point \mathbf{r}' and ω is the frequency. $\hat{G}_+(\mathbf{r}, \mathbf{r}', \omega)$ is the Green's function that describes the expanding circular disturbances generated at the focus \mathbf{r} , based on the measurement of the disturbance at the point \mathbf{r}' , from which the acoustic wave is assumed to propagate backwards in time to the focus.

³<http://jsoc.stanford.edu/ajax/exportdata.html>

The *HMI* Dopplergrams provide the information on the acoustic field $\psi(\mathbf{r}, t)$, which is related to the complex amplitude $\hat{\psi}(\mathbf{r}, \omega)$ by the Fourier transform

$$\psi(\mathbf{r}, t) = \frac{1}{\sqrt{2\pi}} \int_{-\infty}^{\infty} e^{i\omega t} \hat{\psi}(\mathbf{r}', \omega) d\omega \quad (2.16)$$

The real acoustic egression $H_+(\mathbf{r}, t)$ is also defined by a Fourier transform

$$H_+(\mathbf{r}, t) = \frac{1}{\sqrt{2\pi}} \int_{-\infty}^{\infty} e^{i\omega t} \hat{H}_+(\mathbf{r}', \omega) d\omega \quad (2.17)$$

The photospheric acoustic emission power can be computed over different frequency ranges and is then equal to the square of the amplitude

$$P(\mathbf{r}, t) = |H_+(\mathbf{r}, t)|^2 \quad (2.18)$$

In the present work, the *HMI* data for the selected region of interest was tracked to remove the effect of solar rotation and remapped to heliographic coordinates using Postel projection (azimuthal equidistant projection). The egression power maps of the selected area were then computed, centred on the emission at 6 mHz. We then explored the correlation between the acoustic emission and the spectral line profile of chromospheric and transition region lines as observed by *IRIS*.

2.3. Additional Data

The Reuven Ramaty High Energy Solar Spectroscopic Imager (*RHESSI*; [Lin et al., 2002](#)) is one of NASA's Small Explorer (SMEX) missions and was launched in 2002. The main goal of the mission is to provide information on the energy release and particle acceleration resulting from reconnection events, by observing the X-Ray and gamma ray emission of the Sun. It is a Fourier-method based instrument that provides high spectral resolution of the emission of photons with energies ranging from 3 keV to 17 MeV and with a spatial resolution of $2''.3$ across the full disk of the Sun.

The number of particles emitted in this energy range is low and they interact differently with optical components, therefore *RHESSI* does not rely on typical imaging techniques. It uses nine, widely spaced rotating modulation collimators placed in front of the spectrometer, which consists of nine germanium detectors. For a source on the solar surface, as the instrument rotates around its axis, the collimators will obscure parts of the detector and introduce a time-modulation in the incoming signal (Fourier signal). The variations of the arrival time in the different detectors can be then used to pinpoint the location of the emitting source on the solar surface.

We used the *hessi*/SSW module to retrieve the data for the studied flares, to extract the emission in different energy intervals, and to reconstruct the source location and evolution. Some of the detectors have degraded over time and are consequently excluded from the analysis.

The basic image reconstruction techniques available are described by [Hurford et al. \(2002\)](#). Back Projection is the simplest technique and consists of the projection of each detected photon back through the collimator at all possible locations on the solar surface, then summing over all detected photons' probability distribution functions. The result is a so-called 'dirty' emission map, useful as a quicklook tool.

The Clean algorithm starts from 'dirty' map result of the Back Projection method and assumes that any extended source is the result of a superposition of point-like sources. This is then convoluted with a so called 'clean beam' with a Gaussian profile to create a new 'clean' map. Some improvements in the source parameters are explored by [Dennis and Pernak \(2009\)](#).

The Maximum Entropy Method (MEM) assumes that each pixel of the image is an independent source, then iteratively constrains the flux based on the observed data. A visibility

based modulation approach has been applied by [Schmahl et al. \(2007\)](#) and is available as MEM-NJIT.

The Pixion method (used by [Metcalf et al. \(1996\)](#) to fit Yohkoh/HXT data) relies on the assumption that the observed modulation in each detector is the result of a superposition of circular sources (pixions) and attempts to fit the data while minimising the number of pixions needed. This method is the most photometrically accurate, but also the slowest.

The original Forward Fit (FF) method proposed by [Aschwanden et al. \(2002\)](#) is based on the assumption that there are a small number of individual sources, then the parameters of each source are adjusted until the resulting image matches the observation. A new Visibility Forward Fit (VFF) method has been implemented by [Hannah et al. \(2008\)](#).

Additionally, the energy spectrum can be extracted, together with background intensity if desired, and supplied to the *ospex*/SSW module in order to fit the energy distribution curve with different models in order to identify the main components of the emission. Thermal emission dominates the low energy ranges, with Bremsstrahlung emission starting to become significant at energies over 20 keV. The presence of this high energy emission resulting from the deceleration of highly energetic particles by collision with the ambient medium is a clear marker of flaring events.

The Geostationary Operational Environmental Satellites (*GOES*) monitor the changes in the solar activity and play an important role in understanding the space weather of the near-Earth environment by providing measurement of ionospheric conditions. This family of satellites has continuous data since 1976 and have been updated and replaced periodically with advancements in technology. The current primary satellite is *GOES-15*, while *GOES-13* acts as backup, both of which were launched in 2010.

For our study we use measurements of the total solar X-Ray flux in two wavelength bands: 0.5 – 4 Å (HXR) and 1 – 8 Å (SXR), corresponding to 3.1 – 24 keV and 1.5 – 12 keV energy ranges, respectively. The flux in the SXR range is used to define the class of the flaring event. Quicklook data is accessible on NOAA's (National Oceanic and Atmospheric Administration) National Geophysical Data Center (NGDC) website⁴ and is usually available as one minute or one hour averages depending on the phenomenon of interest. Since flares produce changes on small timescales, we used the full 2-second cadence data⁵ of these fluxes to identify the different stages of the flare evolution.

⁴<https://www.ngdc.noaa.gov/stp/satellite/goes/index.html>

⁵<https://satdat.ngdc.noaa.gov/sem/goes/data/full/>

Chapter 3: Statistics of Quiet Sun Emission

“Science, my boy, is made up of mistakes, but they are mistakes which it is useful to make, because they lead little by little to the truth.”

Jules Verne, *Journey to the Center of the Earth*

The purpose of the present work is to analyse the dynamics of different types of quiet Sun chromosphere, to understand the properties of the quiet conditions, before we venture into studying eruptive events such as flares, filament eruptions and the response of the chromosphere to these. A better comprehension of the non-eruptive solar atmosphere is also essential for current and future numerical simulations.

Plasma in the chromosphere can be highly dynamic, inhomogeneous, and rapidly changing in time. The quiet Sun by itself seems to be complicated enough, making the interpretation of local phenomena, including oscillations difficult. For example, the network (edges of supergranules) reveals the presence of magnetic flux penetrating the photosphere and spreading out somewhere above, forming magnetic canopies. Even the 5-min photospheric oscillations are detected in the network. The inter-network (the quiet Sun areas in the interior of supergranules) have less magnetic field and can trap the propagating 3 minutes chromospheric oscillations. Also, the inter-network is a puzzle itself even at the photospheric level.

We aim to study the chromospheric spectral behaviour of the quiet Sun as a function of height and magnetic fields. The chromospheric spectra are important in later interpreting the more dynamic properties of the chromosphere above active regions affected by solar flare events. The intention is to also link these observations with the observations of the photosphere, to be able to discern features such as pores, plages, supergranules.

The data examined here are unique in several ways: they sample areas of the quiet Sun in a range of magnetic conditions (quiet Sun, quiet Sun under the magnetic canopy of an active region and quiet Sun under a coronal hole).

We also seek answers to the following questions: What is the difference in the chromospheric emission above various types of quiet Sun? How does the chromosphere respond to either the network or supergranular inter-network? Is there a correlation between the photospheric and the chromospheric wave field motion? Can we compare the photospheric and chromospheric conditions using the *HMI/SDO* and *IRIS* data, while taking into account the evolution of the underlying magnetic field? Can the dynamics of the photospheric field (such as mixed polarities, rising, falling of supergranules) be reflected somewhere up in the chromosphere?

We also aim at understanding whether the chromospheric lines exhibit a systematic broader line profile in the network region of a coronal hole, when compared to the pure quiet Sun or the under canopy quiet Sun (Peter, 1999).

In this chapter we utilise *IRIS* data, to explore the quiet Sun and to create a comparative study of properties of the quiet Sun under various conditions. We will start with a short

overview of our current understanding of the quiet Sun structure, from the basic morphological characteristics to the impact on the photospheric and chromospheric wave emission. We also discuss the challenges of interpreting chromospheric emission due to its non-trivial relation to the properties of the emitting plasma. Conclusions and discussion are presented at the end of the chapter.

3.1. Introduction

The quiet Sun is usually defined using photospheric continuum data by the absence of significant magnetic activity. However, the quiet Sun is not static, but subjected to continuous convective and surface motions that give rise to surprising complexity. These flows move magnetic flux around and gather the flux in the boundary of supergranular cells, forming a web-like structure of network fields (Leighton, 1964). Even the inside of the cells is not entirely “quiet”, but dotted with small-scale brightenings.

The supergranular cell boundary can hardly be seen in photospheric emission as regions of low intensity, due to suppression of convective motions in the neighbourhood of magnetic field concentrations. Higher in the solar atmosphere, we know from early $H\alpha$ and $Ca II$ observations (e.g. Gibson, 1973) that the emission contrast changes, the cell boundary showing emission enhancements, compared to cell interior, for network magnetic fields as low as 10 G. The network magnetic field reaches up to higher atmospheric layers, having a primarily vertical orientation as deduced from the fibrils in $H\alpha$ observations, while $Ca II$ data suggests some expansion is present.

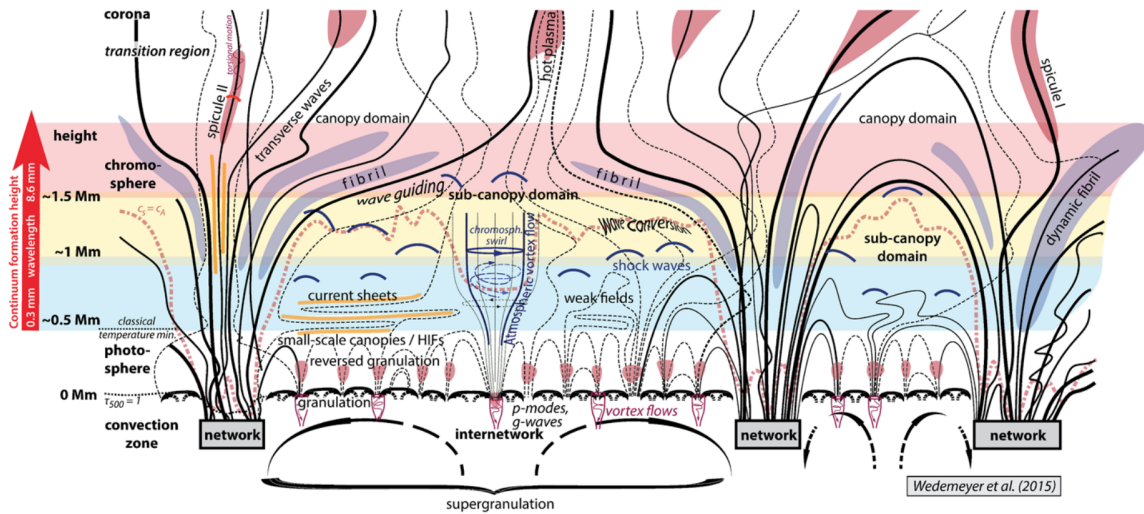


Figure 3.1: Schematic representation of the quiet Sun from Wedemeyer et al. (2016). The horizontal colour bands are defined by the wavelength bands of their ALMA data.

The inter-network region is dominated by the small scale granular motions and low lying magnetic fields. In chromospheric emission lines, Carlsson and Stein (1997) reported the presence of short lived bright grains that appear to be non-magnetic, being the result of pure acoustic wave interactions in the chromosphere (Brandt et al., 1992). Additionally, on time scales of a few hours, small magnetic elements bubble up to the surface and either reconnect with neighbouring elements or are carried towards the cell boundary. This dynamic environment forms the so-called “magnetic carpet” (Title and Schrijver, 1998).

Recently, Wedemeyer-Böhm and Rouppe van der Voort (2009) reported vortex-like flows in the inter-granular lanes under chromospheric quiet Sun conditions and Wedemeyer-Böhm et al. (2012) numerically modelled their formation. However, the observed behaviour may not in fact be a result of flows, but a consequence of wave propagation (Shelyag et al., 2013). Figure 3.1 shows an illustration of the complicated structure in the apparently quiet

Sun conditions as depicted by [Wedemeyer et al. \(2016\)](#).

[Close et al. \(2003\)](#) used magnetic data from MDI (Michelson Doppler Imager), onboard the SOHO (Solar and Heliospheric Observatory) spacecraft, to produce potential field extrapolations of quiet Sun fields. In the absence of strong electrical currents above the photosphere, the potential fields will give an indication of the statistical properties of the overlying magnetic structures. They found that 50% of the quiet Sun magnetic field does not reach higher than 2.5 Mm and only $\sim 10\%$ exceeded 25 Mm. Using the higher resolution *Hinode* magnetic data, [Régnier et al. \(2008\)](#) further explored the topology of the quiet Sun magnetic field by finding the null point height distribution. The null points are located at the intersection of different volumes of magnetic field, surrounded by flux surfaces that, in the absence of magnetic reconnection, do not interact. Most of the identified null points (98%) were located around chromospheric heights, leading the authors to conclude that they could not contribute to coronal heating.

The term “canopy” refers to the region above the $\beta=1$ layer where the magnetic field starts to smoothly expand as the magnetic structure transitions from non-force-free to force-free. In this definition, the canopy will describe a very jagged surface depending on the underlying magnetic structure.

Using data from MDI and SUMER instruments together with data from TRACE, [Judge et al. \(2001\)](#) investigated atmospheric oscillations, from the photosphere to the transition region, and conclude that they are simply an extension of the p-modes in the absence of interfering magnetic structures. In the cell boundary, the network fields expand with height and enhance the strength of the chromospheric lines, suppressing the photospheric p-mode oscillations within the network region and casting “magnetic shadows” around the magnetic elements by damping out the oscillations.

[Kontogiannis et al. \(2011\)](#) compare MDI and *Hinode* magnetic field extrapolations and argue that using low resolution magnetic data misses weaker field, thus placing the canopy level higher in the atmosphere. Therefore, especially in the analysis of wave propagation, it is important to use high resolution magnetic data to obtain the correct location of the canopy transition ([Kontogiannis et al., 2016](#)). The upward propagation of waves across the $\beta=1$ layer has been investigated by [Khomenko and Calvo Santamaria \(2013\)](#), while the effect of a downward wave is discussed by [Hansen et al. \(2016\)](#).

At the photospheric level, different dynamics signals the presence of waves. Enhanced local power of high-frequency sound waves surrounding strong magnetic field structures such as sunspots, plages, and large pores presents an intriguing wave phenomenon observed in the photosphere. The excess of local motion power (“haloes”) is observed at photospheric and chromospheric heights, at frequencies above the photospheric acoustic cut-off of 3.3 mHz. It has been noticed that the enhancement occurs over regions of weak to mild (50-180 G) photospheric magnetic strength. [Donea et al. \(2000\)](#) have also noticed enhanced seismic emission, named acoustic glories, which suggests that localised 6 mHz seismic events (sources) are generated in the haloes or quiet Sun, but their emission mechanism is not clear. [Chitta et al. \(2012\)](#) find that acoustic power suppression is present even for small magnetic structures.

When observing the quiet Sun chromosphere using broad band filters, we are faced with a practical difficulty: the chromospheric lines of interest have a width much smaller than the width of the filter, therefore the wing emission at wavelengths above 2000 Å dominates, and usually contains photospheric contributions (e.g. [Reardon et al., 2009](#)). These types of filters will mix the true fibrillar structure of the chromosphere as seen for instance in $H\alpha$ imaging, with the far brighter wing emission from the photosphere.

The Mg II *k* and *h* lines generally show the same behaviour as the Ca II lines, being usually broader and more intense over the network boundary due to resonance scattering, meaning that

the optical depth in the emitting region is higher in the atmosphere in the boundary, compared to the cell interior (Fredga, 1969; Lemaire and Skumanich, 1973; Doschek and Feldman, 1977).

Recently, a renewed interest in the Mg II resonance lines from more instruments has sparked new investigations of their quiet Sun characteristics. Using SuFI data, Riethmüller et al. (2013) report the presence of reversed granulation in the inter-network region even in images with high temporal integration. Based on an *IRIS* full-disk mosaic, Schmit et al. (2015) explore Mg II *h* line profile variations, finding the limb darkening profile to be steeper than previously measured. Also based on *IRIS* data, Martínez-Sykora et al. (2015) discuss the evolution of non-magnetic bright grains and the delay between events in the different spectral lines, concluding they are the result of upward propagating acoustic waves.

3.2. The Data

We need to establish a baseline of activity in quiet conditions. To accomplish this task we have selected a number of *IRIS* observations close to disk-centre, under various magnetic conditions. We have selected one data set in a quiet region, far from active regions or coronal holes; one set near an active region (more like a large sunspot) where the quiet region is located under the magnetic canopy fields; and two coronal hole sets, with various levels of activity. All regions were chosen at or close to disk centre, to allow the study of the local helioseismology in the photospheric areas, underlying the *IRIS* FOV. We will mainly focus on the emission of the Mg II *k* and *h* lines, because the noise level in the other *IRIS* filters is comparable to the actual line emission, especially for the inter-network region.

To avoid any LOS effects, we searched for *IRIS* datasets with no spectral binning and close to disk-centre, for each of the above categories. We also excluded datasets with a highly unstable pointing. Naturally, the *IRIS* slits crossed areas of supergranular network and inter-network, which we will follow with *HMI/SDO* and *AIA/SDO* imaging. The instruments onboard *SDO* provide the photospheric Doppler and magnetic field information; the low atmosphere UV emissions in the 1700 Å and 1600 Å wavelengths can provide additional interesting possibilities for the study of acoustic wave propagation.

The selected “pure” quiet Sun dataset is referred as to QQS (31-Jul-2014T18:21) and the active region one as ARQS (27-Jul-2014T18:09). These two sets are both very large sit-and-stare observations, have identical spatial and spectral properties and were observed only 4 days apart, making them ideal for our purpose. The QQS dataset contains 600 exposures, while the ARQS contains 645. The exposure time for the NUV filter is 8 seconds and together with the readout time gives a cadence of ~ 9.2 seconds.

The set initially selected to represent conditions in the neighbourhood of a coronal hole, referred as CHQS1 (24-May-2015T11:49), did not have the same line-list. A major downside is that it included only the Mg II *k* line, but we decided to include it in our analysis as the slit location crosses a region of strong magnetic field. The CHQS1 set is a 6960 large sit-and-stare observation, but we restricted ourselves to the time interval between exposure 2000 and 4000, for convenience, as the other datasets were around two hours in length. With an exposure time of 4 seconds, the cadence for the NUV wavelength range is ~ 5.1 seconds.

We selected an additional coronal hole set, denoted CHQS2 (10-Jan-2014T00:17), that consists of 26 very large dense 8-step rasters, pointing slightly off disk centre. There is a slight fluctuation in the pointing along the x-axis, but as we are interested in the statistical behaviour of the various spectral properties, the fluctuation does not impact our result. The dataset contains a total of 208 spectral sets of 15 seconds exposure. Although we ideally wanted a sit-and-stare observation, the small distance between the slit positions makes this set adequate for our needs.

In Figure 3.2 we have included context SJI images for each datasets, as seen in the emission centred on the Mg II *k* 2796 Å, at the start of the observation. The intensity has been normalized

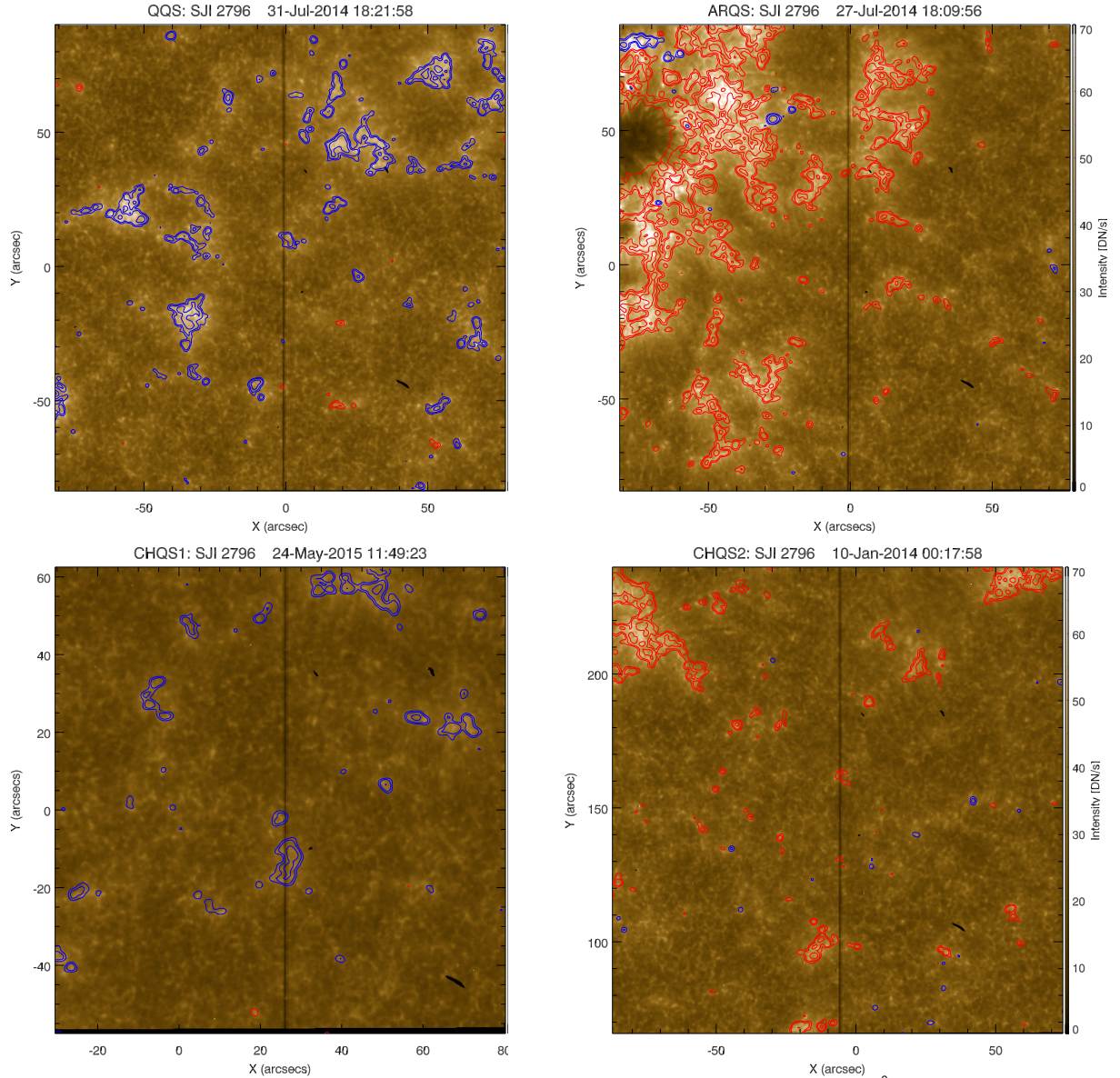


Figure 3.2: Snapshots in the *IRIS* SJI data centred on the $\text{Mg II } k$ 2796 Å emission for the four datasets considered. The observed intensities have been normalized to the used exposure time and plotted using the same intensity scaling. The blue and red contours highlight areas of measurable *HMI* B_{LOS} magnetic field at levels of ± 300 , ± 100 and ± 50 G. The vertical dark line represents the position of the *IRIS* slit.

to the exposure time and the scaling was kept the same. The corresponding *HMI* B_{LOS} magnetic field configuration has been overplotted as contours and manually adjusted where needed.

Although the SJI filter is centred on the $\text{Mg II } k$ emission, the obtained images are speckled with bright features corresponding to the boundaries of convective cells. We know that the oscillatory pattern of granulation is not present in the line cores formed in the high chromosphere, but dominate the emission peaks and inner wing emission (Leenaarts et al., 2013b). Therefore, the 4 Å wide filter used in NUV imaging is dominated by the lower atmosphere contributions, producing images retaining the granulation signatures.

More details on the observational characteristics of the selected datasets is available in Table 3.1, from the exact temporal interval used in the analysis to the available SJI context data and their details.

The *IRIS* slits crossed areas of supergranular network and inter-network regions, which we will follow with *HMI* and *AIA* imaging data. These instruments onboard *SDO* provide the photospheric Doppler and magnetic field information from photosphere to the upper

Table 3.1: Summary of the observational properties of the selected datasets.

	QQS	ARQS	CHQS1	CHQS2
Date	31-Jul-2014	27-Jul-2014	24-May-2015	10-Jan-2014
Time	18:22–19:57	18:09–19:53	11:50–14:50	00:17–01:14
Lines	Mg II <i>k</i> & <i>h</i>	Mg II <i>k</i> & <i>h</i>	Mg II <i>k</i>	Mg II <i>k</i> & <i>h</i>
$\Delta\lambda$	0.0254 Å	0.0254 Å	0.0254 Å	0.0254 Å
Δy	0'16635	0'16635	0'16635	0'16635
Δt	8 s	8 s	4 s	15 s
xc	-0'9	-0'9	25'9	-6'81
yc	3'2	2'6	2'5	152'92
SJIFOV	169"x182"	169"x182"	121"x128"	171"x182"
SJI2832	-	-	✓	-
SJI2796	✓	✓	✓	✓
SJI1400	✓	✓	✓	✓
SJI1330	✓	✓	✓	✓
SJI-exp	8 s	8 s	4 s	15 s

The above information has been taken from the data headers. The xc and yc values correspond to the coordinates of the FOV centre at the start of the observation. The available SJI data is marked by the checkmark (✓).

photospheric layer; the UV emissions in the 1700 Å and 1600 Å wavelengths also provide interesting possibilities for our studies, as they sample the emission containing photospheric continuum.

The magnetic field underlying the *IRIS* slit position in the different datasets was then selected. The near disk centre position of our data sets, suggests that projection effects are minimal for the magnetic field, therefore we use the 45 seconds cadence LOS magnetic field from *HMI*. Given the lower cadence of the *HMI* data, we use the Julian date format to identify the slit data recorded at a time closest to the *HMI* frame. The x-coordinate of the slit position is then used to identify the magnetic field underlying the slit, and then we restrict our attention to the data between the y-coordinate limits of the *IRIS* slit. To ease comparison, the spatial dimension of the spectral data was further re-sampled to match the magnetic data spatial resolution. The *HMI* data was de-rotated prior to this selection.

For each of the datasets we identified $\sim 15''$ wide regions corresponding to different levels of chromospheric activity, namely the quiescent inter-network regime (cell interior) and two regions of network (cell boundary) activity overlaying, or in the proximity of, measurable photospheric B_{LOS} magnetic field. The selected intervals for individual datasets are included in Table 3.2.

Table 3.2: Solar Y coordinates in arc-seconds for the intervals denoted as Inter-network, Network and Enhanced Network for the different datasets.

	QQS	ARQS	CHQS1	CHQS2
Inter-network	-22.83: -7.86	-37.72:-22.75	12.93:27.90	177.15:192.12
Network	-45.29:-30.32	-72.65:-57.68	41.38:56.35	154.70:169.67
Enhanced Network	2.12: 17.09	27.16: 42.13	-19.51:-4.56	94.81:109.78

3.3. Spectral Analysis

Once the four datasets were identified, their corresponding Level-2 data (the recommended science product with basic calibrations applied) was retrieved from the *IRIS* instrument page. The residual orbital variation was then computed and removed as described in Section 2.1.1.

We focus on the Mg II resonance lines emission (see Figure 1.5 for typical profile and

feature naming convention) and provide an in depth analysis of the various profile characteristics under diverse surrounding large scale magnetic configurations and different local activity levels. These lines' formation height ranges from the photosphere to the top of the chromosphere (Vernazza et al., 1981), thus offering information on the whole low solar atmosphere.

The observed intensities, measured in DN/s, were converted to physical units for a meaningful comparison of the different datasets and to avoid any observation bias. The calibrated intensity $I(\lambda, t)$ in units of $\text{erg s}^{-1} \text{cm}^{-2} \text{sr}^{-1} \text{\AA}^{-1}$ was obtained using the method detailed in Section 2.1.2.

The Mg II resonance lines showed typical profile shapes throughout the datasets, with a central absorption surrounded by two emission peaks. Analysing the variation of profile characteristics, such as intensity, Doppler shift and line width can provide information on the macroscopic changes without taking into account the detailed structure of the emission profile. Therefore, investigating the relation between important spectral features, such as the peak dominance or depth of the central absorption, can provide important clues on the conditions at the formation height of these lines.

In the following sections the scaling of the figures containing the same computed quantity has been kept the same across the datasets in order to highlight differences and similarities that may be present. Additionally, we only plotted the results for temporal intervals of comparable length from each dataset. However, we point out that the smaller extent of the CHQS1 slit (only 120'' compared to the 170'' of the other datasets) resulted in the slightly stretched appearance of the presented images. Due to the rastering used for the CHQS2 dataset, the images will have a less continuous appearance.

3.3.1. Mg II moment maps

The moment analysis method described in Section 2.1.3 was used to calculate the first three profile moments of the Mg II k line emission, namely the integrated intensity, the Doppler shift of the line centroid and the width of the line. The rest wavelength for each dataset was computed as corresponding to the location of the central absorption core in the average spectra of the dataset. The continuum intensity was subtracted from the data, using the intensity in a nearby quasi-continuum region recorded in that dataset, namely the 2795.10 – 2795.33 Å wavelength range, choice imposed by the CHQS1 restricted wavelength interval, although the 2800.34 – 2008.51 Å region was present in the other three datasets.

The temporal variation of the computed moments for the QQS dataset is presented in Figure 3.3(a). The network is marked by high values of integrated intensity and line width, and slow oscillation from blueshift to redshift in the Doppler map. The cell interior integrated intensity is dominated by the 3-minute oscillation, which is also apparent in the line Doppler shift variation. Even barely distinguishable photospheric pores make themselves noticeable in the Mg II emission. The region we have defined as enhanced network (located between 0-20'') shows the highest contrast compared to neighbourhood features. The red shift enhancements are associated with the increased downflow toward the cell boundary.

Figure 3.3(b) contains the moment variation for the ARQS dataset that shows similar characteristics to the QQS dataset in the lower part of the image. The proximity of a nearby active region leads to increased emission and line widths close to its canopy fields. Additionally, in the Doppler map at around 40'', the blue and red shift variation shows an almost doubled period when compared to inter-network oscillations.

The CHQS1 data includes emission from an enhanced network located in the middle of the IRIS SG slit. Figure 3.4(a) contains the profile moment temporal variation. The integrated intensity and Doppler shifts in the inter-network are comparable those from previous sets. The line width shows slightly larger overall values, even in the cell interior. The boundary between the cell interior and the network is marked by episodic occurrences of strong upflow

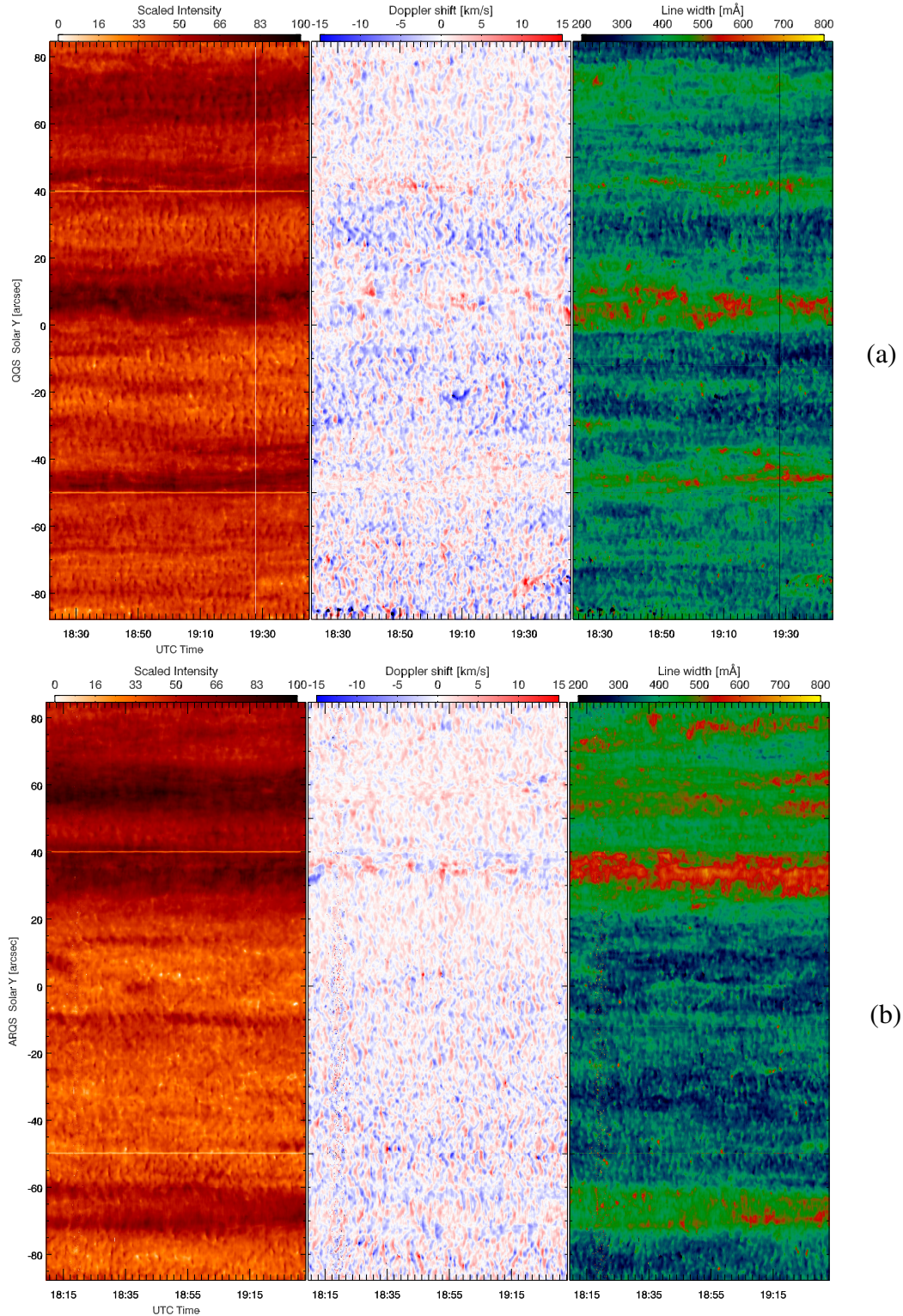


Figure 3.3: Temporal evolution of the Mg II k line moments for the QQS dataset (a) and ARQS dataset (b). Left: Integrated intensity with cubic root scaling applied to enhance the variations within the data. Centre: Doppler shift of the line, with blue corresponding to upflows and red to downflows. Right: Variation of line width during the observation. The corresponding colourbar ranges are included at the top of each moment map.

and downflow, also associated to enhanced line widths. The emission from the network element is almost completely red shifted with rather modest widths.

The line width in the CHQS2 dataset also appear to be higher than the QQS and the ARQS datasets. The variation of all the computed moments is included in Figure 3.4(b). The dataset contains 26 rasters which have been plotted as a continuous image as a function of time, that is

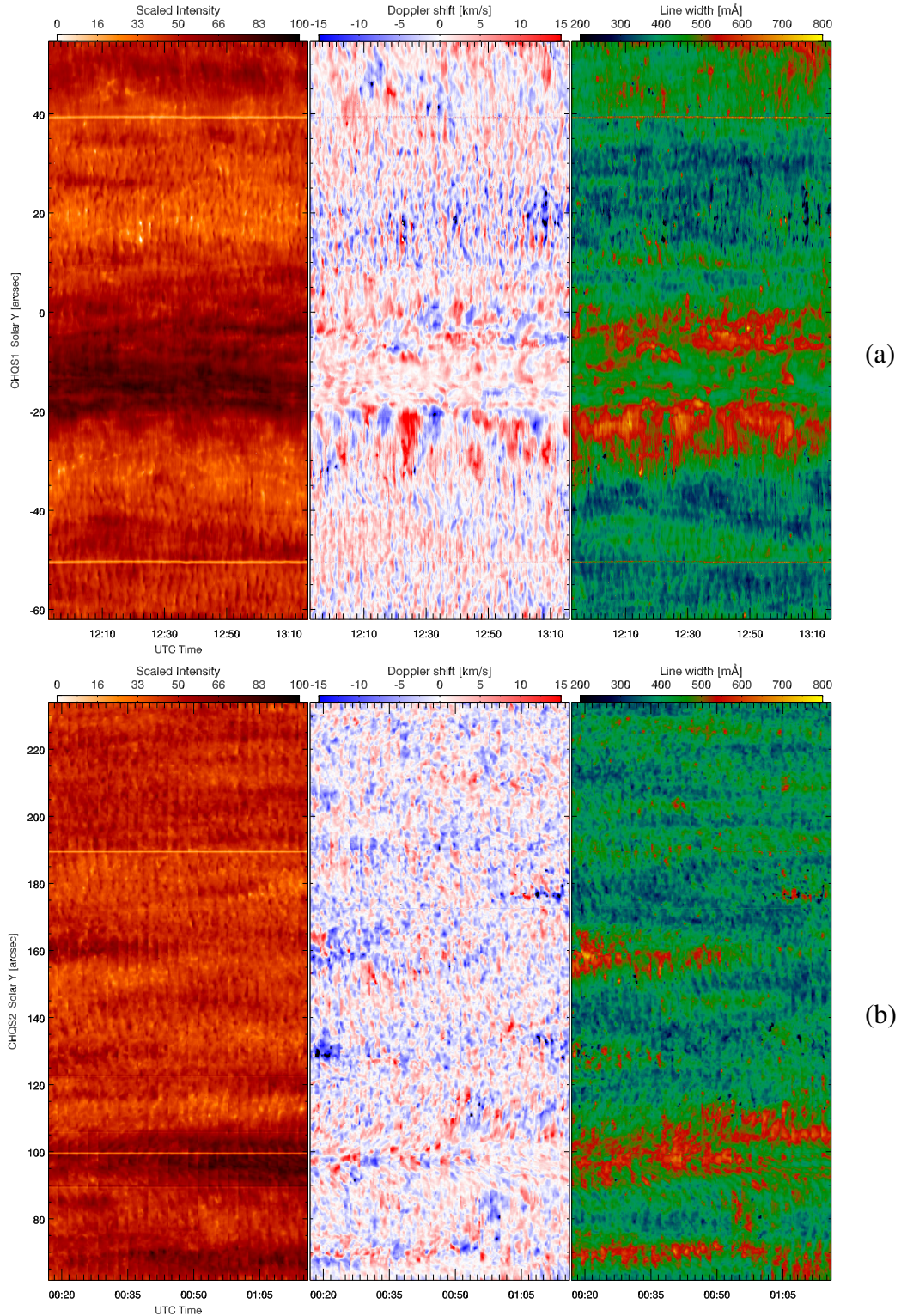


Figure 3.4: Same as Figure 3.3 for the CHQS1 dataset (a) and CHQS2 dataset (b). The jagged pattern in CHQS2 image is given by the different rasters.

the origin of the jagged pattern seen in the data. The sampled network element is rather modest compared to the other CH set, but comparable to the observation of “pure” quiet Sun.

Overall, while the integrated intensity shows enhancements over network elements compared to the cell interior, the different quiet Sun conditions are indistinguishable from each other in the Mg II emission. The Doppler shift maps could be useful to find regions associated with stronger photospheric magnetic field. The line widths show larger contrast, with the CH emission displaying higher values even in the inter-network.

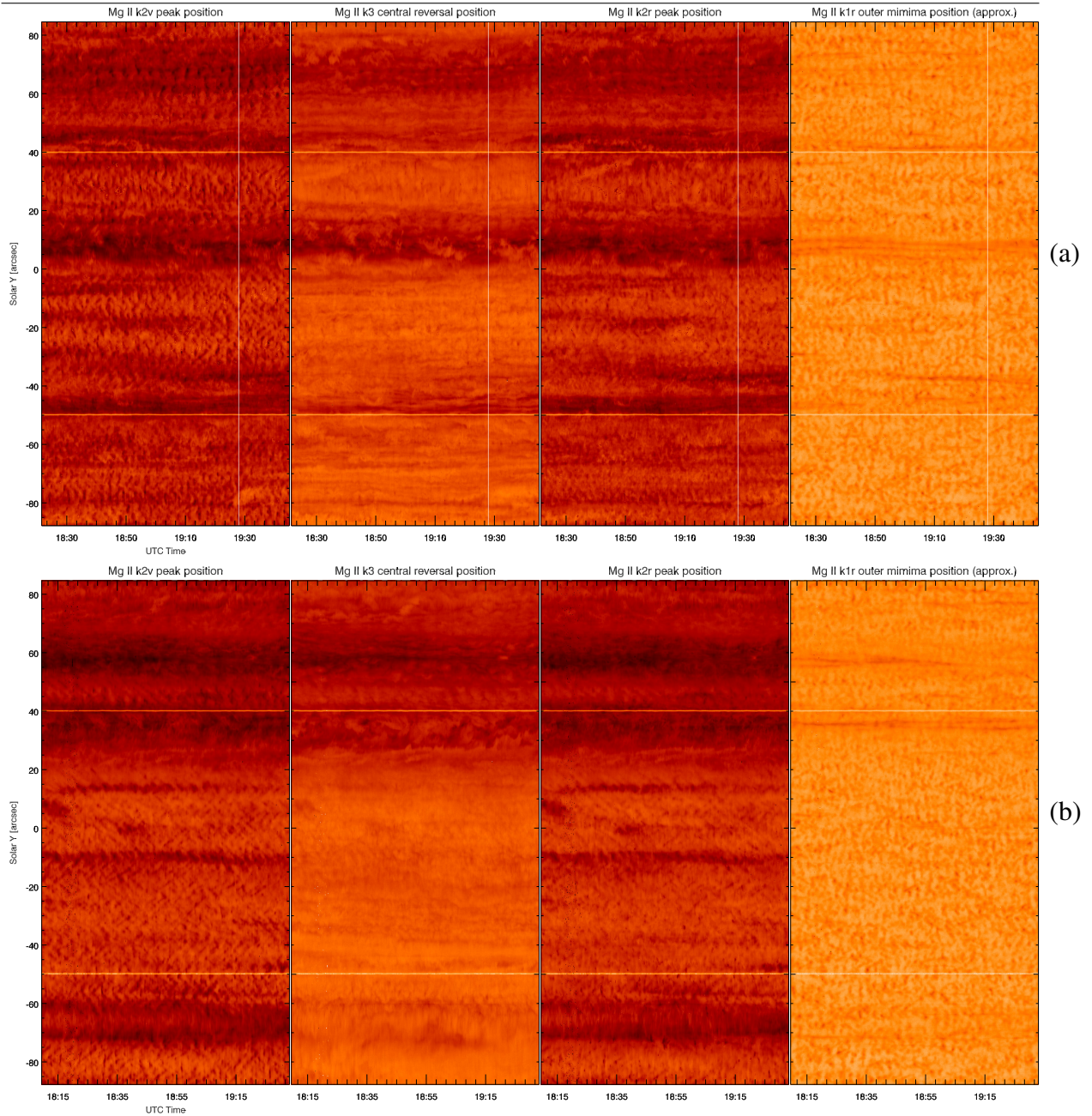


Figure 3.5: Temporal variation of the intensity of different Mg II profile features for the QQS (a) and ARQS (b) datasets. Left: Mg II k_{2v} peak emission. Centre-Left: Intensity of the Mg II k_3 central reversal. Centre-Right: Mg II k_{2r} peak emission. Right: Intensity of the Mg II k_{1r} outer minima. Cubic root scaling has been applied to all feature maps and the same intensity limits have been applied.

3.3.2. Mg II emission features

For each of the selected datasets, we used quartile analysis (Section 2.1.4) to identify the spectral features of both Mg II k and h lines, namely the position and intensity of the k_3 and h_3 central reversal, the k_2 and h_2 emission peaks, and the k_1 and h_1 outer minima. The peaks and outer minima on either side of the central reversal position are assigned a ‘v’ or ‘r’ to reflect their position toward blue (violet) or red wavelengths. Once these positions are found, we can plot the intensity maps corresponding to each of them. The scaling has been kept the same for all the presented maps in order to highlight the intensity contrast between these features. We only include the maps for the k line, as the two resonance lines show marginal differences in the captured structure, with the major distinction being that the h lines has overall lower intensities.

Figure 3.5(a) contains the resulting maps for the QQS dataset. The k_1 outer minima are

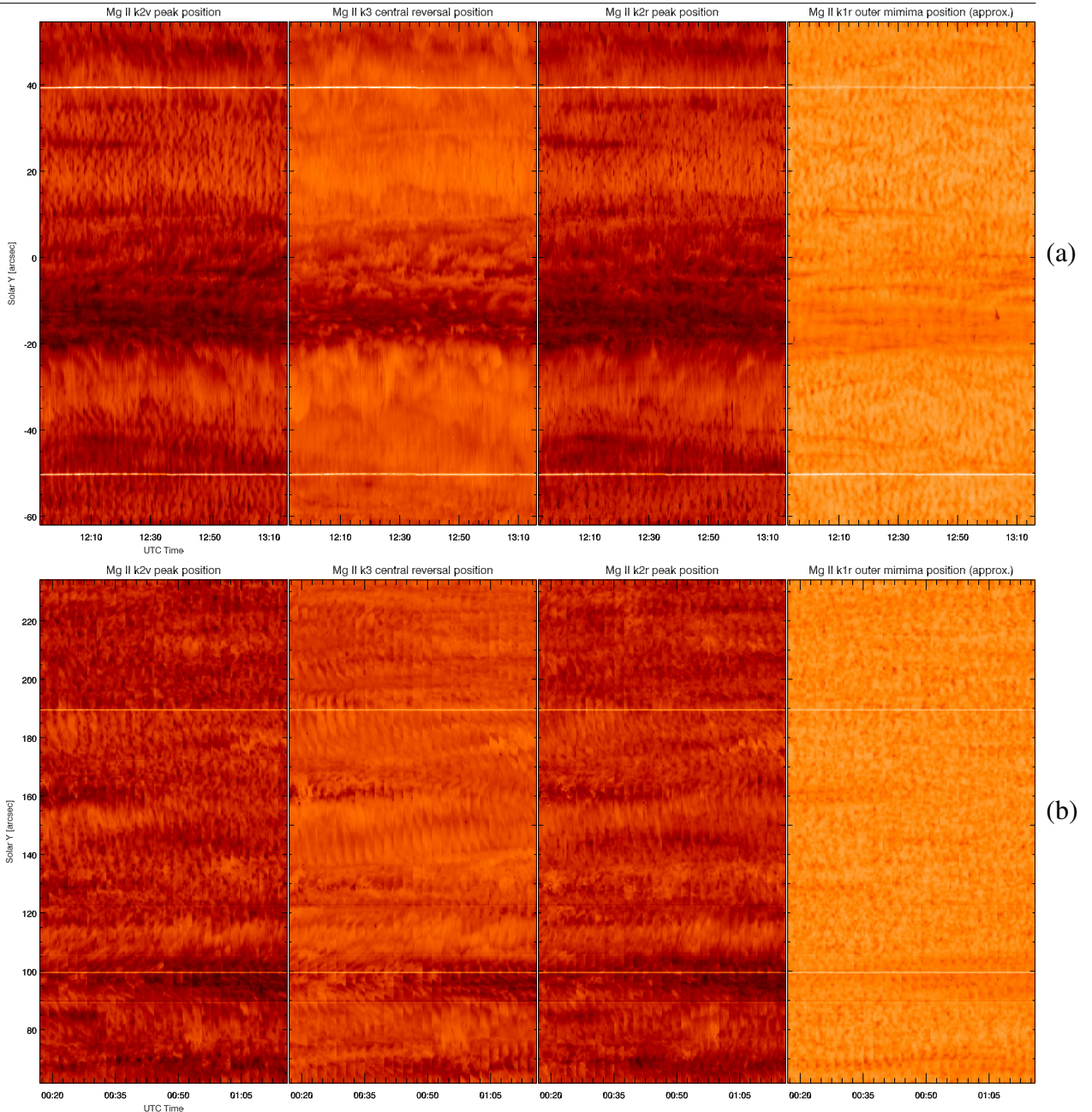


Figure 3.6: Same as Figure 3.5 for the CHQS1 dataset (a) and CHQS2 dataset (b).

formed at heights close to the lower limit of the chromosphere, the T_{\min} layer in the solar atmosphere and the inter-network is dominated by the convective oscillation and the network is seen as narrow regions of slightly increased intensity. The k_{2v} and k_{2r} maps show the most structure, with oscillations dominating the inter-network and enhanced intensity covering regions we identified as network. The k_3 central absorption shows very faint oscillations in the inter-network region and lower intensities overlaying network fields.

The intensity maps for the ARQS dataset are included in Figure 3.5(b). We point out the presence of additional regions of enhanced intensity in the k_2 emission, persistent bright structures that can be seen at $15''$ and $-10''$ and some shorter-lived brightening.

Fibrils resembling the structure usually seen in $H\alpha$ images are present at the border of the network region in the CHQS1 intensity in Figure 3.6(a), especially in the k_2 emission. The better contrast between the network and inter-network is also apparent in the intensity of the CHQS2 dataset Figure 3.6(b).

The variation of optical depth across the emission profile is emphasized in the slow suppression of the photospheric convective motion in the inter-network region: the oscillatory

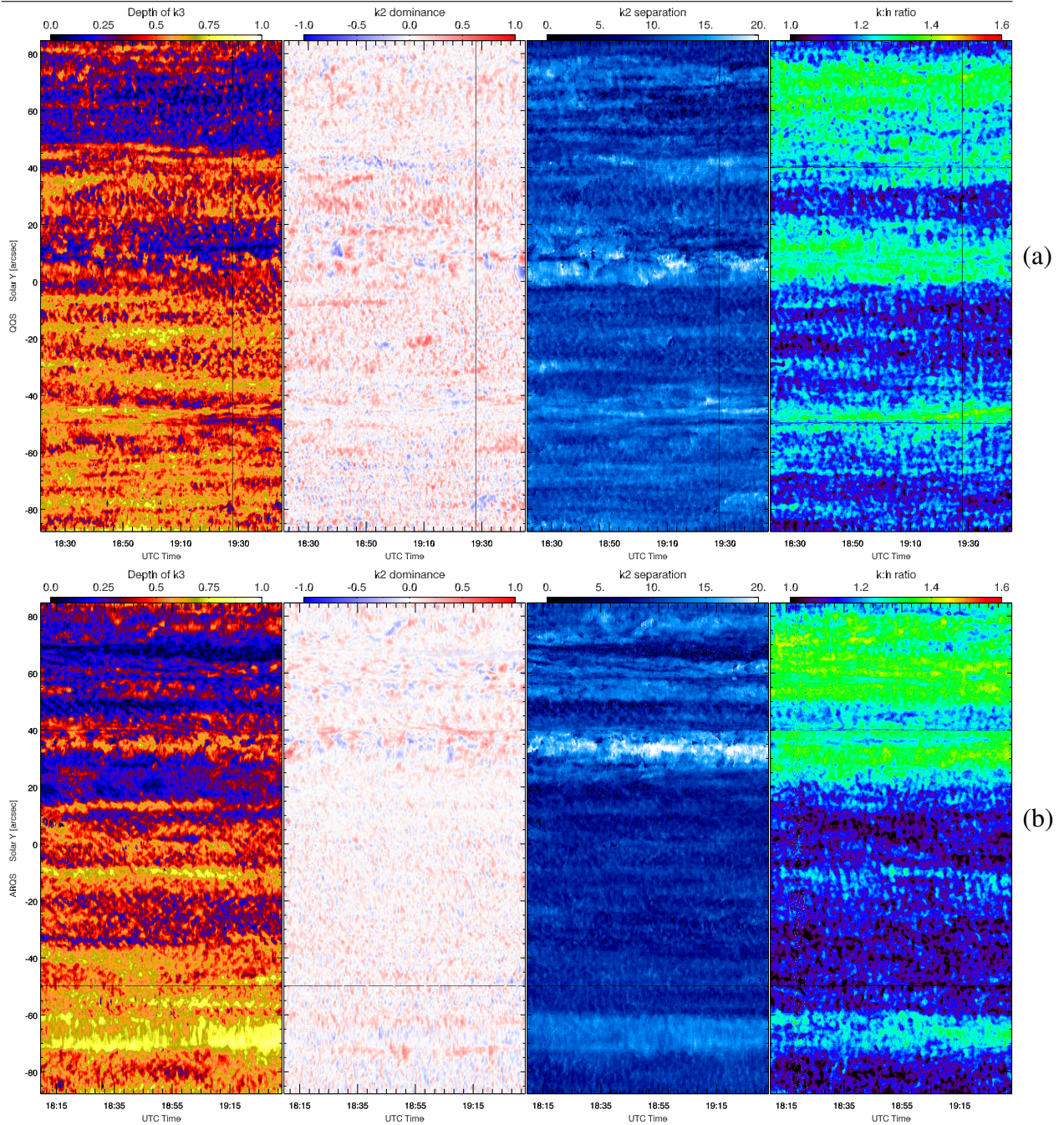


Figure 3.7: Variation in the computed values for the Mg II k_3 core depth (left), k_2 peak emission asymmetry (centre-left), k_2 peak separation (centre-right) and the $k:h$ ratio (right) for the QQS (a) and ARQS (b) datasets. The colourbar for the scaling of each of the maps has been included at the top of the corresponding panel.

pattern dominates the Mg II k_{1r} emission, starts to fade in the k_2 peaks and is barely noticeable in the k_3 core. The network region is marked by the near complete suppression of the convective oscillations even at the height of formation of the outer minimum, and is marked by high intensity in the chromospheric emission at the k_2 and k_3 positions. The k_2 peaks show more variation and are dominated by filamentary structures in the network region, that are more smoothed out in the core emission.

Using the feature identification results, we can further explore the properties of the Mg II emission following the procedure described in Section 2.1.4. We use equations (2.9) and (2.11) to (2.13) to compute the D_{k_3} depth of the k_3 line core compared to the surrounding k_2 emission peaks, the W_{k_2} separation of the k_2 peaks, the R_{k_2} asymmetry of the k_2 peaks and the R_{kh} ratio between the resonance lines intensity. In optically thin conditions the ratio between the

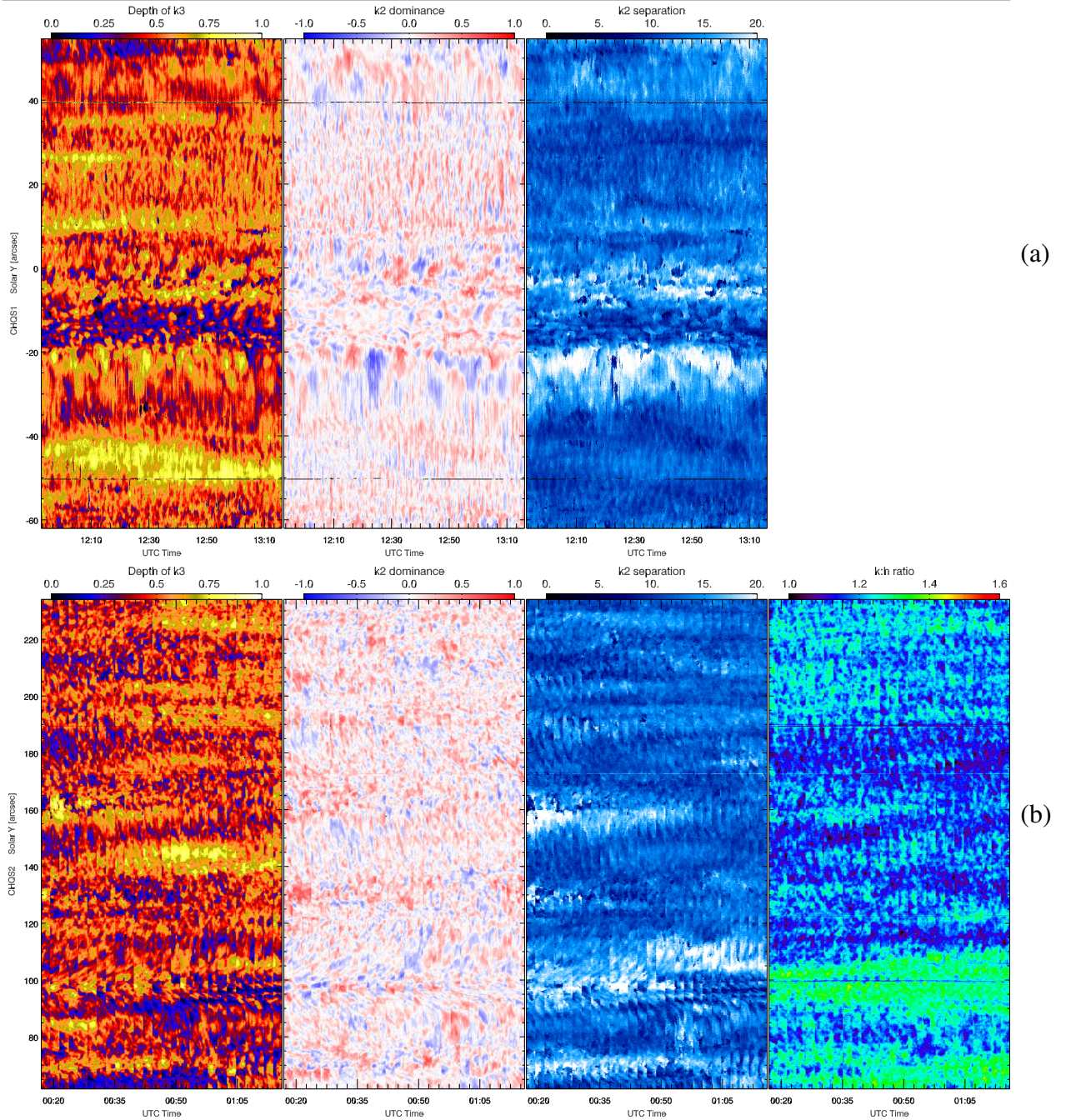


Figure 3.8: Similar to Figure 3.7 for the CHQS1 (a) and CHQS2 (b) datasets. The CHQS1 dataset does not contain the Mg II h line so the ratio could not be computed.

Mg II k and h lines is equal to 2 : 1 and is given by the oscillator strength ratio. However, in solar conditions the departures from the thin ratio is a good proxy for the optical thickness of the emitting plasma. The integrated intensity of the k and h lines was obtained by summing the intensity between the locations of 15% and 85% CDF, and multiplying by the spectral resolution of a pixel. This analysis was performed on the QQS, ARQS and CHQS2 datasets. The CHQS1 did not record the h line emission, so it could not be used.

The time-distance plots for the QQS set are included in Figure 3.7(a). The network shows shallower central depression of the line core, higher separation of the emission peaks, and higher values for the ratio between the resonance lines. The oscillatory pattern is present in the inter-network in all variables. The peak dominance map shows a similar trend to the Doppler shift map in Figure 3.3(a).

The depth of the central reversal for ARQS, included in Figure 3.7(b), shows peculiarly high values for the network region below $-60''$, suggesting higher opacity, the observed emission

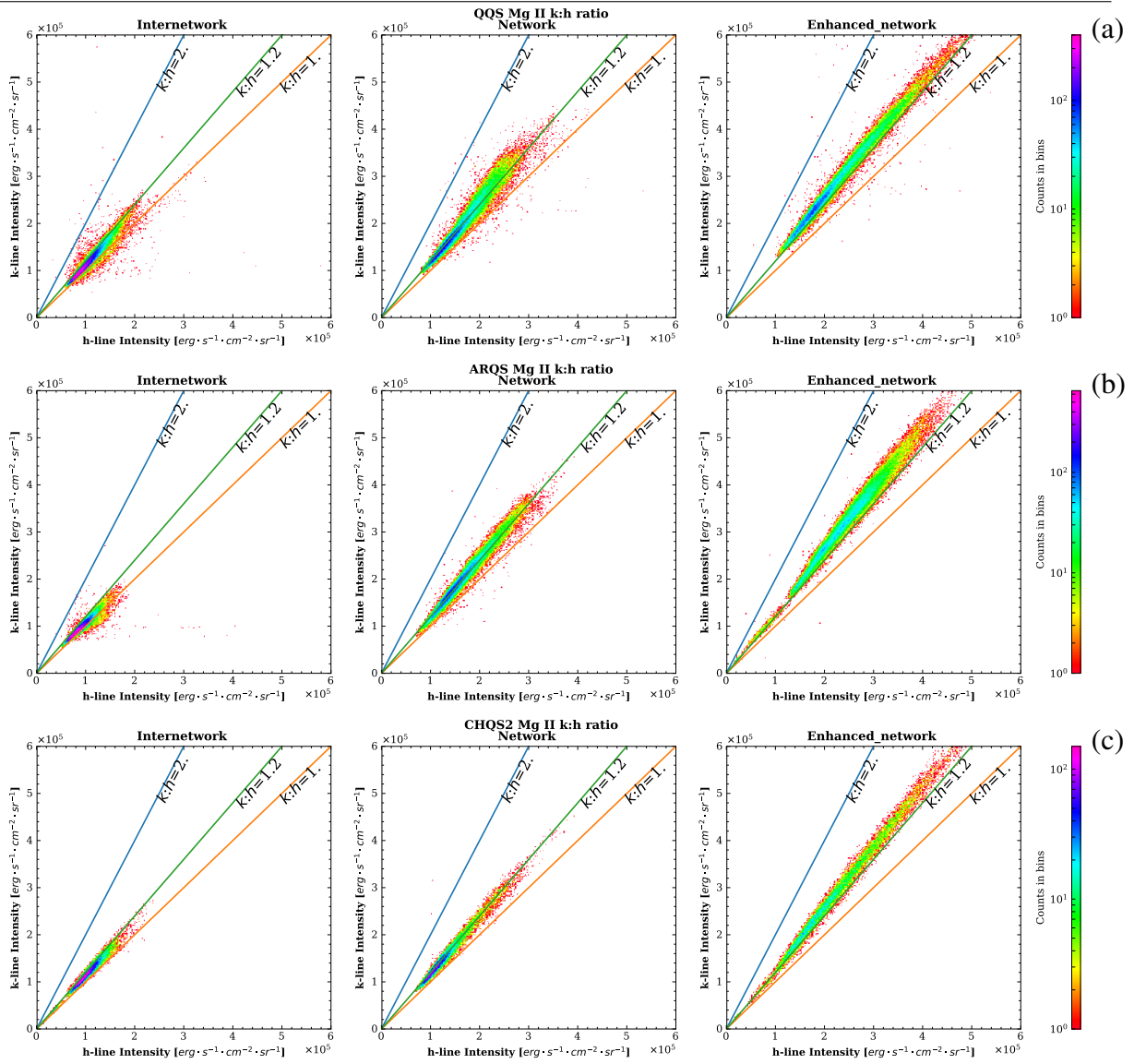


Figure 3.9: 2D histogram highlighting the correlation between the Mg II k and h line intensities for the QQS (a), ARQS (b) and CHQS2 (c) datasets. The lines represent reference ratio values. In optically thin conditions the ratio of k and h is 2:1. A ratio of ~ 1.2 is typical for the low solar activity regime of the quiet Sun. All panels pertaining to a given dataset have the same colour scale represented by the colourbar on the right.

in the core originating from higher in the atmosphere. Enhanced separation and ratio, with shallower profiles are characteristic of the region overlaying the network closer to the active region. The inter-network behaves similarly to the QQS set, but shows lower peak separation.

The evolution of these variables for the coronal hole sets is presented in Figure 3.8 and shows variation comparable to the QQS set, with deep line cores, except in the region immediately overlaying the network region. The higher strength of the network region sampled in the CHQS1 set is highlighted by the higher peak separation and persistent peak dominance.

For a better comparison of the intensity of the resonance lines and their ratio we also present in Figure 3.9 the 2D density distributions between the k and h intensities, for the different chromospheric activity levels as defined in Table 3.2. Lines corresponding to ratio values of 1, 1.2 and 2 have been included to aid comparison. The same scale was kept for the different activity levels in order to highlight the intensity contrast and gradual increase with increased levels of activity. The ratio for the inter-network is under the 1.2 value corresponding to the average solar ratio. The increase of activity tends to lead to higher intensity ratio.

3.3.3. Magnetic field correlation

Previous work on chromospheric oscillatory behaviour reported differences between spatial regions such as the supergranule edge and centre of supergranule (e.g. Deubner and Fleck, 1990), or the magnetic “network” and non-magnetic “inter-network” (Lites et al., 1993; McAteer et al., 2004). The quiet Sun is also dominantly made of granulation (an understood dynamical feature visible at the surface of the quiet Sun in photospheric intensity and cellular flow patterns).

Indeed, moderately strong magnetic field concentrations are associated with enhancements in the Mg II k and h emission. Using *HMI* magnetic field data we have selected in each data set regions of $\sim 15''$ along the spectrograph slit, representative of network and inter-network emission, respectively. The different resolution of the two instruments means that the *IRIS* data oversample the same *HMI* pixel. Additionally inter-network magnetic intensities are close to the noise level of the instrument and may not be reliable. The line of sight effects are minimized by the choice of regions close to disk centre. We decided against using the *HMI* vector magnetic field data, even if available, due to the low cadence which would have increased the uncertainties in identifying the correct location underlying the *IRIS* slit. Higher cadence line of sight magnetic data was not available.

As previously discussed, the enhanced emission and overall variation of the spectral profiles is associated with regions of magnetic field concentrations, at the boundary of supergranular convective cells.

3.3.4. Statistical Properties

Once the data analysis is complete, we further examine the network/inter-network contrast from a statistical perspective. In order to extract the typical numerical values of the different parameters we fit their distribution with a simple Gaussian profile. The fit results provide an approximation for the mean value of the different characteristics and their scatter. Figure 3.10 contains a sample fit of the integrated intensity distribution for the ARQS, under the various activity levels. We acknowledge that the pure Gaussian may not correctly describe the distribution, but it is a reasonable approximation in describing average characteristics.

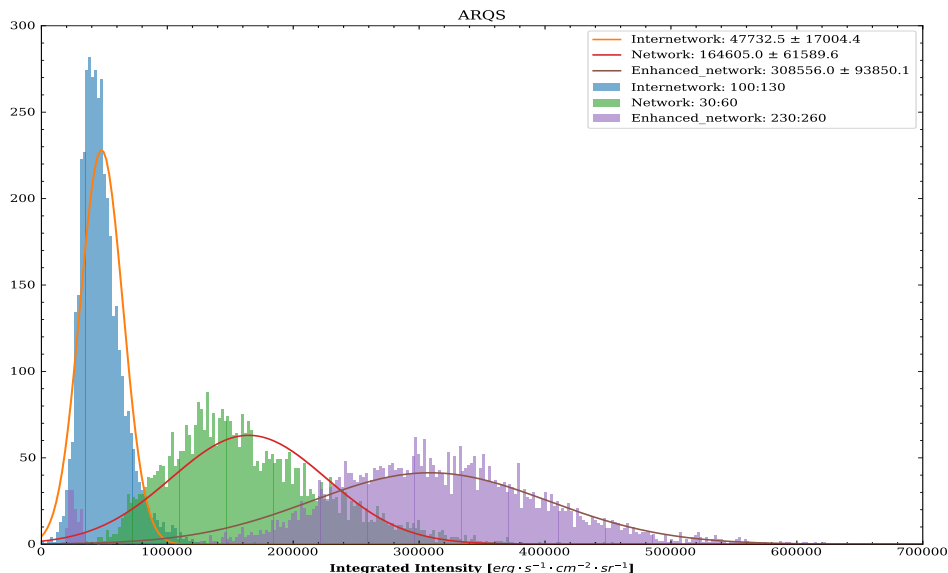


Figure 3.10: Gaussian fit of the Integrated intensity distribution for the k line for the different activity levels in the ARQS dataset.

First we compute the average parameters for the integrated intensity, Doppler shift and line widths of the Mg II k line obtained in the moment analysis, together with average values of the photospheric magnetic field. The results are included in Table 3.3. The increase of magnetic

Table 3.3: Gaussian fit parameters for the profile moments of the Mg II k line and the *HMI* magnetic field distributions under different activity levels in the datasets: Inter-network, Network and Enhanced Network.

Set	Activity Level	Intensity (10^5) [erg s $^{-1}$ cm $^{-2}$ sr $^{-1}$]	Doppler Shift [km/s]	Line Width [mÅ]	Magnetic field [G]
QQS	Inter	0.62 ± 0.21	-0.97 ± 3.58	345 ± 42	1.07 ± 7.37
	Net	1.50 ± 0.64	0.05 ± 2.51	407 ± 65	2.21 ± 13.40
	E Net	2.68 ± 1.03	0.13 ± 2.65	454 ± 54	15.07 ± 27.02
ARQS	Inter	0.47 ± 0.17	-0.11 ± 2.32	312 ± 37	-0.02 ± 7.07
	Net	1.64 ± 0.61	-0.06 ± 2.34	426 ± 54	-2.54 ± 18.86
	E Net	3.09 ± 0.94	0.46 ± 2.31	495 ± 52	-17.75 ± 29.74
CHQS1	Inter	0.84 ± 0.27	0.64 ± 3.28	342 ± 70	-0.35 ± 5.94
	Net	1.73 ± 0.48	0.47 ± 2.53	446 ± 50	5.68 ± 9.62
	E Net	4.12 ± 1.13	0.17 ± 2.63	554 ± 48	195.04 ± 198.37
CHQS2	Inter	0.73 ± 0.28	-0.21 ± 3.74	398 ± 60	-1.06 ± 8.46
	Net	1.08 ± 0.50	-0.63 ± 4.07	441 ± 70	-10.45 ± 26.50
	E Net	2.61 ± 1.21	0.80 ± 3.50	507 ± 51	-31.64 ± 60.06

field is accompanied by at least a doubling of the intensity and increases of line widths in excess of ~ 100 mÅ. The Doppler shift shows little change, as expected given the oscillation between blue and redshift experienced by each position along the SG slit; It would be averaged out by a simplistic Gaussian fit. However, the measured variance can be used to conclude that the shift variations show similar values, supporting their common origin as results of oscillations excited by the photospheric convective motions.

The typical values for the variables measuring the relation between the different profile features of the Mg II k line are included in Table 3.4. They are similarly obtained by fitting a simple Gaussian to the value distribution of the various parameters for identically sized regions sampling the regions of different levels of activity. The depth of the line core given by D_{k3} shows a decrease with increased photospheric field, with the exception of the region chosen as medium strength network in the ARQS dataset that has unusually high values. The R_{k2} peak dominance is again unsuited to be fitted by a Gaussian function as the interchange of enhanced emission between the peaks is averaged out. The W_{k2} shows an increase with the increase of

Table 3.4: Gaussian fit parameters for the profile feature characteristics under different activity levels in the dataset: Inter-network, Network and Enhanced Network.

Set	Activity Level	Core Depths	Peak Dominance	Peak Separation mÅ	$k:h$ Ratio
QQS	Inter	0.53 ± 0.12	0.07 ± 0.14	271 ± 38	1.12 ± 0.08
	Net	0.52 ± 0.12	0.04 ± 0.12	302 ± 56	1.19 ± 0.07
	E Net	0.33 ± 0.15	0.06 ± 0.16	323 ± 79	1.27 ± 0.05
ARQS	Inter	0.42 ± 0.12	0.04 ± 0.09	226 ± 31	1.08 ± 0.06
	Net	0.70 ± 0.09	0.05 ± 0.12	317 ± 38	1.20 ± 0.05
	E Net	0.36 ± 0.14	0.05 ± 0.13	355 ± 75	1.30 ± 0.05
CHQS1	Inter	0.52 ± 0.12	0.09 ± 0.16	309 ± 46	-
	Net	0.46 ± 0.11	0.05 ± 0.15	356 ± 53	-
	E Net	0.38 ± 0.16	0.04 ± 0.18	332 ± 81	-
CHQS2	Inter	0.43 ± 0.12	0.05 ± 0.17	309 ± 50	1.14 ± 0.08
	Net	0.47 ± 0.14	0.08 ± 0.19	358 ± 78	1.17 ± 0.05
	E Net	0.41 ± 0.16	0.02 ± 0.19	389 ± 86	1.27 ± 0.05

emission and so does the R_{kh} ratio between the Mg II doublet.

To further explore the correlation between the different computed characteristics we used the *pandas* Python Data Analysis Library to create a data structure with all the computed parameters and to extract their pairwise correlations. Values close to one suggest a strong correlation, while those approaching minus one imply an inverse correlation. If the correlation value is close to zero, two variables are considered to be uncorrelated.

We then used the *Seaborn* visualization library to visualize the correlation matrix. Figure 3.11 shows the correlation matrices for the ARQS dataset under the different activity levels considered. The correlation matrix for the other datasets differ only marginally in the obtained correlation values and we choose to not include them.

There is a strong correlation between the integrated intensities of the k and h lines, irrespective of the integration method used, and between the intensities of their analogous spectral features. This is expected as the intensities of both lines respond to identical atmospheric conditions.

The measured W_{k2} emission peak separation and the $\Delta\lambda_D$ line width obtained from the moment analysis also show a moderate correlation, as they are tightly linked, wider separation of the emission peaks naturally translates to wider overall profile.

Surprisingly, there appears to be an inverse correlation between the R_{k2} ratio describing which of the emission peaks around the central absorption dominates the line and the Δv Doppler shift of the line centroid. This suggests that, for instance, the red peak shows a higher intensity when the overall line profile is shifted toward the blue, and vice versa.

3.4. Photospheric acoustic analysis

We wish to examine the inter-relations between the physical properties of different layers of the quiet Sun. We will focus our analysis on correlations between the chromosphere and photosphere observations at the location of the *IRIS* slits. We specifically follow the areas of super-granular inter-network and network regions in the quiet Sun. The acoustic properties of the photosphere are studied in the quiet areas that contain the FOV of *IRIS* observations.

For each of the considered datasets we used *HMI* data to compute the local acoustic power (magnitude of the local acoustic oscillation amplitude) and the seismic emission power (distribution of acoustic emitters). We are using signal processing algorithms to study the oscillations in the photosphere. The power in the local acoustic waves of high frequencies (6 mHz) is calculated. Helioseismic holography (see Section 2.2.1) is also used to identify enhanced seismic emission in the photosphere, and compare our findings with the location of bright grains. There is a difference between calculating the acoustic power of the local field and the emission power of a potential seismic source triggered at the same location. We are seeking any correlation between the local acoustic response of the photosphere and possible propagation of waves up into the chromosphere.

When performing the acoustic analysis of the photosphere we have to keep in mind the following:

- The acoustic cut-off frequency plays an important role in establishing the wave propagation conditions from the photosphere into the chromosphere.
- Study of waves and oscillations in different solar conditions (umbra, penumbra, network, inter-network) have significant importance as these structures play a particular role in transporting energy from the interior/photosphere to the upper layers of the solar atmosphere.
- Inter-network regions are the places of very weak magnetic flux and they support acoustic waves propagation. (Lin and Rimmele, 1999)
- Photospheric network regions have average magnetic field strengths of 100–150 G.

3.4.1. Results

We analysed a comprehensive data set comprised of a mosaic of *HMI* data, together with computed acoustic emission and local oscillation in the region of quiet Sun named ARQS. This is presented in Figure 3.12. The figure covers a zoomed out region compared with the FOV observed by *IRIS*. Simultaneous maps containing the magnetogram of B_{LOS} field (top left), Dopplergram of line of sight velocity (top middle) and intensity continuum are included (middle centre). The local acoustic emission power at 6 mHz (middle left) and the map of seismic emission in the region (top right) reveal an excess acoustic halo surrounding the sunspot. The high frequency 6 mHz local intensity power map (middle right) better highlights the regions of wave suppression near magnetic field concentrations. The arrows identify features in the map such as magnetic network, supergranules and plages. The fine structure in acoustic maps is the realization noise.

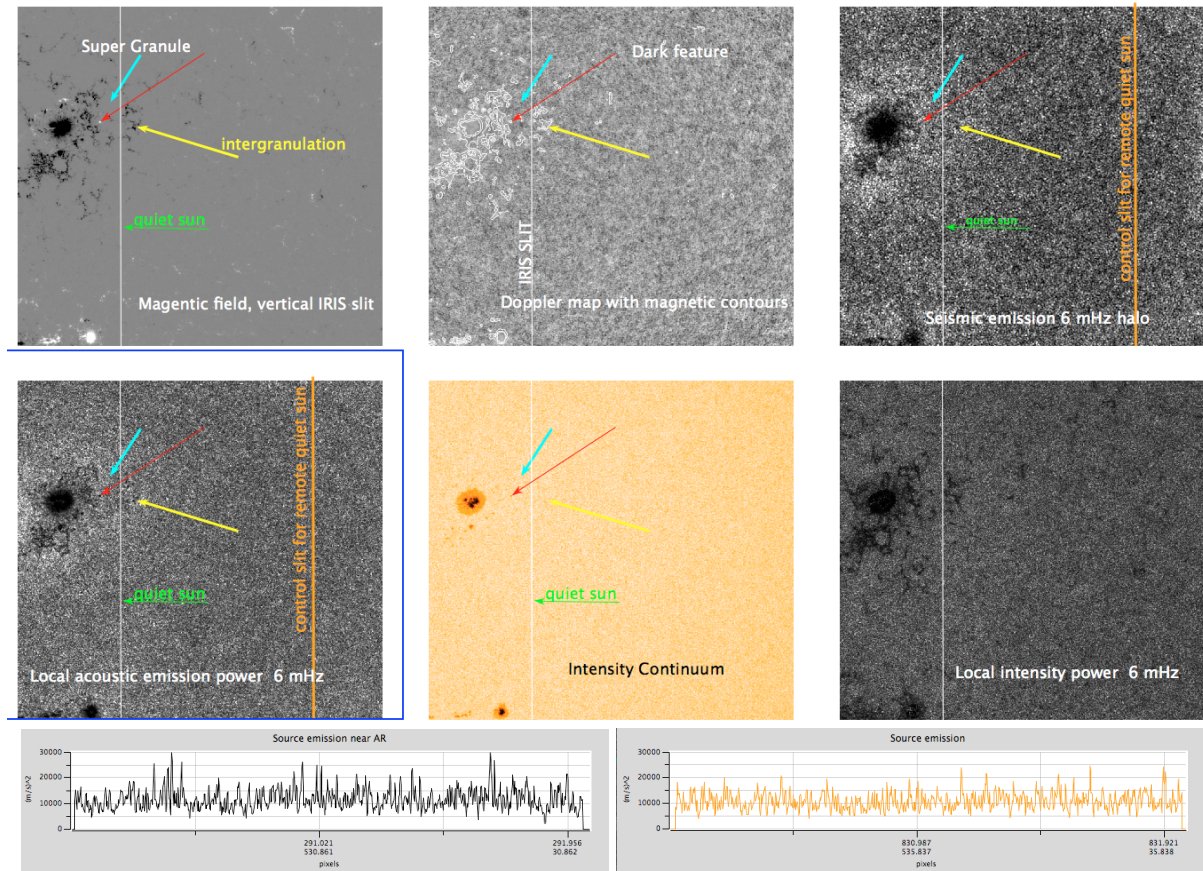


Figure 3.12: *HMI/SDO* magnetogram, Dopplergram and intensity continuum maps for the ARQS data. The seismic emission at 6 mHz and the local acoustic emission power at 6 mHz highlight the haloes around the main sunspot. The local intensity continuum power at 6 mHz is shown in the last panel. The *IRIS* slit crosses over a part of the acoustic haloes. Another control “slit” is plotted in orange in the acoustic maps. Bottom row: Spatial profile of the high-frequency seismic emission for the *IRIS* slit position of under-canopy quiet Sun (black) and the second slit sampling a quiet Sun away from the main sunspot (orange).

The vertical lines in Figure 3.12 sample different activity regimes. The *IRIS* slit (white vertical line) traverses the acoustic halo but the lower part of the slit crosses a zone identified as a “quiet” area, away from the magnetic canopy of the active region and even the acoustic haloes. An additional slit is considered in a more “quiet” region away from the active region (vertical orange line). The bottom row of the figure presents the profile of the 6 mHz seismic emission (egression power) for both *IRIS* and the orange slit locations as the black and orange lines, respectively. The plots show a typical profile of the 6 mHz seismic power for the

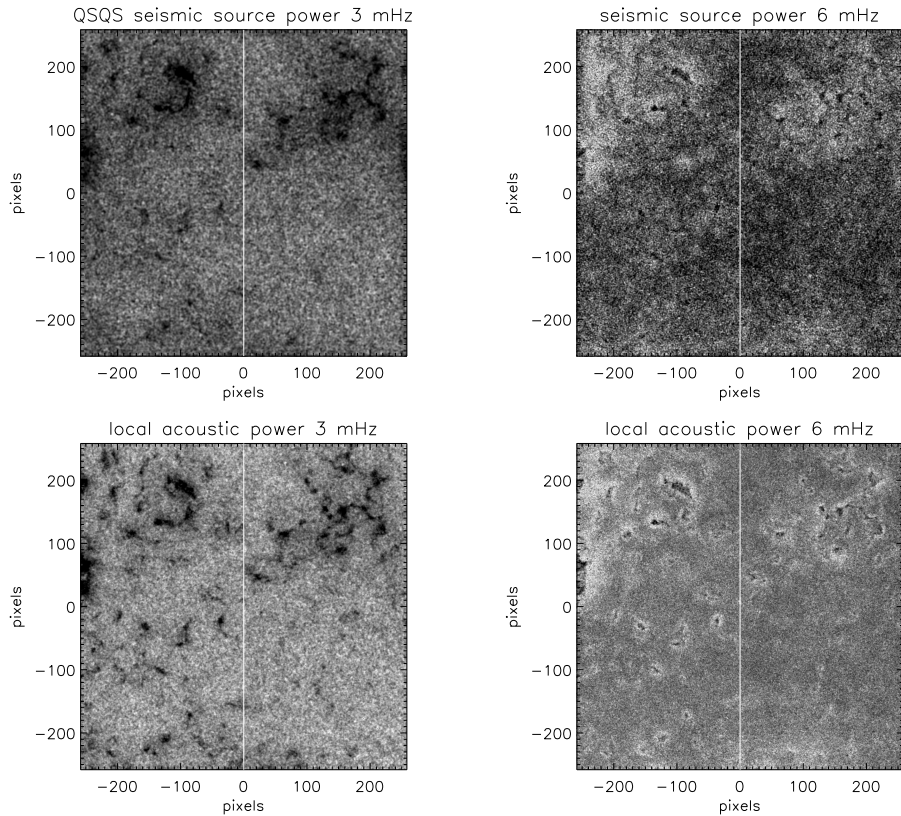


Figure 3.13: QQS: The local response to the photospheric oscillations is represented as the acoustic power $(m/s)^2$ in the 3 mHz and 6 mHz frequency respectively, in the lower frames. Top panels show the seismic emission $(m/s)^2$ maps at 3 mHz and 6 mHz.

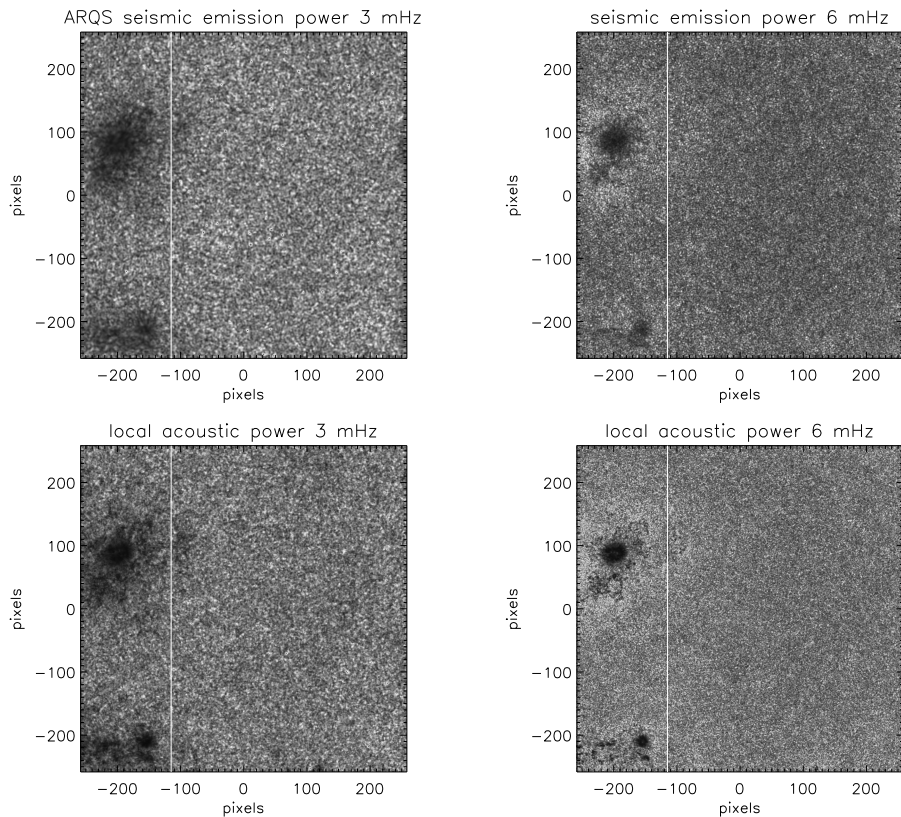


Figure 3.14: As above but for the area of quiet Sun labelled ARQS (see Table 3.1).

quiet Sun oscillations (orange plot) displaying small amplitudes. We found that the excess high-frequency local power corresponds to regions where the magnetic field is 20–100 G (B_{LOS} field component). The magnetic field strength in the acoustically suppressed region is around

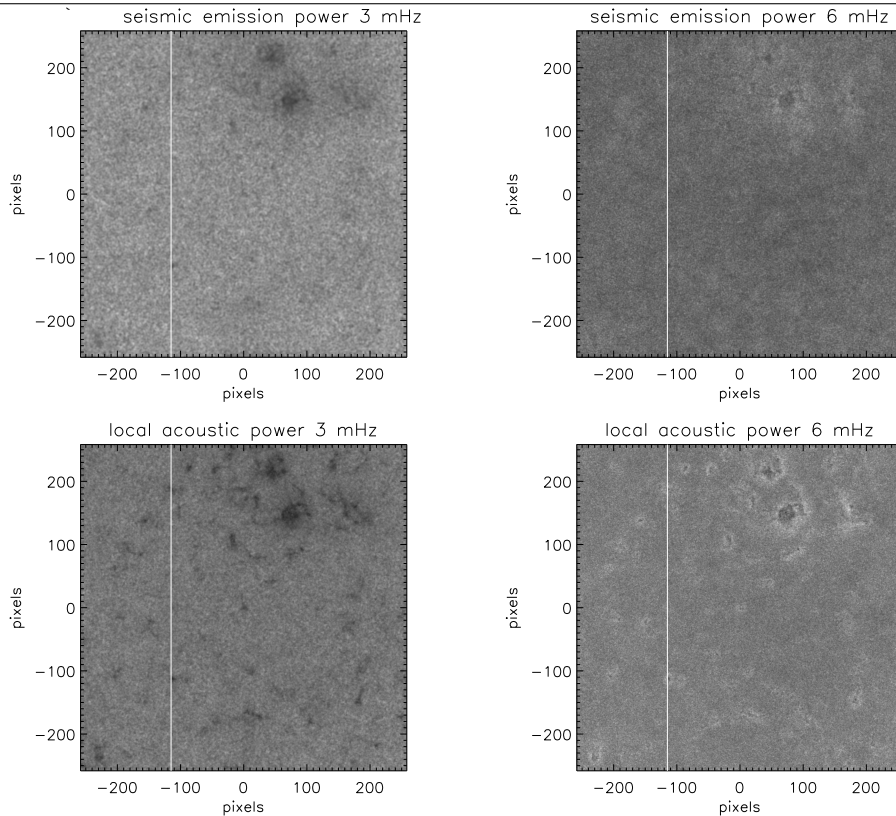


Figure 3.15: *HMI/SDO* local acoustic power and seismic emission maps of CHQS1 at 3 and 6 mHz. The enhanced 6 mHz local oscillations around the north plages and other magnetic concentrations in the photosphere is evident. Local seismic emission at 6 mHz is detected inside supergranules. Evident absorption of 3 mHz acoustic and seismic power is seen in magnetic regions of $B \approx 90\text{--}110$ G.

100–150 G. The enhanced local acoustic emission surrounds mainly magnetic plages near the main sunspot.

It is generally accepted that quiet-Sun oscillations are stochastically excited by solar convection at the top part of the convection zone (Goldreich and Kumar, 1990; Nordlund and Stein, 2001). We obtain acoustic power maps of the regions averaged over 1 mHz intervals. These maps allow studies of the spatial and frequency distributions of acoustic power in the quiet Sun. These are mapped in Figures 3.13 to 3.15.

The enhanced 6 mHz local oscillations around magnetic features are evident. The magnetic plages and the photospheric network of supergranule also suppress the 3 mHz acoustic oscillations. A novelty of our research is the detection of enhanced seismic emission at 6 mHz, in the centre of supergranules.

The oscillation power within any pixel is a strong function of the magnetic field strength within that pixel. The amplitudes of oscillations with frequencies less than 5 mHz decrease with field strength. The local acoustic-power haloes are regions in which the local acoustic oscillations at the surface have a conspicuously higher amplitude than in the "quiet Sun".

Bringing together the magnetic maps of all regions of quiet Sun (labelled ARQS, QQS, CHQS1), and their corresponding 6 mHz local acoustic maps, we identify enhanced high-frequency seismic emission around plages and some small magnetic areas (corresponding to network regions). The magnetic field in the very quiet areas of supergranulae interior is too small to affect the acoustic emission.

Figure 3.17 shows the histogram distributions of the 6 mHz seismic emission, known also as egression power (EGRESS_PWR in units of $(m/s)^2$) and of the local acoustic power (DOPP_PWR measured in $(m/s)^2$). The histogram distribution representing the whole area of study (QQS) is rendered in gray. Coloured histogram distributions for the chosen masks are

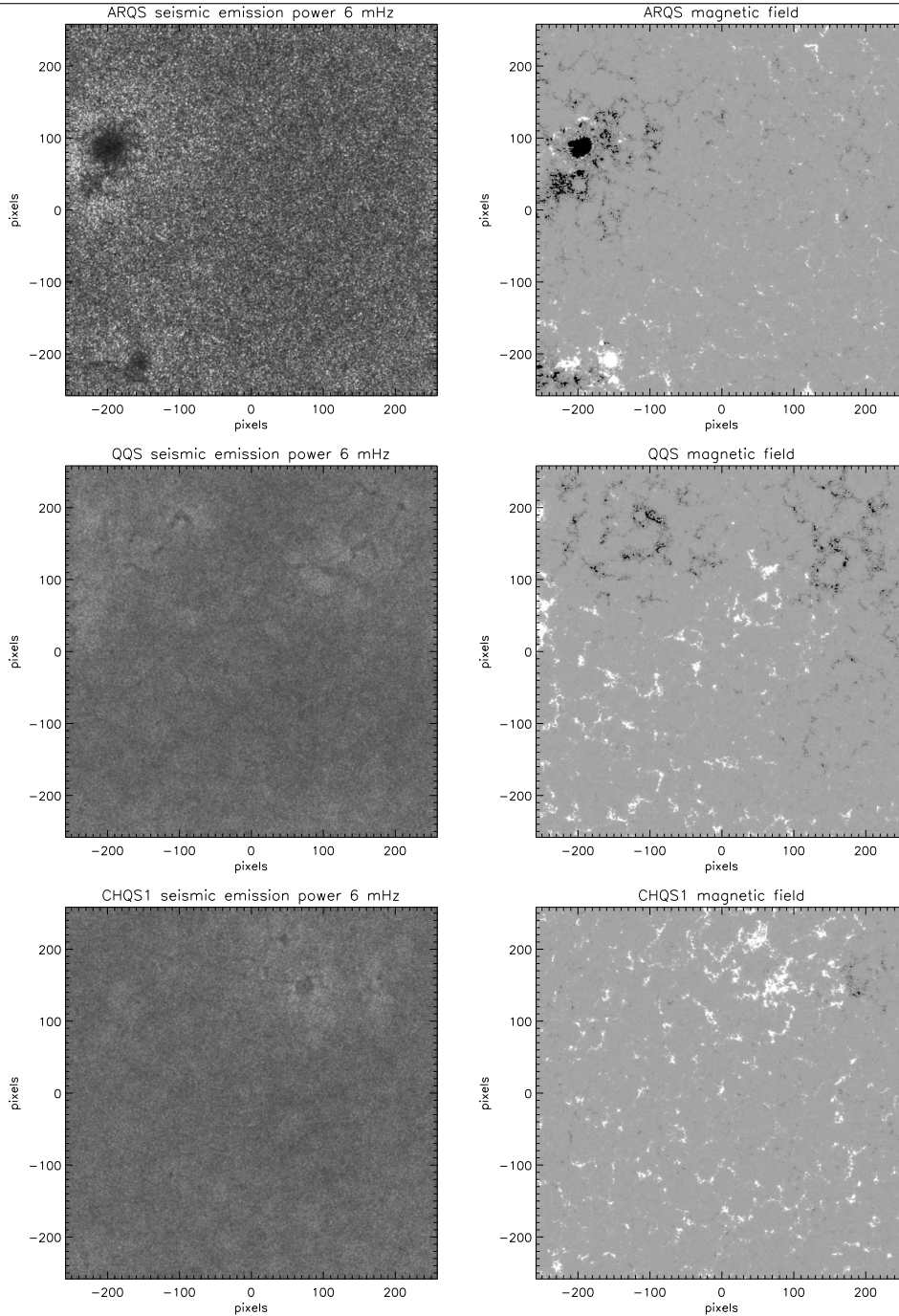


Figure 3.16: An ensemble picture of all 6 mHz acoustic maps for wider regions containing the three regions of quiet Sun: ARQS, QQS, CHQS. The maps emphasize enhanced high-frequency seismic emission in some magnetic areas.

overimposed and are subsets of the full set. The masks are sampling areas of supergranulation (pink, green and yellow markers) and of magnetic plages (red). Both distributions show lower values for the measured variables in quiet Sun conditions.

3.5. Summary and Discussion

We used *IRIS* spectroscopic data of the Mg II resonance lines to investigate properties of the chromosphere in regions of quiet Sun. We studied specific areas of the quiet sun, localized either close to the canopy fields of an active region or far in the so called "pure" quiet sun or in coronal holes. While these regions may look different in coronal emission, the lower atmosphere shows less contrast.

The profile moments were computed and the locations of the different profile features

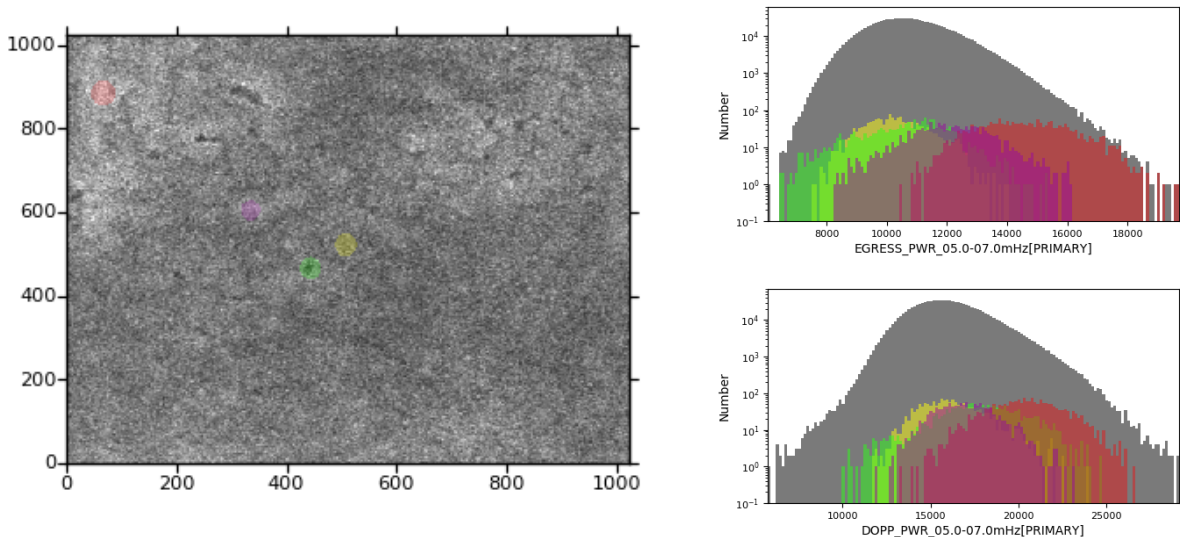


Figure 3.17: The 6 mHz local acoustic power map of the area including the QQS set: regions of the quiet Sun with a few coloured masks over-imposed which are used for our statistical analysis of distributions. The corresponding histograms are included on the right.

were identified. We compared the temporal evolution of various parameters and finally extracted some average values characterizing the network/inter-network contrast in each set. The acoustic emission of the underlying photosphere was also investigated.

The integrated intensity increased with the strength of the underlying network magnetic field and showed little variation in the inter-network region across the selected datasets. The emission peaks measured on either side of the central absorption of the Mg II resonance lines showed more structured features across the observed regions. If they overlaid regions of higher network field, as was the case for the CHQS1 dataset, the observed morphology was reminiscent of the H α fibrils.

The Doppler shift of the Mg II k line is dominated by oscillatory motion, most likely excited by the convective flows, in the inter-network region, while showing a slightly larger period for the regions overlaying network field. Time series observations of the profile of the Mg II k line in the CHQS1 dataset hosted episodic enhanced downflows at the boundary of the network, suggesting the presence of intermittent plasma flows.

There is a visible contrast between the network and inter-network regimes in the measured width of the resonance lines. Overall higher values are characteristic of the coronal hole observations, even in the cell interior.

Computed $k:h$ ratios of the two resonance lines were well below the optically thin conditions and show higher values over the supergranular cell boundary. The CHQS2 dataset stood out, with a lower ratio, suggesting a greater optical depth.

The depth of the central absorption was reduced in regions of network field, while the separation between the emission peaks was enhanced even in regions covering the boundary flows. The peak asymmetry showed a similar variation to the computed Doppler shift, to which it appeared to be anti-correlated.

The analysis of oscillations in the solar atmosphere can be a useful tool to understand its structure and properties. In the photosphere, the power of local oscillations was generally suppressed at all frequencies, both in the umbra and in the penumbra of sunspots, and in plages and around magnetic pores. The analysed magnetic network regions (with magnetic fields of 100–120 G) also presented significant acoustic suppression at all frequencies, but were surrounded by 6 mHz high-frequency halos of enhanced local-seismic-amplitude/power. The effect of the magnetic field on the oscillation power was thus significant. Vertical magnetic fields, correlated with the network, revealed their signatures in the acoustic maps as well as in

the spectroscopy of chromospheric lines.

Acoustic enhancements of 150% were observed around some patches of network and small pores in our quiet sun datasets. The enhancement around small pores was as large as the acoustic enhancement reported around large active regions (haloes) by [Donea et al. \(2000\)](#). For the case of the quiet sun patch in the neighbourhood of an active region, the IRIS slit captured the area of the acoustic haloes under the magnetic canopy. This area could be thus analysed also at chromospheric heights.

Our aim was to examine whether differences between the magnetic and acoustic properties of the quiet sun areas can tell us a story about the wave interaction between the acoustic oscillations and the magnetic fields of the network or of the magnetic canopy. Simultaneous observations of the photosphere and chromosphere pointed toward the detection of vertical wave propagation from the photosphere to the chromosphere. The supergranular network and inter-network was also analysed by a number of IRIS observations close to the disk-center which allowed us to "zoomed into" the supergranular networks of interest.

Therefore, our finding provided observational evidence for the presence of magnetic field sensitive acoustic oscillations as well as intensity line oscillations in the chromospheric locations, which in turn suggested the existence of magneto-acoustic waves travelling into the chromosphere. From a comparison of integrated line maps and SJI images, we concluded that the chromosphere supports several wave types that are believed to play a role in the dynamics and heating of the atmosphere. In the interior of supergranules, where the magnetic fields were weak, we identified chromospheric acoustic waves. On the boundary of supergranular cells, where magnetic fields were densely packed, the waves in action could be local modes such as longitudinal and transverse (kink), as well as torsional waves.

A further analysis of the wave periods seen in the intensity at the different profile positions will be performed in order to explore the damping of oscillations as a function of height. Additionally, we want to check which spectral characteristic is most reliable in determining the wave frequency and amplitude, in order to ease future investigation of the chromospheric and photospheric connectivity.

We presented a thorough analysis of the Mg II profile characteristics. We investigated the acoustic properties of the supergranular structure for various quiet Sun regions and focused on the physics of acoustic enhancements (pores haloes, glories) around some patches of network. In conclusion, the quiet sun exhibited a large range of dynamic spectral profiles associated with small scale magnetic field concentrations. Shuffled by convection and near surface local motions, the magnetic field accumulated at the boundaries of supergranules to form magnetic networks. At chromospheric level it can be seen as bright web-like patterns, betraying the presence of magnetic flux tubes which expand with height.

Chapter 4: Flaring Atmosphere Spectroscopy

“A process cannot be understood by stopping it. Understanding must move with the flow of the process, must join it and flow with it.”

Frank Herbert, *Dune (First Law of Mentat)*

The Sun is an average star, but it is far from being unexciting and presents cycles of high and low activity. In the previous chapter we analysed the complex chromospheric properties of what we generally consider quiet sun regions. This chapter is in turn dedicated to the investigation of how the solar atmosphere responds to strong flaring conditions.

Solar flares are the most energetic events that can take place in the solar atmosphere releasing tremendous amounts of energy. Part of the energy is headed into interplanetary space and can influence space weather. Another part of the energy will interact with the low solar atmosphere, heating the medium and triggering additional events, from exciting waves and causing additional eruptions, to producing intense white light flares. The famous flare observed by Carrington (1859) had both components: it produced an intense geomagnetic storm affecting the telegraphs system and triggered an enhancement of visible solar emission.

An interesting question still torments those that study energetic solar phenomena: how can the flare energy propagate from the reconnection site in the corona to the dense photosphere to produce a photospheric impact, noticeable as an acoustic signature, sometimes identified as a solar quake. The energy must cross increasingly denser layer of the chromosphere without being absorbed and simply radiated away. We present an overview of the current understanding of solar energetic events, focusing on their observational properties. The challenges faced by both observations and simulations are briefly reviewed, together with the attempts at precisely predicting the occurrence of such events.

Our aim is to use both spectral and imaging data to investigate the emission from different layers of the atmosphere in the different stages of flare evolution in order to find any correlation to the downward energy propagation and their photospheric responses. For the first time, we will temporally and spatially link the chromospheric observations to the photospheric data, to provide the history of the vertical energy flow from the flare into the sun. This work will help in elucidating the mechanism that induce solar quakes.

We will explore the flare response across multiple instruments and wavelengths, discussing its precursors, the magnetic environment and the aftermath of the reconnection. The main analysis of two X-class flares is based on *IRIS* data, with supporting observations from other instruments (such as *SDO* and *RHESSI*) where required. The seismic signatures are investigated and their relation to the overlying atmosphere is highlighted. The flare triggering mechanism, line enhancements and the subsequent relaxation of the atmosphere will be analysed. Furthermore, magnetic field data is used to study the magnetic structure of the active region, and its changes in response to the flaring events.

4.1. Introduction

Solar flares are a sign of a magnetic reconnection event and in the span of a few minutes they can release an energy of more than 10^{32} erg across the whole electromagnetic spectrum, by exciting non-thermal particles and producing heating, seen as excess emission from EUV to IR radiation. They are also connected to the acceleration of particles into the heliosphere and can be accompanied by Coronal Mass Ejections (CMEs). The flare strength is usually defined based on the intensity of emission in the 1-8 Å soft X-Ray channel of *GOES*. An extensive overview of observational characteristics has been compiled by [Fletcher et al. \(2011\)](#).

Regardless of their size, flares tend to originate in or near active regions, where the magnetic configuration shows strong gradients. This mostly is the case of polarity inversion lines (PILs), regions where two opposite magnetic polarities are moving with respect to each other, increasing the inclination and shear of the loops connecting them.

Typically, the flare evolution can be separated in a three main stages based on their emission properties. The pre-flare phase, usually marked by small intensity enhancements or in the case when a filamentary structure is present, it can be seen to expand, eventually becoming unstable. The impulsive phase consist in abrupt enhancements across all wavelengths, especially in the shorter wavelengths and X-Ray emission. There are two kinds of the gradual phase of flares: a gradual phase during which no energy is released (cooling follows the impulsive phase), and a gradual phase during which the flare energy release continues. The latter is a characteristics of dynamic flares.

In the “standard model” of solar flares, also known as the CSHKP model ([Carmichael, 1964](#); [Sturrock, 1966](#); [Hirayama, 1974](#); [Kopp and Pneuman, 1976](#)), the observed features are considered the result of magnetic reconnection that decreases the magnetic stresses of the host active region. The reconnection site is usually considered to be located in coronal conditions. The energy resulted from the reconnection can lead to energetic particle acceleration away from the reconnection site, both towards the surface and into the interplanetary medium. The particles in the downward accelerated beam will encounter increasing densities, thus lose their energy leading to impulsive heating of the local plasma, that evaporates along the newly reconnected loops. The location of the beam energy deposition is seen as HXR emission kernels and the evaporation can be seen as blue shifted emission in hotter emission lines. The observed SXR emission reveal the hot emission in the newly reconnected loops. The abrupt heating heads to overpressure around the location of energy deposition, that will compress the lower atmospheric layers and produce red shifted emission of the spectral lines forming in transition region or chromospheric conditions. As successive field lines are reconnected, their footpoints light up and appear to sweep the atmosphere, as they move away from the reconnection site.

If a filament is involved in the flaring event, the rise of the filament can lead to distortions of the local magnetic field configuration in such a way as to produce a thin current sheet. Magnetic field lines in this current sheet reconnect and form flare loops, allowing for separation of $H\alpha$ ribbons at their footpoints. Part of the reconnected structure can also be ejected as Coronal Mass Ejection (CME) carrying energy in addition to the accelerated particles.

Following from early 1D simulations of [Fisher et al. \(1985\)](#) the value of the injected energy flux decides the gentleness of the associated evaporation. If the injected energy is above a critical value of $F_{20} = 10^{10}$ erg cm⁻² s⁻¹, the ‘explosive’ evaporation of low atmosphere material will ensue. The coronal line emission will show blueshifts, corresponding to chromospheric evaporation, while the lines formed in the lower chromosphere will be seen as redshifted, corresponding to the process of chromospheric condensation, when the sudden heating and evaporation of material will actually push the lower atmosphere downward. For input energy values lower than the critical threshold, all lines will show a blueshift, corresponding to a more ‘gentle’ evaporation of chromospheric plasma.

The only evaluation of the response of the Mg II emission lines to a flaring event, prior to the launch of *IRIS*, was by [Lemaire et al. \(1984\)](#). They explore the properties of the lines in comparison with simultaneously obtained spectra and find resonance line ratios to decrease as the flare progressed. With the wealth of data from *IRIS* a number of authors have looked at different aspects the flare emission, from the response of the Mg II lines ([Kerr et al., 2015](#); [Liu et al., 2015b](#)) to the response to seismic activity ([Matthews et al., 2015](#)). Despite its importance in understanding the energy deposition and subsequent radiation of the flare energy, chromospheric observations are still not well understood, making the modelling of this complex layer challenging. Additionally, the magnetic structure of this layer is usually extracted from extrapolations of photospheric fields, which include a series of assumptions, that may oversimplify the true configuration.

Solar flares can have a strong impact at the photospheric level. For example, [Kosovichev and Zharkova \(1998\)](#) reported the first clear acoustic signature of a solar flare in observations from the Michelson Doppler Imager (MDI) onboard the Solar and Heliospheric Observatory (SOHO). The acoustic excitation sources are seen as photospheric ripples which move radially outward from a source region, strongly correlate with the impulsive flare phase, and are believed to be caused by the energy and momentum transport from the reconnection site of the flare. The seismic source generates acoustic waves that travel into the Sun and refract back to the photosphere. Many of the previously detected seismic ripples and acoustic sources associated with flares were found to be co-spatial with the hard X-ray (HXR) source locations (e.g. [Donea and Lindsey, 2005](#)).

However, how this transport is executed is not yet known, since any considered process has to penetrate the dynamic and dense chromosphere. On the basis of the observed characteristics of sunquakes at least three apparently feasible source mechanisms were suggested: (1) hydrodynamic shocks, (2) photospheric back-warming, and (3) Lorentz-force transients ([Donea et al., 2006](#)). Also considered have been (4) protons beams ([Moradi et al., 2007](#); [Zharkova and Zharkov, 2007](#)) and (5) magnetic ropes ([Zharkov et al., 2011](#)).

Recently [Sharykin et al. \(2017\)](#) analysed the energy release from a flare near the polarity inversion line and found a strong link between the photospheric seismic location and the electron deposition site as marked by the HXR source, indicating that high-energy electrons accelerated during the impulsive phase induced strong disturbances in the photosphere, causing the sunquake. They also found a delay between the HXR peak and the photospheric signature of less than 4 seconds.

In Section 4.2 we explore the effect of an X-class flare on spectral line emission spanning formation heights from the photosphere to the high temperature corona. We report the detection of a related seismic event and for the first time, we are able to follow the vertical structure of the downflows. Additional clues on the relation between the atmospheric emission and the seismic source are explored in the case of another flare in Section 4.3. As a cautionary tale, the coronal connectivity of a small flaring ribbon is explored in Section 4.4.

4.2. March 11, 2015 X2.1 flare

The main flare on which most of this research chapter is focused is the March 11, 2015 X2.1 flare (SOL2015-03-11T16:22). It originated from AR NOAA 12297 and was triggered by the rise of a filament that became unstable and reconnected with the overlying magnetic field. The flare began near 16:16 UT, reached its emission peak at 16:21 UT and the atmosphere returned to its near-quiet state near 16:35 UT. The different aspects of the flare, from the evolution of the flaring region and the rise of the filament, to the evolution of magnetic field are discussed below. A peculiar phenomenon was observed in the wake of the flare: a highly redshifted and persistent coronal rain event, to the exploration of which the whole Chapter 5

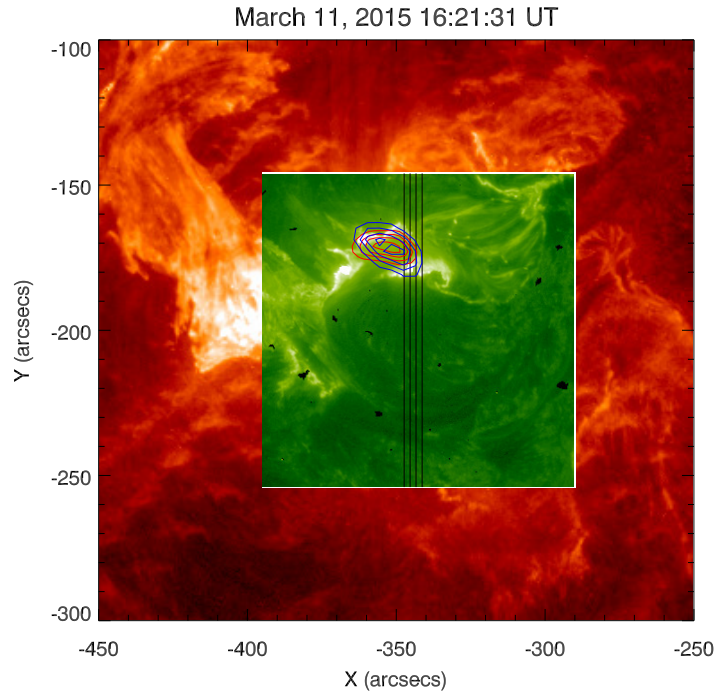


Figure 4.1: Position of the soft (red) and hard (blue) X-ray kernels with respect to the *IRIS* slit positions (black vertical lines). The background (red) is *AIA304* emission and the foreground (green) is *SJI 1330 Å*.

has been devoted.

A composite image containing most of the observational data sources used in the analysis of this flare for a time instance close to the maximum flare emission, is presented in Figure 4.1. The background (red) shows the emission in the *AIA304* channel containing predominantly emission from singly ionized Helium, the foreground is the emission from the transition region (TR) as seen by the 1330 Å lines of singly ionized Carbon. The position of the *IRIS* spectrograph slits are included, as well as contours of the soft and hard X-ray emission. The *IRIS* spectrograph (SG) data does not sample the full flaring region, but has a good coverage of the flaring ribbons and the post-flare flows. In the *AIA304* image, the bright, recently reconnected filament can also be clearly seen expanding to the left of the image.

The *IRIS* data was acquired during a flare watch campaign of the AR, where the tracking of the main spot in the region was enabled. The spectral data was a “large coarse 4-step raster” and consisted of a total of 1230 rasters, each composed of four slit positions, offset by 0″, 2″, 4″, and 6″ in the E-W direction on the solar disk. At each slit position, the data in nine spectral windows was recorded, a complete set of spectra taking ≈ 21 seconds to be acquired. The spatial sampling for the spectral data is 0′′.33/pixel and the typical exposure was 4 seconds, but during the flare the FUV exposure time was automatically decreased to avoid overexposure. The spectral data was obtained with a spectral binning factor of two, leading to a spectral sampling for the NUV channels of 0.05092 Å/pixel, while for the FUV channels it is either 0.02596 Å/pixel (FUV1) or 0.02544 Å/pixel (FUV2).

Context Slit-Jaw Images (SJI) spanning a total FOV of 120″x119″, with a spatial sampling of 0′′.33/pixel were also recorded. The SJI data was obtained in the broad filters centred on 1330, 1400 and 2832 Å corresponding to raster steps 0, 3 and 1, respectively. Each SJI set had a temporal cadence of ~ 20 s.

Further context image data covering coronal emission was used from *AIA/SDO*. The *IRIS* pointing differs from *AIA* by a few arcseconds, thus slight corrections were required. As both *SJI1330* and *AIA1600* show similar features corresponding to continuum FUV emission (Tian et al., 2015), we selected a random *AIA1600* frame and then identified the temporally closest SJI frame. The two images were then scaled and the correct alignment was found. Magnetic data

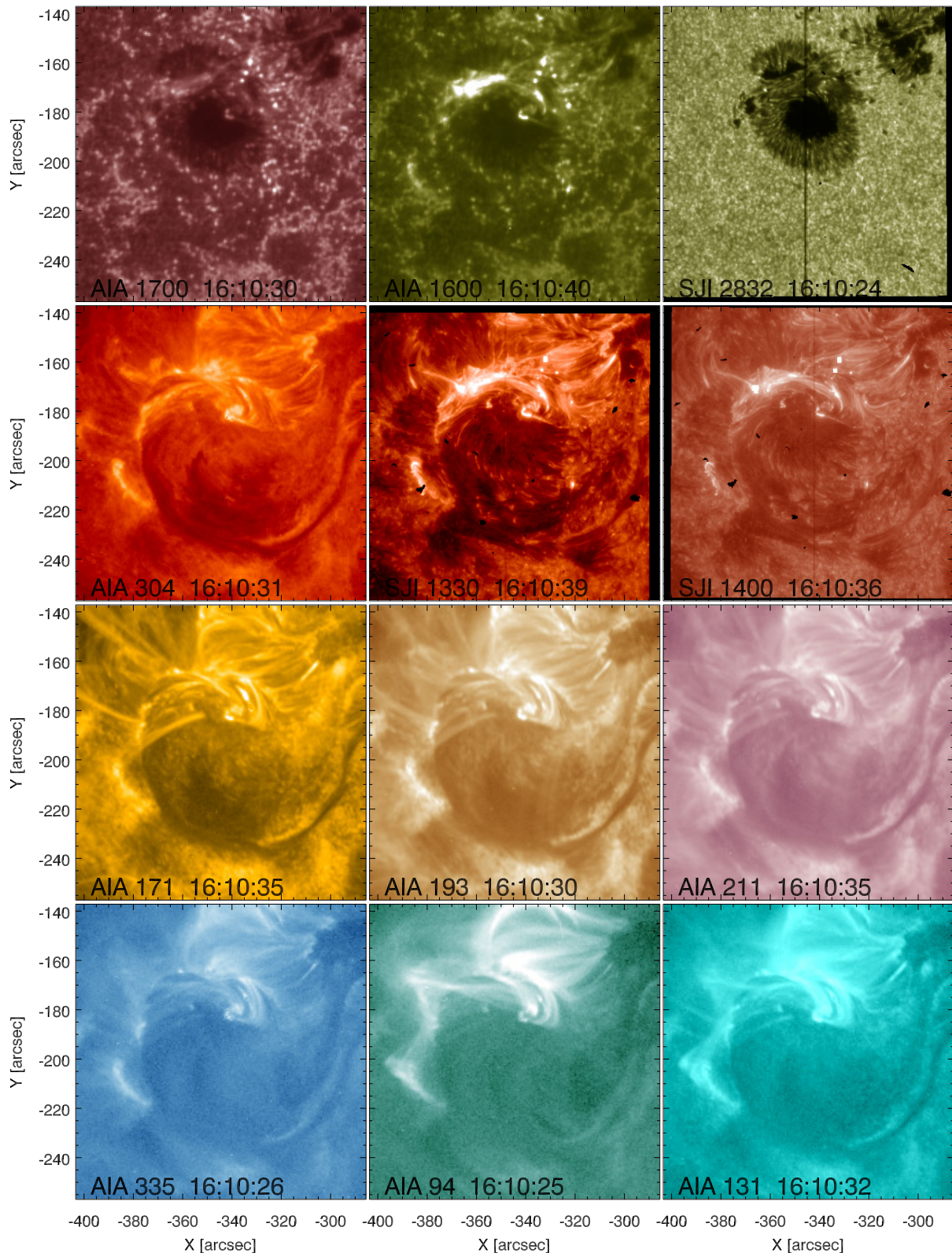


Figure 4.2: The solar atmosphere prior to the X2.1 flare of March 11, 2015 as seen by *IRIS* and *AIA/SDO*. The FOV has been restricted to the *IRIS* field. The dark vertical line in the SJI images represents the position of the slit. The top row contains the emission of filters containing photospheric contribution, the second row shows chromospheric emission and the last two rows capture the ‘hot’ coronal plasma.

from *HMI/SDO* was used to explore the evolution of the magnetic field underlying the flaring region. A similar pointing correction process was applied, using *HMI* intensity continuum and SJI2832 data, to find the correct alignment of the two data sources.

The flare timing was identified using *GOES* and *RHESSI* high energy X-ray data. *RHESSI* was further used to identify the location of the emission in different energy bands and to obtain an estimation of the energy release.

Figure 4.2 reveals the pre-flare conditions as seen in all the context data used, from the low atmosphere, dominated by granulation and network structures, to the high temperature corona.

4.2.1. High energy emission

The high energy component of the flare emission was investigated using *RHESSI* data. The flare took place between *RHESSI*'s night phase and its passage through the South Atlantic anomaly, but luckily data covering a temporal interval from just before the peak emission to a few minutes into the decay phase was obtained. The locations of the soft and hard X-ray sources were obtained using imaging techniques and spectral fitting of the energy distribution was carried out in order to extract the partition between the thermal and non-thermal energies.

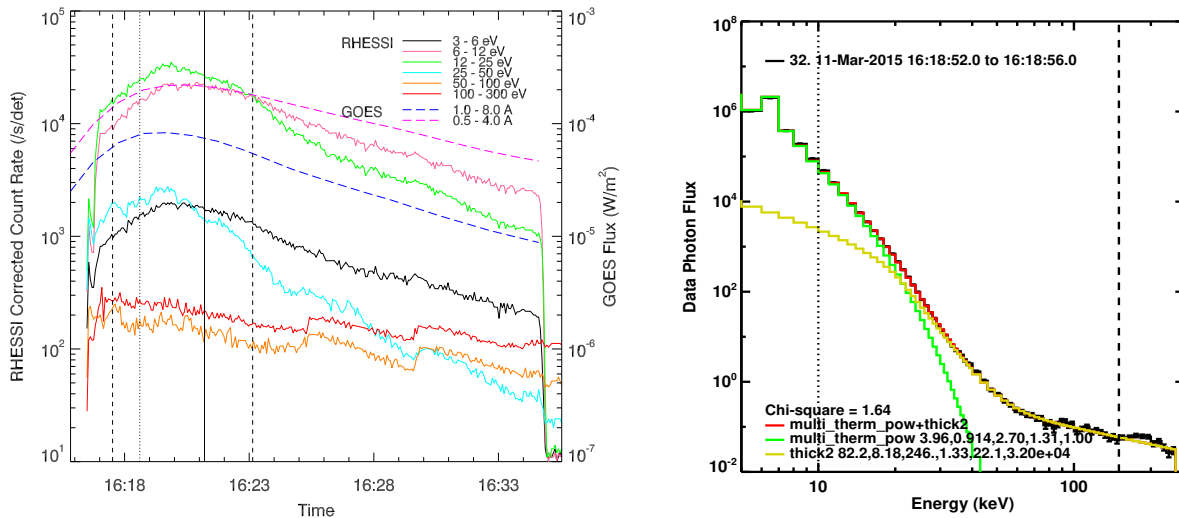


Figure 4.3: Left: Evolution of the *GOES* (dashed curves) and *RHESSI* (continuous curves) high energy emission for the March 11, 2015 X2.1 flare. The vertical black line marks the position of the flare maximum. The vertical dashed lines mark the interval explored in Figure 4.4, while the dotted line points to the position of the spectrum fit included on the right. Right: Total photon spectrum integrated from 16:18:52 to 16:18:56 UT, shown as the black curve. The green, yellow and red curves mark the thermal, non-thermal and total fit components. The vertical lines mark the interval between 10 and 110 keV for which the fit was performed.

Flaring events show an excess emission in the thermal range, especially in the case of very energetic ones, thus in order to keep the signal manageable, the *RHESSI* detectors can be covered with Aluminium attenuators of different thickness. During our studied flare the attenuator was either in the A1 (thin attenuator) or A3 (both thin and thick attenuators) state, therefore the count rates in the 3-10 keV range are contaminated with photons resulting from K-shell fluorescence in the detector (Smith et al., 2002) and the analysis of these low energies should be treated carefully.

Figure 4.3 (left) contains the temporal evolution of different X-ray energy bands of both *GOES* and *RHESSI*. The continuous vertical black line marks the flare peak. The interval containing the impulsive phase of the flare is marked by the vertical dashed lines. The location of the sample spectral fit included on the right is marked by the dotted vertical line.

We used the *hessi* routines from the SSW tree, and after testing the different imaging techniques we decided to rely on the Pixon integration method (Metcalf et al., 1996) and clean algorithms to identify the positions of the soft and hard X-ray kernels, seen as contours in Figure 4.1. The location of the SXR kernels was identified by integrating the emission in the 6-25 keV interval, while the 40-100 keV interval was used for the HXR location.

The *RHESSI* energy spectrum was then fitted using the *ospex* GUI in the SSW tree. For the non-thermal component we employed a thick target Bremsstrahlung function (*thick2*) and for the thermal contribution we used a multi-thermal power law (*multi_therm_pow*). Using the fitting parameters of the different function components, we can estimate the thermal and non-thermal energies of the flare, and their evolution as the flare progresses.

Figure 4.3 (right) presents a sample spectrum close to the flare peak. Due to the A3 state of the attenuator possibly affecting the emission at low energies and the high noise ratio for high energies, we only fit the emission between 10 - 110 keV, marked by the vertical lines in the above figure. The thermal and non-thermal components are marked by the green and yellow curves, respectively, while the total fit is marked by the red curve. In order to avoid errors due to attenuator state changes we only focus on the interval between 16:17:46 and 16:23:26 UT.

The non-thermal energy of the flare can be computed using

$$E_{\text{nth}} = 1.6 \times 10^{-9} \frac{\delta - 1}{\delta - 2} F(E) E_c \Delta t \quad (4.1)$$

where 1.6×10^{-9} is the conversion term from keV to erg, $F(E)$ is the integrated electron flux above the cut-off energy, δ is the spectral index of the electron distribution, E_c is the value of the electron cut-off energy and Δt is the integration time of the energy spectrum (e.g. [Wright et al., 2017](#)). These parameters are the results of fits of *RHESSI* data.

Assuming the thermal emission originates from a purely isothermal plasma, the thermal energy component can be computed using the relation based on [Saint-Hilaire and Benz \(2005\)](#), with the temperature and emission measure (EM) obtained from the fit of the thermal portion of the emission spectra,

$$E_{\text{th}} = 3 k_B T_e \sqrt{EM f V} \quad (4.2)$$

where k_B is Boltzmann constant, T_e is the plasma temperature, EM is measured in cm^{-3} , f is the filling factor and V is the volume of the emitting region in cm^3 . We assume a near unity

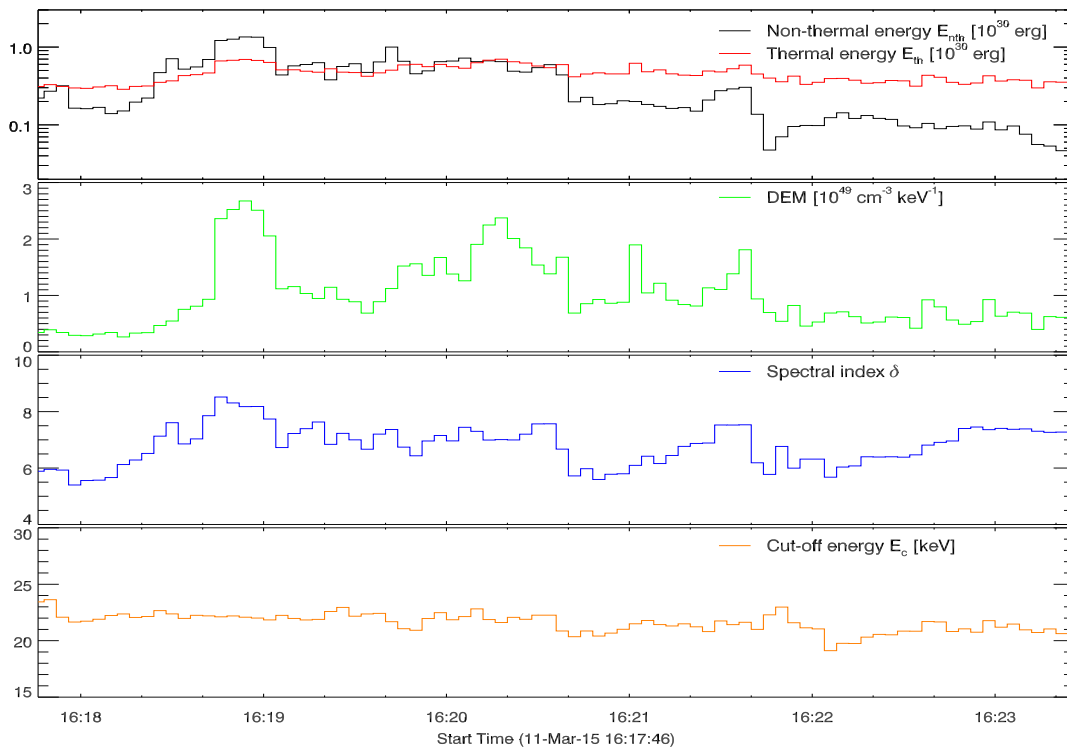


Figure 4.4: Evolution of the thermal (red) and non-thermal (black) energies obtained from the fits of the *RHESSI* spectrum. The SXR derived DEM is included in green. The spectral index of electron distribution and the cut-off energy for the HXR component are plotted in blue and orange, respectively.

filling factor (Dere, 1982). For a loop length of 10^9 cm and the area corresponding to thermal emission of 10^{17} cm², we estimate an emitting volume equal to 10^{26} cm³.

The evolution of different fit parameters (DEM, δ , E_c) and the resulted thermal and non-thermal energies are included in Figure 4.4. In the impulsive stage of the flare (around 16:19 UT) most of the energy is found in the non-thermal component, while as the flare begins its decay phase the two components become comparable, before the thermal component dominates. The decrease of non-thermal energy is due to the lack on additional energy injection from the flaring site, while energy continues to be radiated as thermal emission. This trend of the energy distribution fits in the standard flare model. In the impulsive phase of the flare non-thermal particles are accelerated from the reconnection site toward the low atmosphere where they produce intense heating. While the non-thermal input is limited to a short temporal interval, the resulted heating continues to dissipate well into the decay phase. The evaporation of chromospheric plasma is expected to show blue shifts in coronal lines, while the lines originating from lower down should be redshifted due to overpressure triggered by the evaporation.

4.2.2. Spectral signatures in IRIS data

The flare evolution has been examined using the *IRIS* SG spectral data, with an emphasis on the behaviour of the Mg II lines. Prior to any analysis, the residual orbital thermal variations have been corrected for (see Section 2.1.1) and the intensity has been converted to physical units of erg s⁻¹ cm⁻² sr⁻¹ Å⁻¹ (see Section 2.1.2). These corrections are important as they ensure no instrumental or observational effects are retained in the analysed data (e.g. variations of exposure time).

The full spectral range available from *IRIS* samples the emission from the photospheric continuum in the red wing of the Mg II lines, to the coronal emission of Fe XXI that becomes active in flaring conditions. We explore the response of the the mid solar atmosphere, as seen in the Si IV, C II and Mg II emission lines, to the flare excitation and evaluate the energy propagation through the different layers.

We compute the first three profile moments, namely the integrated intensity of the line, the shift of the line centroid and the width of the line, following the procedure described in Section 2.1.3. We identify the rest wavelength of a given transition by first taking the average profile along the slit over a region away from the active region, namely between -250'' and -240'' and then fitting the result with a Gaussian function.

Chromospheric and TR emission

The Mg II *k* and *h* lines, with vacuum wavelengths of 2796.35 Å and 2803.52 Å, sample the solar atmosphere from the temperature minimum to the upper chromosphere. Additionally, the subordinate triplet lines, due to the closeness of their transition energy to that of the resonance lines, are located within the same spectral range, enabling their simultaneous observation. One of the subordinate line is located in the blue wing of the *k* line at 2791.64 Å and the other two are seen as a blend in the bump between the *k* and *h* lines, having wavelengths of 2798.75 Å and 2798.82 Å. All these lines require temperatures of $\log T \approx 4$. in order to form, as higher temperatures will lead to the further ionization of Mg, thus decreasing their emission.

The *k* and *h* lines are optically thick, their source function being partially to completely decoupled from the local atmospheric conditions. In quiet solar conditions, the resonance lines show complex profile, with a central reversal surrounded by two emission peaks, with the intensity then dropping to outer minima before increasing toward continuum levels in the wide outer wings. The subordinate lines are typically seen as narrow absorption features. The presence of strong magnetic fields is apparent in the profile of the *k* and *h* lines by the absence of a central reversal, and an overall lower intensity compared to quiet conditions (Staath and

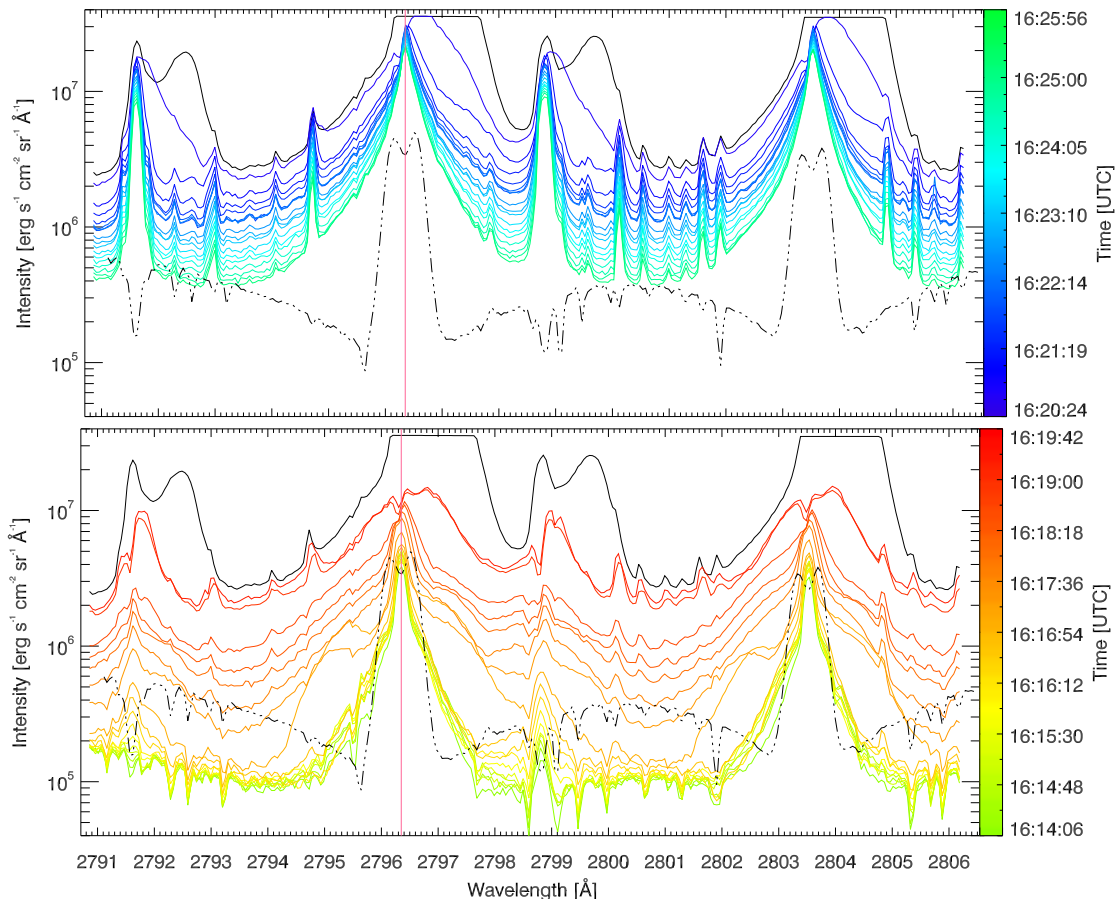


Figure 4.5: Emission intensity at $y=-175''16$ for the first slit position as recorded in the Mg II window before (bottom) and after the flare maximum (top). The colors denote different time frames and are described by the colorbar on the right. The black dash-dotted line corresponds to quiet sun spectrum, while the black continuous spectrum corresponds to the maximum emission at 16:20 UT, when significant saturation is present. The vertical magenta line corresponds to the Mg II k line rest wavelength.

Lemaire, 1995). In flaring conditions, the excess energy deposition causes the subordinate triplet to go into emission and leads to enhanced emission in the resonance lines.

In Figure 4.5 we present the evolution of the emission in the Mg II spectral window, for the location along the first slit position where the maximum flare emission was recorded and compare the observed intensities with the quiet sun spectrum (dash-dotted line) taken as an average far from the sunspot. In the pre-maximum panel (bottom), the magnetic field was apparent from the low continuum intensity and single peaked resonance lines profile. The accelerated rise of the filament can be seen as blueshifted components in the spectra after 16:16 UT (yellow-orange), marking the start of the flaring activity. All absorption lines in this spectral range, most of them photospheric and corresponding to neutral atoms, started to emit, while the overall intensity of the whole spectral window increased by an order of magnitude. After the maximum at 16:20 UT, the emission began to decrease slowly across all wavelengths, although the lines maintained enhanced widths, with red asymmetries.

We point out the shape of the subordinate triplet emission in Figure 4.5, that showed a similar profile to the resonance lines, especially close to the flare peak. Throughout the dataset, the subordinate lines were preponderantly in emission in the region sampling the penumbral regime between the two magnetic polarities, between $-180''$ and $-150''$. In quiet solar conditions Pereira et al. (2015) found that the triplet emission indicates the presence of steep temperature gradients in the lower chromosphere, but in more active conditions the underlying cause may be different or the result of multiple processes. During the ascending phase of emission, beside the

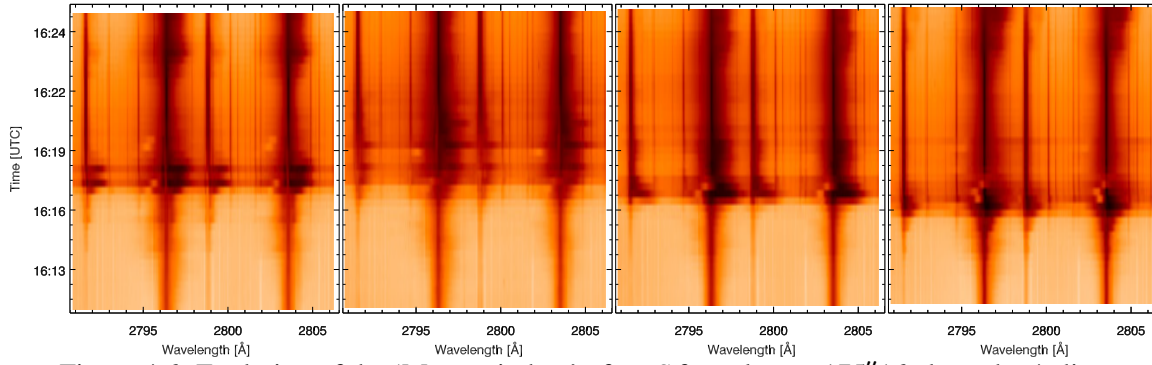


Figure 4.6: Evolution of the ‘Mg II window’ of *IRIS* for solar $y=-175''16$ along the 4 slits.

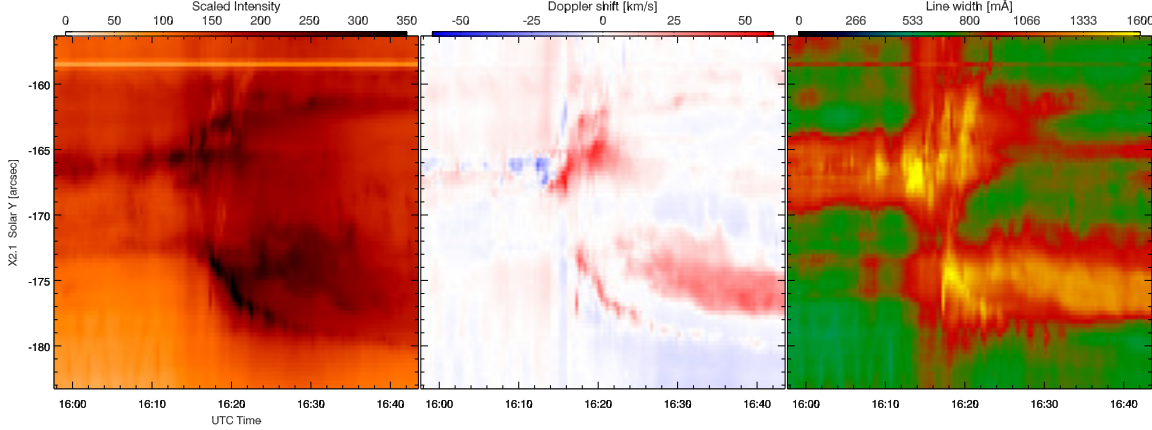


Figure 4.7: Spectral moments computed for the Mg II k line: integrated intensity in units of $\text{erg s}^{-1} \text{cm}^{-2} \text{sr}^{-1}$, with a cubic root scaling applied for better contrast (left), Doppler shift in units of km s^{-1} (centre) and line width measured in $\text{m}\text{\AA}$ (right).

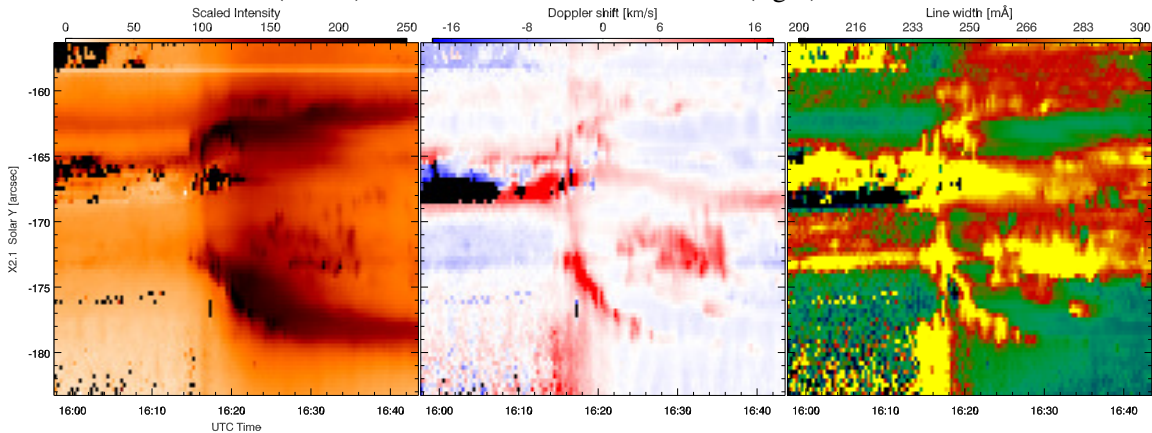


Figure 4.8: Integrated intensity (left), Doppler shift (centre) and line width (right) for the Mg II subordinate lines blend in the bump between the resonance lines.

obvious intensity enhancement, they showed an extended red wing, and even display a double peaked profile near the maximum: one peak at the reference wavelength position of the emission line, and one redshifted by $\sim 30 \text{ km s}^{-1}$.

Figure 4.6 highlights the variation of the intensity of the spectral range containing the Mg II lines for one location along the four slit positions. The onset of the intensity enhancements differs between the slits, as they sample different locations along the flaring structure, with the last slit being closer to the main footpoint of the filament. All slits display red-shifted profiles, with the first two slits also showing episodic downflows as different strands of plasma become heated. In the case of explosive evaporation induced by strong flares, the overpressure resulted from the hot evaporating material compresses the low atmosphere (e.g. Fisher et al., 1985) and can produce such effects. The subordinate emission is again evident, with the blend being more intense, and show a profile mirroring the resonance lines, though

with smaller widths.

A more meaningful representation of the profile shape variations can be done by computing the moments maps for a given emission line. In Figure 4.7 we include the results for the moment analysis for the Mg II k line, for the first slit position. The initial intensity enhancements in the integrated intensity (left panel) starting at 16:16 UT correspond to the locations of the flaring ribbons undergoing heating as non-thermal particles accelerated in the reconnection reach the chromosphere. The southern ribbon is clearly distinguishable as it sweeps into the penumbral region of the sunspot. The northern intensity enhancements show a more complex behaviour, mainly due to the overlap of the departing filament emission with the footpoint emission. The intensity drops in the wake of the ribbon, but returns after a few minutes. The Doppler shift map (central panel) also has the southern ribbon clearly visible with condensation flows of $\sim 20\text{-}30 \text{ km s}^{-1}$, followed by a brief period of no detectable shifted emission, before the downflows resume. It also captures the filament slow rise can be seen at $-166''$, followed by the presence of high blueshift as it starts to accelerate away. The filament location is further highlighted in the line width map (right panel). Prior to the flare at the southern ribbon location, the Mg II line has a very narrow profile, as is located close to the sunspot umbra, but after the flare the enhanced line width persists long after the enhanced widths in the northern ribbon have subsided.

Additional information can be provided by a similar analysis of the Mg II subordinate lines emission. In Figure 4.8 we present the profile characteristics of the 2798.75 \AA and 2798.82 \AA blend. In the pre-flare evolution, the low intensity of this line made its correct identification challenging, therefore any information extracted from this interval must be treated carefully. After the flare commenced, the integrated intensity showed a similar intensity variation with the k line emission for the southern ribbon, but a more abrupt change for the northern one. This may be due to the absence of filament associated emission obscuring the footpoint. The centroid shift for the southern ribbon varies between $\sim 10\text{-}15 \text{ km s}^{-1}$, with line widths of $\sim 300 \text{ m\AA}$. The line widths remained enhanced between the flaring ribbons, suggesting excess heating of the region.

The evolution higher atmospheric layers can be extracted by analysing some of the other spectral lines sampled by *IRIS*. The C II ion is present, with the lines at 1335.71 , 1335.66 and 1334.54 \AA being available. They have formation temperature of $\log T \approx 4.3$ corresponding to the upper chromospheric and low TR conditions. The Si IV 1402.77 \AA line forms at $\log T \approx 4.8$ in the upper TR and is assumed to be formed under optically thin conditions, as the plasma densities are expected to be lower.

The C II emission shows a similar variation to the Mg II lines, suggesting close formation heights of the observed emission of the two ions. The intensity evolution in the *IRIS* spectral range containing the C II lines for the location of maximum emission in all slits is presented in Figure 4.9. The red shifts show periodic enhancements as different strands of plasma cross the location of the slits.

As the 1335.71 and 1335.66 \AA lines are seen as a wide blend at the spectral resolution of *IRIS*, we apply the moment analysis to the single 1334.54 \AA emission. The resulted moment maps are presented in Figure 4.10. The integrated intensity shows enhancements at the same locations as the Mg II k line, but the enhancements fade faster for a given position. In the Doppler map the redshifts dominate, decreasing after the ribbon emission with centroid shifts of $\sim 30 \text{ km s}^{-1}$, for all flare locations. The line widths measurements show increased values in the filament before its eruption and at the flare ribbon locations. The region swept by the flare ribbon shows a return of enhanced line width and red shift after a ~ 5 minute intermission.

In contrast to the Mg II and C II lines that show emission in all solar conditions and always have an emission component at the rest wavelength, the 1402.7 \AA line of Si IV is

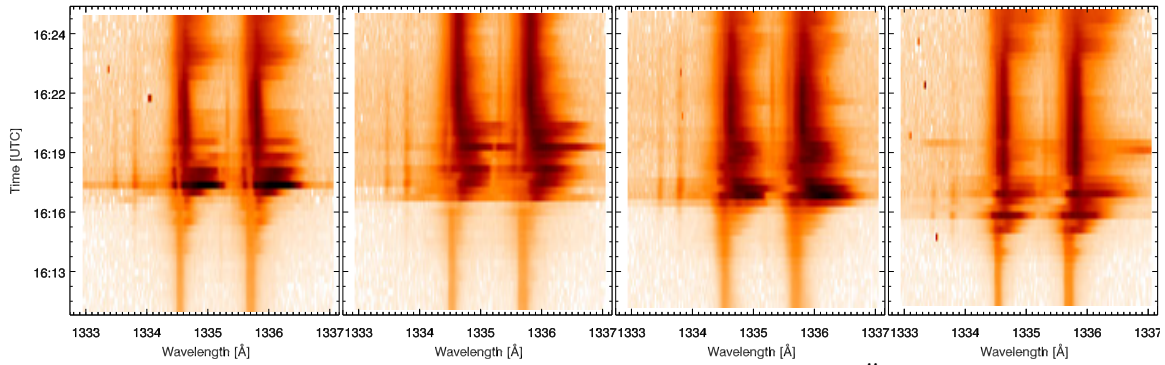


Figure 4.9: Evolution of the ‘C II window’ of *IRIS* for solar $y=-175''16$ along the slits.

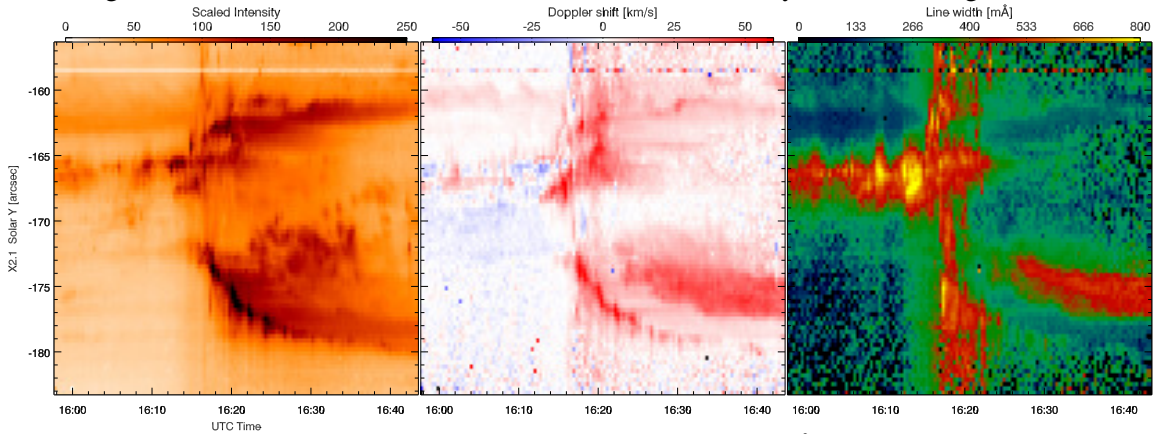


Figure 4.10: Spectral moments computed for the C II 1334.54 Å line: integrated intensity (left), Doppler shift (centre) and line width (right).

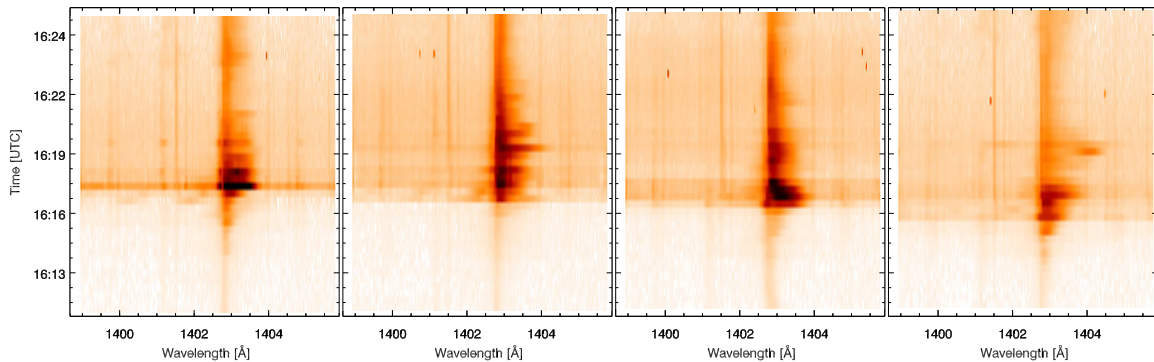


Figure 4.11: Evolution of the ‘Si IV window’ of *IRIS* for solar $y=-175''16$ along the slits.

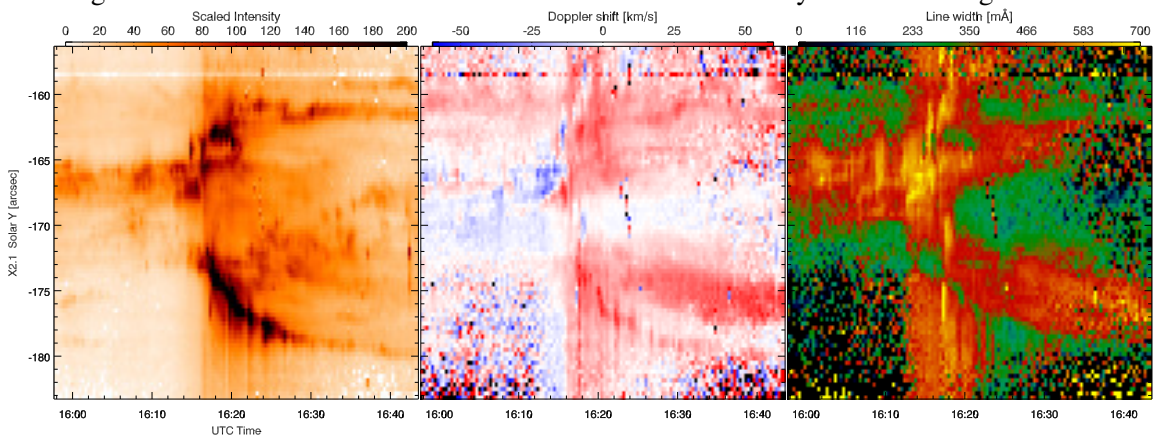


Figure 4.12: Spectral moments computed for the Si IV 1402.77 Å line: integrated intensity (left), Doppler shift (centre) and line width (right).

usually absent in average quiet sun conditions, with modest intensities at locations overlying small magnetic concentrations. Therefore the Si IV line can be fully redshifted, with no rest component, but with extensive width as shown in Figure 4.11. This behaviour is usually

associated with an intense downflow with an superimposed smaller upflow from which can not be clearly distinguished (Li et al., 2017c).

Figure 4.12 displays the moment maps of the Si IV line. The integrated intensity shows an increase by more than two orders of magnitude at the location the flare ribbons, and again some clusters of emission in the wake of the flare that slowly decrease to pre-flare values. The peculiar emission seen in C II and Mg II k is less persistent, but this may be either due to a lower sensitivity of the Si IV line or maybe the emitting material has a lower temperature, making it invisible at $\log T = 4.8$. The Doppler map shows stronger red shifts, while the line width map show a lot of scatter, but both better reveal the the presence of returned emission in the post flaring region.

As the Si IV line is formed under optically thin conditions, a Gaussian fitting of the line profile can be applied, but in the case of flaring, there may be additional components in the emission that can complicate the result. Brannon et al. (2015) observed a ‘saw tooth’ pattern with period of ~ 140 s in a post flare ribbon and applied a double Gaussian fitting to the flaring pixels. They distinguished between a stationary redshifted component and an oscillating component, and they argued that the short post-flare loops move quasi-statically the with respect to the LOS, under the influence of an elliptical wave triggered in the flare.

The peculiar emission covering the region above the penumbra between $-178''$ and $-172''$, starting a few minutes after the flare ($\sim 16:26$ UT), and visible in all chromospheric and TR lines to various degrees of persistence, from half an hour in Si IV to more than an hour in the Mg II emission, is explored in more detail in Chapter 5. We concluded that these profiles belong to a form of coronal rain, with a highly turbulent velocity component, most likely excited during the impulsive phase of the flare, that slowly dampens over the course of the following hour.

Coronal emission

Our choice for this flare was guided by the fact that the *IRIS* slit covered the footpoints of the flaring loops, providing us with diagnostics on the dynamics of the chromospheric and coronal plasma. The *IRIS* slits covered a region of the active region which was close to the seismic activity at the photospheric level. As such, complementing the chromosphere spectral analysis with a discussion on the coronal emission at the same location, creates a complete picture of the related flows during this impulsive flare event.

The forbidden line of Fe XXI at 1354.1 \AA is the only coronal emission line observed by *IRIS* during the flare and is located in the ‘O I spectral window’. It corresponds to the ($^3P_0 - ^3P_1$) ground transition and it was first identified in the solar spectra by Doschek et al. (1975) using Skylab observations. The high ionization levels are reached at temperatures ≥ 10 MK, thus this line goes into emission mainly during flaring events. Typically an upward motion of hot plasma is observed as a highly blue shifted emission of up to 200 km s^{-1} corresponding to the evaporation flows triggered by the flare. The relationship between the Fe XXI emission and X-Ray emission has been explored by Tian et al. (2015), finding a strong correlation between the evaporation flow and the energy deposition rate as extracted from *RHESSI* data. Li et al. (2017a) linked the location of the microwave footpoint of a flare to the location of 1354.1 \AA emission, but further conclusions are hindered by the low resolution of the microwave data.

Figure 4.13 shows the temporal evolution of the Fe XXI spectra before, during and after flare. It starts as faint emission between the flaring footpoints. Later the emission revealed the multi-stranded structure of newly reconnected loops. The data shows very wide and shifted emission corresponding to plasma upflow in the evaporation phase. The spectral profiles show alternation of bright and dark horizontal features, suggesting that different strands become visible at temperatures ≥ 10 MK, as they were being filled with plasma.

Figure 4.14 shows the evolution of the line intensity for a narrow location close to the

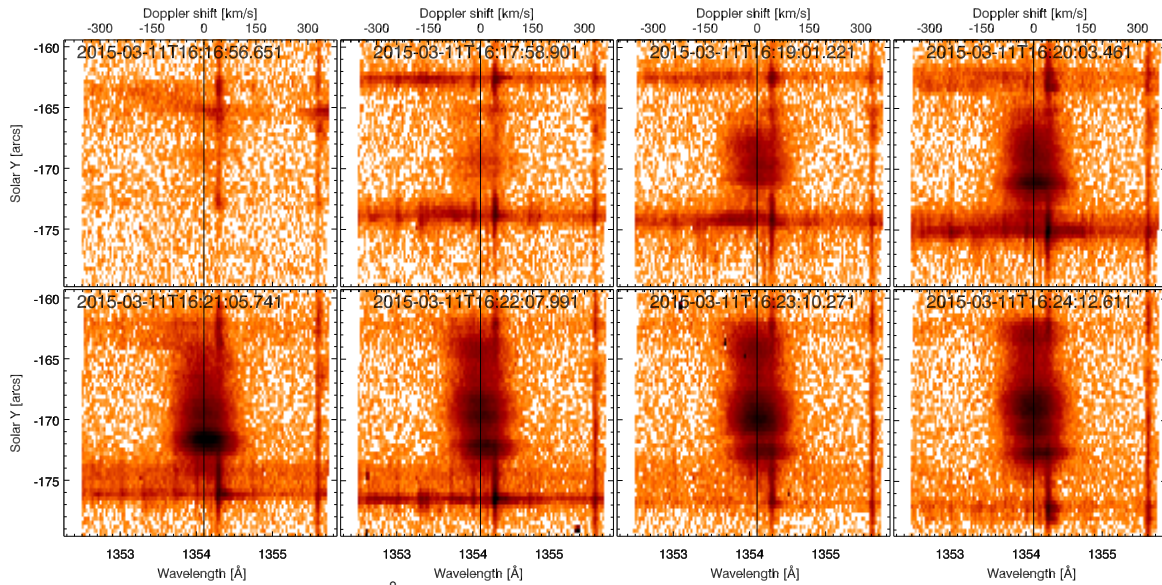


Figure 4.13: Fe XXI 1354.1 Å line emission snapshots at the specified times, corresponding to the first slit position. The emission originates between the flare footpoints and displays variations of intensity, which suggests that different loop tops become visible in this high temperature line. The vertical black line corresponds to the rest wavelength of the transition.

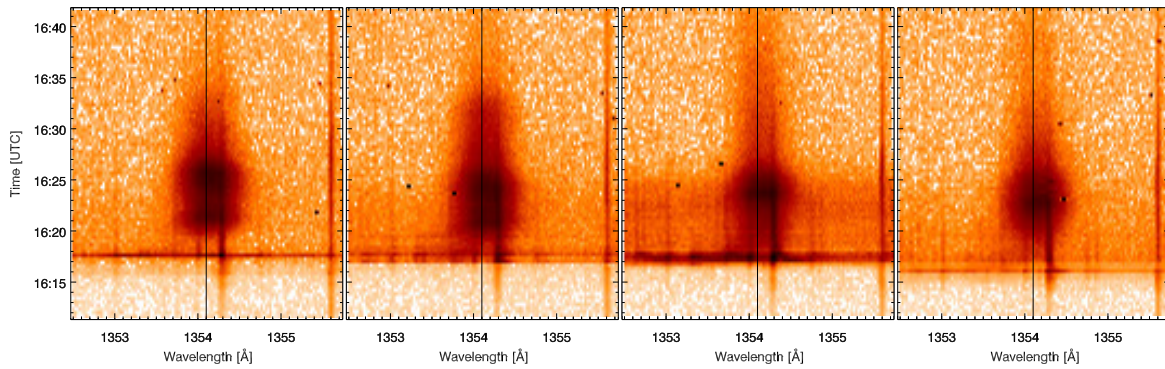


Figure 4.14: Evolution of ‘O I window’ of *IRIS* as obtained from three pixel average around $y=-172''67$ for the 4 slits. The narrow line at 1354.28 Å belongs to the C I emission and the far right line at 1355.59 Å pertains to the namesake of the window, the O I. The Fe XXI 1354.1 Å emission dominated across all slit positions near the *RHESSI* peak.

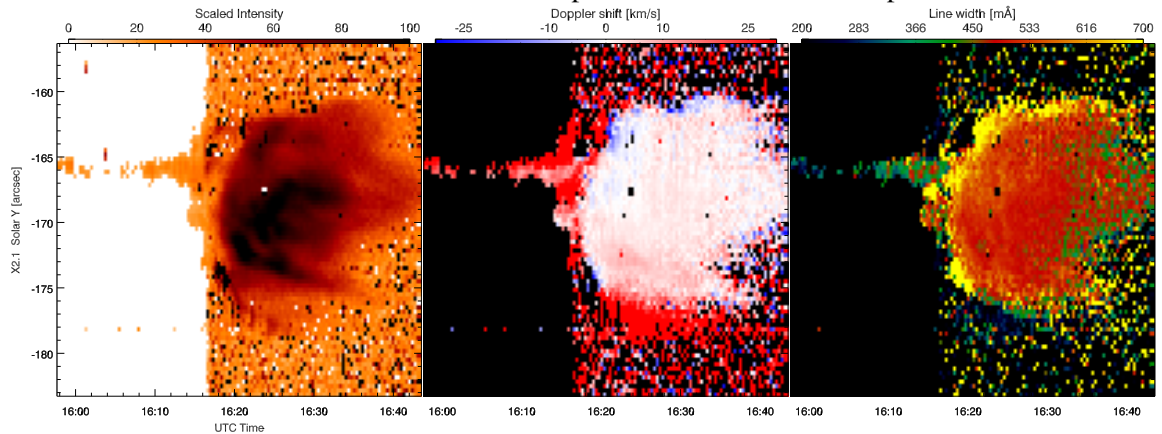


Figure 4.15: Spectral moments computed for the Fe XXI 1354.1 Å line: integrated intensity (left), Doppler shift (centre) and line width (right). The line width range has been adjusted for better contrast. The onset of the flare is clearly seen at around 16:16 UT.

location of the flare. The bulk of the Fe XXI emission starts ~ 250 seconds after the flare initiation and lasts for ≈ 15 minutes, until the temperature of the plasma drops significantly. The different slit positions sample different locations along the flaring loops, therefore the extent and

variation of the emission differs between the slits.

Figure 4.15 shows the profile moments maps for this line. The line width map best highlights the extend of the post flare arcades, while the integrated intensity reconstructs variations of the coronal emission of the hot flare loops. In the Doppler shift map (middle panel), it can be seen that prior to the flare, the emission is dominated by noise, but after the flare the line is slightly blue-shifted, with velocities between -10 and 10 km s^{-1} . At the location of the footpoints, the line is blue-shifted in the regions where the chromospheric lines show red shifts. It is worth mentioning that the footpoint emission may be affected by the narrow C I emission.

The Fe XXI 1354.1 Å line typically forms at temperatures of $\log T = 7.06 \text{ K}$, which correspond to a thermal width of 92 km s^{-1} or 0.43 Å . In the case of our event, the widths of the profile over the flaring loops have values between 0.41 and 0.53 mÅ . Assuming the emission is fully thermal we can compute the temperature of the emitting plasma

$$T_{\text{th}} = \frac{W^2}{\lambda_0^2} \frac{m c^2}{8 k_B \ln(2)} = 1.96 \times 10^{12} \frac{N W^2}{\lambda_0} \quad (4.3)$$

where W is the observed width of the line, λ_0 is the rest wavelength of the transition, c is the speed of light, k_B is Boltzmann's constant, $m = Nu$ is the mass of the emitting element, u is the atomic unit mass and N is the mass number of the emitting element ($N=55.84$ for iron). Thus the inferred thermal temperatures are $\log T = 7 - 7.22 \text{ K}$. The lower limit may be an underestimation, due to the uncertainties in measuring the widths for low intensity profiles.

However, the above argument only works under the assumption of isothermal conditions, which may not be true in the aftermath of a flare. Thus, the observed width can also be considered a blend of a standard thermal broadening with a micro-turbulent component. The non-thermal velocity can be then computed as

$$\xi = \sqrt{\frac{(W^2 - W_{\text{th}}^2) c^2}{4 \ln 2 \lambda_0^2}} \quad (4.4)$$

Based on the measured widths, we obtain $\xi = 41.18 \text{ km s}^{-1}$ as the upper limit for the non-thermal velocity. Young et al. (2015) found similar values in the study of another flare. However, the partition of thermal and non-thermal components may be different in this flare, with a predominant higher coronal temperature, implying therefore a lower micro-turbulent motion. This cannot be distinguished from the observation of a single emission line, and requires additional spectral input on the high temperature corona.

4.2.3. Filament eruption

The flare was triggered by the eruption of the filament anchored across the polarity inversion line of the AR. Many thin threads wrapping along the filament spine made up its fine structure. The AIA data shows indications of twist of approximately one and a half turns, consistent with the widely but not universally adopted assumption that the magnetic structure of filaments is that of a weakly twisted magnetic flux rope. The right foot of the filament is anchored in the main positive photospheric polarity. The negative magnetic polarity (Figure 4.20, left yellow arrows) hosted the rather extended eastern footpoints of the filament.

The destabilization process started ~ 40 minutes before the flare with the slow rise of the filamentary material, gradually detaching from its western footpoint. The filament material is seen to rise and slide towards the eastern side of the active region. In the last ~ 5 minutes before the flare the accelerated rise of the filament is clearly seen in the Doppler shift maps of chromospheric and TR lines. Chromospheric fibrils reconnected with threads of the erupting filament, mainly on the northern side. Some of the energy was carried by the filament as it was rapidly accelerated away from the surface, while subsequent reconnection leads to emission at

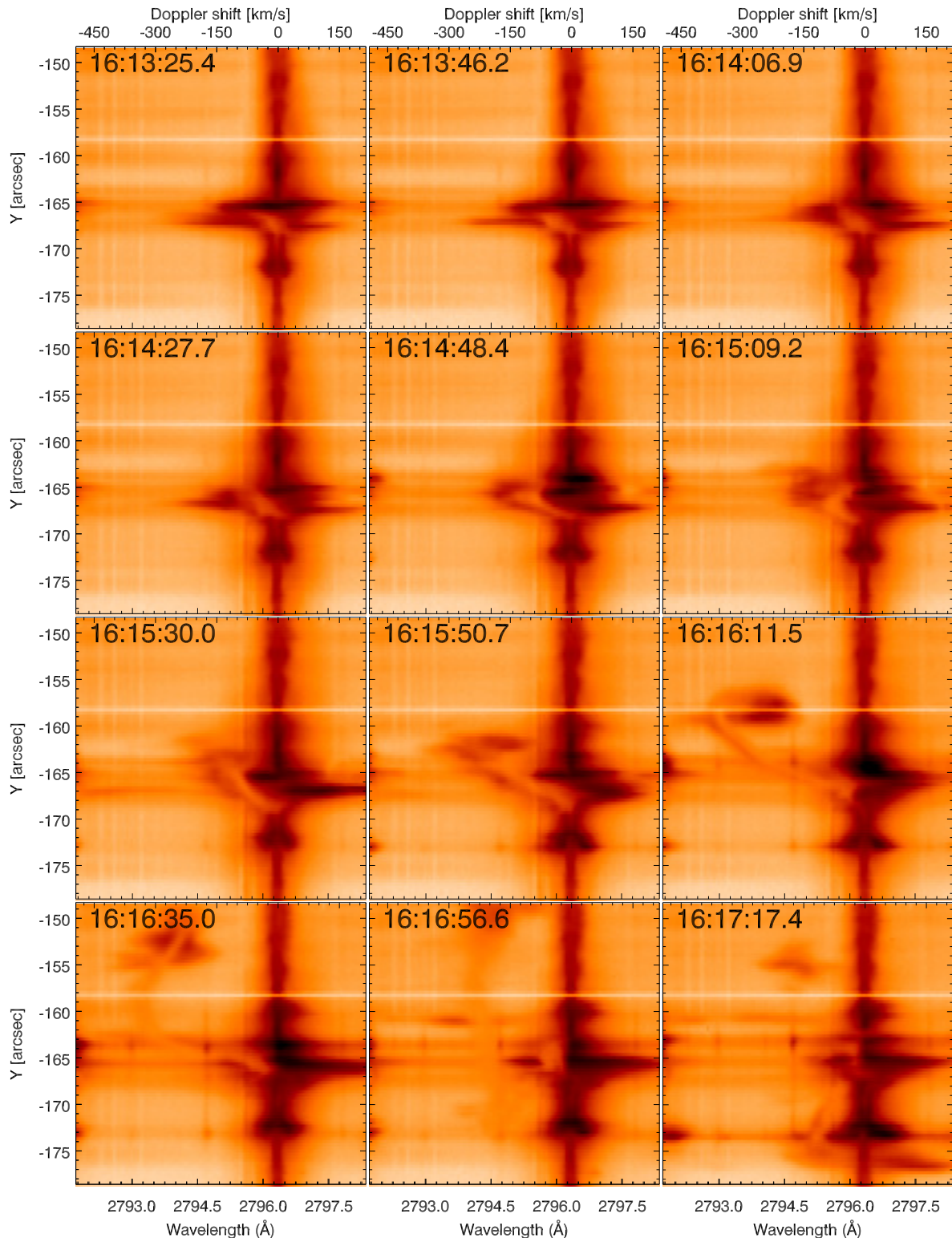


Figure 4.16: The filament eruption as seen in the Mg II k line emission of *IRIS* at the first slit position. The emission line first show enhanced linewidths, which develops into a blue-asymmetry that then rapidly expands across $\sim 20''$ in the spectral window. The maximum Doppler shift of the erupting filament is $> 300 \text{ km s}^{-1}$, which slowly decreases as the flux tubes are evacuated.

additional footpoints anchoring the filament. The final break of one of the filament footpoints generated the intense flare emission. The erupted filament displayed an untwisted motion as it expanded away from the reconnection site.

Figure 4.16 shows the evolution of the filament as seen in the Mg II k line emission. At 16:13:30 UT the filament was seen as only a slightly blue shifted component in the profile.

The blueshift slowly increased for the next minute, becoming clearly separated from the core emission. At 16:15:35 UT the filament material could be seen as a C-shaped structure on the blue side of the core that seemed to have expanded and covered more of the spatial direction, reaching Doppler shifts up to $\sim 400 \text{ km s}^{-1}$. This corresponds to the moment when the magnetic structure confining the filament snapped and reconnected producing the X-class flare. After 16:16:41 UT, the ejected material showed lower Doppler shifts, as the acceleration of the ejected material decreased.

The filament had similarly high blueshifts across all observed lines, though the C II and Si IV lines showed shifts typically $\sim 10\text{--}20 \text{ km s}^{-1}$ higher for the same time instance. Tracing the leading edge of the filament in successive spectra we find acceleration rates of $2\text{--}4 \text{ km s}^{-2}$, similar to the value found by Kleint et al. (2015) for a similar filament precursor of another solar flare (the 29 March 2014 flare).

Li et al. (2016) also explored the slow rise of the same filament and discuss the flare precursor, attributing the destabilization to slipping reconnection. They find quasi-periodic brightenings in Si IV emission for an hour prior to the flare, which they associate to peeling of magnetic structure confining the filament. They also report the decay of the penumbra of the northern spot after the flare.

4.2.4. Emission Measure analysis

The EUV filters of AIA integrate over multiple lines from ions formed at different temperatures, thus interpretation of the observed intensity becomes convoluted, especially

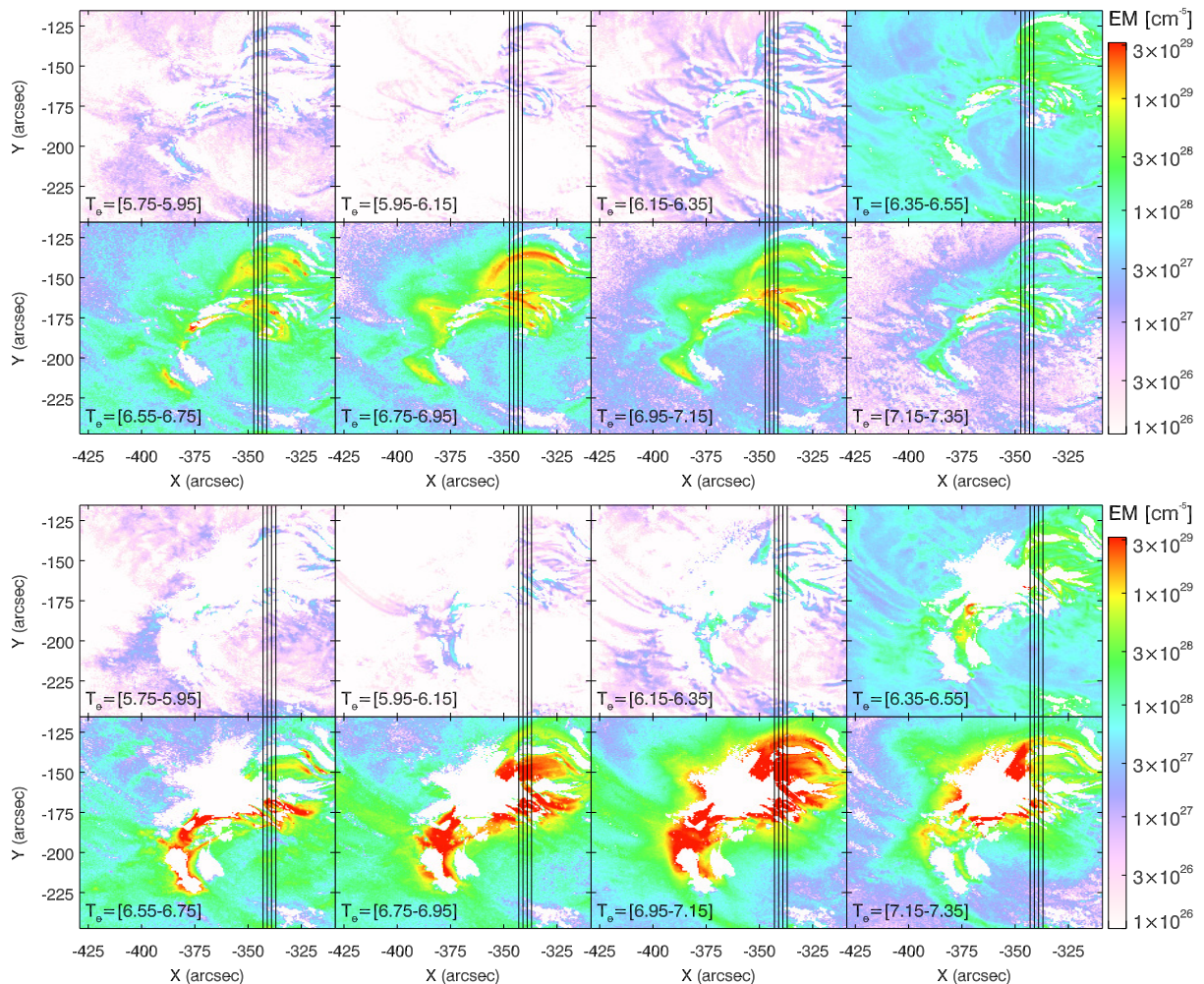


Figure 4.17: The EM maps prior to the flare event at 16:12 UT (top) at after some of the flaring and saturation had subsided at 16:50 UT (bottom). The vertical black lines represent the corresponding locations of the *IRIS* slits for the *AIA* data used in the inversion.

during flaring conditions, when the different lines contribution to the observed intensity is no longer well behaved. In order to identify the emission at different temperatures we need to extract the plasma parameters from a set of integrated intensities. There are a number of ways to solve this inverse problem, but for our event we opted for the sparse inversion method of [Cheung et al. \(2015\)](#). We applied the inversion to six *AIA* filters, namely those centred around the emission at 94, 113, 171, 193, 211 and 335 Å, and extracted the Emission Measure of the observed AR in different temperature intervals. Due to the intense saturation of the *AIA* passbands during the flare, the thermal structure of the reconnection site could not be recovered.

The emission measure (EM) maps at the different temperature bins are shown in [Figure 4.17](#). The maps show the result of the inversion code for two time instances, one prior to the flare initiation and the other after the saturation of the *AIA* filters decreases, and the post flare configuration can be seen. In the pre flare set most of the EM is at $\log T \in [6.35, 7.15]$ K, but some structure is present, although negligible, at $\log T \leq 6.35$. The structures seen in the high temperature maps describe very sheared arcades confining the filament, that can be seen in the $\log T \in [6.75, 6.95]$ K interval as a twisted structure about to reconnect and be ejected. The post flare EM maps show enhancements in all high temperature maps, suggesting heating to temperatures exceeding 10 MK that lasts well after the flare impulsive phase.

We point out the similarity between the loop system seen in the intensity map of the Fe XXI line of *IRIS* (left panel of [Figure 4.15](#)) and the emitting strands seen in the $\log T = 6.95 - 7.15$ map in the post flaring time. The multi stranded structure is well recovered by the *IRIS* emission and, if a fast scanning raster was used during the observation, a reconstruction of the post flaring loops could have been done, even for strong flares that saturated the *AIA* filters. However, such a reconstruction will be limited to showing the coronal structure around the formation temperature of Fe XXI at 10 MK.

4.2.5. Magnetic field evolution

The AR 12297 crossed the eastern limb having a simple, although sheared, bipolar configuration (β - δ class), but due to continuing new flux emergence between the main polarities, at the time of the studied flare, its structure became more complex (β - γ - δ class). The new emerged flux added to the already significant magnetic shear across the polarity inversion line, slowly sets the stage for a number of flares that originated from this region during its trek across the solar surface. The filament, whose destabilization was the trigger of the X2.1 flare, was anchored across the sheared PIL.

To explore the changes in magnetic configuration induced by the filament eruption and flare reconnection we use the *HMI* vector magnetogram data as recorded in the SHARP 5298 region. The polarization data used to compute the vector field is recorded with a cadence of 12 minutes. Using the processed SHARP data for the total magnetic field strength B , the inclination angle γ with respect to the LOS direction and the azimuth angle ϕ , we computed the “true” solar magnetic field components and the associated electric current density components.

The vertical component of the magnetic field B_z is presented in the lower panels of [Figure 4.18](#). We note the presence of a filamentary penumbral intrusion (magenta ellipse), whose depth and structure changed compared to the pre-flare state. The location of the intrusion corresponds to the location of intense spectral emission and underlies the location of the *RHESSI* HXR footpoints, suggesting the complex structure of the magnetic field in this region was most susceptible to being destabilized during the filament rise. This formation facilitated the formation of the sunquake. The electric current is strong at the location of the seismic source (discussed in the next section).

Compared to the pre-flare morphology, the sunspot also appears to rotate around its axis and continued to do so well after the flare. This is in line with previous studies, for instance in the analysis of another flaring event, [Török et al. \(2013\)](#) run simulations of the associated

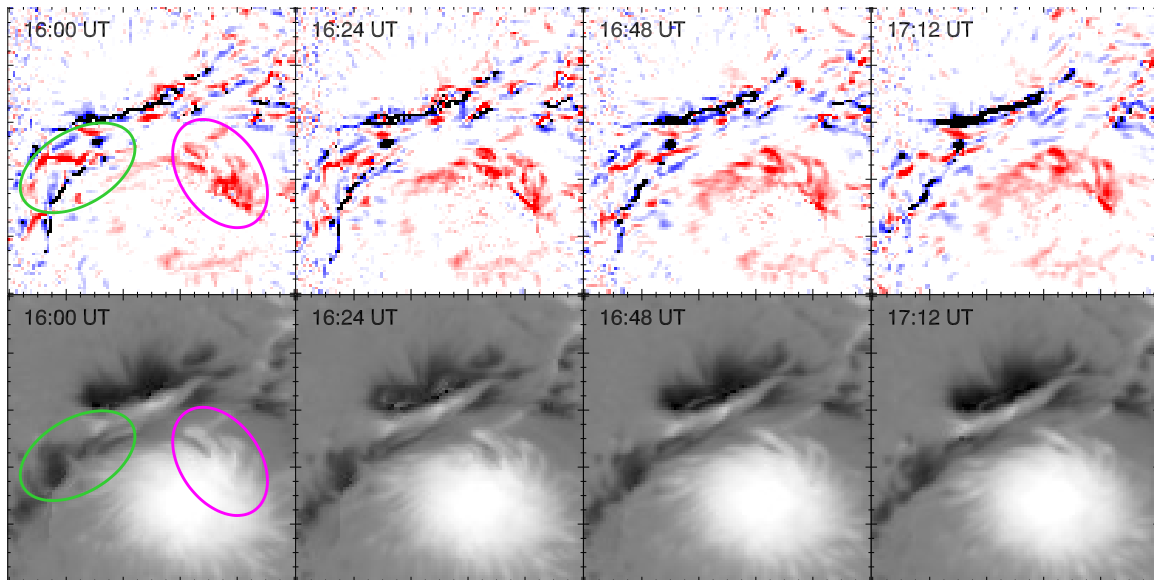


Figure 4.18: Top: Evolution of the J_z component of the current, scaled between $\pm 60 \text{ mA m}^{-2}$; Bottom: B_z component of the magnetic field, scaled between $\pm 2500 \text{ G}$. The green ellipse shows the region that undergoes important changes as a consequence of the flare, while the magenta ellipse indicates the presence of penumbral intrusion.

filament eruption, and attribute the initial destabilization of the filament to the slow rotation of the sunspot. Such a rotation would increase the twist and stress on the footpoints anchoring the filament, eventually causing the reconnection. The slow rise of the filament observed in our study is consistent with the slow rotation of the sunspot, that keeps pushing different strands of the filament against each other and against the overlying field.

The sheared magnetic structure is illustrated by the presence of strong currents of opposite sign in the region inside the green ellipse in the upper panels of Figure 4.18. After the flare the current contrast appears to be diminished inside the ellipse, while it continues to increase above the main sunspot as the two polarities drift toward each other. Recently, [Liu et al. \(2017\)](#) discuss the balance between the different J_z polarities and the shear across the PIL, suggesting a strong correlation to the eruptive events productivity of the active region.

We further investigated the vertical structure of the magnetic field and its change using magnetic field extrapolations based on the measured *HMI* photospheric magnetic field components. While all methods adopt a force free approximation for the magnetic field, considering the influences of other forces negligible, the choice of the force free parameter α used in the extrapolation varies, depending on the requirements. A potential force free field (PFF) extrapolation (no current, or twist everywhere), is useful to provide the large scale morphology far from the solar surface, but can not reliably offer information on the complicated structures inherent to the interaction of active regions. On the other hand non-linear force free field (NLFFF) extrapolations, where each point can have different α , may complicate vertical field structure by over estimating the twist in the structure, relies on a larger number of assumptions and can be computationally expensive.

We opted for the intermediary solution of considering a constant twist for a given region and employed the [Alissandrakis \(1981\)](#) method that computes the linear force-free (LFF) magnetic field extrapolation (with a constant force-free parameter α). We ran a number of extrapolations, using different α values corresponding to different patches in the sheared region close to the PIL or to locations associated to the filament footpoints.

The magnetic field structure for one of the extrapolations is included in Figure 4.19. We present the configuration at different stages in the flare evolution and highlight some of the observed morphological changes. In the pre-flare case the extrapolation showed a tightly

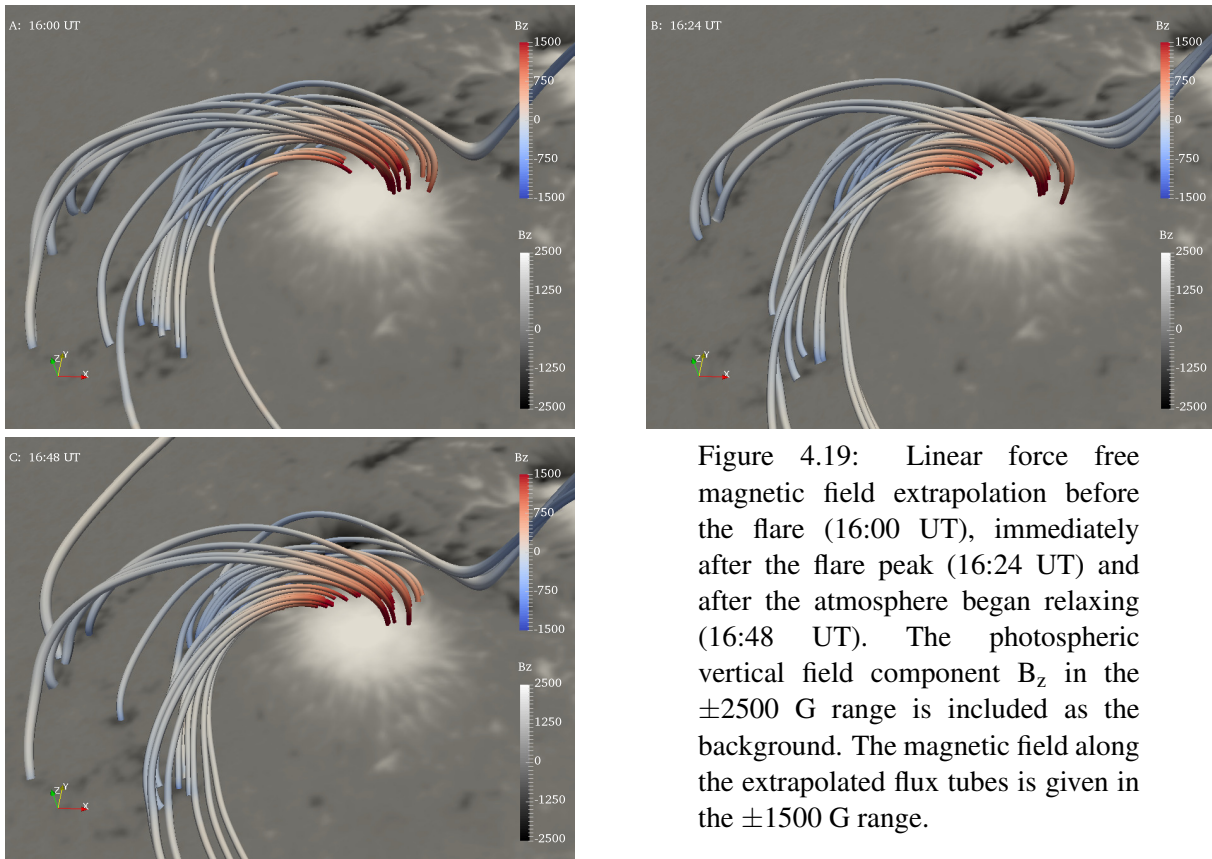


Figure 4.19: Linear force free magnetic field extrapolation before the flare (16:00 UT), immediately after the flare peak (16:24 UT) and after the atmosphere began relaxing (16:48 UT). The photospheric vertical field component B_z in the ± 2500 G range is included as the background. The magnetic field along the extrapolated flux tubes is given in the ± 1500 G range.

twisted, low lying structure across the PIL, in addition to interlaced field lines connecting regions on the west of the main sunspot to the scattered magnetic patches to the east. After the flare, the field reached a more relaxed state, with loops reaching higher in the atmosphere and diminished braiding, suggesting changes in the overall connectivity of the active region.

4.2.6. Seismic activity

The flare also presents a very impulsive phase which triggered seismic sources at the photospheric level. We used Doppler data from *HMI* to explore the seismic impact of the flare on the photosphere. The photospheric magnetic and intensity continuum signatures of the flare also show strong transients at the location of the flare, which are better visible in the running differences of Doppler and intensity maps. The locations of these transients are marked in Figure 4.20 with yellow arrows, suggesting multiple anchoring points of the magnetic field strands hosting the flare. This is understood now, as the filament itself erupting from the same location, with its stranded structure being rooted at the locations of strong transients. The two green circles show the main location of significant seismic signal as measured in the 6 mHz acoustic emission power maps during the impulsive phase of the flare event. It is a lucky coincidence that the last *IRIS* slit crossed over the region just $4''$ away from the main seismic source, allowing for the study of downflows in the vicinity of a seismic source.

The flare Doppler and magnetic signatures at the photospheric layer have multiple components, probably triggered at different times, but all within just less than 1 minute from the impulsive moment. At the photospheric level the pressure dent cause by the downflows is read as an $\approx 330 \text{ m s}^{-1}$ Doppler speed, averaged over the seismic area, which coincides with the small area of the penumbral intrusion in the umbra, marked by high J_z current in the magenta ellipse in Figure 4.18 (identified as *k1* in Figure 4.22).

The two 6 mHz detected acoustic sources were located in the penumbra of the sunspot (yellow arrows in Figure 4.20) with the left source sitting exactly at the location of extended penumbral magnetic fibrils, anchored deep into the umbra. The sources have a diameter of

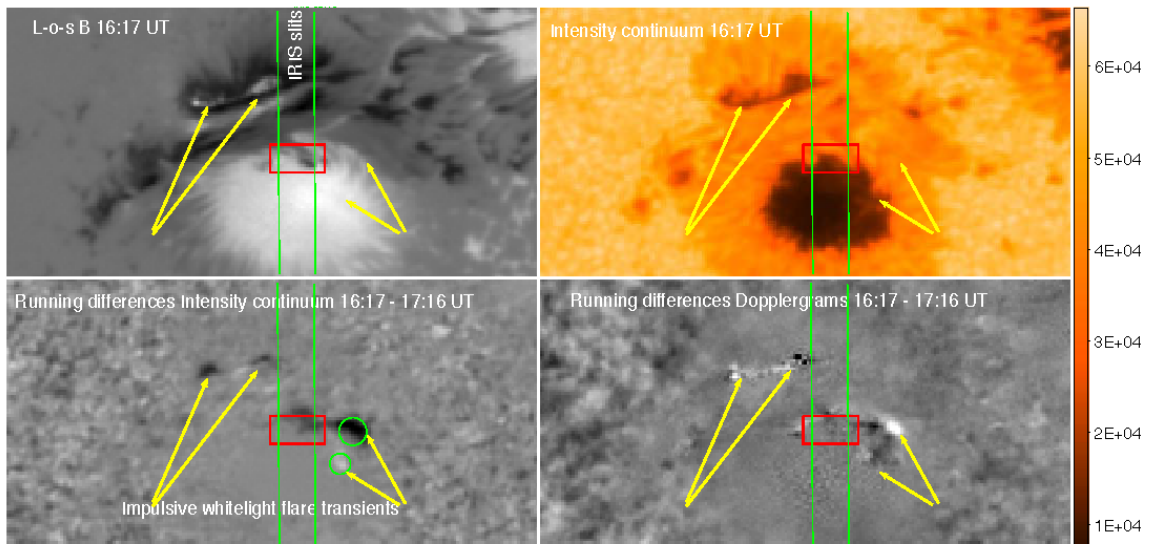


Figure 4.20: Photospheric data from *HMI/SDO* emphasizing the transients related to the flare: LOS Magnetic field, Intensity continuum, Intensity continuum running difference and Dopplergram running difference. The region between the vertical green lines is sampled by the *IRIS* SG, while the yellow arrows show the strongest transients. The green circles mark the locations of enhanced acoustic power. Red rectangle is the region covered by *IRIS* which we used in our estimations of downflows and interpretation of sunquakes.

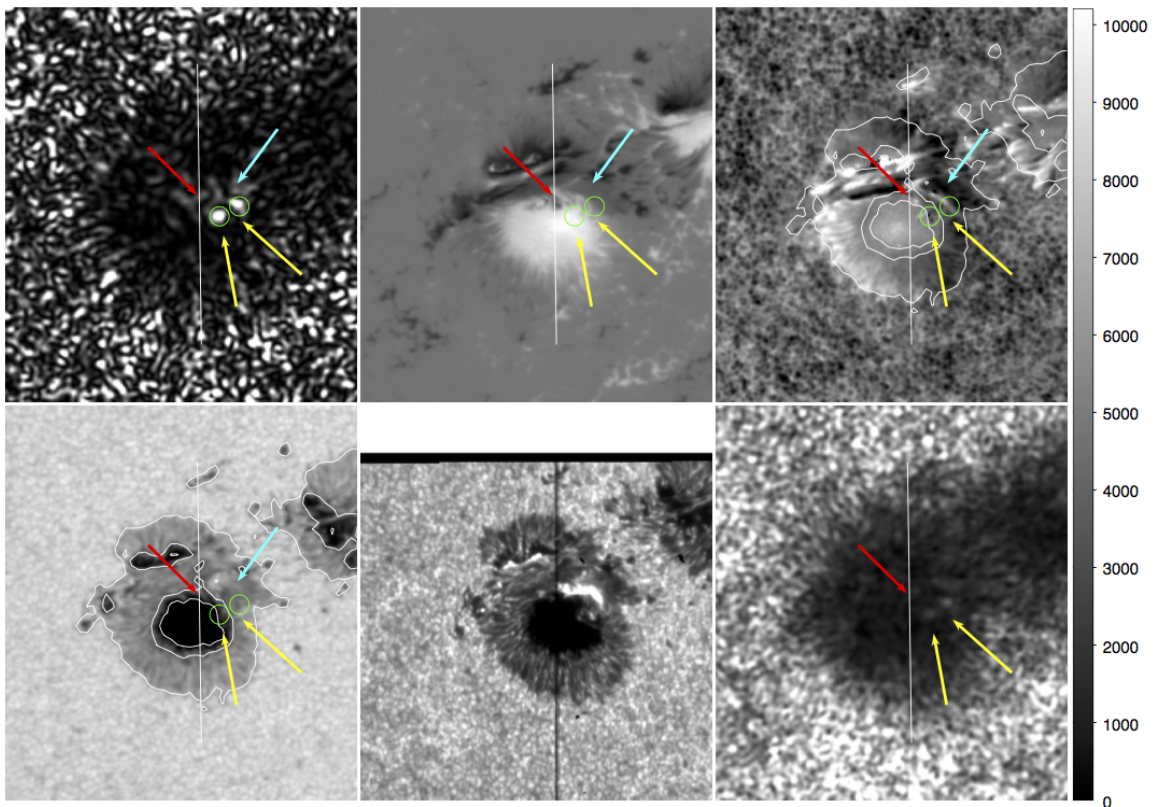


Figure 4.21: A composite image showing the location of the main 6 mHz seismic sources. From left to right, top to bottom: 1) the 5–7 mHz seismic emission map of the main sunspot at 16:17 UT, also shown with yellow arrows; 2) LOS magnetic field *HMI/SDO*; 3) Dopplergram map at 16:16 UT; 4) Intensity continuum map for identification of the penumbra boundaries; 5) *IRIS* 2832 Å SJI at 16:16:58 UT; 6) total 5–7 mHz acoustic emission map integrated over 2.5 hours of observation. The colour bar corresponds to the first frame of the 6 mHz egression power map at 16:17 UT. Cyan arrow points at the region which undertook most of dramatic reconfiguration. The vertical white line is the *IRIS* slit.

about 12 *HMI* pixels or $6''$, and are shown as green circles in the 6 mHz acoustic source map. See Donea et al. (1999) and Donea and Lindsey (2005) for references on the detection method using the helioseismic holography as acoustic emission power diagnostics in solar flares. The mosaic in Figure 4.21 contains additional information on the location of the seismic source. A maximum value of the emission sources reads $\approx 15,000 \text{ (m/s)}^2$ at their simultaneous peaks. The two locations are labelled kernel *k1* and *k6* in our discussions. The map also shows more of a diffused but still enhanced seismic emission (red arrow), four times weaker than the seismic emission accompanying the main acoustic kernels. The detection is considered significant and is attributed to the flare and its local complex transients.

The acoustic sources slowly fade in about two minutes following the impulsive flare phase. Unfortunately, the *IRIS* slits do not cross exactly over these circled areas, so spectral information regarding the chromospheric emission in regions overlaying the acoustic sources is available only $4''$ east of the seismic sources, still covering only the weak diffuse seismic emission.

It is worth mentioning that the detection of seismic emissions (acoustic sources) depends on their amplitude relative to the background solar noise, which for this flare was very strong at the eastern foot of the filament, where the X-ray emission was also detected. We focused our analysis on the seismicity generated near the *IRIS* slits.

In conclusion, the detected seismic sources are very compact with a diameter of 12 *HMI* pixels or approximately 3–4 Mm, and can be linked to a few of the magnetic field strands left behind by the erupting filament. This is a new discovery, and is significant for the interpretation of the origin of sunquakes.

Kernel evolution

The *IRIS* slits missed the main seismic emission. However we made use of the *IRIS* SJI data to explore the intensity fluctuation of a selected number of regions of interest (kernels) located at different locations along the flare ribbon. In the right panel of Figure 4.22 we include a photospheric SJI 2832 frame with white contours enclosing regions of ± 2500 , ± 1500 and ± 500 G magnetic field strength and in red contours the location of the two detected main acoustic sources. In the left panel the small black squares highlight the positions of the selected kernels. Some of the important locations are: *k5* corresponding to the position partly covered by the spectrograph slits; *k1* and *k6* cover the penumbral intrusion that corresponds to the location of the detected acoustic signatures; *fil-k* is selected to cover the location of a footpoint anchoring the filament away from the main sunspot. The square marked *QS* is selected to be at a location as far as possible from the atmospheric disturbances generated by the flare by careful analysis of all SJI filters and is used as reference.

The evolution of the integrated intensity over each box, for the three *IRIS* SJI filters is shown in Figure 4.23. Most of the locations considered reached their maximum intensities at the time corresponding to the *RHESSI* flare initiation at 16:16 UT, but an additional peak was present at the maximum X-ray flare emission around 16:21 UT. At the position of the *QS* patch the photospheric filter centred at 2832 \AA , in the red wing of the Mg II resonance lines, showed no response to the flare, while the transition region lines displayed some small oscillations after the flare maximum, especially the filter centred on the Si IV emission sampling a region higher in the solar atmosphere.

The *k1* and *k6* locations sampling the acoustic kernels and the complex part of the southern flare ribbon presented a small enhancement two minutes before the filament began its accelerated rise suggesting the footpoint started to become unstable. Despite its spatial closeness to the acoustic kernels, the *k5* kernel overlying the location of the *IRIS* slits and part of the southern ribbon does not present strong acoustic signature, but showed an atmospheric evolution similar to the seismically active kernels. It did show transients in the *HMI* running

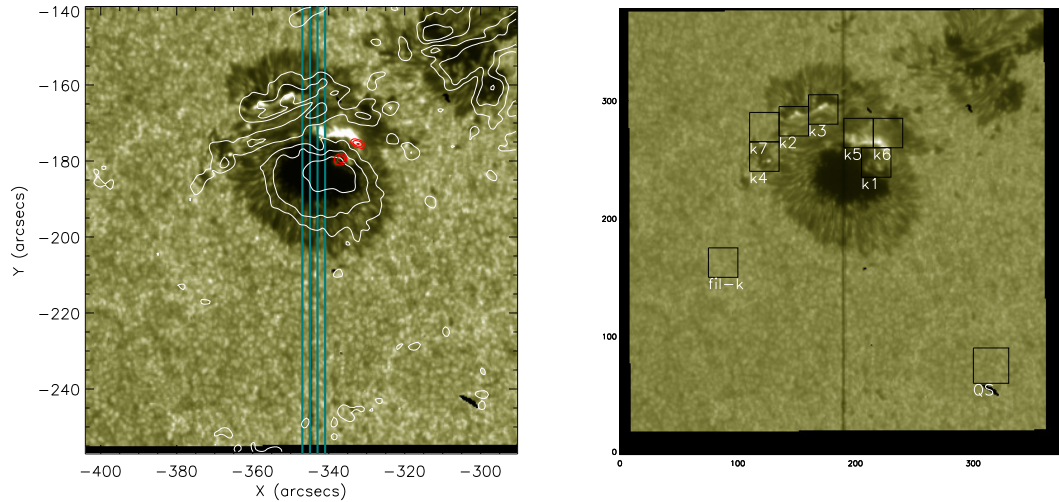


Figure 4.22: Left: SJI 2832 emission at the flare maximum, together with contours of magnetic field intensity (white) and the locations of acoustic enhancement (red). The vertical teal lines mark the positions of the *IRIS* SG slits. Right: Important positions along the flaring ribbon and outside the flaring region which are explored in Figure 4.23 are marked by black squares.

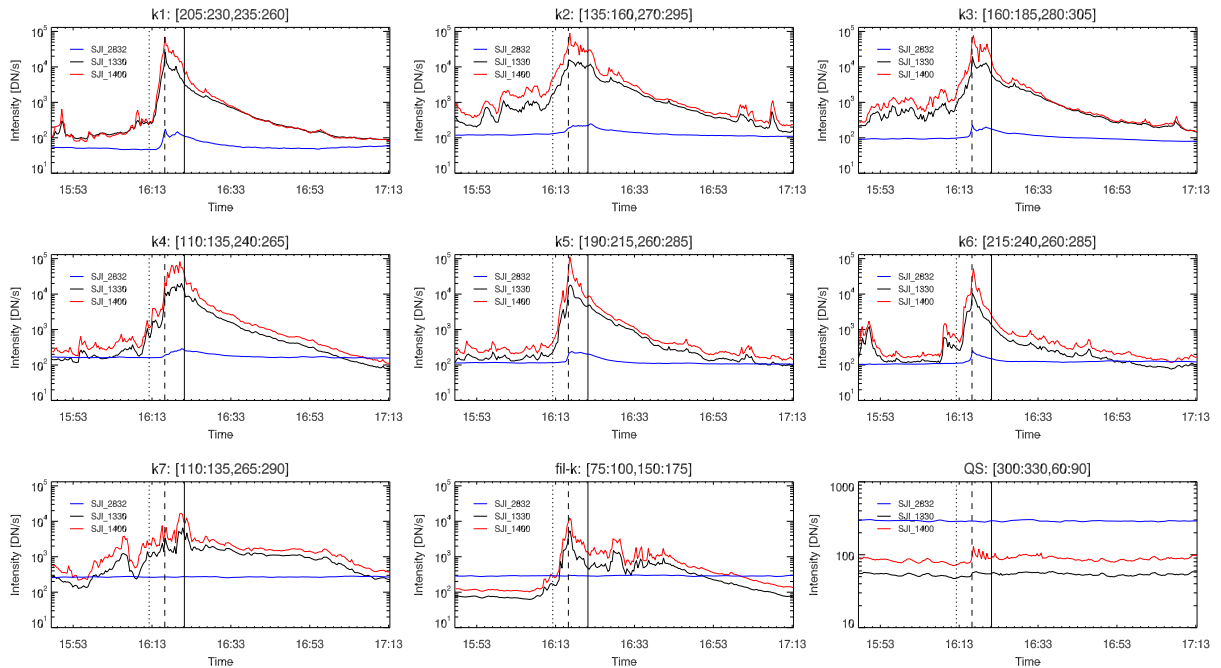


Figure 4.23: Evolution of *IRIS* SJI intensity at different positions of along the flaring ribbon at locations highlighted in Figure 4.22. The dotted line marks the start of the filament rise, the dashed line marks the start of the flare, while the continuous line is at the position of the *GOES* maximum emission.

differences, but weaker than at the locations of *k1* and *k6*.

The regions overlying the northern opposite polarity region and northern flare ribbon, *k2*, *k3* and *k4*, also showed a similar behaviour in chromospheric and TR emission, but due to LOS effects the emission may all originate from the rising and reconnecting filament, and not sample the footpoints. Multiple reconnection events can be observed as the quasi periodic brightness enhancements in the plotted profile. The intensity maximum in the photospheric filter tends to reach its maximum close to the maximum X-ray emission in all three kernels.

The *fil-k* location revealed no changes in the photospheric emission, but became highly variable as the filament rose and continued to show activity for a while after the flare, as different strands of the filament were stretched by the erupting filament leading to subsequent

reconnection. The *k7* kernel similarly only sampled the episodic reconnection of loops confining the filament and the subsequent emission from filament strands, showing no photospheric changes.

We do not have information on the spectral properties of the atmosphere overlying exactly the location of the seismic sources, but we do have information from along the same flare ribbon, just a few arcseconds away. Thus we can approximate the variation of the spectral characteristics to be similar, considering the ribbon properties were relatively uniform. This gives most likely an underestimation of the variability, as the acoustic signal originates from a more complex magnetic configuration, that may have enabled some kind of energy transport mechanism to penetrate through to photospheric levels. We consider the average LOS velocities as obtained from the centroid shifts of the different *IRIS* emission lines in the impulsive phase of the flare:

Ion	Doppler velocity	Temperature	Solar Atmospheric Layer
Fe XXI	-335 km s ⁻¹	log <i>T</i> =7.0	corona
Si IV	35.4 km s ⁻¹	log <i>T</i> =4.8	TR
C II	31.1 km s ⁻¹	log <i>T</i> =4.3	low TR
Mg II k	14.7 km s ⁻¹	log <i>T</i> =4.	high chromosphere
Mg II blend	8.1 km s ⁻¹	log <i>T</i> =3.8	chromosphere

The obtained Doppler shifts at different heights fit the standard flare model, as the accelerated particles from the reconnection site travel to somewhere in the lower atmosphere, where they deposit their energy and excite the cool material, to further produce impulsive heating and evaporation of plasma. This is seen in the high values of blue shift measured in Fe XXI emission at coronal temperatures. Simultaneously, the explosive evaporation produces a downward disturbance that is seen as red shifted emission in lower temperature lines. The decrease of the observed shifts is in line with the expected behaviour of the perturbation being damped as it travels through the density gradient toward the solar surface.

Additionally, the photospheric Doppler speed measured from the *HMI* Dopplergram at the location of the seismic sources was ~ 0.4 km s⁻¹, which is well under the supersonic threshold $c_s=7-8$ km s⁻¹, however, we can compute the momenta of this downward velocity.

The volume of the kernel can be approximated as the product between the average areas of the seismic kernels (red contours in Figure 4.22) and the distance travelled by the wave front in the 45 seconds between consecutive *HMI* images with the measured LOS velocity.

$$dV = h dA = v d\tau dA \quad (4.5)$$

For the *k1* and *k6* kernels, considering the seismic source is 1/4 of the kernel area, thus some 10^{17} cm², we obtain volumes of the order of 10^{24} cm³.

The momentum of impact at the seismic kernel is then given by

$$p = \int \rho v dV = \int \rho v^2 d\tau dA \quad (4.6)$$

where $\rho=2.7 \times 10^{-7}$ g cm⁻³ is the local photospheric density (e.g. Vernazza et al., 1981), $v=10^5$ cm s⁻¹ is the LOS speed and $d\tau$ is considered to be 10^2 s. The obtained momenta is then equal to 10^{22} g cm s⁻¹ for both seismic sources.

Inferences about the momentum during the flare: there is sufficient momentum in the photospheric energy flux to explain the seismic generation; the filament acceleration predicts at least one photospheric impulse; the magnetic forces should be of particular significance where the magnetic field is significantly inclined from vertical, which is the case in this solar flare, after the snapping of the filament. We do not know which particular mechanism couples best into the sunquake yet.

4.3. March 29, 2014 X1.0 flare

The March 29, 2014 X1.0 flare (SOL2014-03-29T17:48) was dubbed by NASA ‘the best-ever observed flare’ in a press release, as it was simultaneously observed by a multitude of instruments, both ground- and space-based. The large amount of data covering this event also made it the most studied recent flare, with an impressive number of authors exploring different aspects of its development. The flare peak emission was at 17:47 UT and originated from AR NOAA 12017.

The *IRIS* spectral data was obtained between 14:10 and 17:54 UT, during a “Very large coarse 8-step raster” flare watch campaign, with an 2'' step between each of the 8 slit positions. The exposure time of all spectral windows at each slit position was set to 8 s, but was automatically decreased for NUV lines to 2.44 s during the flare, without changing the raster cadence of 75 s. The spectral sampling was 0.02546 Å/pixel for the NUV channels, while for the FUV channels it is either 0.02596 Å/pixel (FUV1) or 0.02544 Å/pixel (FUV2). The *IRIS* observing run ended shortly after the flare maximum, thus the observation of the full chromospheric relaxation phase is missing.

Complementary context SJI data was also captured in filters centred at 1400 Å including the Si IV emission (captured at raster steps 0, 4 and 6), at 2796 Å including the Mg II *k* line (steps 1, 3, 5 and 7) and at 2832 Å in the red wing of Mg II (step 2). The FOV was centred on AR 12017 and covered a 167''x174'' region, with a spatial sampling of 0'.166.

Before discussing our results, an overview of the studies focusing on this event is required.

[Heinzel and Kleint \(2014\)](#) reported the first NUV continuum brightness enhancements using *IRIS*, finding no detectable spectral dependence, and attributed the increase to Balmer continuum hydrogen recombination. In a subsequent study, [Kleint et al. \(2016\)](#) explored the overall continuum enhancements associated with the flare using data from FUV to IR wavelengths. Based on the spectral fitting of the *RHESSI* flare emission they found that energy deposition by accelerated electron > 40 keV is enough to explain the observed intensities. [Kowalski et al. \(2017\)](#) also concluded that a high energy beam flux can produce the observed continuum enhancements and additionally modelled the Fe II profiles present in the red wing of the Mg II resonance lines.

[Li et al. \(2015\)](#) used a combination of spectral data from both *IRIS* and *EIS*, covering a spectral range from UV to EUV, in order to analyse evaporation flows at different locations of the active region associated with the flare event. They detected both gentle and impulsive evaporation as the flare progressed and noted that the evaporation flows appeared to coincide with the location of the ribbon.

An in-depth analysis of the observed Mg II emission during the flare and a summary of the observed characteristics were provided by [Liu et al. \(2015b\)](#). They found an increase in the integrated intensity, redshifts and line broadening, while the *k:h* ratio appeared to remain rather constant during the flare. They investigated the parameter space needed to produce these characteristics by computing some synthetic spectra. In a subsequent study, [Rubio da Costa et al. \(2016\)](#) employed the RADYN code to obtain more realistic, data-driven synthetic spectra of H α , Ca II 8542 Å and Mg II *k* chromospheric emission during the flare. They found general good agreement between the simulated and observed profiles, but while the flaring *k* line emission matched in intensity, it was still too narrow and double peaked, while the observed profiles were single peaked and much broader throughout. The discrepancies were attributed to the sensitivity of the *k* line emission to variations of the chromospheric conditions in its narrow formation region. Cool flows along post-flare loops in the gradual phase were explored by [Mikuła et al. \(2017\)](#). They obtained synthetic spectra of Mg II and compared them with observation, finding a good fit for the velocity increase from loop-top toward footpoint and decrease in intensity with increase in velocity.

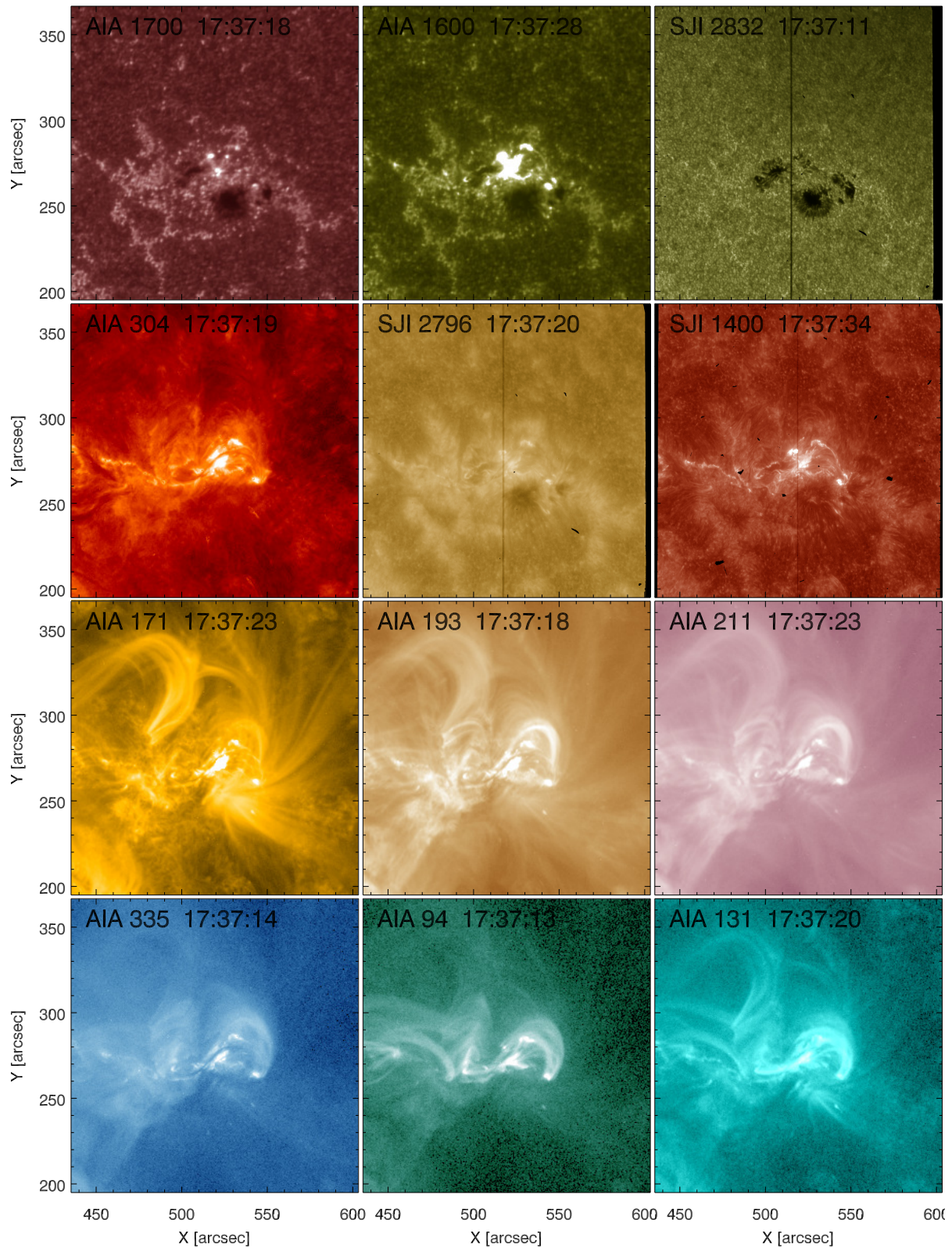


Figure 4.24: The solar atmosphere before the X1. flare of March 29, 2014 as seen by *IRIS* and *AIA/SDO*. The FOV has been restricted to the *IRIS* dataset. The dark vertical line in the SJI images represents the position of the slit. The intensity of each image has been adjusted for best contrast. The top row contains the emission of filters containing photospheric contribution, the second row shows chromospheric emission and the last two rows capture the ‘hot’ coronal plasma.

The behaviour of the coronal Fe XXI 1354.1 Å forbidden line captured by *IRIS* was studied by [Young et al. \(2015\)](#) and [Battaglia et al. \(2015\)](#). The former found a strong blueshift present

in the initial stage of the flare at the locations of the flare ribbons, but close to the line rest position emission in the post-flare loops. The latter went into more details on the importance of electron beams in the excitation of chromospheric evaporation, by investigating the spatial and temporal correlation between the HXR footpoints and the enhanced blueshifts in the Fe XXI emission. The lack of spatial correlation in the decay phase was attributed to conduction flux being responsible for the evaporation instead of beam energy deposition.

The filament involved in this flare was investigated using data from *IRIS*, *RHESSI*, *IBIS* and *SDO* by a number of authors. Kleint et al. (2015) focused on the filament evolution as seen in the emission of TR and chromospheric lines and reported the first detection of a filament eruption in the Si IV emission, measuring accelerations of $\sim 3\text{-}5 \text{ km s}^{-1}$ during the impulsive phase of the flare, noting that the *RHESSI* HXR emission appears after onset of the filament acceleration. Liu et al. (2015a) used imaging data together with NLFFF extrapolations of the photospheric magnetic field to propose the asymmetric filament eruption as the cause of the subsequent reconnection producing the circular ribbon flare, with torus and kink instabilities being dominant in different regions of the filament. Based on NLFFF extrapolations and spectral analysis, Woods et al. (2017, 2018) hinted at the transient nature of the reconnection within the filament leading up to the flare, discussing how different reconnection mechanisms may inject energy into the emitting region, suggesting torus instability was the main cause of the filament eruption, due to predominant blueshifts observed. Yang et al. (2016) tackled evolution of the magnetic topology of the filament, but over the course of a few days prior to the X-class flare, but arguing that kink instability acted in different segments of the filament and played a key role in all the associated flares.

Aschwanden (2015) investigated the magnetic energy dissipation and calculated the free energy evolution by applying an automated loop identification algorithm to *IRIS* and *AIA/SDO* imaging data. They found the free energy to be decreasing throughout the solar layers.

Polarization of the He I 1083 nm multiplet during the impulsive phase of the flare was investigated by Judge et al. (2015), concluding that the polarization is due to anisotropic scattering of photons in an optically thick slab above the photosphere.

The relation between the flare induced emission and the acoustic source of this event was evaluated by Matthews et al. (2015) using *IRIS* and *EIS* spectroscopic data and by Judge et al. (2014) using data from *IBIS* and *FIRS*. The former compared the observed spectra of the two flare footpoints, finding that the footpoint overlying the location of the acoustic signature showed an overall higher emission, shift and width, throughout the lower solar atmosphere. The latter investigated the emission of several photospheric lines together with continuum data and using 1D modelling computed the penetration depth of the flare heating, finding it reached photospheric heights of $100\pm 100 \text{ km}$, but could not identify the process capable of reaching such depths and transporting enough energy to produce the observed seismic event.

Abramov-Maximov et al. (2015) studied the microwave emission leading up to the flare (using RATAN-600 data) finding it showed a similar behaviour to the magnetic field gradient for ~ 2 days prior to the flare. Both variations are the result of new emergence near the main polarity, that unsurprisingly increased the complexity of the active region.

Finally, Francile et al. (2016) discussed the Moreton-wave event (global perturbation propagating across the disk) triggered by this flare and analysed the evolution of the associated CME into interplanetary space.

4.3.1. Seismic activity

I will further discuss the *IRIS* emission and the seismic signature, together with their evolution and implication to the energy propagation from the high solar corona, down to the photosphere, where the acoustic signature was detected.

The locations of strong photospheric transients were identified from running difference

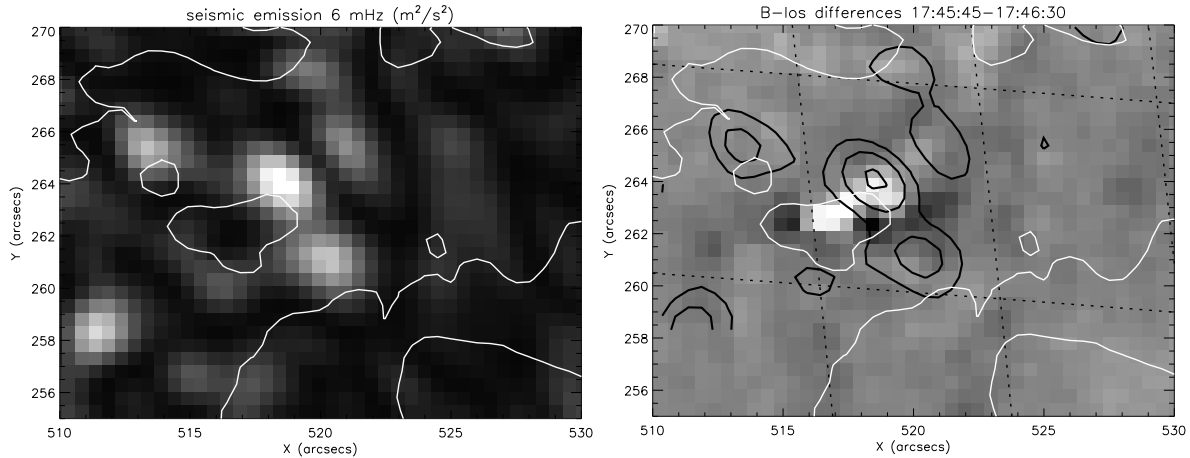


Figure 4.25: Left: The computed acoustic emission map at 6 mHz with white contours marking levels of *HMI* continuum emission. Right: *HMI* B_{LOS} running differences showing the location of magnetic transients associated with the flare. The contours mark continuum (white) and seismic (black) emission.

sequences of *HMI* LOS magnetic field and Dopplergram images, then we applied holographic techniques to obtain acoustic and egression maps covering the active region. The left panel of Figure 4.25 shows the egression power map of acoustic emission at 6 mHz for a region centred on the location of detected strong photospheric transients as seen in the right panel. Given the unpredictable nature of solar flares and the yet unknown mechanism that produces sunquakes, we are fortunate to have *IRIS* sample this location, which enables us to explore the emission overlying the acoustic source.

We have to bear in mind that given the integration time at each slit position only the emission at slit positions 4 and 5 temporally coincide to the seismic signal. Additionally, the SG slit positions are located $2''$ apart, meaning the emission maxima may fall between the locations sampled by the slit. The left panel of Figure 4.26 provides a broader view of the relation between the positions of the *IRIS* SG slits during the raster containing the maximum flare emission and the location of the acoustic source (blue contours). The background is the corresponding frame from *IRIS* SJI 2832 and the white contours highlight the photospheric configuration of the magnetic field. We can state that the acoustic signature overlaps the location of the flare ribbon in the impulsive stage and is located in a region of modest photospheric magnetic field.

The profile characteristics of the Mg II k line are depicted in the right panel of Figure 4.26 for the raster simultaneous to the flare peak emission. The blue contour correspond to the acoustic source. In the integrated intensity map all slit locations show enhancements corresponding to the southern flare ribbon, with the northern ribbon only visible in the first two slits. The emission at the location of the acoustic signature does not appear to differ much from any other point along the flare ribbon, being even comparatively lower in some locations. The ribbons are associated to downflow of a few tens on km and line widths of around $\sim 1.2 \text{ \AA}$. Additionally, the spectral profiles show red asymmetries in both the Mg II resonance lines and the subordinate triplet emission of up to $\sim 70 \text{ km s}^{-1}$.

Excluding the saturated spectra in the FUV regions that sometime can coincide to the seismic source, we have computed the profile moment maps and found a similar trend in C II and Si IV emission, with high intensities and important red asymmetries. The presence of a red shifted component is apparent even in the saturated spectra, and extends a narrow region of only a few pixels overlying the ribbon location.

We also know that some of the flare energy has reached lower than the formation height of of these upper chromospheric lines as we have enhanced continuum emission throughout the spectral range, and the usually absorption features of photospheric neutral elements are in

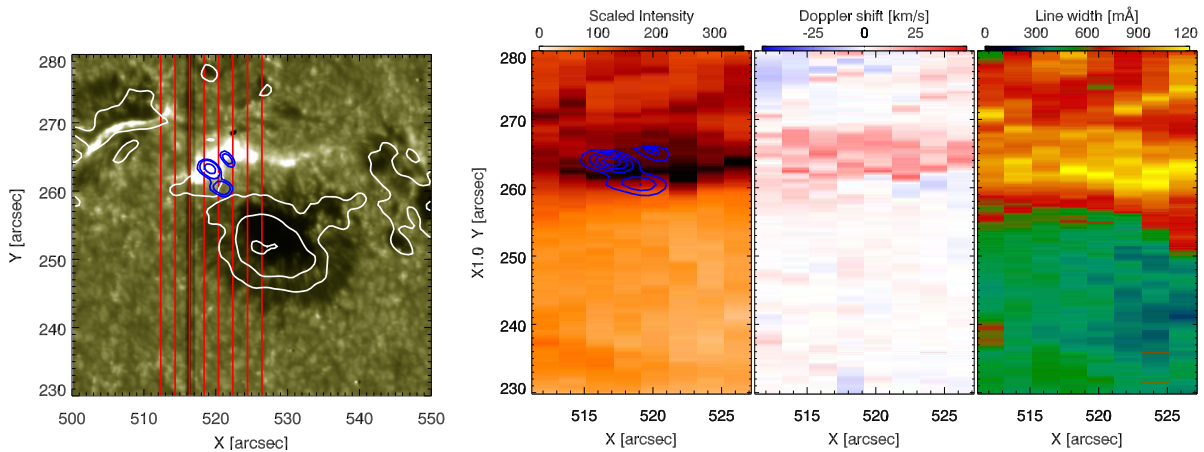


Figure 4.26: The *IRIS* SJI 2832 frame at the flare maximum, with the SG slit positions as the vertical red lines. The white contours mark levels of ± 1500 , ± 1000 and ± 500 G of B_{LOS} field and the blue contours mark the position and extent of the acoustic source. The computed Mg II k profile moments for the raster set between 17:45 and 17:47 UT, capturing the impulsive phase of the flare: integrated intensity, centroid shift and line width.

emission. The simultaneity of the enhancements throughout the observed spectral range points to a highly rapid propagation of the flare excitation. However, in order to reach the solar surface and produce the seismic disturbance, the perturbation needs to go through increasingly denser regions, without losing all of the transported energy.

We could be dealing with the energy being delivered to the photospheric level by some kind of non-compressible wave, which would not have an impact on the emitting plasma or the magnetic field itself may play an important role in carrying the energy, but the study by [Judge et al. \(2014\)](#) suggests none of these can carry the energy necessary to excite the acoustic emission.

4.4. *Disconnected chromospheric ribbon*

So far we have discussed large and energetic flares, with a reconnection site located somewhere in the corona, from which highly energetic particle beams (non-thermal beams) are accelerated and as they travel downward into denser atmospheric layers they produce dramatic changes, from excess radiation to acoustic signatures at the photospheric level. But the correlation between the observed low atmosphere emission and the energy transport is not always straightforward, as the flare ribbons extend larger regions than just the location of HXR emission ([Fletcher et al., 2011](#)), suggesting energy release may not be restricted to the location of energy deposition. Furthermore, in the case of small flares, the location of the HXR emission can not be identified and we may consider if there is a need for a coronal connection. This brings into question the universality of the flare model, and the possibility that in the case of some events the energy storage and release is strictly local, without any energy input from the overlying corona.

We consider the coronal connectivity of a small scale ribbon recorded by the *IRIS* instrument during a short sit-and-stare flare watch campaign focused on AR NOAA 11890 on 2013 November 9, between 12:04 and 12:17 UT. The analysis presented in this section discusses chromospheric losses as derived from *IRIS* spectral data and is part of the study published in [Judge et al. \(2017\)](#).

A mosaic of *SDO* and *IRIS* SJI data at the time the small ribbon became active is presented in Figure 4.27. The ribbon location has been marked by the black polygon to ease identification. Most of the emission appeared to be restricted to channels sampling chromospheric and TR emission, like He II seen by *AIA*304 and Mg II k 2796 Å and Si IV 1402 Å recorded by *IRIS* SJI. The emission in the high temperature *AIA* filters was very low to non-existent. *AIA*94 and

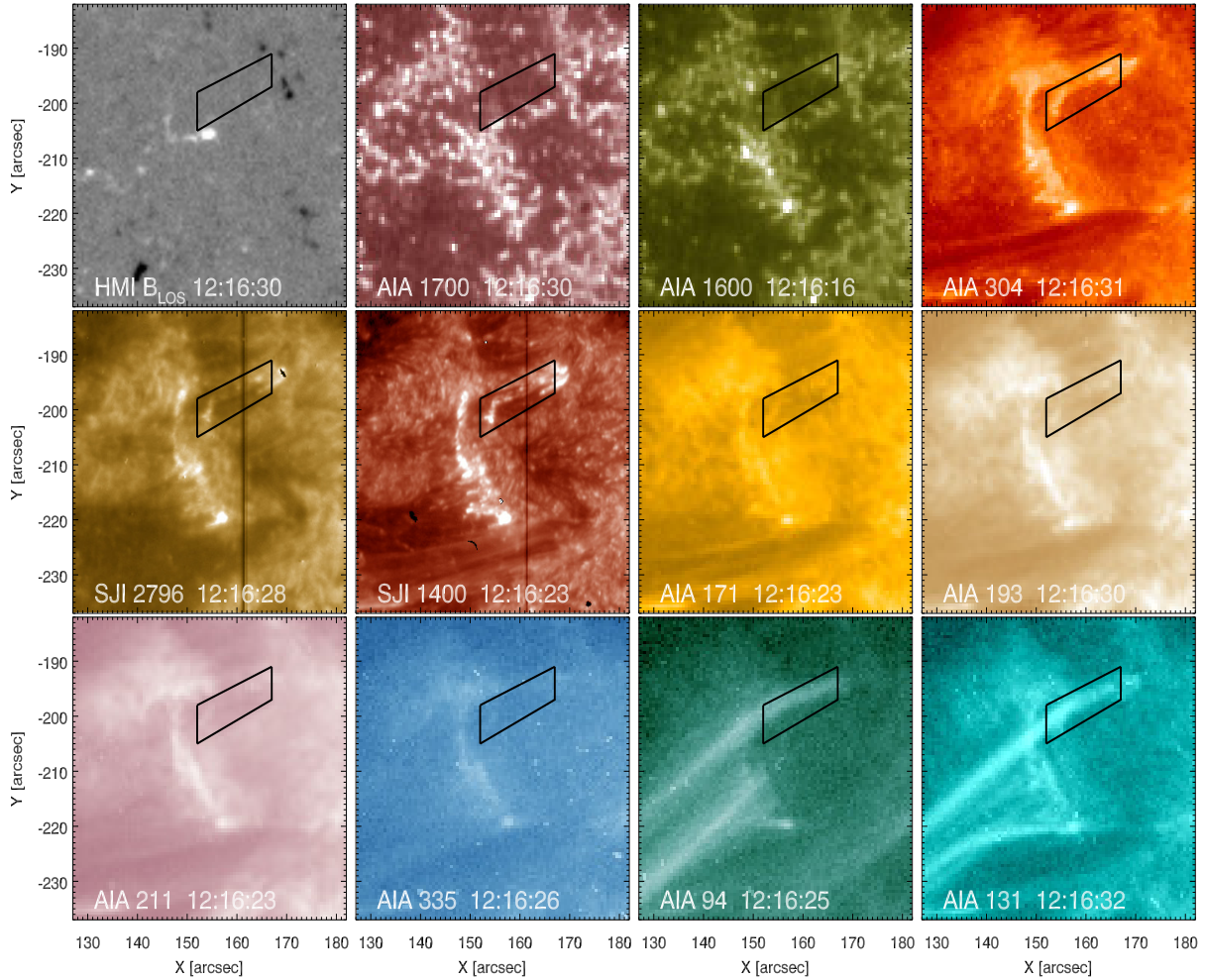


Figure 4.27: LOS magnetic field configuration from *HMI* (top-left) and intensity data from *AIA* and *IRIS* SJI, sampling the solar atmosphere during a small scale flare. The black polygon highlights the location of the studied ribbon and the vertical lines mark the *IRIS* slit position during the observing campaign. The FOV has been restricted to and centred on the flaring ribbon.

*AIA*131 showed excess emission, but from an overlying loop rooted on the right side of the polygon, at $(X, Y) = (167, -192)$, effectively obscuring the ribbon location. The lack of upward connectivity of the ribbon was supported by the low B_{LOS} component measured by *HMI* and the low emission in the *AIA*1600 and *AIA*1700 channels that contain photospheric continuum contributions.

Based on Si IV Doppler shift measurements, [Testa et al. \(2014\)](#) modeled the observed emission by considering non-thermal particle beams originating from a coronal reconnection site, while dismissing a chromospheric origin. We investigate the magnetic field configuration using *HMI* and *Hinode* data and find magnetic field with $B_{\text{L}} = 11 \pm 10$ G and $B_{\text{T}} = 73 \pm 24$ G components. The longitudinal magnetic field is too weak to support the coronal connection (see [Judge et al. \(2017\)](#) for further information regarding the magnetic field analysis), and in turn propose that at least one of their studied events is purely chromospheric.

The spectral data was calibrated to physical units and was used to estimate the total radiative losses from the chromosphere. At the location of the ribbon the Mg II k line recorded an excess emission $I_k = 1.5 \times 10^5 \text{ erg s}^{-1} \text{ cm}^{-2} \text{ sr}^{-1}$. Based on the fact that the k line emission represents $\sim 10\%$ of the total chromospheric losses, as prescribed by [Vernazza et al. \(1981\)](#), and considering the important losses by Fe II ([Anderson and Athay, 1989a](#)), the total chromospheric losses can be considered to be $\approx 20 \times 4 \pi I_k \approx 4 \times 10^7 \text{ erg cm}^{-2} \text{ s}^{-1}$. The excess intensity in the Si IV 1402.7 Å emission, which constitutes less than 1% of the TR losses, is only $6 \times 10^3 \text{ erg}$

$\text{s}^{-1} \text{cm}^{-2} \text{sr}^{-1}$, some ~ 25 times lower than I_k .

Using the upper limit for the measured longitudinal field of ~ 10 G, for a straight flux tube of length $L \approx 10^{10}$ cm, the total energy per unit area would be equal to $L B^2/8\pi \approx 4 \times 10^{10}$ erg cm^{-2} . Based on the *AIA304*, the ribbon is seen in emission for ~ 100 seconds, thus the overlying corona can supply up to 4×10^8 erg $\text{cm}^{-2} \text{s}^{-1}$. If we consider that 10% are available as free energy, then less than 4×10^7 erg $\text{cm}^{-2} \text{s}^{-1}$ is available for heating. This is on par with the chromospheric losses computed above and with the energy requirements of the quiet-Sun chromosphere (Anderson and Athay, 1989b). An alternative limit can be found by using the Alfvén crossing time of the flux tube, L/V_A . Based on a pre-flare density of 2×10^{-15} g cm^{-3} (Jordan, 1992) we obtain $V_A \approx 700$ km s^{-1} , thus the crossing time would be ~ 140 s.

However, one must keep in mind that our estimate is an upper limit, given that: (1) the 10 G value is for photospheric fields, and the magnetic strength decreases with height; (2) the flux tube length is based on neighbouring coronal loops rooted in much stronger field concentrations; (3) the 10% of the magnetic energy available for release is an optimistic consideration. Furthermore, considering the fact that reconnection typically takes place at 0.1 of the Alfvénic speed V_A , the dynamical time for energy release is $L/0.1V_A \approx 1400$ seconds.

If we allow for the transverse field to be connected to the corona under a highly oblique direction to the LOS, the energy available would be some 50 times higher and the beam heating mechanism would be plausible, with an energy release rate of $\sim 2 \times 10^9$ erg $\text{cm}^{-2} \text{s}^{-1}$ and a dynamical time of ~ 200 s. Still, the absence of coronal moss structure and the morphology of horizontal field do not support this assumption.

We further consider the measured B_T to be a component of a small emerging flux that interacts and reconnects with the canopy fields. The reconnection will convert the magnetic energy to thermal emission at a rate of $\approx 0.1V_A \sin \vartheta B_T^3/8\pi\sqrt{4\pi\rho_u}$. Assuming the angle between the emerging flux and the canopy fields is $\vartheta \approx 30^\circ$, with an upper chromospheric density of $\rho_u \approx 10^{-12}$ g cm^{-3} (Vernazza et al., 1981), the obtained rate is 5×10^7 erg $\text{cm}^{-2} \text{s}^{-1}$, comparable to the measured chromospheric losses.

Thus we have established that the studied small scale flare ribbon was magnetically disconnected from the overlying corona at the time of enhanced emission. The emerging flux is carrying enough energy for local dissipation in the upper chromosphere to explain the observed behaviour. This prompts a more prudent analysis of imaging and spectroscopic data, as the observed behaviour can not be exclusively attributed to energy transport from a coronal reconnection site, but chromospheric reconnection can also play an important role, at least in the case of small scale events.

4.5. Summary and Discussion

We presented a comprehensive observational investigation of chromospheric and photospheric signatures during the X-class flare of March 11, 2015. An erupting filament, which triggered the flare, was also well observed by *IRIS* and analysed in this chapter. The *HMI* vector magnetogram data allowed us to obtain the 3D field structure of the reconnection region. The dynamics of the footpoints of the flare were studied in relation to the associated seismic signatures. The multi-wavelength analysis and the *IRIS* data allowed to generate a qualitative image of the response of the chromosphere during the impulsive phase of a flare.

We used high energy observations from *RHESSI* and extracted the location of the coronal reconnection source using imaging reconstruction techniques. The flaring region appeared to overlay the PIL and the location of the twisted filament present in *AIA* EUV data. The energy partition between thermal and non-thermal components was then investigated by performing a multi component fitting of the high energy spectrum and we found the two components to have comparative values, similar to those of previous studies (Emslie et al., 2004). The

temporal evolution of the partition showed the non-thermal part increase sharply, dominating the impulsive phase, followed by continuing emission of thermal energy into the decay phase.

IRIS provided a wealth of spectroscopic information on the atmospheric response covering the evolution of the flare, in a convenient location, very close to the seismic sources. In fact, the *IRIS* slit locations close to the seismic source enabled us to extract the parameters needed to extrapolate the physics of the seismic kernels. After the corresponding *IRIS* data was retrieved and calibrated to physical units, we computed the integrated intensities, identified the centroid shifts and measured the widths of various emission lines, sampling atmospheric conditions from the chromosphere to the hot corona.

The Mg II *k* and *h* resonance lines and the subordinate triplet lines offered information on the chromospheric variation. The doublet showed an assortment of profile shapes, from the typical double-peaked to single peaked profiles, with blue or red peak dominance, while the triplet lines were generally in absorption. In the pre-flare spectra the rise of the associated filament can be seen for half an hour before its destabilization. The flaring profiles were characterized by intensity enhancements, with strong red asymmetries and increases in line width. The location of the flare ribbon and its southward drift can be clearly identified in the moments maps. The regions swept by the flare ribbons is observed again in emission, some 5 minutes after the impulsive phase. At the flare location the subordinate lines were seen in emission even before the flare commencement. In the flare spectra their profile shapes appeared similar to those of the resonance lines. In the post-flare phase, the continued emission may suggest persistent temperature gradients, but further analysis and modelling of the line emission in flaring conditions is required.

Higher atmospheric layers were sampled by the C II and Si IV lines in the FUV region of *IRIS* SG. They too show the presence of the rising filament before the flare and sample the southward drifting of the flaring footpoints. The intensity enhancements are stronger than those of chromospheric lines, suggesting more impulsiveness in the heating experience at their formation heights. The line widths also showed an increase that was diminished as the flare evolved.

All analysed lines show episodic red shifts after the impulsive phase, suggesting multiple strands of plasma crossing the SG slit become visible with downward propagating plasma. The variations between the slits emission can be attributed to them sampling slightly different regions along the flaring loops and footpoints. Additionally, the measured downward speeds show a decreasing trend with lower atmospheric heights, as expected from a perturbation being slowly damped as it propagates through denser plasma.

The analysis of the Fe XXI 1354.1 Å line revealed the presence of hot coronal emission in the impulsive phase of the flare, showing blue shifts of $\sim 400 \text{ km s}^{-1}$ and enhanced line widths. The low intensity of this line and the presence of additional lines in the same spectral region complicated the identification of this line. However, this is consistent with the observations of [Young et al. \(2015\)](#), who pointed out the same limitations. The main emission is delayed by $\sim 250 \text{ s}$ from the start of the flare and corresponds to steady emission from freshly reconnected loops, now filled with hot plasma. A similar delay was found by [Graham and Cauzzi \(2015\)](#) in the case of another flare. Using the observed profile characteristics and temperature of the coronal loops of $\log T = 7$ we found a micro-turbulent velocity of 41 km s^{-1} is needed to explain the extended line width.

Spectral investigation of the pre-flare conditions revealed the presence of a filamentary structure anchored in various locations of the active region. The slow rise could be seen as small blue shifted components in chromospheric and TR spectral lines. Eventually the structure became unstable and displayed blue shifts of $\sim 400 \text{ km s}^{-1}$ and acceleration rates of $2\text{-}4 \text{ km s}^{-2}$. In imaging data the filament strands appeared to untwist as they propagated away, while

some plasma could be seen draining toward the various footpoints in cool emission channels.

The EM analysis of *AIA* imaging data revealed increased emissivity in the high temperature bins lasting tens of minutes after the impulsive stage of the flare. The $\log T = 7$ K emission highlighted the same loop structure visible earlier in the *IRIS* Fe XXI emission, thus the spectral emission can provide crucial information on the corona during the saturation of *AIA* filters.

The photospheric magnetic field configuration of the active region before and after the flare was investigated, together with the evolution of the electric current density. The southern ribbon was found to overlay regions of filamentary magnetic structure close to regions of mixed polarity. We further explored the 3D configuration of the magnetic field in LFF extrapolations and found a decrease of field line twist and weaving in the aftermath of the flare. The J_z electric current is spatially and temporally aligned with the seismic measurements and the HXR sources, suggesting that particles accelerated in the reconnection play a significant role in igniting the seismic sources (Sharykin et al., 2015; Donea et al., 2006; Sharykin and Kosovichev, 2015).

The photospheric transients and acoustic emission associated to this flare were also identified using *HMI* data and found to be located in the western side of the active region, over the penumbral intrusion hosting one of the filament footpoints. The *IRIS* SG did not sample this location, therefore we used the context SJI neighbouring data, to compare the location of the seismic source with locations overlying other important variability (only 4'' away from the seismic source). This allowed us to estimate that the downward momenta at the locations of the acoustic signal was equal to 10^{22} g cm s⁻¹, comparable to the values computed by Zharkova and Zharkov (2007), but for much stronger flares (X10-class). The high value obtained prompts the question of whether the more complex magnetic configuration of the penumbral intrusion is to blame, suggesting that the Lorentz force might have contributed, together with the accelerated particles, to the triggering of this seismic event.

The acoustic source of the well studied March 29, 2014 X-class flare was also further investigated, with an emphasis on the characteristics of the associated emitted spectra from *IRIS*. We find the emission lines throughout the *IRIS* spectral range to show enhanced red asymmetries corresponding to downward propagating plasma motions. The saturation of the SG detectors for the location of the impulsive energy deposition restricted the analysis, but the presence of enhanced shifts and line widths was still obvious. Additionally, continuum and line emissions from lower atmospheric lines were also present at this location, suggesting some of the flare energy may reach the photosphere, but not enough to excite the sunquake.

Finally, a small chromospheric ribbon was analysed and its radiative losses were approximated based on the observed spectral information from Mg II and Si IV emission. We then investigate the coronal connectivity of the flaring region and found that the magnetic field configuration could not allow for a vertical energy input from a coronal reconnection site. Further analysis revealed a small emerging flux to be involved in a reconnection, taking place most likely in the low atmosphere, and could provide enough energy to explain the observed radiative losses.

Through this analysis we aimed to better understand the flare energy propagation through the solar atmosphere and potentially link the observed spectroscopic characteristics with the associated acoustic source. However, the mechanism responsible for transfer of energy from the reconnection site to the solar surface is still unknown. We may require multi-height, high resolution (spatial, spectral and temporal), simultaneous observations of a more modest sunquake-producing flare (to avoid unwanted saturation), together with magnetic data of the chromosphere to be able to solve this puzzle, but with the opportunities offered by DKIST, this may be just over the horizon.

Chapter 5: Peculiar Profiles in Coronal Rain

“We are trying to prove ourselves wrong as quickly as possible, because only in that way can we find progress.”

Richard Feynman

In our journey of understanding of the response of the chromosphere to a solar flare, we came across an unexpected puzzle, which emerged from the spectroscopic analysis of one of our datasets. In the wake of the X2.1 flare of 11 March 2015 (SOL2015-03-11T16:22), the Mg II lines remained excited and highly redshifted for a prolonged time after the flare excitation had subsided. We were faced with the question of why would such a behaviour persist and this prompted us to perform a thorough analysis of the local plasma condition that had given rise to the observed spectral profile.

We focused our analysis on the broad red-shifted emission in chromospheric and transition region lines, proposing the hypothesis that the observed characteristics correspond to a long lasting post-flare coronal rain event. Emission profiles of Mg II, C II and Si IV lines were obtained using the *IRIS* instrument before, during and after the flare. We analyse the profiles of the five transitions of Mg II: the $3p - 3s$ (h and k) transitions, and the three lines belonging to the subordinate triplet $3d - 3p$ transitions. We use analytical methods to understand the unusual profiles, together with higher resolution observational data of a similar phenomenon observed by [Jing et al. \(2016\)](#).

The peculiar line ratios obtained indicate anisotropic emission from thin strands which have cross-strand line centre optical depths (for the k line) between 1 and 10. The lines are broadened by unresolved Alfvénic motions whose energy exceeds the radiation losses in the Mg II lines by an order of magnitude. The decay of the line widths is accompanied by a decay in brightness, suggesting a causal connection. Assuming the emitting plasma is $\lesssim 99\%$ ionized, ion-neutral collisions can account for the dissipation, otherwise some kind of dynamical process seems necessary.

Our work implies that the motions were initiated during the impulsive phase, to be dissipated as radiation over a period of more than an hour, predominantly by strong chromospheric lines. The coronal “rain” we observed is far more turbulent than most earlier reports have indicated, with implications for plasma heating mechanisms. The full analysis and discussion was published in [Lacatus et al. \(2017\)](#).

5.1. Introduction

The aim of the present work is to analyse some curiously broad and red-shifted profiles of emission lines obtained with the *IRIS* instrument a few minutes after the impulsive phase of a flare. The X2.1 flare of 11 March 2015 began near 16:16 UT, reached a peak at 16:21 UT and the atmosphere returned to its near-quiet state near 16:35 UT. The broad, redshifted emission of interest here started abruptly near 16:26 UT. Typical profiles of the Mg II h and

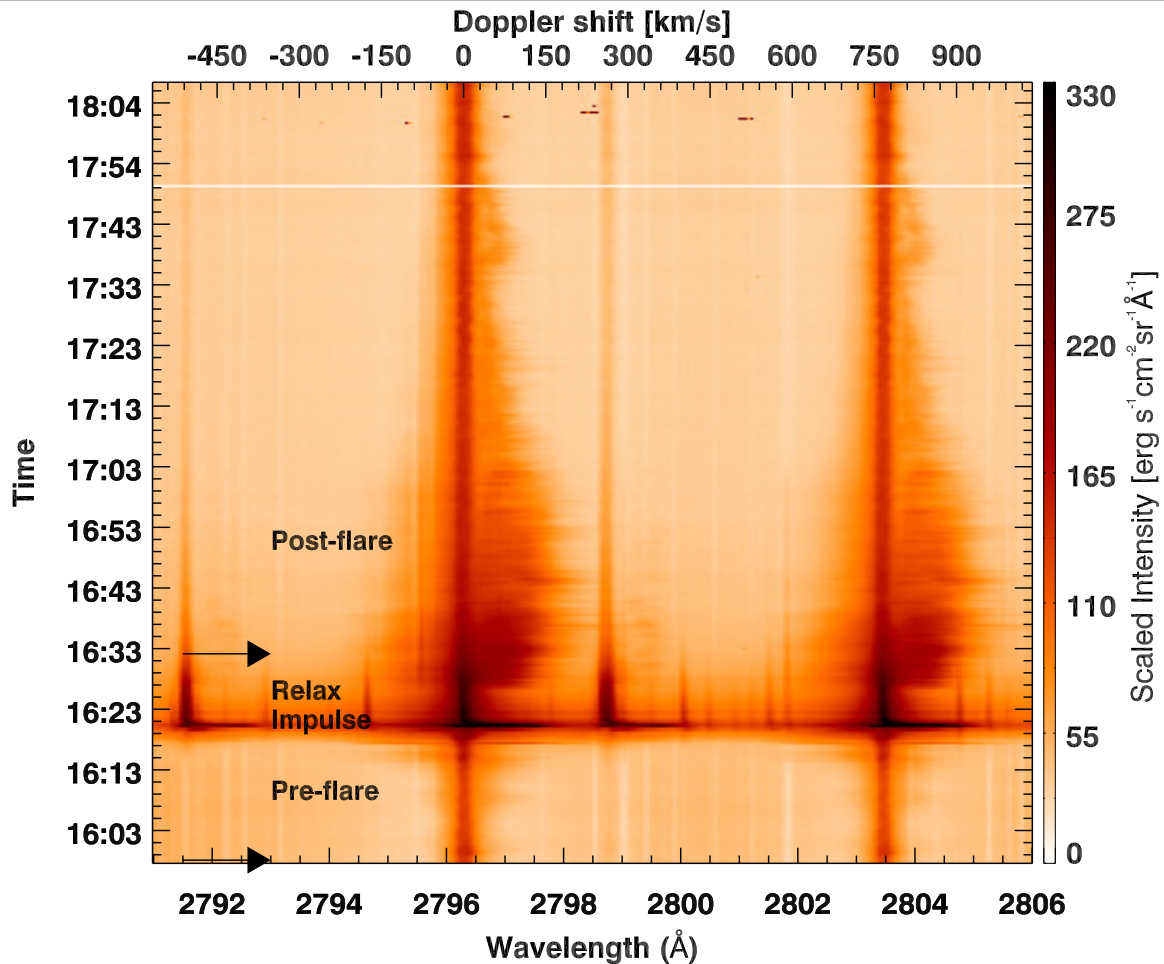


Figure 5.1: Cubic root scaled intensity profiles of the Mg II h and k lines are shown as a function of wavelength and time at $y = -175''$ along the first slit position. Doppler shift scale with respect to the k -line position are also included on the top x -axis. The two profiles shown in Figure 5.3 are from 15:57:51 and 16:32:31 UT positions, indicated by arrows.

k (at air wavelengths 2802.7 Å and 2795.5 Å, respectively) lines during this phase are shown in Figures 5.1 and 5.3. These profiles appear to differ qualitatively from all earlier theoretical and most observational studies on coronal rain, the emission lines being unusually broad and persistent.

By themselves, these data admit several possibilities of interpretation. Fortuitously, some partly resolved “fine structure”, corresponding to plasma flows, with similar spectral properties has been observed in another solar flare by Jing et al. (2016). Their work focused on the M6.5 flare of June 22, 2015 and uses observations with $0''.03$ spatial sampling, through narrow-band filters at H α 6563Å line centre and off-bands at ± 0.6 Å and ± 1.0 Å. Although not discussed by them, Fig. 7b in their paper also shows Mg II spectral data from *IRIS* during the post-flare stage that, without doubt, arises from the same phenomenon we analyse here. Thus, the broad, red-shifted emission features of Figures 5.1 and 5.3 are coincident with the onset of a return of emitting plasma along post-flare loops (see Jing et al., 2016, Fig.7c and 7d). These phenomena shown by Jing et al. (2016) and in the present work are unquestionably a form of *coronal rain*.

This phenomenon was initially detected in H α limb observations of mostly quiet conditions by Kawaguchi (1970) and Leroy (1972), who noted the presence of rain-like events during observations of prominences. Tandberg-Hanssen (1974) highlighted the importance of the magnetic field configuration on the rain evolution, inferring its role as a guide for the plasma descend. It has since been established that coronal rain is generally observed in emission in chromospheric and transition region lines in neutral or partly ionized plasma; and in absorption, as dark flows along the coronal loop system, in fully ionized coronal plasma observations.

Thermal instability leads to catastrophic cooling in non-flaring conditions whenever the local radiative losses overwhelm the heating input as predicted by Parker (1953) and Field (1965); see also Cally and Robb (1991). The onset of such catastrophic cooling and the formation of dark blobs was observed with increasing resolution (Schrijver, 2001; Vashalomidze et al., 2015; Kohutova and Verwichte, 2016), and their physical properties have been measured. Typically, the observed blobs are short-lived, on the order of a few minutes, have a length of a few tens of Mm and average speeds of 75 km s^{-1} .

The downflow speed of the rain has been observed to be much lower than that induced by pure gravitational acceleration, so Heinzel et al. (1992) proposed a few mechanisms to explain the deceleration based on NLTE loop modelling. For slow blobs, the inhomogeneities in the flux tube may be enough to significantly decrease the initial speed, while for faster falling blobs, the helicity of the tube or inhomogeneities inside the flow as it penetrates to deeper layers of the atmosphere will reduce the speed.

Numerous simulations of coronal rain formation and evolution have been performed over the years (Moschou et al., 2015; Oliver et al., 2016, and references therein). They find typical redshifts in the range $\sim 10 - 150 \text{ km s}^{-1}$ for the multi-stranded and multi-thermal structures. They also find that after catastrophic cooling takes over and starts forming blobs, composed of denser and partly neutral chromospheric material suspended by the magnetic field, interchange instability conditions are fulfilled and the blobs motion will be forced to move to a more gravitationally stable position. Additionally, they identify magneto-acoustic waves with periods of about 100 s excited by the falling blobs.

Plasma condensation after eruptive flares can produce similar phenomena, although the physical parameters may differ, from higher mass loading to more accelerated cooling. Recently, Song et al. (2016) measured dark flows of different widths in *AIA/SDO* observations following X-class flares. Such flows can be seen as late as ~ 4 hours after the flare, but the lifetimes of an individual flow is ~ 10 minutes. On-disk flare-driven coronal rain was investigated by Scullion et al. (2016) using the CRISP Imaging Spectro-Polarimeter (CRISP: Scharmer et al., 2008), located at the Swedish 1m Solar Telescope (SST: Scharmer et al., 2003). They follow the evolution of the evaporated plasma and measure the subsequent catastrophic cooling rate, finding multi-thermal and multi-stranded flows along the newly formed post-flare arcade. Their observed rain is however a very short lived phenomenon, although they note that flows sometimes follow the same paths.

Also using *IRIS*, Kleint et al. (2014) found bursty supersonic downflows of $\sim 200 \text{ km s}^{-1}$ associated with bright-points at the edge of the sunspot umbra. No lag between the different chromospheric and transition region wavelengths was observed and the profiles presented by them have the same large redshift, but the duration is only $\sim 20 \text{ s}$.

Li et al. (2017b) observed downflow threads near the footpoint of a filament in the pre-eruptions phase. These threads show a more continuous flow compared to the more blob-like structure of coronal rain and are the result of the draining effect accompanying the slow filament rises, and are considered a precursor to its eruption.

Here we study the Mg II and other lines from *IRIS* in order to constrain the physical nature of the unusually broad lines associated with raining plasma. The various observed parameters, when judiciously combined with the results of Jing et al. (2016), constrain the nature of the raining plasma and its origins more tightly than has been achieved in the past. The primary lines of interest here are listed in Table 5.1.

Being a consequence of still debatable mechanisms by which mass and energy are transported into the solar corona, there are many outstanding questions concerning coronal rain. In what follows we focus upon extracting as much information as possible from the *IRIS* data to study the origins of the cool material arising from the flare, and its remarkable thermal

Table 5.1: Atomic transitions of interest

Ion	λ Å	upper level	lower level	gf	$\Upsilon(T_e)$
Mg II	2802.705	$3p\ ^2P_{1/2}^o$	$3s\ ^2S_{1/2}$	0.64	5.6
	2795.528	$3p\ ^2P_{3/2}^o$	$3s\ ^2S_{1/2}$	1.3	12.3
	2790.777	$3d\ ^2D_{3/2}$	$3p\ ^2P_{1/2}^o$	1.9	9.1
	2797.930	$3d\ ^2D_{3/2}$	$3p\ ^2P_{3/2}^o$	0.39	4.8
	2797.998	$3d\ ^2D_{5/2}$	$3p\ ^2P_{3/2}^o$	3.5	18.3
	...	$3d\ ^2D_{5/2}$	$3p\ ^2P_{1/2}^o$...	2.5
	...	$3d\ ^2D_{3/2}$	$3s\ ^2S_{1/2}$...	1.2
	...	$3d\ ^2D_{5/2}$	$3s\ ^2S_{1/2}$...	1.8
C II	1334.5323	$2s^22p\ ^2D_{3/2}$	$2s^22p\ ^2P_{1/2}^o$	0.26	1.4
	1335.6625	$2s^22p\ ^2D_{3/2}$	$2s^22p\ ^2P_{3/2}^o$	0.051	0.9
	1335.7077	$2s^22p\ ^2D_{5/2}$	$2s^22p\ ^2P_{3/2}^o$	0.46	2.9
	...	$2s^22p\ ^2D_{5/2}$	$2s^22p\ ^2P_{1/2}^o$...	0.5
Si IV	1402.77	$3p\ ^2P_{1/2}^o$	$3s\ ^2P_{1/2}$	0.54	7.3

Data are from the NIST spectroscopic database (Kramida et al., 2015), wavelengths above 2000 Å are in air, otherwise they are in vacuum. Collisional data are from Sigut and Pradhan (1995); Blum and Pradhan (1992); Zhang et al. (1990). The Maxwellian-averaged collision strengths $\Upsilon(T_e)$ are given for $T_e = 10^4$ K for the singly charged ions, and at $T = 10^5$ K for Si IV.

structure. Post-flare chromospheric spectra have been obtained for decades in lines such as $H\alpha$ and Ca II H and K . The Mg II data analysed here have advantages: compared to $H\alpha$ the line emissivities and opacities are more simply related to thermal properties of the emitting plasma (discussed below), and compared to the H and K lines, the higher abundance of Mg gives rise to a profile more sensitive to changes in the density structure of the chromosphere.

We study five Mg II lines (two of which are blended); collectively they are sensitive to different thermal conditions and heights in the solar atmosphere. Thus, we can perform a simple quantitative analysis of the data with minimal assumptions. Our work complements much recent work (e.g. Antolin et al., 2015; Jing et al., 2016) which studies broad- or narrow-band imaging, by analysing the behaviour of line profiles. These profiles differ so dramatically from those previously modelled using existing numerical methods, that we adopt analytical methods. This work should later inspire further numerical simulations, such as that of Fang et al. (2013), which might attempt to better understand the origin of the enormous linewidths spanning over 300 km s^{-1} , pointing to energetic magnetic waves or (less likely) turbulence as the culprit.

5.2. Observations

On 11 March 2015, the *IRIS* instrument acquired data of AR NOAA 12297 during a flare watch campaign. Data were downlinked from nine spectral windows. Here we analyse those containing the lines of Mg II, C II and Si IV, together with data obtained by *HMI/SDO*. The *IRIS* slit was moved sequentially and repeatedly to four positions offset by 0, 2, 4, 6'' in the E-W direction on the solar surface. A total of 1230 such pointings were acquired. We focus on data from exposures 110 to 490. Subsequent references to exposures refer to exposures after 110. At each slit position, spectral data with exposures of 4 seconds was acquired. To complete one cycle of 4 slit positions took ≈ 21 seconds. During the flare, the exposure times were decreased for the FUV wavelengths by an automatic flare-triggered mechanism, to prevent over-exposure, without affecting the total raster duration. The projected slit is 0.33'' wide. The spatial and

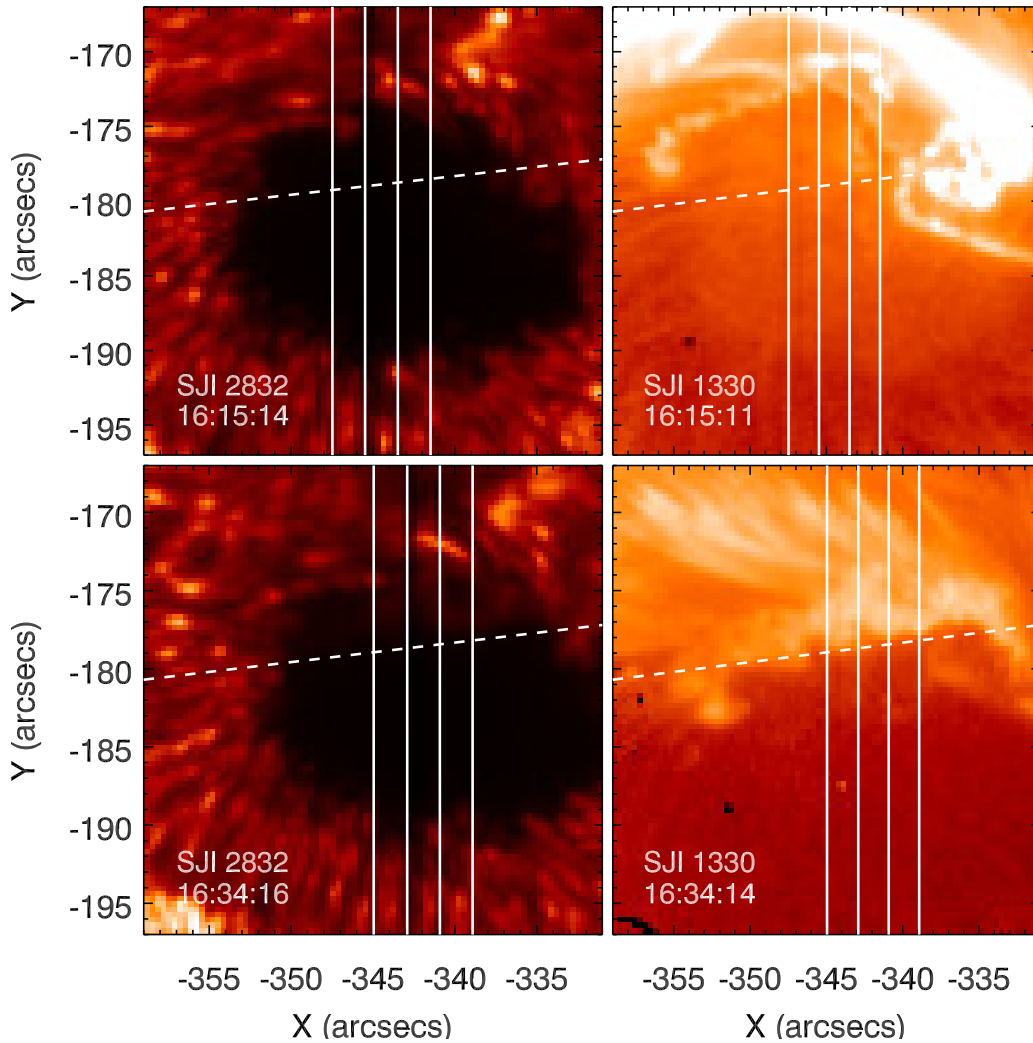


Figure 5.2: *IRIS* SJI images in the 2832 Å (left) and 1330 Å (right) channels, right before and after the impulsive phase of the March 11, 2015 X2.1 flare. A logarithmic scaling has been applied to SJI1330. The vertical lines are the positions of the *IRIS* slits during the observation and the oblique dashed line is the lower boundary (in the N-S direction) of the peculiar spectra. Plasma flows can be seen above this dashed line in the SJI 1330 post-flare images.

spectral samplings were $0.33''/\text{pixel}$ and $0.05092 \text{ \AA}/\text{pixel}$ for the NUV region. For the FUV regions the spectral sampling was $0.02544 \text{ \AA}/\text{pixel}$ (FUV2) and $0.02596 \text{ \AA}/\text{pixel}$ (FUV1).

IRIS slit-jaw images (SJI) at 1330, 1400 and 2832 Å were also acquired during the raster steps 0, 3, and 1 respectively. Each SJI set had a temporal sampling of 20.76 seconds on average, and spatial sampling of $0.33''/\text{pixel}$, spanning a total field of view (FOV) of $126'' \times 119''$. Figure 5.2 shows the SJI images in two of the *IRIS* channels and highlights the position of the slits and the locations of the observed peculiar profiles.

To correct for residual spacecraft orbital variations present in the spectral data, we applied `iris_orbitvar_corr_l2s.pro`, a routine in the *IRIS* SolarSoft package. We then followed the procedure in Liu et al. (2015b) to obtain wavelength-integrated emission-line intensities in physical units (see Table 5.2), which refer to the obvious components in emission above the photospheric absorption line and continua. More information on the flare can be found in Section 4.2 and the calibrations applied to the *IRIS* data can be found in Chapter 2. For comparison we include the values for a quiet sun (QS) patch outside the active region along with those from a representative position within the peculiar spectrum region at different time instances. These values are the sum over both line core and extended red-shifted profile,

Table 5.2: Observed frequency-integrated emission-line intensity ($\text{erg s}^{-1} \text{cm}^{-2} \text{sr}^{-1}$).

Multiplet	Mg II $h + k$	Mg II $3d - 3p$	C II 1334	Si IV 1403
Phase			+1335	
QS	5.36×10^5	...	6070	572
Pre-flare	1.83×10^6	...	5.16×10^4	2840
Impulse	4.36×10^7	$\approx 1.36 \times 10^7$	1.73×10^7	$> 3.86 \times 10^6$
Relax	2.77×10^7	4.81×10^6	4.39×10^6	3.51×10^5
Post-flare	1.82×10^7	$\approx 4.51 \times 10^5$	1.45×10^6	2.04×10^5

Quiet Sun data are from the darkest regions along the *IRIS* slit. We used calibration factors returned by `iris_get_response.pro`: `dn2phot_sg = 4.0` (FUV) and 18.0 (NUV), and effective areas of 0.474, 1.042 and 0.23 cm^2 for the 1335, 1400 and 2800 Å wavelengths, respectively. The intensities in **boldface** will be used throughout this article.

including multiple lines where they are present. All velocities are determined relative to the average quiet Sun spectrum.

The flare appears to have been triggered by the accelerated rise of a filament starting near 16:13 UT. Flare emissions started at 16:16 UT, the flaring reaching the emission maxima at 16:20 UT. This maximum high energy flare emission, as observed by *RHESSI*, was located at $(X,Y)=(-354,-171)''$, a region not covered by the spectral slit positions.

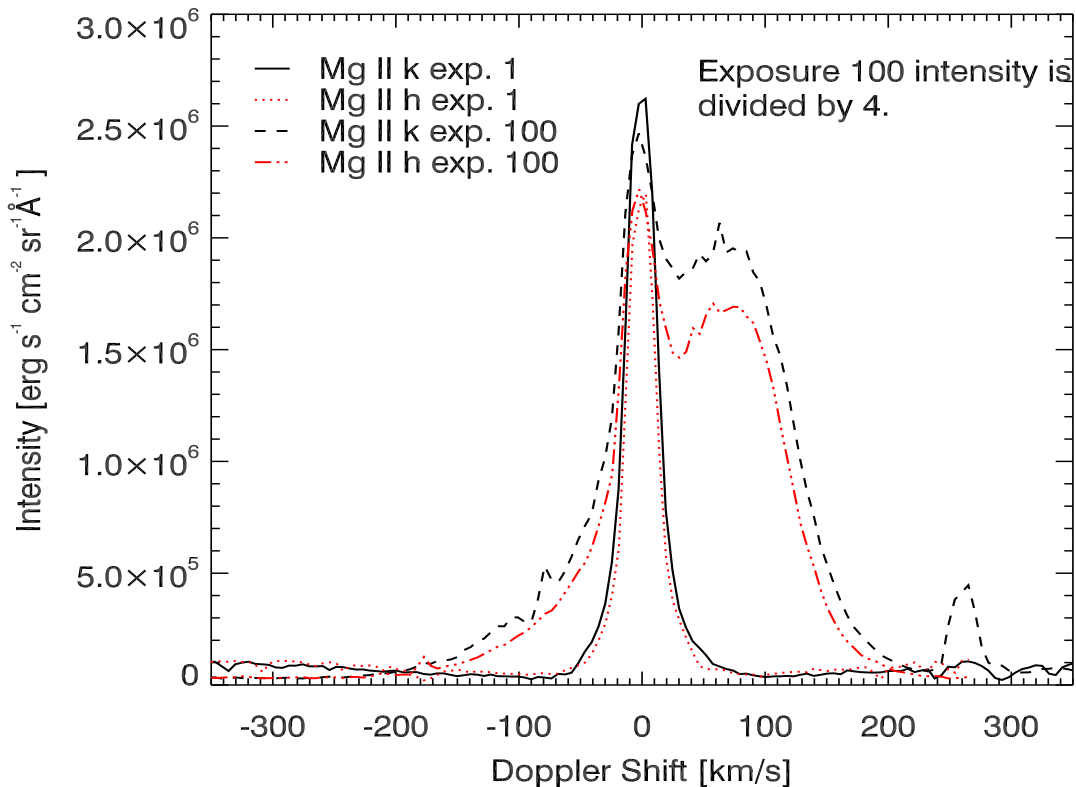


Figure 5.3: Typical intensity profiles of the Mg II h and k lines are shown as a function of Doppler shift, for the positions indicated by arrows in Figure 5.1. The two profiles shown are those for 15:57:51 UT (exp. 1), from the pre-flare phase, and those for 16:32:31 UT (exp. 100), from the post-flare phase, respectively. The very broad profiles seen during the later exposure are the focus of the present work.

For convenience, in Figure 5.1, we identify four episodes in the evolution of the Mg II: a pre-flare phase (before 16:20 UT); an impulsive phase (16:21 UT); a relaxation phase (16:21 to 16:27 UT); a post-flare (PF) phase (16:25 UT to beyond 17:00 UT). The PF phase is the

subject of the present paper. These phases are self-evident in the data. The relaxation phase is simply the transient response of the line profiles to the sudden release of energy in the impulsive phase, judging by the time scale of the decay which seems appropriate. The chromosphere has a thickness of ≈ 1500 km, and pressure perturbations (shocks) will propagate a little above the sound speed of $\approx 7 - 10$ km s $^{-1}$. A few sound crossing times corresponds to about 5 minutes. The relaxation phase is most clearly seen in the narrow $3d - 3p$ lines of Mg II, close to 2791 and 2798 Å in this figure. The h and k resonance lines of Mg II are at 2796.3 and 2803.5 Å.

Intensity profiles of the Mg II h and k lines are shown in Figure 5.3. Representative data of interest here are from exposure number 100 in our sample obtained at 16:32:31 UT. In the figure these are shown as dashed lines. The time dependence of these profiles is shown in Figure 5.1. The *IRIS* instrument's compensation for the Sun's average rotation was used, so that the profiles show the changing conditions over approximately the same areas of the Sun.

We examine the evolution of the spectra at different locations along the flare ribbon. We found locations of extended very broad and redshifted emission at the same locations swept over by the evolving and propagating flare ribbon, lasting for more than an hour after the flaring event. To highlight typical Doppler shifts and line widths, in Figure 5.4 we show the first velocity-weighted moment (Doppler shift) and second moment (line width) of the Mg II k -line, normalized to the zeroth moment (see Section 2.1.3). Only data for the first slit position is presented, while the same behaviour is present at all slit position, with slight variations in the size of the peculiar emission region. In passing, we note that the smaller amplitude blue-shifts in the sunspot umbra probably correspond to umbral flashes (e.g. Bard and Carlsson, 2010).

To highlight the evolution of the line width over the whole region of interest, we represented the normalized intensity of the profile as a function of the line width in Figure 5.5, along with an insert of the same dependence for a quiet sun patch outside the active region. The colour represents the time of the exposure, with early times being masked by later emission. The QS distribution is centred around 400 mÅ and shows little scatter. The distribution for the peculiar emission region is centred around 500 mÅ before the flare and it shows an increase in both intensity and line width after the flare. The intensity decreases in time to pre-flare values, while the width still has an extended tail up to about 1100 mÅ suggesting that the raining phenomenon is still ongoing.

Figure 5.6 shows the position of the four *IRIS* slits projected onto an image constructed from data from the *HMI/SDO* instrument. The *HMI* data are the standard reductions of the 720s product, including vector magnetic field data. The field azimuth in the plane perpendicular to the line of sight (LOS) has not been disambiguated. Note that the four slit positions extend across the entire sunspot centred near $(X,Y)=(-340,-182)''$. The broadened profiles are found above the penumbra, they are marked as the solid components of the dashed lines shown in the figure. The lengths and positions of these lines correspond to the average locations where the anomalously broad profiles occur. These regions are quite separate from the magnetic neutral line. Instead, they lie above regions of modest LOS field and large perpendicular field, whose direction follows parallel or anti-parallel to the axis of a “dark intrusion” (Figure 5.6) centred at $(X,Y)=(-343,-176)''$, a location of where systematic upward-directed photospheric motions of $\approx 1-1.5$ km s $^{-1}$ are present (but not shown here).

Profiles of C II resonance lines near 1335 Å show similar spectral line shapes to h and k , as does the 1403 Å line of Si IV. Both lines are slightly broader (in Doppler units) than the h and k lines. However, the duration of the broad PF profiles in both cases are appreciably shorter. The intensities of these lines are also 10-100× smaller than h and k (Table 5.2). A possible explanation is that the raining plasma cools past the temperatures needed to excite emission in these lines or that the emission is too faint to be clearly distinguished from the generally brighter background of these lines.

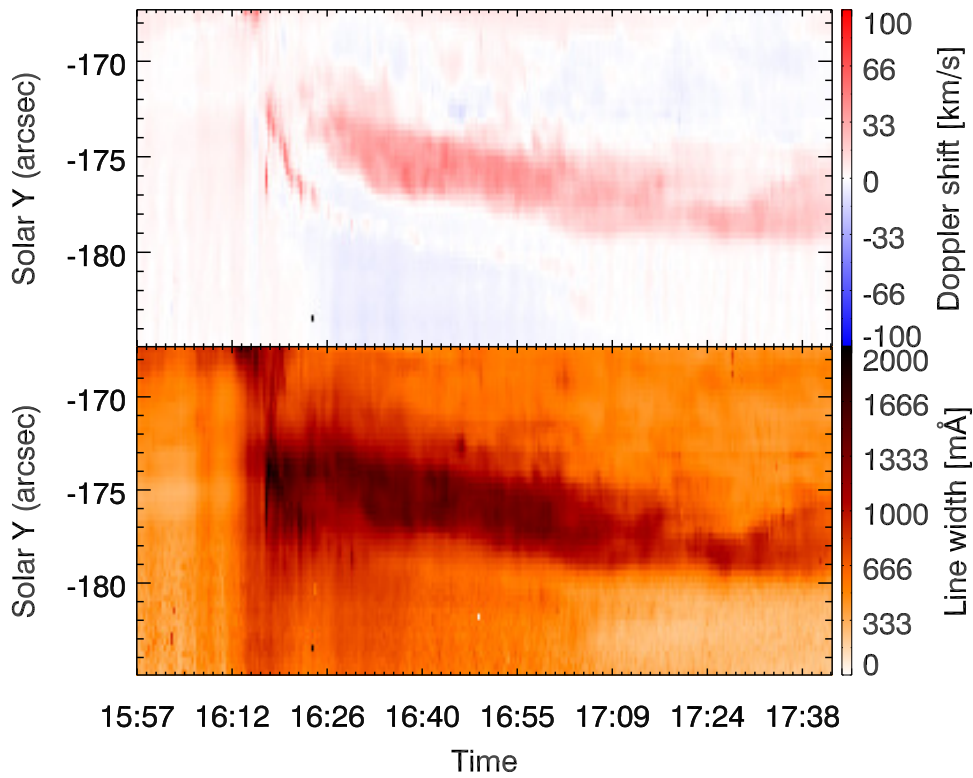


Figure 5.4: Doppler shift (top) and line widths (bottom) maps for the Mg II k-line, showing the temporal evolution of the extended redshifted emission for the first slit position. The peculiar emission appears originate from the same region that was swept by the flare ribbon during the impulsive phase. Positive Doppler shift values refer to red shift and negative values to blue shift.

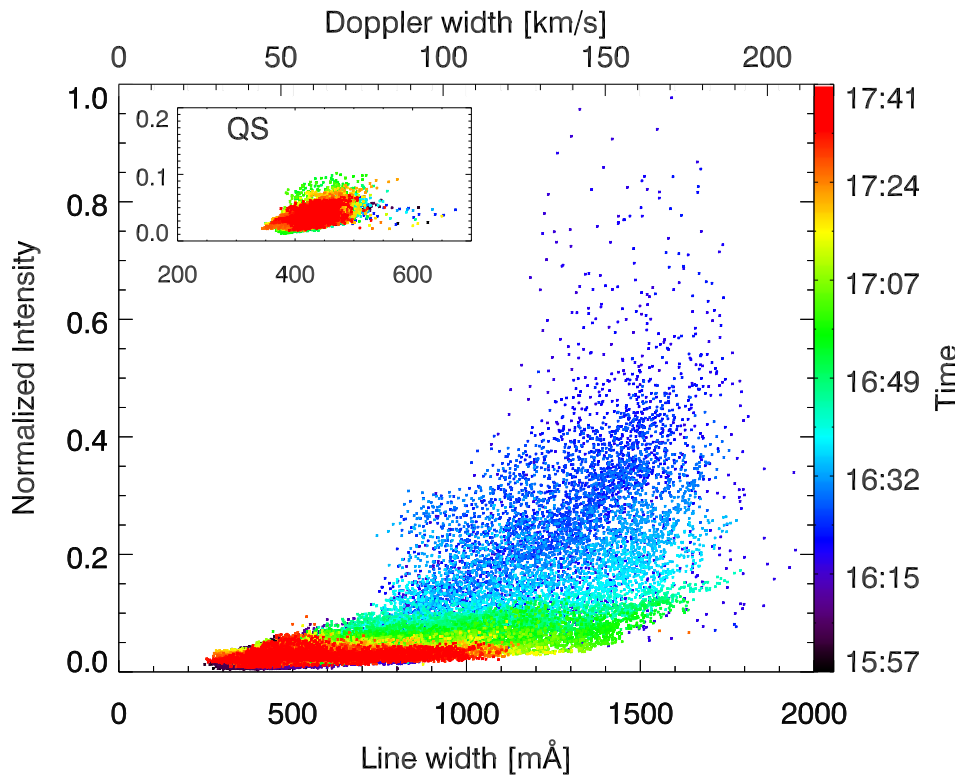


Figure 5.5: Normalized Intensity vs. line width correlation for all the pixels between $-170''$ and $-180''$. The color represents the time of the observation and the insert represents the data from a QS patch outside the active region.

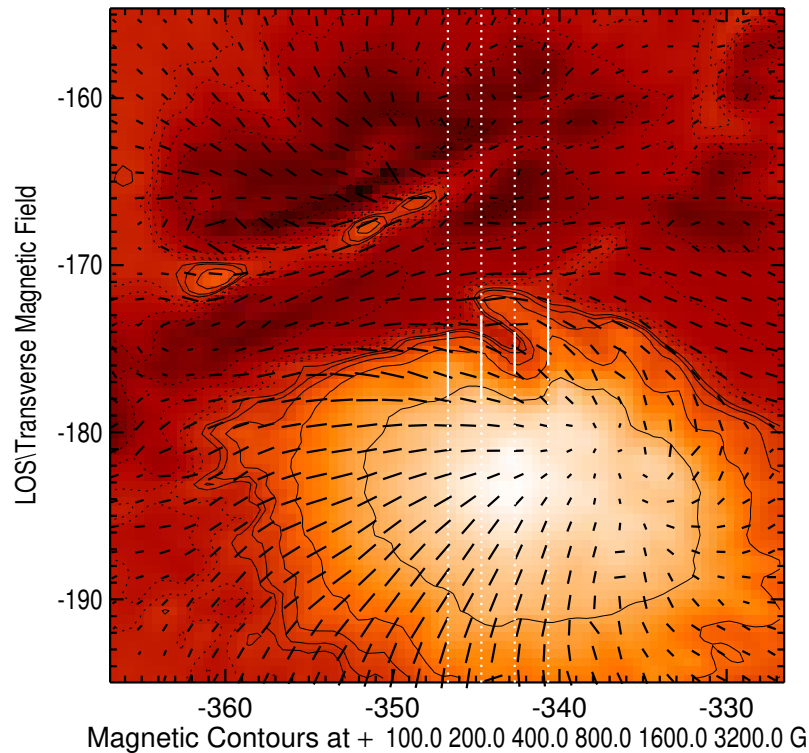


Figure 5.6: Vector magnetic field parameters at 16:24 UT. The vertical dashed lines show the positions of the IRIS slit, the solid portion of which approximately shows the extent of very broad lines seen in the Mg II h and k lines shown in previous figures.

5.3. Analysis

In the following analysis we focus only on the “postflare” (PF) phase, since these profiles are yet unexplained. The spatial and temporal behaviour of the broad PF profiles appears to be unrelated to other phases (see Figure 5.1). They are most readily interpreted as simple (unreversed) emission superposed onto the more “normal” profile represented by exposure 1 shown in Figure 5.3.

5.3.1. Summary of observed properties

The observed Mg II k and h profiles have several salient features during the PF phase:

- (1) the integrated intensities originating from the broad profiles are larger than the core intensities, and the time variations are largely independent of the core intensities, which remain more or less constant;
- (2) the PF k and h line intensities are remarkably smooth across the line profile at each time of observation, but they change slightly between exposures, decreasing in both intensity and shift;
- (3) the integrated intensities of the resonance lines are in the ratio $k:h = 1.15$ across almost the entire extent of the line profiles (see Figure 5.3);
- (4) the lines are far broader than the net redshift;
- (5) the PF emission originates from relatively small patches $\approx 4 - 5$ Mm in the penumbral region of the sunspot;
- (6) in both the k and h lines the bright PF profiles begin abruptly 6 – 7 minutes after the impulsive phase of the flare (see Figures 5.1 and 5.4);
- (7) the broad components show no obvious self-reversal;
- (8) the profiles are very similar across all regions sampled by the spectrometer’s slit.

It is interesting to relate these profiles to the other Mg II lines. The PF $3d - 3p$ transitions of the subordinate triplet lines are far weaker than during the impulsive and relaxation phases,

compared with the k and h lines ($3p - 3s$). This low emission suggests that the temperature has decreased and little energy goes into increasing the population of the $3d$ level. To the above points we also add:

- (9) the k and h lines, and those of Si IV and C II all have widths in Doppler units of about $w = 100 \text{ km s}^{-1}$, and the line centroids are red-shifted by about $+60 \text{ km s}^{-1}$, as inferred from Figures 5.4 and 5.5.

Point (1) implies that the *PF profiles are not caused by scattering of bright photons away from the core*. Regarding point (3), optically thin conditions will produce ratios of intensities of 2:1. Hence the PF plasma is *optically thick in the k and h lines*. Remarkably, the same is true for the 1334/1335 ratio of the C II lines whose intensities are close to 1:1, compared to the optically thin ratio of 1:2. Point (2) suggests that the unresolved motions are physically *much* smaller than resolvable scales. Points (4) and (8) suggest that, if the opacity broadening of the line is negligible, there is *more energy involved in unresolved motions (widths) than in resolved motions (shifts)*. Photon scattering can, however, both broaden and shift the lines, aspects that will be discussed below in detail. We use as reference the integrated intensities of the various lines, at the different phases, as listed in Table 5.2.

5.3.2. A reference model

We examine the PF profiles using parameters in a reference model of the emitting plasma. We will assume that the plasma exists in thin strands with a width $W \approx 100 \text{ km}$ (Jing et al., 2016), that has a number densities of hydrogen nuclei n_H close to 10^{12} particles per cm^3 , and that these particles are all at temperatures of $\approx 10^4 \text{ K}$. The temperature assumption is based on the fact that if T_e exceeds $2 - 3 \times 10^4 \text{ K}$, Mg becomes doubly ionized, thus decreasing the emission in the k and h lines. The justification for the adopted density is weak. It exceeds that at the very top of the pre-flare chromosphere by an order of magnitude, but this assumption is reasonable as in flare models mass is propelled from deeper layers of the chromosphere higher into the corona, on time scales of a minute or less for M and X class events. (e.g. Abbett and Hawley, 1999; Allred et al., 2005).

If we assume that in the case of an X-class flare the energy flux directed towards the chromosphere is $\approx 10^{11} \text{ erg cm}^{-2} \text{ s}^{-1}$, then the mass per unit of ejected material is expected to be about $m = 10^{-2} F_{11} \text{ g cm}^{-2}$, estimated based on the last panels of Figures 3 and 5 of Allred et al. (2005). Here F_{11} is the downward-directed energy flux in units of $10^{11} \text{ erg cm}^{-2} \text{ s}^{-1}$. If this mass is spread uniformly along a tube of constant cross-section with length L , then the number density on average is $\approx m/\mu m_H L$, where $\mu = 1.36$ is the mean atomic weight of the largely neutral pre-flare plasma and m_H is the mass of the hydrogen atom. With $L = 10^9 L_{10} \text{ cm}$ and $L_{10} = 1$ corresponding to 10 Mm, we have:

$$n_H \approx 5 \times 10^{12} L_{10}^{-1} F_{11} \text{ cm}^{-3} \quad (5.1)$$

Assuming $L_{10} \approx 5$, corresponding to one coronal pressure scale height, and that the material is ejected along flux tubes of this length or longer, we construct a crude justification for our adopted estimate of $n_H = 10^{12} \text{ cm}^{-3}$ for the raining plasma after this X2 class flare.

We use variables normalized to the average values: $W = 10^7 W_{100} \text{ cm}$, $n = 10^{12} n_{12} \text{ cm}^{-3}$, and $T = 10^4 T_{e4} \text{ K}$. We will also assume that the unresolved “microturbulent” velocities are of order $\xi = 10 \xi_{10} \text{ km s}^{-1}$, with $\xi_{10} = 1$, which is of order the sound speed at $T_4 = 1$. In this reference model, $W_{100} = n_{12} = T_{e4} = \xi_{10} = 1$. Note that the observed line widths are $w = \xi = 100 \text{ km s}^{-1}$, ten times broader than the reference width, for reasons we will discuss in detail in the ensuing sections¹.

This model is used below to explore conditions under which these lines might form, understanding that the chosen values are only educated guesses. We consider the formation

¹ We will conclude that $\xi_{10} \approx 10$ will characterize our final choice of best parameters.

of the Mg II lines in a structure that consists of an array of strands that comprise an episode of coronal rain. Thus we look first at the spectrum emitted by one elemental strand of width $W_{100} = 1$.

5.3.3. Strand optical depths

Two observational details hint that the optical depth of the k line across the emitting strands is $\gtrsim 1$, at line centre. Firstly, the emission is self-excited within the raining plasma itself, i.e. there is no identifiable dominant external source of irradiation. Secondly, the $k:h$ line ratios are far from the optically thin ratio of 2:1 (Figure 5.3). We consider a simplified model of the Mg II ion, with level 1 being the ground level and level 2 and level 3 the upper levels of the h and k transitions, respectively. We only discuss the Mg II k line, but the same argument follows for the h line.

The efficiency of energy removal from the beam is given by the total cross-section (e.g. [Mihalas, 1978](#), Chap. 4)

$$\sigma = \frac{\pi e^2}{m_e c} \quad (5.2)$$

where m_e is the electron mass, e is the elementary charge and c is the speed of light. As the above cross-section is based on the classical atom and electromagnetic field approximations, it only describes correctly very strong lines. An additional coefficient is usually added based on the quantum mechanical approach, namely the oscillator strength of the transition f , that gives the ‘effective number’ of classical oscillators involved in the considered transition.

Thus the opacity at line centre (in units of cm^{-1}) for the transition between levels 1 and 3 is given by

$$\kappa_0 = \frac{\pi e^2}{m_e c} f n_1 / \Delta\nu = 0.0264 n_1 f / \Delta\nu \quad (5.3)$$

where n_1 is the number density of absorbers, Mg II ions in the ground level in the present case, and $\Delta\nu$ is the Doppler width of the line in Hz. The $0.0264 \text{ cm}^{-1} \text{ Hz}$ value is also known as the extinction coefficient per particle. Then, the optical depth across a strand of width W , whose axis has an angle ϑ with the line-of-sight is given by:

$$\tau_0 = \kappa_0 \frac{W}{\cos \vartheta} = 0.0264 \frac{n_1 f W}{\mu \Delta\nu}, \quad \mu = \cos \vartheta \quad (5.4)$$

Let us assume that most Mg atoms in the strands are in the ground state of Mg II, then, considering the logarithmic abundance of Mg of relative to hydrogen to be 7.42 ([Allen, 1973](#)), we have $n_1 = n_H \times 10^{7.42-12} = 3 \times 10^6 n_{12} \text{ cm}^{-3}$. Considering a Doppler width ξ of 10 km s^{-1} , $\Delta\nu \approx 3.6 \times 10^{10} \xi_{10} \text{ Hz}$, and the oscillator strength for k line, $f = 0.6$, then

$$\kappa_0 = 1.1 \times 10^{-5} n_{12} / \xi_{10} \text{ cm}^{-1} \quad (5.5)$$

With $W_{100} = W/100 \text{ km}$ we have

$$\tau_0 = 110 \frac{n_{12} W_{100}}{\xi_{10} \mu}. \quad (5.6)$$

The condition that $\tau_0 \gg 1$ appears to be satisfied and, in this reference model, both the k and h lines have $\tau_0 \approx 10^2$ across the strands.

However, the observation that the $k:h$ ratio in the PF profile is 1.15, far from the thin ratio of 2:1, has two possible explanations. The first is that the lines might be *effectively thick*, a condition that is true for the Mg II k and h lines formed in the stratified chromosphere (e.g. [Linsky and Ayres, 1978](#)) causing the Sun’s $k:h$ ratio from various non-flaring regions on the Sun to be close to 1.1-1.5 (e.g. [Staath and Lemaire, 1995](#); [Kerr et al., 2015](#)). The second possibility is that the radiation emerging from the strands is anisotropic, and that the k and h lines have different anisotropy under conditions of modest optical depth.

The latter case seems far more likely, as can be seen by comparing the escape probability of line photons from the strand core with their destruction probability. In Section 5.3.4 we show that the absorption of Mg II photons by background continuum is negligible in the reference model. The probability of destruction by collisions from the k line can be evaluated simply as the ratio

$$\varepsilon = \frac{C_{31}}{A_{31} + C_{31}} \quad (5.7)$$

In the above relation C_{31} is the collision de-excitation rate from level 3 to level 1, the dominant collision rate out of the line's upper level (level 3), and A_{31} is the Einstein coefficient for spontaneous radiative emission (Allen, 1973; Gabriel and Jordan, 1971):

$$A_{31} = 0.6670 \times 10^8 g f / g_3 \lambda^2 \quad \text{and} \quad C_{31} = 8.63 \times 10^{-6} \Upsilon(T_e) / g_3 \sqrt{T_e} \quad (5.8)$$

where 8.63 is from Maxwellian integration of cross sections over all thermal speeds making Υ a function of T_e only and g_3 is the statistical weight of the upper energy level. Using parameters from Table 5.1 we find

$$A_{31} = 2.7 \times 10^8 s^{-1} \quad \text{and} \quad C_{31} \approx 4 \times 10^4 n_{e12} T_{e4}^{-1/2} s^{-1} \quad (5.9)$$

Here we must use the electron density n_{e12} because electrons are responsible for the bulk of the collisions. The destruction probability is then

$$\varepsilon \approx \frac{C_{31}}{A_{31} + C_{31}} \approx 10^{-4} n_{e12} / \sqrt{T_{e4}}. \quad (5.10)$$

The electron density of raining material is determined by the hydrogen nuclei density n_H primarily through the electron temperature T_e when the temperature $T_e \gtrsim 10^4$ K, as we will find below. Then $n_e \approx n_H$.

A reasonable approximation for escape probability P_{esc} for resonance lines is

$$P_{esc} \approx \frac{1 - \exp(-\tau_0)}{\tau_0} \quad (5.11)$$

(e.g. Frisch, 1984), so that in the reference model for the k line, using equation (5.6) we obtain

$$P_{esc}/\varepsilon \approx \frac{10^2 \xi_{10} \mu \sqrt{T_{e4}}}{n_{e12} n_{12} W_{100}}. \quad (5.12)$$

It seems $P_{esc} \gg \varepsilon$ for reasonable physical parameters.

Together with the observation that the broad profiles are not self-reversed, we conclude that the lines are likely effectively thin in the coronal rain.

5.3.4. Background opacities near 2800 Å

For absorption in the background continuum with opacity κ_C , effectively thick conditions prevail when

$$P_{esc} < \kappa_C / \kappa_0. \quad (5.13)$$

At 2800 Å, the dominant source of continuous opacity within the strands is probably the Balmer continuum of hydrogen. This can be computed approximately assuming that the $n = 2$ levels of hydrogen are populated not too far from LTE relative to the proton density n_p , because the radiation temperature in the Balmer continuum (≈ 6000 K) and the electron temperature are within a factor of two or so. Then

$$\kappa_C = n_2 \sigma \approx \frac{n_2^*}{n_p^*} n_p \sigma \quad (5.14)$$

Let n_e be the electron number density in cm^{-3} and T_e the electron temperature in K. Then

with the LTE number densities ratio (Mihalas, 1978)

$$\frac{n_2^*}{n_p^*} = 2.07 \times 10^{-16} n_e \frac{g_2}{g_p} T_e^{-3/2} \exp\left(\frac{I_2}{k_B T_e}\right), \quad (5.15)$$

using the energy difference to the continuum $I_2 = 3.399$ eV, scaled values for the electron density and temperature $n_{e12} = n_e/10^{12}$ cm⁻³, $T_{e4} = T_e/10^4$ K, and considering the cross-section $\sigma \approx 10^{-17}$ cm² (Allen, 1973), the continuum opacity becomes

$$\kappa_C \approx 1.7 \times 10^{-14} n_{e12} T_{e4}^{-3/2} \exp(3.945/T_{e4}) n_{p12} \quad (5.16)$$

By further assuming $n_p \approx n_e$ and dropping subscripts p, e for convenience, we find

$$\kappa_C/\kappa_0 \approx 2.5 \times 10^{-9} n_{12} \exp(3.945/T_4) \xi_{10}/T_4^{3/2} \quad (5.17)$$

Given equation (5.5), this ratio would need to be higher than the escape probability, computed in the previous section to be ≈ 0.01 , for the line to be effectively thick due to background continuum absorption. If we set extreme density and temperature conditions (photosphere-like) of $n_{12} \approx 10^1$ and $T_4 \approx 0.5$, respectively, we can obtain a ratio of 7×10^{-5} , as an upper limit, which is orders of magnitude lower than the required value.

Therefore we can safely ignore continuum absorption at 2800 Å in the coronal rain.

5.3.5. $k:h$ ratio and radiation anisotropy

How can *radiation anisotropy* explain the line ratios in the rain phenomenon? The lines of h and k differ in opacity by a factor of two. We can imagine a simple case of cylindrical strands where the optical depth of h is $\approx 1/2$, and that of k is ≈ 1 . The h line photons can escape directly from deeper within the strand than the k line photons. In essence, the h line will radiate more isotropically from the core of the strand, whereas k photons will scatter preferentially into the path of shortest escape, i.e. perpendicularly to the main axis of the strand. The observed line ratio will change from 2 : 1 even if the total emission into all directions is in the ratio 2:1. We would expect $k:h > 2:1$ perpendicular to the strand's main axis of symmetry, and $k:h < 2:1$ in other directions. Figure 5.7 shows a small strand section with ellipses denoting the photon escape layer for the Mg II k and h lines.

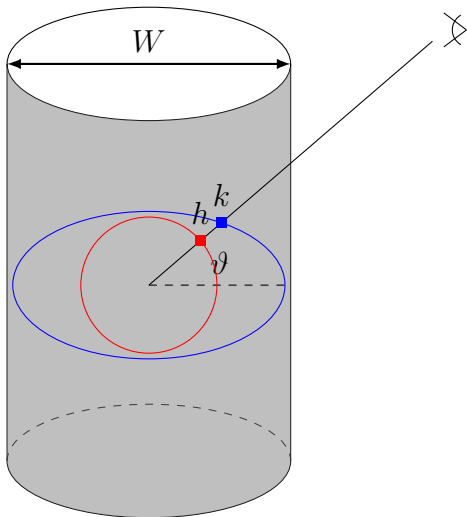


Figure 5.7: Schematic for anisotropic emission for the Mg II k and h lines. Given a strand of width W , the h line (red) will emit isotropically from deeper in the strand, while the k line (blue) emits preferentially perpendicular to the strand. Based on the observer direction, given by an angle ϑ , the intensity of the resonance lines will vary, therefore the $k:h$ will change with the angle ϑ .

If the optical depths are substantially higher ($\tau_0(k) \approx 10$, say), then the differential effect is reduced to the outermost cylinders comprising the strand (assuming it is a cylinder, cf. Lipartito et al., 2014), the radiation being more isotropic in the opaque deeper core of the strand.

We conclude that we are seeing the strands at a slant angle far from 90° and 0° to the strand's main axis, and that τ_0 should be > 1 but less than ≈ 10 in the k line, in these strands. The value of 110 computed from our reference calculation lies close to the necessary optical depth, when we note that the nearest boundary of the strand for escape is at a distance of at most

$W/2$ not W , and, as we will argue below, ξ_{10} is an underestimate by a factor of ten, thus the k line core photons will see a boundary $\lesssim 6$ photon mean free paths distant.

Related to this problem is the effect of *atomic polarization* when scattering dominates the source function ($\varepsilon \ll 1$). The $J = 1/2$ upper level of h is not polarizable, and the scattered intensity of the $J = 1/2 \rightarrow J = 1/2$ transition (h line) is isotropic. However, the polarizable $J = 3/2$ upper level's *atomic polarization* can change the observed *intensity* ratios under conditions of anisotropy even by the “diffuse” photons self-generated within the cylinder (Landi Degl'Innocenti and Landolfi, 2004). We estimated these effects to be small, a few percent, using calculations similar to those applied to He I lines by Judge et al. (2015).

5.3.6. Frequency-integrated intensities

If a line is *effectively thin* across an emitting strand, the emission is simply the sum of the emission along the line-of-sight. To an accuracy of a factor of two, we can ignore the anisotropy, and we find, for the k line, the thin intensity in units $\text{erg s}^{-1} \text{cm}^{-2} \text{sr}^{-1}$

$$I_{thin} \approx \frac{h\nu_{31}}{4\pi} n_1 C_{13} \frac{W}{\mu} = \frac{hc}{4\pi\lambda_{13}} n_1 C_{13} \frac{W}{\mu} \quad (5.18)$$

where h is Planck's constant, ν_{31} is the transition frequency, and λ_{13} is the wavelength of the transition. C_{13} is the collisional excitation rate from the ground level to the line's upper level (Gabriel and Jordan, 1971; Burgess and Tully, 1992) and is related to the collisional de-excitation by an Einstein relation (see equation (1.11)), where n_i is the population of the given energy level and k_B is Boltzmann's constant. Thus

$$C_{13} = C_{31} \frac{n_3}{n_1} = C_{31} \frac{g_3}{g_1} \exp\left(\frac{-hc}{\lambda_{13} k_B T_e}\right) \quad (5.19)$$

Substituting this back into equation (5.18) we obtain

$$I_{thin} \approx \frac{hc}{4\pi\lambda_{13}} n_1 2 \frac{W}{\mu} n_{e12} C_{31} \frac{g_3}{g_1} \exp\left(\frac{-hc}{\lambda_{13} k_B T_e}\right) \quad (5.20)$$

Within a factor of 2 or so, we can set $\mu = 0.5$, and this expression gives, multiplying by two for the sum of the two lines,

$$I_{thin} \approx 1.4 \times 10^6 n_{12} n_{e12} \exp\left(4.86\left(1 - \frac{1}{T_{e4}}\right)\right) W_{100} \quad (5.21)$$

for our reference calculation. The observed intensities for both resonance lines are of the order of $1.6 \times 10^7 \text{ erg s}^{-1} \text{cm}^{-2} \text{sr}^{-1}$. With $T_{e4} = 2$ we find $I_{thin} \approx 1.1 \times 10^7 \text{ erg s}^{-1} \text{cm}^{-2} \text{sr}^{-1}$. We regard this as reasonable agreement with our adopted reference calculation, noting that the calculation depends exponentially on the choice of T_{e4} and on the product $n_{12} n_{e12}$. Furthermore, the computed intensity can also increase if we consider the strand to have a higher width or by allowing for the possibility that there is more than one such strand of emission along each line of sight observed by *IRIS*.

5.3.7. Doppler widths and shifts

The observed Doppler shifts of $50\text{-}60 \text{ km s}^{-1}$ are compatible with the acceleration of cool plasma elements due to gravity under free fall from a few Mm above the solar surface. But more interesting constraints come from the observed linewidths. We work in units of the Doppler broadening parameter, ξ . The observed lines are $\approx 10\times$ broader than our reference model can produce. Particle densities are far below those needed for significant collisional broadening. The obtained optical depth of 100 at the centre of the k line would produce photon emission only up to about $\xi_{10} \sqrt{\ln \tau_0} \approx 2.1 \xi_{10}$ from line centre, assuming complete redistribution and using an argument due to Osterbrock (1962), that beyond this value the width of the profile no longer increases and photons can directly escape in the inner wings after a limited number of

interactions.

It seems highly unlikely that photon scattering at high optical depths is the source of the broad line emission. The lack of a clear self-reversal near the cores of the PF broad profiles appears to suggest also that photon scattering is not a major contributor to the PF profile widths. It then follows that unresolved Doppler motions are responsible for the measured line widths, with values of $\xi_{10} \approx 100 \text{ km s}^{-1}$. With equation (5.6) we find that $\tau_0(k) \lesssim 10$ across each of the 100 km-wide strands.

We are forced to conclude that the lines are formed under conditions of modest optical depth, but in which the radiation is anisotropic. The broad Doppler-dominated emission widths are some $15 - 20\times$ the sound speed where Mg II emission usually forms ($T_e \lesssim 2 \times 10^4 \text{ K}$). Under these extreme conditions it is likely that shocks would quickly dissipate such small-scale motions, if they were purely hydrodynamic and small-scale. Thus, *magnetic fields are the most likely mechanism responsible for the unresolved motions*, by hosting largely transverse Alfvénic oscillations.

5.3.8. Mg II h and k and the $3d - 3p$ transitions

Unlike the $3p - 3s$ transitions, the $3d - 3p$ transitions, when in emission, are certainly not optically thick within the strands. The lower levels for the triplet transitions ($3p$) have a population of $\lesssim \exp(-4.86/T_{e4})$ times the lower level of the h and k lines ($3s$), thus the $3d - 3p$ optical depths are orders of magnitude smaller than those of the Mg II k and h lines. The observed triplet intensity ratios (of the blend of the 2797.930 and 2797.998 Å lines, relative to the 2790.930 Å line) are indeed close to the optically thin ratios of 2:1.

The $3d - 3p$ transitions differ from h and k in another essential way. Electron excitation to the $3d$ levels from the $3s$ ground level is optically forbidden. Thus, the cross sections are dominated by core penetration of the Mg+ ion by the incoming electrons. There is no long-range interaction. When the $3p$ level populations are far below the Boltzmann distribution relative to $3s$, as is the case when the lines are effectively thin (when the photon can escape in h and k emission reducing the $3p$ populations), collisional excitation of the $3d$ levels occurs predominantly only from the $3s$ ground level. Then, again neglecting possible anisotropies in the radiation field, the ratio between the triplet and resonance lines intensities is proportional to the ratio of their respective collisional excitation rates, as given by

$$\frac{I_{3d-3p}}{I_{3p-3s}} \approx \frac{C_{3s-3d}}{C_{3s-3p}} \quad (5.22)$$

which becomes

$$\frac{I_{3d-3p}}{I_{3p-3s}} \approx \frac{\Upsilon_{3s-3d}}{\Upsilon_{3s-3p}} \exp\left(-\frac{4.86}{T_{e4}}\right) \approx \frac{1}{6} \exp\left(-\frac{4.86}{T_{e4}}\right) \quad (5.23)$$

Inserting the observed ratio of $\approx 1/40$ (see Table 5.2) into equation (5.23), we find $T_{e4} \approx 2.5$, or ≈ 2.0 allowing for the radiation anisotropy in the k line.

We note that the work of [Pereira et al. \(2015\)](#) forces the formation of the $3d - 3p$ transitions into the much denser, lower chromosphere, through their choice of model atmosphere parameters. In their model, the h and k lines are already thermalized where the $3d - 3p$ transitions form, and so the $3d$ levels are populated largely through the two allowed transitions $3s - 3p$ followed by $3p - 3d$. This choice would make computing the above ratio more convoluted, as the triplet and resonance lines would no longer share the same ground level for the excitation.

5.3.9. Dielectronic recombination

The process of dielectronic recombination (DR) takes place when a positively charged ion collides with and captures a free electron and uses some of the newly available energy to promote one of its bound electron to a higher bound energy level, followed by the emission of a

photon corresponding to the doubly excited state. This process can lead to emission on the red side of resonance lines (e.g. [Gabriel and Jordan, 1971](#)).

In the case of Mg II, $3pnl$ states can form as intermediate states in a $\text{Mg}^+ 3s + e^-$ collision, process also called dielectronic capture. If the intermediate states decay radiatively to $3snl$ states emitting a $3p - 3s$ photon, called a “stabilizing transition”, the process is a dielectronic recombination. For singly charged ions, DR rates are typically some 10^{2-3} times smaller than the direct rate for collisional excitation. For $\text{Mg}^+ - e^-$ DR the results of [Altun et al. \(2006\)](#) yield a total rate of about 0.003 of the direct rate. Therefore, if the broad PF profiles were caused by a superposition of DR then their intensities would be some 10^{2-3} times smaller than that of the core emission. This is not observed in our data (see Figures [5.1](#) and [5.3](#)).

5.3.10. Sudden onset of post-flare coronal rain emission.

Inspection of Figure [5.1](#) shows that the PF profiles begin abruptly near 16:26 UT. They exhibit a two-fold rise in intensity across all wavelengths that takes between 2 and 3 time steps, say $t = 40$ seconds. Fast changes continue to be present throughout the PF phase in Figure [5.1](#), but with much smaller amplitudes.

These data are difficult to reconcile if we assume that the linewidths of the emitting plasmas arise from a mixture of LOS velocities on macroscopic scales. At a given slit position, various plasma elements would arrive at different times as they each follow their own trajectory along individual strands. Let us suppose that plasma is ejected into the corona from one or both flare footpoints. On their way to crossing the slit, they acquire various LOS velocities as a result of the (still unknown) dynamics in the post-flare tubes of magnetic flux. Depending on the trajectories, if one assumes that the PF line profiles are superpositions of macroscopic flows, then the elements will cross the slit with a broad distribution of arrival times. This is contrary to the observed profile behaviour. The short rise time $t \approx 40$ seconds across the entire profile implies that, if caused by different arrival times, the plasma elements would have to coordinate themselves such that 50 km s^{-1} upward moving plasma would “know” when to cross the slit as well as the 150 km s^{-1} downward moving plasma. Simply put, there would have to be a linear relationship between velocity and projected distance d from the slit,

$$v \cos \vartheta = d \cos \vartheta / t. \quad (5.24)$$

It does not make sense that the Sun would know about the special position of the *IRIS* slit in such a fashion, and coordinate the flows to produce the observed spectra.

What then is the cause of the two-fold rise in intensity across all wavelengths within $t = 40$ seconds? We can conceive of two explanations: (1) The rain plasma has small-scale motions (with a magnitude of $\approx 100 \text{ km s}^{-1}$) within a coherent large-scale flow, making $\xi_{10} \approx 10$, or alternatively (2) The plasma is indeed moving at a variety of macroscopic velocities, but that there is a special thermodynamic process making the plasma visible on a time scale of 40 seconds.

The second explanation can be discounted because the history of each plasma element determines whether lines of a certain element will become visible at a certain time. For example, if the raining plasma is unheated and is at densities close to 10^{12} cm^{-3} , the cooling time is of order of 10 seconds ([Anderson and Athay, 1989a](#)). At 100 km s^{-1} the plasma can travel $\approx 1 \text{ Mm}$ before it cools significantly. Again, we are faced with the untenable position that the *IRIS* slit would have to be a “special” place on the Sun for this explanation to hold water, when each element is evolving along its own trajectory. A sudden change in opacity is discounted because we know of no mechanism to suddenly reveal *only* the PF broad profiles at 16:26 UT.

Thus we are left with the first explanation, of material falling from various heights as a coherent flow with internal small-scale turbulent motions, which is similar to the rain on Earth.

5.3.11. Origins of the broad lines

The large value of the unresolved velocities $\xi \approx 100 \text{ km s}^{-1}$ is consistent with the required optical depths to make the radiation differentially anisotropic between k and h lines, because for k the optical depth (from thread centre to edge) $\tau_0 \approx 5.5$. We must explain why the line widths are so large, and the fact that the line shifts are about half those of the widths. The red-shifts correspond to plasma dropped in free fall from a height of $\approx 5 \text{ Mm}$. It seems that gravity at least can easily account for such red-shifts, even if it is superposed onto more energetic small-scale dynamics. The red-shifts will therefore concern us no more.

The field strength needed to achieve an Alfvén speed of 100 km s^{-1} when $n_{12} = 1$ is $\approx 50 \text{ G}$. This is a factor of 30 less than the observed photospheric fields that lie below the raining plasma region, which have $B \gtrsim 1500 \text{ G}$ (Figure 5.6). So it appears that Alfvén waves generated after the impulsive phase of the flare can easily carry enough kinetic energy to account for the broad lines, if otherwise undamped, for some tens of minutes after the impulsive phase. The kinetic energy density involved in the unresolved motions with $n_{12} = 1$ is

$$E_{\text{kin}} \approx \rho \xi^2 \approx 230 \text{ erg cm}^{-3} \quad (5.25)$$

If these persist along a length $L_{10} = 1$ of a strand, then these motions amount to an energy density per unit area of about $2.3 \times 10^{11} \text{ erg cm}^{-2}$. A large X-class flare releases some $10^{11} \text{ erg cm}^{-2} \text{ s}^{-1}$ during the impulsive phase, for some 10^{2-3} seconds, giving an available energy density per unit area of $10^{13-14} \text{ erg cm}^{-2}$. It therefore seems reasonable that one part in 10^2 of the impulsive flare energy might reside in some residual wave motions in the post-flare magnetic fields, and become evident in the widths of the lines observed with *IRIS* reported here. Also, the strands occupy a small volume of the magnetic structures in which they exist (Jing et al., 2016), therefore considerably more magnetic energy might feed into the strands from neighbouring plasma not revealed in the Mg II or other UV emission lines.

Can MHD (Magneto-Hydro-Dynamic) oscillations live for a period of more than an hour or so during which the broad Mg II lines decay? To answer this question would require MHD simulations across multiple scales, since the dissipation of magnetic energy requires the (non-linear) generation of small physical scales. A recent physical discussion of various incomplete calculations done to date shows that it may take a very long time to dissipate wave energy in loops containing small-scale density inhomogeneities (Cargill et al., 2016). Incidentally, this also calls into question the viability of the proposed phase mixing process to describe coronal heating, in support of work by Parker (1991).

5.4. Discussion

We have examined all salient features of the peculiar *IRIS* post-flare line profiles of Mg II, C II and Si IV, with accompanying slit-jaw and magnetic data. By elimination we are led, remarkably, to a consistent picture in which unresolved Alfvénic motions – waves or turbulence – are generated during the impulsive phase of the flare and gradually decay over a period of more than one hour. The estimated time-integrated decay of the magnetic energy is about an order of magnitude larger than the radiation losses from the strong Mg II lines, suggesting a causal connection between them. The peculiar line ratios and profiles are consistent with strands of plasma with width of 100 km , and they require an optical depth across them of between 1 and 10 in the k line.

If we apply the observed intensities and ratios to equations (5.21) and (5.23) to solve for model parameters, we have $T_e \approx 2 \times 10^4 \text{ K}$, and $n_{12}^2 W_{100} \approx 1$. But this analysis does not acknowledge that because of the evidence of unresolved motions there is certainly a distribution of plasma with temperature, and that lines such as the Mg II subordinate triplet of the $3d - 3p$ transitions and C II 1335 form in hotter plasma than the Mg II k and h lines. Given the

exponential dependence of radiative losses on temperature, we therefore suspect, but cannot prove, that for k and h a smaller value of T_e is appropriate. If this is the case then we should have $n_{12} > 0.6$. Below we will adopt $n_{12} = 1$ for the sake of argument.

The total flux radiated during the coronal rain phenomenon, as seen in k and h line emission, is $\approx \pi I t_r = 5 \times 10^7 \times 600 \approx 3 \times 10^{10}$ erg cm⁻². Here we have used a relaxation lifetime of $t_r = 10$ minutes appropriate for the first part of the relaxation phase where these line intensities were measured (Figure 5.1). The *total* radiation losses from chromospheric plasma (due to losses in other elemental emission, such as calcium, iron, hydrogen,..) are between $4\times$ and $10\times$ larger, with larger values occurring at lower plasma temperatures (Anderson and Athay, 1989a, Fig. 4). We adopt a value of $4\times$ the k and h losses, to arrive at a total time-integrated radiative flux of 10^{11} erg cm⁻².

Above, we found $\rho \xi^2 L \approx 2.3 \times 10^{11} n_{12} L_{10}$ erg cm⁻². Remarkably, these rough estimates are within a factor of 2 of one another. Perhaps even more noteworthy, Figure 5.1 shows that *as the broad line intensities decrease, so does the power in the fluctuations (linewidths)*. It appears that the Alfvénic fluctuations excited during the impulsive phase, might decay ultimately into radiation via a process that slowly (when compared with dynamical time scales $\approx L/V_A$) converts the wave energy into thermal energy.

Various dynamical mechanisms might achieve this on time scales of an hour, such as (slow) phase mixing, resonant absorption (e.g. Narain and Ulmschneider, 1990, 1996), although detailed fully dynamical numerical simulations need to be performed to address the very long damping times suggested by Cargill et al. (2016). Gas-kinetic processes can also very efficiently damp oscillations when neutral H or He are abundant within the raining plasma. Ion-neutral collisions will efficiently damp out the high frequency wave energy. The damping time τ_D for these kinetic processes can be computed following, for example, Holzer et al. (1983).

Consider, simply for reference, an Alfvén wave with a period of 10 seconds, which has $\omega \approx 0.6$ rad sec⁻¹, oscillating in the plasma with a number density $n_{12} \approx 1$ and neutral number density $n_{n12} \approx 0.1$, consisting entirely of neutral helium. The ion-neutral helium collision time, τ_{ni} is $\approx 10^{-3} n_{n12}^{-1} \approx 10^{-2}$ sec⁻¹, which gives $\omega \tau_{ni} \approx 6 \times 10^{-3}$. Under this regime, eq. 17 of Holzer et al. (1983) applies, yielding a wave energy dissipation time of

$$\tau_D \approx \frac{n_{12}}{n_{n12}} \frac{1}{\tau_{ni} \omega^2} \approx 2500 \text{ sec.} \quad (5.26)$$

The observed decay time of $\approx 10^3$ seconds may or may not be naturally explained without needing to invoke dynamical MHD processes, depending on the (unknown) frequency ω of the oscillations.

Lastly, the *IRIS* profiles reported here resemble those seen in the flares of very active stars (Linsky et al., 1989). It is likely our solar analysis can help better understand such enormous flares and the associated enhanced line asymmetries observed.

Chapter 6: Conclusions and Prospects

“There is yet insufficient data for a meaningful answer.”

Isaac Asimov, *The Last Question*

This work aimed to enhance our understanding of the low solar atmosphere under different activity regimes, from quiet solar conditions to impulsive flaring. We used high resolution spectral data from *IRIS* together with context imaging and magnetic field data from *SDO* to investigate the relation between the structures observed at different wavelengths.

We first focused on better understanding the spectral properties of the Mg II resonance lines in quiet chromospheric conditions, overlying regions of “pure” photospheric quiet sun, near active region canopy fields, and coronal hole interior. The temporal evolution of the emission in the chromospheric Mg II lines was considered by exploring the variation of different parameters describing the line profiles. We found an obvious contrast between the subgranular cell interior and its boundary, suggesting that the magnetic field plays an important role in establishing the characteristics of the radiation field all the way up to the chromosphere. The emission peaks of the resonance lines proved to be sensitive to small variations in the chromosphere, and in the case of enhanced network field the observed structures were reminiscent of the H α fibrils. The acoustic and seismic emission in these regions was then explored. We found the acoustic signal was suppressed over the weak network field, but were surrounded by enhancements comparable to the acoustic haloes of larger magnetic elements.

The oscillations observed in the Mg II parameters need to be further investigated in order to better explore the upward propagation of waves from the photosphere. Additionally, the longer period network motions and associated episodic plasma flows may offer new details on the small scale magnetic field interaction with the wave field. The transition region emission, although noisier and restricted mostly to regions overlying the cell boundary may provide additional clues. Higher resolution magnetic field data will improve the correlation between the observed chromospheric features and the underlying photosphere.

The response of the solar atmosphere to a flaring event was scrutinized in the case of the X2.1 flare of March 11, 2015. The partition of thermal and non-thermal energy in the impulsive phase and the location of the beam energy deposition sites were computed using X-ray data from *RHESSI*. The evolution of the chromospheric and transition region emission, as seen in the Mg II, C II, and Si IV lines, was analysed. We found that the slow rise of the filament was apparent for more than half an hour before the flare as enhanced blue shifted emission in the considered lines. The subsequent accelerated expansion of the filament destabilized the magnetic configuration of the active region, producing the observed flare. The locations of the flare ribbons was marked by enhanced emission and line widths, with important red asymmetries, and measured red shifts of tens of km s^{-1} . The coronal emission of Fe XXI was used to infer the micro-turbulent velocity in the evaporated plasma. The coronal emission of the *AIA* filters was used to extract the emission measure at different temperatures.

Vector magnetic field data from *HMI* was employed to examine the underlying photospheric fields and identify the locations of the flare footpoints. Using linear force-free extrapolation, the 3D structure of the field was computed and its analysis suggested a decrease of the field line braiding after the flare. The associated seismic sources were identified and found to correspond to a location of deep penumbral intrusion. Given the proximity of the IRIS data to the seismic source, a vertical characterization of the downflows from the transition region down into the photosphere was possible, for the first time for a sunquake. Using the measured line of sight transient speeds and the local properties we computed the available momentum, which was higher than expected, suggesting the configuration of the penumbral intrusion played a key role in exciting the acoustic signal.

The energy propagation from the flaring site to the footpoints is a challenging topic, but paramount to understanding the excitation of acoustic emission. The magnetic field configuration appears to play an important role in channelling the energy, but our observations are not sensitive enough to sample the impulsive energy propagation. We plan to explore additional seismically active flares using spectral data in order to develop a statistically relevant set of profile characteristics. Magnetic field measurements at chromospheric heights may also prove especially useful in understanding the real 3D structure of the active region.

Finally, we performed an in depth analysis of the peculiar profiles observed during the decay phase of the March 11, 2015 X2.1 flare in chromospheric and transition region lines. We used analytical methods to explore the possible causes for the extended red shifts and line widths, persisting for more than an hour after the flare. Using the characteristics of the Mg II emission we performed radiative transfer calculations and found that the observed profiles can be explained as anisotropic emission from a highly turbulent coronal rain phenomena. The unresolved Alfvénic motion was likely excited during the impulsive phase of the flare and gradually decayed to radiation over the following hour. The presence of such long lasting asymmetries in solar observations is a novel result, but similarly red enhancements have been observed in stellar flares, suggesting the universality of such phenomena.

The chromosphere plays an important role in dissipating incoming energy, from both flares and underlying convective motions, therefore, a better grasp of the processes dominating this layer and their associated emission lines response is essential. Magnetic field measurements in this dense region are also a key ingredient in understanding its role in long-standing issues like the coronal heating problem. High spectral and spatial resolution observations of solar flares and subsequent, large scale plasma flows are also important in the context of stellar astrophysics.

The recent launch of the Parker Solar Probe and the commencement of operations of the Daniel K. Inouye Solar Telescope (DKIST), the first 4-meter class solar telescope, next year offer exciting possibilities for the future of solar research. The high resolution spectro-polarimetric data will enable us explore the small scale structure of the solar atmosphere at unprecedented details and obtain simultaneous multi-height magnetic field information. The higher resolution will prove invaluable to studies on wave propagation and their interaction with the magnetic structures. The study of flaring events and their associated seismic signatures will also greatly benefit and with the enhanced resolution maybe shed some new light on the energy transport and deposition. Together with in-situ data, the particle acceleration of flares and the magnetic reconfiguration can be better constrained observationally, enabling the improvement of current modelling efforts.

The future appears promising and we hope new observations continue to challenge our understanding as we continue to strive for a perfect model of the Sun!

Acknowledgements

I have never been good with words and never know what to say, but I know some thanks are in order to a number of people, so I will do my best. I was fortunate to receive encouragements, support, and kind words from colleagues, friends, and family during the course of this stage of my life and I am immensely grateful for everything. I could not have gotten here without you.

Firstly, I would like to thank my supervisors, Alina Donea, with her unending enthusiasm, and Paul Cally, with his always on point questions, for guiding me on this path and for being the best mentors I could wish for. I am grateful for all the opportunities and encouragements. I would especially want to thank Alina for being such a great influence in my life, both professionally and personally, and for going above and beyond to ensure I can make the most out of these last four years.

I would be remiss to not acknowledge Phil Judge for his sincerity, so scarce nowadays, his vast knowledge and willingness to share, and his patience in guiding me to always look for the deeper physical meaning. I am also thankful to Charlie Lindsey for his ever interesting conversations and for always going out of his way to assist in all and everything.

A big thank you goes to the lovely people that have made these last months a little more enjoyable: Sarah Jabbari, Jens Grimm, and Darcy Best. I will really miss hanging out with you.

I am deeply indebted to the administrative staff at the School of Mathematical Sciences, Linda Mayer, Karen Hogeboom, Gertrude Nayak, and John Chan, for making my life so much easier and for going beyond their job description to help and support me. Special thanks to John for his dedication and invaluable efforts to insure everything runs smoothly.

I would also like to thank Ovidiu Tercu for enabling my passion for observational astronomy, Ovidiu Teşileanu and Andrea Mignone for the glimpse into computational astrophysics, and the lovely Marilena Mierlă, Diana Beşliu-Ionescu, and Georgeta Muntean for guiding me toward solar research.

I am grateful to my parents, Maria and Vasilică Lăcătuş, for their support and sacrifices through all of these years, without which I may have never gotten here. My brother, Petrişor Lăcătuş, also deserves thanks for his support and for offering his help, despite his busy life.

Finally, my sincerest gratitude goes to my precious, Alin Răzvan Paraschiv, for always encouraging me and being there for me through all the ups and downs we encountered along the way. I thank you for always being dependable, for taking care of me, and for being on this journey to the far reaches of the Earth with me.

This research would not have been possible without the School of Mathematical Sciences, Monash University and the Australian Government Scholarship programme.

I am also grateful to all the conference and summer school organisers for the opportunities to travel, share my research and learn new things. Special thanks to the HAO and NWRA institutes in Boulder, Colorado, for enabling me to work and talk with some amazing researchers and expand my knowledge.

We welcome and appreciate the open data policy of the *IRIS*, *SDO*, and *RHESSI* missions. Raw data and calibration instructions are obtained courtesy of the *LMSAL/IRIS*, *NASA/SDO*, and *NASA/RHESSI* science teams.

References

- Abbett, W. P. and Hawley, S. L. *Dynamic Models of Optical Emission in Impulsive Solar Flares. Astrophys. J.*, **521**: pp. 906–919 (Aug. 1999).
- Abramov-Maximov, V. E., Borovik, V. N., Opeikina, L. V. and Tlatov, A. G. *Precursors of the solar X flare on march 29, 2014, in the active region NOAA 12017 based on microwave radiation and magnetographic data. Geomagnetism and Aeronomy*, 55 (Dec. 2015).
- Alissandrakis, C. E. *On the computation of constant alpha force-free magnetic field. Astron. Astrophys.*, **100**: pp. 197–200 (Jul. 1981).
- Allen, C. W. *Astrophysical quantities* (Athlone Press, Univ. London, 1973).
- Allred, J. C., Hawley, S. L., Abbett, W. P. and Carlsson, M. *Radiative Hydrodynamic Models of the Optical and Ultraviolet Emission from Solar Flares. Astrophys. J.*, **630**: pp. 573–586 (Sep. 2005).
- Altun, Z., Yumak, A., Badnell, N. R., Loch, S. D. and Pindzola, M. S. *Dielectronic recombination data for dynamic finite-density plasmas. XI. The sodium isoelectronic sequence. Astron. Astrophys.*, **447**: pp. 1165–1174 (Mar. 2006).
- Anderson, L. S. and Athay, R. G. *Chromospheric and coronal heating. Astrophys. J.*, **336**: pp. 1089–1091 (Jan. 1989a).
- Anderson, L. S. and Athay, R. G. *Model solar chromosphere with prescribed heating. Astrophys. J.*, **346**: pp. 1010–1018 (Nov. 1989b).
- Antolin, P., Vissers, G., Pereira, T. M. D., Rouppe van der Voort, L. and Scullion, E. *The Multithermal and Multi-stranded Nature of Coronal Rain. Astrophys. J.*, **806**: 81 (Jun. 2015).
- Aschwanden, M. J. *Magnetic Energy Dissipation during the 2014 March 29 Solar Flare. Astrophys. J. Lett.*, **804**: L20 (May 2015).
- Aschwanden, M. J., Schmahl, E. and RHESSI Team. *Reconstruction of RHESSI Solar Flare Images with a Forward Fitting Method. Solar Phys.*, **210**: pp. 193–211 (Nov. 2002).
- Asplund, M., Grevesse, N., Sauval, A. J. and Scott, P. *The Chemical Composition of the Sun. ARA&A*, **47**: pp. 481–522 (Sep. 2009).
- Auer, L. H., Rees, D. E. and Stenflo, J. O. *Resonance-Line Polarization - Part Six - Line Wing Transfer Calculations Including Excited State Interference. Astron. Astrophys.*, **88**: p. 302 (Aug. 1980).
- Avrett, E., Landi, E. and McKillop, S. *Calculated Resonance Line Profiles of [Mg II], [C II], and [Si IV] in the Solar Atmosphere. Astrophys. J.*, **779**: 155 (Dec. 2013).
- Ayres, T. R. and Linsky, J. L. *The MG II H and K lines. II - Comparison with synthesized profiles and CA II K. Astrophys. J.*, **205**: pp. 874–894 (May 1976).
- Bard, S. and Carlsson, M. *Radiative Hydrodynamic Simulations of Acoustic Waves in Sunspots. Astrophys. J.*, **722**: pp. 888–898 (Oct. 2010).
- Barthol, P., Gandorfer, A., Solanki, S. K., Schüssler, M., Chares, B. et al. *The Sunrise Mission. Solar Phys.*, **268**: pp. 1–34 (Jan. 2011).
- Bates, B., Bradley, D. J., McKeith, C. D. and McKeith, N. E. *Fabry-Perot Interferograms of the Solar Mg II Doublet and XUV Solar Images obtained during a Stabilized Skylark Rocket Flight. Nature*, **224**: pp. 161–163 (Oct. 1969).
- Battaglia, M., Kleint, L., Krucker, S. and Graham, D. *How Important Are Electron Beams in Driving Chromospheric Evaporation in the 2014 March 29 Flare? Astrophys. J.*, **813**: 113 (Nov. 2015).
- Belluzzi, L. and Trujillo Bueno, J. *The Impact of Quantum Interference between Different J-levels on Scattering Polarization in Spectral Lines. Astrophys. J.*, **743**: 3 (Dec. 2011).

- Blum, R. D. and Pradhan, A. K. *Rate coefficients for the excitation of infrared and ultraviolet lines in C II, N III, and O IV. Astrophys. J. Suppl.*, **80**: pp. 425–452 (May 1992).
- Bonnet, R. M., Lemaire, P., Vial, J. C., Artzner, G., Gouttebroze, P. et al. *The LPSP instrument on OSO 8. II - In-flight performance and preliminary results. Astrophys. J.*, **221**: pp. 1032–1053 (May 1978).
- Brandt, P. N., Rutten, R. J., Shine, R. A. and Trujillo Bueno, J. *Dynamics of the Quiet Solar Atmosphere: K2v Cell Grains Versus Magnetic Elements*. In M. S. Giampapa and J. A. Bookbinder, eds., *Cool Stars, Stellar Systems, and the Sun*, vol. **26** of *Astronomical Society of the Pacific Conference Series*, p. 161 (1992).
- Brannon, S. R., Longcope, D. W. and Qiu, J. *Spectroscopic Observations of an Evolving Flare Ribbon Substructure Suggesting Origin in Current Sheet Waves. Astrophys. J.*, **810**: 4 (Sep. 2015).
- Braun, D. C., Lindsey, C., Fan, Y. and Fagan, M. *Seismic Holography of Solar Activity. Astrophys. J.*, **502**: pp. 968–980 (Aug. 1998).
- Burgess, A. and Tully, J. A. *On the Analysis of Collision Strengths and Rate Coefficients. Astron. Astrophys.*, **254**: p. 436 (Feb. 1992).
- Cally, P. S. and Robb, T. D. *Stability, structure, and evolution of cool loops. Astrophys. J.*, **372**: pp. 329–335 (May 1991).
- Cargill, P. J., De Moortel, I. and Kiddie, G. *Coronal Density Structure and its Role in Wave Damping in Loops. Astrophys. J.*, **823**: 31 (May 2016).
- Carlsson, M. and Stein, R. F. *Formation of Solar Calcium H and K Bright Grains. Astrophys. J.*, **481**: pp. 500–514 (May 1997).
- Carmichael, H. *A Process for Flares*. NASA Special Publication, **50**: p. 451 (1964).
- Carrington, R. C. *Description of a Singular Appearance seen in the Sun on September 1, 1859. Mon. Not. Roy. Astron. Soc.*, **20**: pp. 13–15 (Nov. 1859).
- Cheung, M. C. M., Boerner, P., Schrijver, C. J., Testa, P., Chen, F., Peter, H. and Malanushenko, A. *Thermal Diagnostics with the Atmospheric Imaging Assembly on board the Solar Dynamics Observatory: A Validated Method for Differential Emission Measure Inversions. Astrophys. J.*, **807**: 143 (Jul. 2015).
- Chitta, L. P., Jain, R., Kariyappa, R. and Jefferies, S. M. *Observations of the Interaction of Acoustic Waves and Small-scale Magnetic Fields in a Quiet Sun. Astrophys. J.*, **744**: 98 (Jan. 2012).
- Close, R. M., Parnell, C. E., Mackay, D. H. and Priest, E. R. *Statistical Flux Tube Properties of 3D Magnetic Carpet Fields. Solar Phys.*, **212**: pp. 251–275 (Feb. 2003).
- Danilovic, S., Hirzberger, J., Riethmüller, T. L., Solanki, S. K., Barthol, P. et al. *Comparison between Mg II k and Ca II H Images Recorded by SUNRISE/SuFI. Astrophys. J.*, **784**: 20 (Mar. 2014).
- De Pontieu, B., Title, A. M., Lemen, J. R., Kushner, G. D., Akin, D. J. et al. *The Interface Region Imaging Spectrograph (IRIS). Solar Phys.*, **289**: pp. 2733–2779 (Jul. 2014).
- del Pino Alemán, T., Casini, R. and Manso Sainz, R. *Magnetic Diagnostics of the Solar Chromosphere with the Mg II h-k Lines. Astrophys. J. Lett.*, **830**: L24 (Oct. 2016).
- Dennis, B. R. and Pernak, R. L. *Hard X-Ray Flare Source Sizes Measured with the Ramaty High Energy Solar Spectroscopic Imager. Astrophys. J.*, **698**: pp. 2131–2143 (Jun. 2009).
- Dere, K. P. *The XUV structure of solar active regions. Solar Phys.*, **75**: pp. 189–203 (Jan. 1982).
- Deubner, F.-L. and Fleck, B. *Dynamics of the solar atmosphere. III - Cell-network distinctions of chromospheric oscillations. Astron. Astrophys.*, **228**: pp. 506–512 (Feb. 1990).
- Donea, A.-C., Besliu-Ionescu, D., Cally, P. S., Lindsey, C. and Zharkova, V. V. *Seismic Emission from A M9.5-Class Solar Flare. Solar Phys.*, **239**: pp. 113–135 (Dec. 2006).
- Donea, A.-C., Braun, D. C. and Lindsey, C. *Seismic Images of a Solar Flare. Astrophys. J. Lett.*, **513**: pp. L143–L146 (Mar. 1999).
- Donea, A.-C. and Lindsey, C. *Seismic Emission from the Solar Flares of 2003 October 28 and 29. Astrophys. J.*, **630**: pp. 1168–1183 (Sep. 2005).
- Donea, A.-C., Lindsey, C. and Braun, D. C. *Stochastic Seismic Emission from Acoustic Glories and the Quiet Sun. Solar Phys.*, **192**: pp. 321–333 (Mar. 2000).
- Doschek, G. A. and Feldman, U. *High-resolution spectra of the solar MG II H and K lines from SKYLAB.*

- Astrophys. J. Suppl.*, **35**: pp. 471–482 (Dec. 1977).
- Doschek, G. A., Feldman, U., Dere, K. P., Sandlin, G. D., Vanhoosier, M. E. et al. *Forbidden lines of highly ionized iron in solar flare spectra*. *Astrophys. J. Lett.*, **196**: pp. L83–L86 (Mar. 1975).
- Durand, E., Oberly, J. J. and Tousey, R. *Analysis of the First Rocket Ultraviolet Solar Spectra*. *Astrophys. J.*, **109**: p. 1 (Jan. 1949).
- Emslie, A. G., Kucharek, H., Dennis, B. R., Gopalswamy, N., Holman, G. D. et al. *Energy partition in two solar flare/CME events*. *Journal of Geophysical Research (Space Physics)*, **109**: A10104 (Oct. 2004).
- Fang, X., Xia, C. and Keppens, R. *Multidimensional Modeling of Coronal Rain Dynamics*. *Astrophys. J. Lett.*, **771**: L29 (Jul. 2013).
- Feldman, U. and Doschek, G. A. *The 3s-3p and 3p-3d lines of MG II observed above the solar limb from SKYLAB*. *Astrophys. J. Lett.*, **212**: pp. L147–L150 (Mar. 1977).
- Field, G. B. *Thermal Instability*. *Astrophys. J.*, **142**: p. 531 (Aug. 1965).
- Fisher, G. H., Canfield, R. C. and McClymont, A. N. *Flare Loop Radiative Hydrodynamics - Part Seven - Dynamics of the Thick Target Heated Chromosphere*. *Astrophys. J.*, **289**: p. 434 (Feb. 1985).
- Fletcher, L., Dennis, B. R., Hudson, H. S., Krucker, S., Phillips, K. et al. *An Observational Overview of Solar Flares*. *Space Sci. Rev.*, **159**: pp. 19–106 (Sep. 2011).
- Francile, C., López, F. M., Cremades, H., Mandrini, C. H., Luoni, M. L. and Long, D. M. *Moreton and EUV Waves Associated with an X1.0 Flare and CME Ejection*. *Solar Phys.*, **291**: pp. 3217–3249 (Nov. 2016).
- Fredga, K. *Monochromatic Pictures of the Sun in the MG II Line at 2802.7 Å*. *Astrophys. J.*, **144**: pp. 854–857 (May 1966).
- Fredga, K. *Spectroheliograms in the Mg II line at 2795.5 Å*. *Solar Phys.*, **9**: pp. 358–371 (Oct. 1969).
- Frisch, H. *Mean escape probabilities and mean numbers of scatterings for resonance lines.*, pp. 65–77 (Cambridge Univ., 1984).
- Gabriel, A. H. and Jordan, C. *Case Studies in Atomic Collision Physics, Chapt.4*, pp. 209–291 (North-Holland, 1971).
- Galileo, G. *Istoria e dimostrazioni intorno alle macchie solari e loro accidenti* (Mascardi, Giacomo, fl. 1605-1634, 1613).
- Gandorfer, A., Grauf, B., Barthol, P., Riethmüller, T. L., Solanki, S. K. et al. *The Filter Imager SuFI and the Image Stabilization and Light Distribution System ISLiD of the Sunrise Balloon-Borne Observatory: Instrument Description*. *Solar Phys.*, **268**: pp. 35–55 (Jan. 2011).
- Garrett, D. L., Purcell, J. D. and Tousey, R. *High-Resolution Ultraviolet Solar Spectrum Extending to 2200 Å*. *Astron. J.*, **67**: p. 115 (1962).
- Gibson, E. G. *The quiet sun*. (NASA Special Publication, 1973).
- Goldreich, P. and Kumar, P. *Wave generation by turbulent convection*. *Astrophys. J.*, **363**: pp. 694–704 (Nov. 1990).
- Gouttebroze, P. and Lemaire, P. *A center-to-limb analysis of solar MG II lines*. *Astron. Astrophys.*, **34**: pp. 375–386 (Sep. 1974).
- Graham, D. R. and Cauzzi, G. *Temporal Evolution of Multiple Evaporating Ribbon Sources in a Solar Flare*. *Astrophys. J. Lett.*, **807**: L22 (Jul. 2015).
- Hale, G. E. and Ellerman, F. *Calcium and Hydrogen Flocculi*. *Astrophys. J.*, **19**: p. 41 (Jan. 1904).
- Hannah, I. G., Christe, S., Krucker, S., Hurford, G. J., Hudson, H. S. and Lin, R. P. *RHESSI Microflare Statistics. II. X-Ray Imaging, Spectroscopy, and Energy Distributions*. *Astrophys. J.*, **677**: pp. 704–718 (Apr. 2008).
- Hansen, S. C., Cally, P. S. and Donea, A.-C. *On mode conversion, reflection, and transmission of magnetoacoustic waves from above in an isothermal stratified atmosphere*. *Mon. Not. Roy. Astron. Soc.*, **456**: pp. 1826–1836 (Feb. 2016).
- Heinzl, P. and Kleint, L. *Hydrogen Balmer Continuum in Solar Flares Detected by the Interface Region Imaging Spectrograph (IRIS)*. *Astrophys. J. Lett.*, **794**: L23 (Oct. 2014).
- Heinzl, P., Schmieder, B. and Mein, P. *Structure and dynamics of cool flare loops*. *Solar Phys.*, **139**:

- pp. 81–104 (May 1992).
- Henze, W. and Stenflo, J. O. *Polarimetry in the MG II H and K lines*. *Solar Phys.*, **111**: pp. 243–254 (Sep. 1987).
- Hirayama, T. *Theoretical Model of Flares and Prominences. I: Evaporating Flare Model*. *Solar Phys.*, **34**: pp. 323–338 (Feb. 1974).
- Holzer, T. E., Fla, T. and Leer, E. *Alfven waves in stellar winds*. *Astrophys. J.*, **275**: pp. 808–835 (Dec. 1983).
- Hurford, G. J., Schmahl, E. J., Schwartz, R. A., Conway, A. J., Aschwanden, M. J. et al. *The RHESSI Imaging Concept*. *Solar Phys.*, **210**: pp. 61–86 (Nov. 2002).
- Jing, J., Xu, Y., Cao, W., Liu, C., Gary, D. and Wang, H. *Unprecedented Fine Structure of a Solar Flare Revealed by the 1.6 m New Solar Telescope*. *Nat. Sci. Reports*, **6**: 24319 (Apr. 2016).
- Johnson, F. S., Purcell, J. D., Tousey, R. and Wilson, N. *A New Photograph of the MG II Doublet at 2800 Å in the Sun*. *Astrophys. J.*, **117**: p. 238 (Jan. 1953).
- Jordan, C. *Modelling of solar coronal loops*. *Mem. Soc. Astron. Italiana*, **63**: pp. 605–620 (1992).
- Judge, P. G., Kleint, L., Donea, A., Sainz Dalda, A. and Fletcher, L. *On the Origin of a Sunquake during the 2014 March 29 X1 Flare*. *Astrophys. J.*, **796**: 85 (Dec. 2014).
- Judge, P. G., Kleint, L. and Sainz Dalda, A. *On Helium 1083 nm Line Polarization during the Impulsive Phase of an X1 Flare*. *Astrophys. J.*, **814**: 100 (Dec. 2015).
- Judge, P. G., Paraschiv, A., Lacatus, D., Donea, A. and Lindsey, C. *Are All Flare Ribbons Simply Connected to the Corona?* *Astrophys. J.*, **838**: 138 (Apr. 2017).
- Judge, P. G., Tarbell, T. D. and Wilhelm, K. *A Study of Chromospheric Oscillations Using the SOHO and TRACE Spacecraft*. *Astrophys. J.*, **554**: pp. 424–444 (Jun. 2001).
- Kawaguchi, I. *Observed Interaction between Prominences*. *Pub. Astron. Soc. Japan*, **22**: p. 405 (1970).
- Kelleher, D. E. and Podobedova, L. I. *Atomic transition probabilities of sodium and magnesium. a critical compilation*. *J. Phys. and Chem. Ref. Data*, **37**(1): pp. 267–706 (2008).
- Kerr, G. S., Simões, P. J. A., Qiu, J. and Fletcher, L. *IRIS observations of the Mg ii h and k lines during a solar flare*. *Astron. Astrophys.*, **582**: A50 (Oct. 2015).
- Khomenko, E. and Calvo Santamaria, I. *Magnetohydrodynamic waves driven by p-modes*. In *Journal of Physics Conference Series*, vol. **440** of *Journal of Physics Conference Series*, p. 012048 (2013).
- Kleint, L., Antolin, P., Tian, H., Judge, P., Testa, P. et al. *Detection of Supersonic Downflows and Associated Heating Events in the Transition Region above Sunspots*. *Astrophys. J. Lett.*, **789**: L42 (Jul. 2014).
- Kleint, L., Battaglia, M., Reardon, K., Sainz Dalda, A., Young, P. R. and Krucker, S. *The Fast Filament Eruption Leading to the X-flare on 2014 March 29*. *Astrophys. J.*, **806**: 9 (Jun. 2015).
- Kleint, L., Heinzel, P., Judge, P. and Krucker, S. *Continuum Enhancements in the Ultraviolet, the Visible and the Infrared during the X1 Flare on 2014 March 29*. *Astrophys. J.*, **816**: 88 (Jan. 2016).
- Kneer, F., Mattig, W., Scharmer, G., Wyller, A., Artzner, G., Lemaire, P. and Vial, J. C. *OSO-8 observations of CA II H and K, MG II H and k, L-alpha and L-beta above a sunspot*. *Solar Phys.*, **69**: pp. 289–300 (Feb. 1981).
- Kohl, J. L. and Parkinson, W. H. *The MG II H and K lines. I - Absolute center and limb measurements of the solar profiles*. *Astrophys. J.*, **205**: pp. 599–611 (Apr. 1976).
- Kohutova, P. and Verwichte, E. *Analysis of Coronal Rain Observed by IRIS, HINODE/SOT, and SDO/AIA: Transverse Oscillations, Kinematics, and Thermal Evolution*. *Astrophys. J.*, **827**: 39 (Aug. 2016).
- Kontogiannis, I., Tsiropoula, G. and Tziotziou, K. *Hinode SOT/SP and SoHO/MDI quiet Sun magnetic field. Implications of their differences on the extrapolated chromospheric field and the height of the magnetic canopy*. *Astron. Astrophys.*, **531**: A66 (Jul. 2011).
- Kontogiannis, I., Tsiropoula, G. and Tziotziou, K. *Wave propagation in a solar quiet region and the influence of the magnetic canopy*. *Astron. Astrophys.*, **585**: A110 (Jan. 2016).
- Kopp, R. A. and Pneuman, G. W. *Magnetic reconnection in the corona and the loop prominence phenomenon*. *Solar Phys.*, **50**: pp. 85–98 (Oct. 1976).

- Kosovichev, A. G. and Zharkova, V. V. *X-ray flare sparks quake inside Sun*. **Nature**, 393: pp. 317–318 (May 1998).
- Kowalski, A. F., Allred, J. C., Daw, A., Cauzzi, G. and Carlsson, M. *The Atmospheric Response to High Nonthermal Electron Beam Fluxes in Solar Flares. I. Modeling the Brightest NUV Footpoints in the X1 Solar Flare of 2014 March 29*. **Astrophys. J.**, 836: 12 (Feb. 2017).
- Kramida, A., Ralchenko, Y., Reader, J. and NIST ASD Team. *NIST Atomic Spectra Database (version 5.3)*, [Online]. Available: <http://physics.nist.gov/asd>. National Institute of Standards and Technology, Gaithersburg, MD. (2015).
- Lacatus, D. A., Judge, P. G. and Donea, A. *An Explanation of Remarkable Emission-line Profiles in Post-flare Coronal Rain*. **Astrophys. J.**, **842**: 15 (Jun. 2017).
- Landi Degl'Innocenti, E. and Landolfi, M. *Polarization in Spectral Lines*, vol. **307** of *Astrophysics and Space Science Library* (2004).
- Leenaarts, J., Pereira, T. M. D., Carlsson, M., Uitenbroek, H. and De Pontieu, B. *The Formation of IRIS Diagnostics. I. A Quintessential Model Atom of Mg II and General Formation Properties of the Mg II h & k Lines*. **Astrophys. J.**, **772**: 89 (Aug. 2013a).
- Leenaarts, J., Pereira, T. M. D., Carlsson, M., Uitenbroek, H. and De Pontieu, B. *The Formation of IRIS Diagnostics. II. The Formation of the Mg II h & k Lines in the Solar Atmosphere*. **Astrophys. J.**, **772**: 90 (Aug. 2013b).
- Leighton, R. B. *Transport of Magnetic Fields on the Sun*. **Astrophys. J.**, 140: p. 1547 (Nov. 1964).
- Lemaire, P. *High Resolution Balloon Spectra of the Sun in the Mg II Doublet Lines II*. **Astrophys. Lett.**, **3**: p. 43 (1969).
- Lemaire, P. and Blamont, J. E. *Stigmatic Balloon Spectra of the Solar MG II Doublet*. **Astrophys. J. Lett.**, **150**: p. L129 (Dec. 1967).
- Lemaire, P., Choucq-Bruston, M. and Vial, J.-C. *Simultaneous H and K CA II, H and K MG II, L-alpha and L-beta H I profiles of the April 15, 1978 solar flare observed with the OSO-8/L.P.S.P. experiment*. **Solar Phys.**, **90**: pp. 63–82 (Jan. 1984).
- Lemaire, P. and Gouttebroze, P. *Magnesium II line formation - The contribution of high atomic levels to the resonance lines*. **Astron. Astrophys.**, **125**: pp. 241–245 (Sep. 1983).
- Lemaire, P., Gouttebroze, P., Vial, J. C. and Artzner, G. E. *Physical properties of the solar chromosphere deduced from optically thick lines. I - Observations, data reduction, and modelling of an average plage*. **Astron. Astrophys.**, **103**: pp. 160–176 (Nov. 1981).
- Lemaire, P. and Skumanich, A. *Magnesium II Doublet Profiles of Chromospheric Inhomogeneities at the Center of the Solar Disk*. **Astron. Astrophys.**, **22**: p. 61 (Jan. 1973).
- Lemen, J. R., Title, A. M., Akin, D. J., Boerner, P. F., Chou, C. et al. *The Atmospheric Imaging Assembly (AIA) on the Solar Dynamics Observatory (SDO)*. **Solar Phys.**, **275**: pp. 17–40 (Jan. 2012).
- Leroy, J.-L. *Emissions 'froides' dans la couronne solaire*. **Solar Phys.**, **25**: pp. 413–417 (Aug. 1972).
- Li, D., Ning, Z. J., Huang, Y. and Zhang, Q. M. *Explosive Chromospheric Evaporation Driven by Nonthermal Electrons around One Footpoint of a Solar Flare Loop*. **Astrophys. J. Lett.**, **841**: L9 (May 2017a).
- Li, Q., Deng, N., Jing, J. and Wang, H. *High-resolution Observations of Downflows at One End of a Pre-eruption Filament*. **Astrophys. J.**, **841**: 112 (Jun. 2017b).
- Li, T., Yang, K., Hou, Y. and Zhang, J. *Slipping Magnetic Reconnection of Flux-rope Structures as a Precursor to an Eruptive X-class Solar Flare*. **Astrophys. J.**, 830: 152 (Oct. 2016).
- Li, Y., Ding, M. D., Qiu, J. and Cheng, J. X. *Chromospheric Evaporation in an X1.0 Flare on 2014 March 29 Observed with IRIS and EIS*. **Astrophys. J.**, **811**: 7 (Sep. 2015).
- Li, Y., Kelly, M., Ding, M. D., Qiu, J., Zhu, X. S. and Gan, W. Q. *Spectroscopic Observations of Magnetic Reconnection and Chromospheric Evaporation in an X-shaped Solar Flare*. **Astrophys. J.**, **848**: 118 (Oct. 2017c).
- Lin, H. and Rimmele, T. *The Granular Magnetic Fields of the Quiet Sun*. **Astrophys. J.**, 514: pp. 448–455 (Mar. 1999).
- Lin, H.-H. and Carlsson, M. *The Formation of IRIS Diagnostics. VII. The Formation of the OI 135.56*

- NM Line in the Solar Atmosphere. Astrophys. J.*, **813**: 34 (Nov. 2015).
- Lin, H.-H., Carlsson, M. and Leenaarts, J. *The Formation of IRIS Diagnostics. IX. The Formation of the C I 135.58 NM Line in the Solar Atmosphere. Astrophys. J.*, **846**: 40 (Sep. 2017).
- Lin, R. P., Dennis, B. R., Hurford, G. J., Smith, D. M., Zehnder, A. et al. *The Reuven Ramaty High-Energy Solar Spectroscopic Imager (RHESSI). Solar Phys.*, **210**: pp. 3–32 (Nov. 2002).
- Linsky, J. L. and Avrett, E. H. *The Solar H and K Lines. Pub. Astron. Soc. Pac.*, **82**: p. 169 (Apr. 1970).
- Linsky, J. L. and Ayres, T. R. *Stellar model chromospheres. VI - Empirical estimates of the chromospheric radiative losses of late-type stars. Astrophys. J.*, **220**: pp. 619–628 (Mar. 1978).
- Linsky, J. L., Neff, J. E., Brown, A., Gross, B. D., Simon, T. et al. *Rotational modulation and flares on RS Canum Venaticorum and BY Draconis stars. X - The 1981 October 3 flare on V711 Tauri (=HR 1099). Astron. Astrophys.*, **211**: pp. 173–186 (Feb. 1989).
- Lipartito, I., Judge, P. G., Reardon, K. and Cauzzi, G. *The Solar Chromosphere Observed at 1 Hz and 0."2 Resolution. Astrophys. J.*, **785**: 109 (Apr. 2014).
- Lites, B. W., Rutten, R. J. and Kalkofen, W. *Dynamics of the solar chromosphere. I - Long-period network oscillations. Astrophys. J.*, **414**: pp. 345–356 (Sep. 1993).
- Liu, C., Deng, N., Liu, R., Lee, J., Pariat, É. et al. *A Circular-ribbon Solar Flare Following an Asymmetric Filament Eruption. Astrophys. J. Lett.*, **812**: L19 (Oct. 2015a).
- Liu, W., Heinzel, P., Kleint, L. and Kašparová, J. *Mg II Lines Observed During the X-class Flare on 29 March 2014 by the Interface Region Imaging Spectrograph. Solar Phys.*, **290**: pp. 3525–3543 (Dec. 2015b).
- Liu, Y., Sun, X., Török, T., Titov, V. S. and Leake, J. E. *Electric-current Neutralization, Magnetic Shear, and Eruptive Activity in Solar Active Regions. Astrophys. J. Lett.*, **846**: L6 (Sep. 2017).
- Martínez-Sykora, J., Rouppe van der Voort, L., Carlsson, M., De Pontieu, B., Pereira, T. M. D. et al. *Internetwork Chromospheric Bright Grains Observed With IRIS and SST. Astrophys. J.*, **803**: 44 (Apr. 2015).
- Matthews, S. A., Harra, L. K., Zharkov, S. and Green, L. M. *Spectroscopic Signatures Related to a Sunquake. Astrophys. J.*, **812**: 35 (Oct. 2015).
- McAteer, R. T. J., Gallagher, P. T., Bloomfield, D. S., Williams, D. R., Mathioudakis, M. and Keenan, F. P. *Ultraviolet Oscillations in the Chromosphere of the Quiet Sun. Astrophys. J.*, **602**: pp. 436–445 (Feb. 2004).
- Metcalf, T. R., Hudson, H. S., Kosugi, T., Puetter, R. C. and Pina, R. K. *Pixon-based Multiresolution Image Reconstruction for Yohkoh's Hard X-Ray Telescope. Astrophys. J.*, **466**: p. 585 (Jul. 1996).
- Mihalas, D. *Stellar atmospheres, 2nd Edition.* (San Francisco, 1978).
- Mikuła, K., Heinzel, P., Liu, W. and Berlicki, A. *Structure and Dynamics of Cool Flare Loops Observed by the Interface Region Imaging Spectrograph. Astrophys. J.*, **845**: 30 (Aug. 2017).
- Milkey, R. W. and Mihalas, D. *Resonance-line transfer with partial redistribution. II - The solar MG II lines. Astrophys. J.*, **192**: pp. 769–776 (Sep. 1974).
- Moe, O. K. and Milone, E. F. *Limb darkening 1945-3245 Å for the quiet sun from SKYLAB data. Astrophys. J.*, **226**: pp. 301–314 (Nov. 1978).
- Moradi, H., Donea, A.-C., Lindsey, C., Besliu-Ionescu, D. and Cally, P. S. *Helioseismic analysis of the solar flare-induced sunquake of 2005 January 15. Mon. Not. Roy. Astron. Soc.*, **374**: pp. 1155–1163 (Jan. 2007).
- Morrill, J. S., Dere, K. P. and Korendyke, C. M. *The Sources of Solar Ultraviolet Variability between 2765 and 2885 Å: Mg I, Mg II, Si I, and Continuum. Astrophys. J.*, **557**: pp. 854–863 (Aug. 2001).
- Morrill, J. S. and Korendyke, C. M. *High-Resolution Center-to-Limb Variation of the Quiet Solar Spectrum near Mg II. Astrophys. J.*, **687**: pp. 646–657 (Nov. 2008).
- Moschou, S. P., Keppens, R., Xia, C. and Fang, X. *Simulating coronal condensation dynamics in 3D. Adv. Space Res.*, **56**: pp. 2738–2759 (Dec. 2015).
- Nakariakov, V. M. and Verwichte, E. *Coronal Waves and Oscillations. Living Reviews in Solar Physics*, **2**: 3 (May 2005).
- Narain, U. and Ulmschneider, P. *Chromospheric and coronal heating mechanisms. Space Sci. Rev.*, **54**:

- pp. 377–445 (Dec. 1990).
- Narain, U. and Ulmschneider, P. *Chromospheric and Coronal Heating Mechanisms II*. *Space Sci. Rev.*, **75**: pp. 453–509 (Feb. 1996).
- Nordlund, Å. and Stein, R. F. *Solar Oscillations and Convection. I. Formalism for Radial Oscillations*. *Astrophys. J.*, **546**: pp. 576–584 (Jan. 2001).
- Oliver, R., Soler, R., Terradas, J. and Zaqarashvili, T. V. *Dynamics of Coronal Rain and Descending Plasma Blobs in Solar Prominences. II. Partially Ionized Case*. *Astrophys. J.*, **818**: 128 (Feb. 2016).
- Osterbrock, D. E. *The Escape of Resonance-Line Radiation from an Optically Thick Nebula*. *Astrophys. J.*, **135**: p. 195 (Jan. 1962).
- Parker, E. N. *Instability of Thermal Fields*. *Astrophys. J.*, **117**: p. 431 (May 1953).
- Parker, E. N. *The phase mixing of Alfvén waves, coordinated modes, and coronal heating*. *Astrophys. J.*, **376**: pp. 355–363 (Jul. 1991).
- Parnell, C. E. and De Moortel, I. *A contemporary view of coronal heating*. Philosophical Transactions of the Royal Society of London Series A, **370**: pp. 3217–3240 (Jul. 2012).
- Pereira, T. M. D., Carlsson, M., De Pontieu, B. and Hansteen, V. *The Formation of IRIS Diagnostics. IV. The Mg II Triplet Lines as a New Diagnostic for Lower Chromospheric Heating*. *Astrophys. J.*, **806**: 14 (Jun. 2015).
- Pereira, T. M. D., Leenaarts, J., De Pontieu, B., Carlsson, M. and Uitenbroek, H. *The Formation of IRIS Diagnostics. III. Near-ultraviolet Spectra and Images*. *Astrophys. J.*, **778**: 143 (Dec. 2013).
- Pesnell, W. D., Thompson, B. J. and Chamberlin, P. C. *The Solar Dynamics Observatory (SDO)*. *Solar Phys.*, **275**: pp. 3–15 (Jan. 2012).
- Peter, H. *The Chromosphere in Coronal Holes and the Quiet-Sun Network: an HE I (584 Å) Full-Disk Scan by SUMER/SOHO*. *Astrophys. J. lett.*, **522**: pp. L77–L80 (Sep. 1999).
- Rathore, B. and Carlsson, M. *The Formation of IRIS Diagnostics. V. A Quintessential Model Atom of C II and General Formation Properties of the C II Lines at 133.5 nm*. *Astrophys. J.*, **811**: 80 (Oct. 2015).
- Rathore, B., Carlsson, M., Leenaarts, J. and De Pontieu, B. *The Formation of IRIS Diagnostics. VI. The Diagnostic Potential of the C II Lines at 133.5 nm in the Solar Atmosphere*. *Astrophys. J.*, **811**: 81 (Oct. 2015a).
- Rathore, B., Pereira, T. M. D., Carlsson, M. and De Pontieu, B. *The Formation of Iris Diagnostics. VIII. Iris Observations in the C II 133.5 nm Multiplet*. *Astrophys. J.*, **814**: 70 (Nov. 2015b).
- Reardon, K. P., Uitenbroek, H. and Cauzzi, G. *The solar chromosphere at high resolution with IBIS. III. Comparison of Ca II K and Ca II 854.2 nm imaging*. *Astron. Astrophys.*, **500**: pp. 1239–1247 (Jun. 2009).
- Régnier, S., Parnell, C. E. and Haynes, A. L. *A new view of quiet-Sun topology from Hinode/SOT*. *Astron. Astrophys.*, **484**: pp. L47–L50 (Jun. 2008).
- Riethmüller, T. L., Solanki, S. K., Hirzberger, J., Danilovic, S., Barthol, P. et al. *First High-resolution Images of the Sun in the 2796 Å Mg II k Line*. *Astrophys. J. lett.*, **776**: L13 (Oct. 2013).
- Rubio da Costa, F., Kleint, L., Petrosian, V., Liu, W. and Allred, J. C. *Data-driven Radiative Hydrodynamic Modeling of the 2014 March 29 X1.0 Solar Flare*. *Astrophys. J.*, **827**: 38 (Aug. 2016).
- Rutten, R. J. *Radiative Transfer in Stellar Atmospheres* (2003).
- Saint-Hilaire, P. and Benz, A. O. *Thermal and non-thermal energies of solar flares*. *Astron. Astrophys.*, **435**: pp. 743–752 (May 2005).
- Scharmer, G. B. *Solutions to radiative transfer problems using approximate lambda operators*. *Astrophys. J.*, **249**: pp. 720–730 (Oct. 1981).
- Scharmer, G. B., Bjelksjö, K., Korhonen, T. K., Lindberg, B. and Petterson, B. *The 1-meter Swedish solar telescope*. In S. L. Keil and S. V. Avakyan, eds., *Innovative Telescopes and Instrumentation for Solar Astrophysics*, vol. **4853** of *Proc. SPIE*, pp. 341–350 (2003).
- Scharmer, G. B., Narayan, G., Hillberg, T., de la Cruz Rodriguez, J., Löfdahl, M. G. et al. *CRISP Spectropolarimetric Imaging of Penumbra Fine Structure*. *Astrophys. J. lett.*, **689**: L69 (Dec. 2008).

- Schmahl, E. J., Pernak, R. L., Hurford, G. J., Lee, J. and Bong, S. *Analysis of RHESSI Flares Using a Radio Astronomical Technique*. **Solar Phys.**, **240**: pp. 241–252 (Feb. 2007).
- Schmit, D., Bryans, P., De Pontieu, B., McIntosh, S., Leenaarts, J. and Carlsson, M. *Observed Variability of the Solar Mg II h Spectral Line*. **Astrophys. J.**, **811**: 127 (Oct. 2015).
- Schmit, D. J., Innes, D., Ayres, T., Peter, H., Curdt, W. and Jaeggli, S. *Molecular absorption in transition region spectral lines*. **Astron. Astrophys.**, **569**: L7 (Sep. 2014).
- Schou, J., Scherrer, P. H., Bush, R. I., Wachter, R., Couvidat, S. et al. *Design and Ground Calibration of the Helioseismic and Magnetic Imager (HMI) Instrument on the Solar Dynamics Observatory (SDO)*. **Solar Phys.**, **275**: pp. 229–259 (Jan. 2012).
- Schrijver, C. J. *Catastrophic cooling and high-speed downflow in quiescent solar coronal loops observed with TRACE*. **Solar Phys.**, **198**: pp. 325–345 (Feb. 2001).
- Scullion, E., Rouppe van der Voort, L., Antolin, P., Wedemeyer, S., Vissers, G., Kontar, E. P. and Gallagher, P. T. *Observing the Formation of Flare-driven Coronal Rain*. **Astrophys. J.**, **833**: 184 (Dec. 2016).
- Sharykin, I. N. and Kosovichev, A. G. *Dynamics of Electric Currents, Magnetic Field Topology, and Helioseismic Response of a Solar Flare*. **Astrophys. J.**, **808**: 72 (Jul. 2015).
- Sharykin, I. N., Kosovichev, A. G., Sadykov, V. M., Zimovets, I. V. and Myshyakov, I. I. *Investigation of Relationship between High-energy X-Ray Sources and Photospheric and Helioseismic Impacts of X1.8 Solar Flare of 2012 October 23*. **Astrophys. J.**, **843**: 67 (Jul. 2017).
- Sharykin, I. N., Kosovichev, A. G. and Zimovets, I. V. *Energy Release and Initiation of a Sunquake in a C-class Flare*. **Astrophys. J.**, **807**: 102 (Jul. 2015).
- Shelyag, S., Cally, P. S., Reid, A. and Mathioudakis, M. *Alfvén Waves in Simulations of Solar Photospheric Vortices*. **Astrophys. J. Lett.**, **776**: L4 (Oct. 2013).
- Sigut, T. A. A. and Pradhan, A. K. *Electron-impact excitation of Mg II: collision strengths and rate coefficients*. **J. Phys. B: At. Mol. Opt. Phys.**, **28**: pp. 4879–4893 (Nov. 1995).
- Smith, D. M., Lin, R. P., Turin, P., Curtis, D. W., Primbsch, J. H. et al. *The RHESSI Spectrometer*. **Solar Phys.**, **210**: pp. 33–60 (Nov. 2002).
- Song, Q., Wang, J.-S., Feng, X. and Zhang, X. *Dark Post-flare Loops Observed by the Solar Dynamics Observatory*. **Astrophys. J.**, **821**: 83 (Apr. 2016).
- Staath, E. and Lemaire, P. *High resolution profiles of the MG II H and MG II K lines*. **Astron. Astrophys.**, **295**: pp. 517–528 (Mar. 1995).
- Sturrock, P. A. *Model of the High-Energy Phase of Solar Flares*. **Nature**, **211**: pp. 695–697 (Aug. 1966).
- Tandberg-Hanssen, E. *Solar prominences*. Geophysics and Astrophysics Monographs, **12** (1974).
- Testa, P., De Pontieu, B., Allred, J., Carlsson, M., Reale, F. et al. *Evidence of nonthermal particles in coronal loops heated impulsively by nanoflares*. **Science**, **346**: 1255724 (Oct. 2014).
- Tian, H., Young, P. R., Reeves, K. K., Chen, B., Liu, W. and McKillop, S. *Temporal Evolution of Chromospheric Evaporation: Case Studies of the M1.1 Flare on 2014 September 6 and X1.6 Flare on 2014 September 10*. **Astrophys. J.**, **811**: 139 (Oct. 2015).
- Title, A. M. and Schrijver, C. J. *The Sun's Magnetic Carpet*. In R. A. Donahue and J. A. Bookbinder, eds., *Cool Stars, Stellar Systems, and the Sun*, vol. **154** of *Astronomical Society of the Pacific Conference Series*, p. 345 (1998).
- Török, T., Temmer, M., Valori, G., Veronig, A. M., van Driel-Gesztelyi, L. and Vršnak, B. *Initiation of Coronal Mass Ejections by Sunspot Rotation*. **Solar Phys.**, **286**: pp. 453–477 (Sep. 2013).
- Uitenbroek, H. *The MG II H & K Lines as Diagnostics of the Solar Chromosphere*. In M. S. Giampapa and J. A. Bookbinder, eds., *Cool Stars, Stellar Systems, and the Sun*, vol. **26** of *Astronomical Society of the Pacific Conference Series*, p. 564 (1992).
- Vashalomidze, Z., Kukhianidze, V., Zaqarashvili, T. V., Oliver, R., Shergelashvili, B. et al. *Formation and evolution of coronal rain observed by SDO/AIA on February 22, 2012*. **Astron. Astrophys.**, **577**: A136 (May 2015).
- Vernazza, J. E., Avrett, E. H. and Loeser, R. *Structure of the solar chromosphere. III - Models of the*

-
- EUV brightness components of the quiet-sun. Astrophys. J. Suppl.*, **45**: pp. 635–725 (Apr. 1981).
- Wedemeyer, S., Bastian, T., Brajša, R., Hudson, H., Fleishman, G. et al. *Solar Science with the Atacama Large Millimeter/Submillimeter Array - A New View of Our Sun. Space Sci. Rev.*, **200**: pp. 1–73 (Apr. 2016).
- Wedemeyer-Böhm, S. and Rouppe van der Voort, L. *Small-scale swirl events in the quiet Sun chromosphere. Astron. Astrophys.*, **507**: pp. L9–L12 (Nov. 2009).
- Wedemeyer-Böhm, S., Scullion, E., Steiner, O., Rouppe van der Voort, L., de La Cruz Rodriguez, J., Fedun, V. and Erdélyi, R. *Magnetic tornadoes as energy channels into the solar corona. Nature*, **486**: pp. 505–508 (Jun. 2012).
- West, E., Cirtain, J., Kobayashi, K., Davis, J., Gary, A. and Adams, M. *MgII linear polarization measurements using the MSFC Solar Ultraviolet Magnetograph. In Polarization Science and Remote Sensing V*, vol. **8160** of *Proc. SPIE*, p. 816010 (2011).
- West, E. A., Porter, J. G., Davis, J. M., Gary, G. A., Rabin, D. M., Thomas, R. J. and Davila, J. M. *Overview of the Solar Ultraviolet Magnetograph Investigation. In S. Fineschi, C. M. Korendyke, O. H. Siegmund and B. E. Woodgate, eds., Instrumentation for UV/EUV Astronomy and Solar Missions*, vol. 4139 of *Proc. SPIE*, pp. 350–361 (2000).
- Woodgate, B. E., Tandberg-Hanssen, E. A., Bruner, E. C., Beckers, J. M., Brandt, J. C. et al. *The Ultraviolet Spectrometer and Polarimeter on the Solar Maximum Mission. Solar Phys.*, **65**: pp. 73–90 (Feb. 1980).
- Woods, M. M., Harra, L. K., Matthews, S. A., Mackay, D. H., Dacie, S. and Long, D. M. *Observations and Modelling of the Pre-flare Period of the 29 March 2014 X1 Flare. Solar Phys.*, **292**: 38 (Feb. 2017).
- Woods, M. M., Inoue, S., Harra, L. K., Matthews, S. A., Kusano, K. and Kalmoni, N. M. E. *The Triggering of the 2014 March 29 Filament Eruption. Astrophys. J.*, **860**: 163 (Jun. 2018).
- Wright, P. J., Hannah, I. G., Grefenstette, B. W., Glesener, L., Krucker, S. et al. *Microflare Heating of a Solar Active Region Observed with NuSTAR, Hinode/XRT, and SDO/AIA. Astrophys. J.*, **844**: 132 (Aug. 2017).
- Yang, K., Guo, Y. and Ding, M. D. *Quantifying the Topology and Evolution of a Magnetic Flux Rope Associated with Multi-flare Activities. Astrophys. J.*, **824**: 148 (Jun. 2016).
- Young, P. R., Tian, H. and Jaeggli, S. *The 2014 March 29 X-flare: Subarcsecond Resolution Observations of Fe XXI λ 1354.1. Astrophys. J.*, **799**: 218 (Feb. 2015).
- Zhang, H. L., Sampson, D. H. and Fontes, C. J. *Relativistic Distorted-Wave Collision Strengths for the 85 Li-like Ions with $8 \leq Z \leq 92$. At. Data Nucl. Data Tables*, **44**: p. 31 (1990).
- Zharkov, S., Green, L. M., Matthews, S. A. and Zharkova, V. V. *2011 February 15: Sunquakes Produced by Flux Rope Eruption. Astrophys. J. Lett.*, **741**: L35 (Nov. 2011).
- Zharkova, V. V. and Zharkov, S. I. *On the Origin of Three Seismic Sources in the Proton-rich Flare of 2003 October 28. Astrophys. J.*, **664**: pp. 573–585 (Jul. 2007).
-

List of Figures

1.1	Drawing of the solar disk with a number of sunspot groups present, excerpt from Galileo (1613) catalogue of solar observations.	2
1.2	<i>Left Panel:</i> Schematic of the layers of the solar interior. The energy from the nuclear fusion in the Core is transported outwards by collisions within the Radiative Zone, then by convective motions in the Convection Zone, before finally escaping at the solar surface, the photosphere. The transition from radiative to convective dominated transport takes place the thin Tachocline. <i>Right Panel:</i> Solar atmospheric layers. The Photosphere, with its sunspots, the complicated Chromosphere, and the hot Corona with its active regions.	3
1.3	Bound-bound transition schematic for a two-level-atom along with the corresponding Einstein coefficients for that type of transition. The continuous line transition refers to radiative processes, while the dashed lines refers to collisional processes.	8
1.4	Schematic of the Mg II ion transitions discussed and used in our analysis. For simplification, only the first five levels of the Mg II ion are depicted. The <i>k</i> line is shown in blue, while the <i>h</i> line is in red. The subordinate triplet lines are in black. The energy difference between the $3p - 3s$ and the $3d - 3p$ is similar, meaning all of the discussed lines emit within a narrow 15 \AA interval.	8
1.5	Emission profile of Mg II ion in active chromospheric conditions. The positions of the <i>h</i> and <i>k</i> lines are highlighted by the light blue and orange bands, respectively. For the Mg II <i>k</i> line the profile features are indicated by the arrows. The subordinate triplet line positions are also included. The green dashed line represents the quiet sun profile for comparison.	9
2.1	Result of the thermal variation wavelength calibration. Top: The variation of the Ni I 2799.474 \AA line centroid position and the smooth spline fit. Bottom: The NUV and FUV corrections to be applied to the wavelength array.	15
2.2	Quartile based analysis and peak identification.	18
3.1	Schematic representation of the quiet Sun from Wedemeyer et al. (2016) . The horizontal colour bands are defined by the wavelength bands of their ALMA data.	26
3.2	Snapshots in the <i>IRIS</i> SJI data centred on the Mg II <i>k</i> 2796 \AA emission for the four datasets considered. The observed intensities have been normalized to the used exposure time and plotted using the same intensity scaling. The blue and red contours highlight areas of measurable <i>HMI</i> B_{LOS} magnetic field at levels of ± 300 , ± 100 and $\pm 50 \text{ G}$. The vertical dark line represents the position of the <i>IRIS</i> slit.	29
3.3	Temporal evolution of the Mg II <i>k</i> line moments for the QQS dataset (a) and ARQS dataset (b). Left: Integrated intensity with cubic root scaling applied to enhance the variations within the data. Centre: Doppler shift of the line, with blue corresponding to upflows and red to downflows. Right: Variation of line width during the observation. The corresponding colourbar ranges are included at the top of each moment map.	32
3.4	Same as Figure 3.3 for the CHQS1 dataset (a) and CHQS2 dataset (b). The jagged pattern in CHQS2 image is given by the different rasters.	33

3.5	Temporal variation of the intensity of different Mg II profile features for the QQS (a) and ARQS (b) datasets. Left: Mg II k_{2v} peak emission. Centre-Left: Intensity of the Mg II k_3 central reversal. Centre-Right: Mg II k_{2r} peak emission. Right: Intensity of the Mg II k_{1r} outer minima. Cubic root scaling has been applied to all feature maps and the same intensity limits have been applied.	34
3.6	Same as Figure 3.5 for the CHQS1 dataset (a) and CHQS2 dataset (b).	35
3.7	Variation in the computed values for the Mg II k_3 core depth (left), k_2 peak emission asymmetry (centre-left), k_2 peak separation (centre-right) and the $k:h$ ratio (right) for the QQS (a) and ARQS (b) datasets. The colourbar for the scaling of each of the maps has been included at the top of the corresponding panel.	36
3.8	Similar to Figure 3.7 for the CHQS1 (a) and CHQS2 (b) datasets. The CHQS1 dataset does not contain the Mg II h line so the ratio could not be computed.	37
3.9	2D histogram highlighting the correlation between the Mg II k and h line intensities for the QQS (a), ARQS (b) and CHQS2 (c) datasets. The lines represent reference ratio values. In optically thin conditions the ratio of k and h is 2:1. A ratio of ~ 1.2 is typical for the low solar activity regime of the quiet Sun. All panels pertaining to a given dataset have the same colour scale represented by the colourbar on the right.	38
3.10	Gaussian fit of the Integrated intensity distribution for the k line for the different activity levels in the ARQS dataset.	39
3.11	Correlation matrices for all the computed variables for the ARQS dataset. We have used the following abbreviations: B_{LOS} - photospheric magnetic field; D_{k3} - depth of the k_3 central absorption; I_k (q) and I_k (m) - Integrated intensity of the h line from quartile analysis and moment analysis, respectively, similar for I_h (q) and I_h (m); $I_{h1r,h2r,h2v,h3}$ and $I_{k1r,k2r,k2v,k3}$ are the intensities of the emission features for the h and k lines, respectively; R_{k2} - Intensity ratio of the emission peaks; R_{kh} - Ratio of the integrated intensity of the resonance lines; W_{k2} - Emission peaks separation; $\Delta\lambda_D$ - line width of the k line; Δv - Doppler shift of the k line.	41
3.12	<i>HMI/SDO</i> magnetogram, Dopplergram and intensity continuum maps for the ARQS data. The seismic emission at 6 mHz and the local acoustic emission power at 6 mHz highlight the haloes around the main sunspot. The local intensity continuum power at 6 mHz is shown in the last panel. The IRIS slit crosses over a part of the acoustic haloes. Another control “slit” is plotted in orange in the acoustic maps. Bottom row: Spatial profile of the high-frequency seismic emission for the IRIS slit position of under-canopy quiet Sun (black) and the second slit sampling a quiet Sun away from the main sunspot (orange).	43
3.13	QQS: The local response to the photospheric oscillations is represented as the acoustic power $(m/s)^2$ in the 3 mHz and 6 mHz frequency respectively, in the lower frames. Top panels show the seismic emission $(m/s)^2$ maps at 3 mHz and 6 mHz.	44
3.14	As above but for the area of quiet Sun labelled ARQS (see Table 3.1).	44
3.15	<i>HMI/SDO</i> local acoustic power and seismic emission maps of CHQS1 at 3 and 6 mHz. The enhanced 6 mHz local oscillations around the north plages and other magnetic concentrations in the photosphere is evident. Local seismic emission at 6 mHz is detected inside supergranules. Evident absorption of 3 mHz acoustic and seismic power is seen in magnetic regions of $B \approx 90\text{--}110$ G.	45
3.16	An ensemble picture of all 6 mHz acoustic maps for wider regions containing the three regions of quiet Sun: ARQS, QQS, CHQS. The maps emphasize enhanced high-frequency seismic emission in some magnetic areas.	46
3.17	The 6 mHz local acoustic power map of the area including the QQS set: regions of the quiet Sun with a few coloured masks over-imposed which are used for our statistical analysis of distributions. The corresponding histograms are included on the right.	47

4.1	Position of the soft (red) and hard (blue) X-ray kernels with respect to the <i>IRIS</i> slit positions (black vertical lines). The background (red) is <i>AIA</i> 304 emission and the foreground (green) is SJI 1330 Å.	52
4.2	The solar atmosphere prior to the X2.1 flare of March 11, 2015 as seen by <i>IRIS</i> and <i>AIA/SDO</i> . The FOV has been restricted to the <i>IRIS</i> field. The dark vertical line in the SJI images represents the position of the slit. The top row contains the emission of filters containing photospheric contribution, the second row shows chromospheric emission and the last two rows capture the ‘hot’ coronal plasma.	53
4.3	Left: Evolution of the <i>GOES</i> (dashed curves) and <i>RHESSI</i> (continuous curves) high energy emission for the March 11, 2015 X2.1 flare. The vertical black line marks the position of the flare maximum. The vertical dashed lines mark the interval explored in Figure 4.4, while the dotted line points to the position of the spectrum fit included on the right. Right: Total photon spectrum integrated from 16:18:52 to 16:18:56 UT, shown as the black curve. The green, yellow and red curves mark the thermal, non-thermal and total fit components. The vertical lines mark the interval between 10 and 110 keV for which the fit was performed.	54
4.4	Evolution of the thermal (red) and non-thermal (black) energies obtained from the fits of the <i>RHESSI</i> spectrum. The SXR derived DEM is included in green. The spectral index of electron distribution and the cut-off energy for the HXR component are plotted in blue and orange, respectively.	55
4.5	Emission intensity at $y=-175''16$ for the first slit position as recorded in the Mg II window before (bottom) and after the flare maximum (top). The colors denote different time frames and are described by the colorbar on the right. The black dash-dotted line corresponds to quiet sun spectrum, while the black continuous spectrum corresponds to the maximum emission at 16:20 UT, when significant saturation is present. The vertical magenta line corresponds to the Mg II k line rest wavelength.	57
4.6	Evolution of the ‘Mg II window’ of <i>IRIS</i> for solar $y=-175''16$ along the 4 slits.	58
4.7	Spectral moments computed for the Mg II k line: integrated intensity in units of $\text{erg s}^{-1} \text{cm}^{-2} \text{sr}^{-1}$, with a cubic root scaling applied for better contrast (left), Doppler shift in units of km s^{-1} (centre) and line width measured in mÅ (right).	58
4.8	Integrated intensity (left), Doppler shift (centre) and line width (right) for the Mg II subordinate lines blend in the bump between the resonance lines.	58
4.9	Evolution of the ‘C II window’ of <i>IRIS</i> for solar $y=-175''16$ along the slits.	60
4.10	Spectral moments computed for the C II 1334.54 Å line: integrated intensity (left), Doppler shift (centre) and line width (right).	60
4.11	Evolution of the ‘Si IV window’ of <i>IRIS</i> for solar $y=-175''16$ along the slits.	60
4.12	Spectral moments computed for the Si IV 1402.77 Å line: integrated intensity (left), Doppler shift (centre) and line width (right).	60
4.13	Fe XXI 1354.1 Å line emission snapshots at the specified times, corresponding to the first slit position. The emission originates between the flare footpoints and displays variations of intensity, which suggests that different loop tops become visible in this high temperature line. The vertical black line corresponds to the rest wavelength of the transition.	62
4.14	Evolution of ‘O I window’ of <i>IRIS</i> as obtained from three pixel average around $y=-172''67$ for the 4 slits. The narrow line at 1354.28 Å belongs to the C I emission and the far right line at 1355.59 Å pertains to the namesake of the window, the O I. The Fe XXI 1354.1 Å emission dominated across all slit positions near the <i>RHESSI</i> peak.	62
4.15	Spectral moments computed for the Fe XXI 1354.1 Å line: integrated intensity (left), Doppler shift (centre) and line width (right). The line width range has been adjusted for better contrast. The onset of the flare is clearly seen at around 16:16 UT.	62

- 4.16 The filament eruption as seen in the Mg II k line emission of *IRIS* at the first slit position. The emission line first show enhanced linewidths, which develops into a blue-asymmetry that then rapidly expands across $\sim 20''$ in the spectral window. The maximum Doppler shift of the erupting filament is $> 300 \text{ km s}^{-1}$, which slowly decreases as the flux tubes are evacuated. 64
- 4.17 The EM maps prior to the flare event at 16:12 UT (top) at after some of the flaring and saturation had subsided at 16:50 UT (bottom). The vertical black lines represent the corresponding locations of the *IRIS* slits for the *AIA* data used in the inversion. 65
- 4.18 Top: Evolution of the J_z component of the current, scaled between $\pm 60 \text{ mA m}^{-2}$; Bottom: B_z component of the magnetic field, scaled between $\pm 2500 \text{ G}$. The green ellipse shows the region that undergoes important changes as a consequence of the flare, while the magenta ellipse indicates the presence of penumbral intrusion. 67
- 4.19 Linear force free magnetic field extrapolation before the flare (16:00 UT), immediately after the flare peak (16:24 UT) and after the atmosphere began relaxing (16:48 UT). The photospheric vertical field component B_z in the $\pm 2500 \text{ G}$ range is included as the background. The magnetic field along the extrapolated flux tubes is given in the $\pm 1500 \text{ G}$ range. 68
- 4.20 Photospheric data from *HMI/SDO* emphasizing the transients related to the flare: LOS Magnetic field, Intensity continuum, Intensity continuum running difference and Dopplergram running difference. The region between the vertical green lines is sampled by the *IRIS* SG, while the yellow arrows show the strongest transients. The green circles mark the locations of enhanced acoustic power. Red rectangle is the region covered by *IRIS* which we used in our estimations of downflows and interpretation of sunquakes. 69
- 4.21 A composite image showing the location of the main 6 mHz seismic sources. From left to right, top to bottom: 1) the 5–7 mHz seismic emission map of the main sunspot at 16:17 UT, also shown with yellow arrows; 2) LOS magnetic field *HMI/SDO*; 3) Dopplergram map at 16:16 UT; 4) Intensity continuum map for identification of the penumbra boundaries; 5) *IRIS* 2832 Å SJI at 16:16:58 UT; 6) total 5–7 mHz acoustic emission map integrated over 2.5 hours of observation. The colour bar corresponds to the first frame of the 6 mHz egression power map at 16:17 UT. Cyan arrow points at the region which undertook most of dramatic reconfiguration. The vertical white line is the *IRIS* slit. 69
- 4.22 Left: SJI 2832 emission at the flare maximum, together with contours of magnetic field intensity (white) and the locations of acoustic enhancement (red). The vertical teal lines mark the positions of the *IRIS* SG slits. Right: Important positions along the flaring ribbon and outside the flaring region which are explored in Figure 4.23 are marked by black squares. 71
- 4.23 Evolution of *IRIS* SJI intensity at different positions of along the flaring ribbon at locations highlighted in Figure 4.22. The dotted line marks the start of the filament rise, the dashed line marks the start of the flare, while the continuous line is at the position of the *GOES* maximum emission. 71
- 4.24 The solar atmosphere before the X1. flare of March 29, 2014 as seen by *IRIS* and *AIA/SDO*. The FOV has been restricted to the *IRIS* dataset. The dark vertical line in the SJI images represents the position of the slit. The intensity of each image has been adjusted for best contrast. The top row contains the emission of filters containing photospheric contribution, the second row shows chromospheric emission and the last two rows capture the ‘hot’ coronal plasma. 74
- 4.25 Left: The computed acoustic emission map at 6 mHz with white contours marking levels of *HMI* continuum emission. Right: *HMI* B_{LOS} running differences showing the location of magnetic transients associated with the flare. The contours mark continuum (white) and seismic (black) emission. 76

4.26	The <i>IRIS</i> SJI 2832 frame at the flare maximum, with the SG slit positions as the vertical red lines. The white contours mark levels of ± 1500 , ± 1000 and ± 500 G of B_{LOS} field and the blue contours mark the position and extent of the acoustic source. The computed Mg II k profile moments for the raster set between 17:45 and 17:47 UT, capturing the impulsive phase of the flare: integrated intensity, centroid shift and line width.	77
4.27	LOS magnetic field configuration from <i>HMI</i> (top-left) and intensity data from <i>AIA</i> and <i>IRIS</i> SJI, sampling the solar atmosphere during a small scale flare. The black polygon highlights the location of the studied ribbon and the vertical lines mark the <i>IRIS</i> slit position during the observing campaign. The FOV has been restricted to and centred on the flaring ribbon.	78
5.1	Cubic root scaled intensity profiles of the Mg II h and k lines are shown as a function of wavelength and time at $y = -175''$ along the first slit position. Doppler shift scale with respect to the k -line position are also included on the top x -axis. The two profiles shown in Figure 5.3 are from 15:57:51 and 16:32:31 UT positions, indicated by arrows.	84
5.2	<i>IRIS</i> SJI images in the 2832 Å (left) and 1330 Å (right) channels, right before and after the impulsive phase of the March 11, 2015 X2.1 flare. A logarithmic scaling has been applied to SJI1330. The vertical lines are the positions of the <i>IRIS</i> slits during the observation and the oblique dashed line is the lower boundary (in the N-S direction) of the peculiar spectra. Plasma flows can be seen above this dashed line in the SJI 1330 post-flare images.	87
5.3	Typical intensity profiles of the Mg II h and k lines are shown as a function of Doppler shift, for the positions indicated by arrows in Figure 5.1. The two profiles shown are those for 15:57:51 UT (exp. 1), from the pre-flare phase, and those for 16:32:31 UT (exp. 100), from the post-flare phase, respectively. The very broad profiles seen during the later exposure are the focus of the present work.	88
5.4	Doppler shift (top) and line widths (bottom) maps for the Mg II k -line, showing the temporal evolution of the extended redshifted emission for the first slit position. The peculiar emission appears originate from the same region that was swept by the flare ribbon during the impulsive phase. Positive Doppler shift values refer to red shift and negative values to blue shift.	90
5.5	Normalized Intensity vs. line width correlation for all the pixels between $-170''$ and $-180''$. The color represents the time of the observation and the insert represents the data from a QS patch outside the active region.	90
5.6	Vector magnetic field parameters at 16:24 UT. The vertical dashed lines show the positions of the <i>IRIS</i> slit, the solid portion of which approximately shows the extent of very broad lines seen in the Mg II h and k lines shown in previous figures.	91
5.7	Schematic for anisotropic emission for the Mg II k and h lines. Given a strand of width W , the h line (red) will emit isotropically from deeper in the strand, while the k line (blue) emits preferentially perpendicular to the strand. Based on the observer direction, given by an angle ϑ , the intensity of the resonance lines will vary, therefore the $k:h$ will change with the angle ϑ	95

List of Tables

1.1	Important Mg II lines	9
3.1	Summary of the observational properties of the selected datasets.	30
3.2	Solar Y coordinates in arc-seconds for the intervals denoted as Inter-network, Network and Enhanced Network for the different datasets.	30
3.3	Gaussian fit parameters for the profile moments of the Mg II k line and the <i>HMI</i> magnetic field distributions under different activity levels in the datasets: Inter-network, Network and Enhanced Network.	40
3.4	Gaussian fit parameters for the profile feature characteristics under different activity levels in the dataset: Inter-network, Network and Enhanced Network.	40
5.1	Atomic transitions of interest	86
5.2	Observed frequency-integrated emission-line intensity ($\text{erg s}^{-1} \text{cm}^{-2} \text{sr}^{-1}$).	88

